AN INVESTIGATION OF MULTIPLE ORIFICE WALL JETS

A THESIS

Presented to

The Faculty of the Division of Graduate Studies

by

Virgil Kirkland Smith, III

In Partial Fulfillment

of the Requirements for the Degree

Doctor of Philosophy

in the School of Aerospace Engineering

Georgia Institute of Technology

January, 1977

AN INVESTIGATION OF MULTIPLE

ORIFICE WALL JETS

Approved:

J. E. Hubbartt, Chairman

D. P. Giddens

H. M. McMahon

Date approved by Chairman: 2/11/77

ACKNOWLEDGMENTS

I would like to sincerely thank Professor James E. Hubbartt for his suggestion of the thesis topic and for his guidance and encouragement throughout the course of this investigation. I value very highly the knowledge and insights that he has shared with me.

I am indebted to Dr. Howard M. McMahon and Dr. Don P. Giddens for their critique of the original manuscript and their helpful suggestions. The efforts of Dr. Louis H. Bangert and Dr. Gene T. Colwell in their reading and commenting on the original draft are also appreciated.

The fabrication of the test models and the instrumentation of the test rig would not have been possible without the help of many people. I am particularly indebted to Mr. Dewey Ransom and Mr. Harold Meyers for their skillful machining of the test models. I also gratefully acknowledge the assistance of Mr. John G. Palfery in preparing the instrumentation and in applying the computer-based data acquisition system. I also express my thanks to Dr. John C. Handley, Mr. George Bird, Mr. John Caudell, Mr. Bob Daniels, Dr. Douglas H. Neale, and Mr. Darmanshu Antani for their help in various phases of the research.

The assistance of Dr. Robert L. Young of the University of Tennessee Space Institute, and his encouragement of this effort are gratefully acknowledged.

To my parents, who provided encouragement throughout my education, goes my gratitude. Finally, I thank my wife, Patricia, and our children,

Kirk and Alexis, for their love, patience and sacrifice during the many years we have been in school.

TABLE OF CONTENTS

Page

ACKNOWLEDGMENTS ii

LIST OF TABLES vii

LIST OF ILLUSTRATIONS viii

LIST OF SYMBOLS xiii

SUMMARY xv

Chapter

I. INTRODUCTION AND LITERATURE REVIEW 1

Introduction 1

Literature Review 3
Multiple Circular Orifice Free Jet
Single Circular Orifice Wall Jet
Multiple Circular Orifice Wall Jet

Purpose of the Present Investigation 9

II. EQUIPMENT AND INSTRUMENTATION 10

General Facility Description 10

Experimental Configurations 14

Data Acquisition Components 23

III. EXPERIMENTAL PROCEDURE 34

Evaluation of Equipment 34
Temperature Measurement Instrumentation
Pressure Measurement Instrumentation
Bourdon-tube Barometer
Pressure Acquisition System
Probes
Probe Traverse
Test Bed Grid

Flow Measurement Procedures 42
Mainstream Flow

TABLE OF CONTENTS (Continued)

Chapter — Page

Jet Flow
Jet Plenum Conditions
Jet Profiles

Data Acquisition and Reduction. 45
Setting and Stabilization of Flow Conditions
Locating Probes
Calibration and Checks of Data Acquisition System
Data Acquisition
Data Reduction

IV. RESULTS AND DISCUSSION. 51

Areas of Investigation. 51
Phase 1
Phase 2
Phase 3

Flow Evaluation 54
Phase 1
Phase 2
Phase 3

Results 63
Wall Jet Growth
Wall Jet Velocity Decay
Wall Jet Velocity Profile Similarity
Wall Jet Iso-velocity Profiles
Wall Jet Integrated Velocity Profiles
Wall Jet Skin Friction
Friction Coefficient
Law of the Wall

V. CONCLUSIONS 188

VI. RECOMMENDATIONS 191

Appendices

A. PHASE 1 EXPERIMENTAL DATA 193

B. PHASE 2 EXPERIMENTAL DATA 205

C. PHASE 3 EXPERIMENTAL DATA 249

D. DERIVATION OF INTEGRATED MEAN THICKNESSES 293

TABLE OF CONTENTS (Continued)

Page

BIBLIOGRAPHY 296

VITA 299

LIST OF TABLES

Table		Page
1.	Phase 1 Data Index.	105
2.	Phase 2 Data Index.	106
3.	Phase 3 Data Index.	107
4.	Wall Jet Characteristic Thicknesses, Phase 3.	173

LIST OF ILLUSTRATIONS

Figure		Page
1.	Wall Jet Test Facility Floor Plan	11
2.	Experimental Test Bed	13
3.	Two-dimensional Jet Nozzle Assembly	16
4.	Multiple Orifice Wall Jet, Basic Configuration	18
5.	Multiple Orifice Jet Nozzle Block, Basic Configuration	19
6.	Multiple Orifice Wall Jet, Integrated Configuration	20
7.	Multiple Orifice Jet Nozzle Block, Integrated Configuration	21
8.	Multiple Orifice Jet Nozzle Assembly	22
9.	Total Pressure Probe Geometry	24
10.	Static Pressure Probe Geometry	25
11.	Thermocouple Probe Geometry	26
12.	Preston Probe Geometry	27
13.	Probe Actuator Assembly	28
14.	Typical Pressure Sensing Sequence	31
15.	Data Acquisition System	32
16.	Probe Pitch and Yaw Sensitivity	39
17.	Typical Combined Influence of Yaw Angle	40
18.	Wall Jet Velocity Profile Nomenclature	108
19.	Phase 1 Composite Wall Jet Development for the Basic Multiple Orifice Configuration	109
20.	Phase 2 Composite Wall Jet Development for the Integrated Multiple Orifice Configuration	110

LIST OF ILLUSTRATIONS (Continued)

Figure		Page
21.	Phase 3 Composite Wall Jet Development for the Integrated Multiple Orifice Configuration	111
22.	Jet Vertical Velocity Profile at the Exit	112
23.	Jet Horizontal Velocity Profile at the Exit	113
24a.	Phase 1 Downstream Flow Evaluation.	114
24b.	Phase 1 Downstream Flow Evaluation.	115
24c.	Phase 1 Downstream Flow Evaluation.	116
25.	Phase 2 Downstream Flow Evaluation.	117
26.	Phase 3 Mainstream Dynamic Pressure Survey.	118
27.	Phase 3 Mainstream Boundary Layer Evaluation.	119
28.	Phase 3 Mainstream Boundary Layer Momentum Thicknesses	120
29.	Phase 3 Downstream Flow Evaluation.	121
30.	Phase 3 Downstream Momentum Thicknesses	122
31.	Phase 3 Downstream Integrated Momentum Thicknesses	123
32.	Phase 1 Wall Jet Growth	124
33.	Phases 1 and 2 Wall Jet Growth.	125
34.	Phase 2 Wall Jet Growth	126
35.	Phases 2 and 3 Wall Jet Growth.	127
36.	Phase 1 Wall Jet Velocity Decay	128
37.	Phases 1 and 2 Wall Jet Velocity Decay.	129
38.	Phase 2 Wall Jet Velocity Decay	130
39.	Phase 2 Wall Jet Velocity Decay	131
40.	Phases 2 and 3 Wall Jet Velocity Decay.	132

LIST OF ILLUSTRATIONS (Continued)

Figure		Page
41.	Phase 3 Wall Jet Velocity Decay	133
42.	Comparisons of Wall Jet and Free Jet Velocity Decay	134
43.	Phase 2 Wall Jet Velocity Decay	135
44.	Profile Similarity Parameter.	136
45.	Phase 1 Wall Jet Velocity Profile	137
46.	Phase 2 Wall Jet Velocity Profile	138
47.	Phase 2 Wall Jet Velocity Profile	139
48.	Phase 2 Wall Jet Velocity Profile	140
49.	Phase 2 Wall Jet Velocity Profile	141
50.	Phase 2 Wall Jet Velocity Profile	142
51.	Phase 2 Wall Jet Velocity Profile	143
52.	Phase 2 Wall Jet Velocity Profile	144
53.	Phase 2 Wall Jet Velocity Profile	145
54.	Phase 2 Wall Jet Velocity Profile	146
55.	Wall Jet Velocity Profile; Definition of Δ_2 and Δ_j.	147
56.	Phase 2 Wall Jet Velocity Profile	148
57.	Phase 2 Wall Jet Velocity Profile	149
58.	Phase 2 Wall Jet Velocity Profile	150
59.	Profile Similarity Parameter.	151
60.	Phase 3 Wall Jet Velocity Profile	152
61.	Phase 3 Wall Jet Velocity Profile	153
62.	Phase 3 Wall Jet Velocity Profile	154
63.	Phase 3 Wall Jet Velocity Profile	155

LIST OF ILLUSTRATIONS (Continued)

Figure		Page
64.	Phase 3 Wall Jet Velocity Profile	156
65.	Phase 3 Wall Jet Velocity Profile	157
66.	Phase 3 Wall Jet Velocity Profile	158
67.	Phase 3 Wall Jet Velocity Profile	159
68.	Phase 3 Wall Jet Velocity Profile	160
69.	Phase 3 Wall Jet Velocity Profile	161
70.	Phase 3 Wall Jet Velocity Profile	162
71.	Phase 2 Iso-velocity Profiles	163
72.	Phase 2 Iso-velocity Profiles	164
73.	Phase 2 Half-velocity Growth.	165
74.	Phase 3 Iso-velocity Profiles	166
75.	Phase 3 Iso-velocity Profiles	167
76.	Wall Jet Displacement Thickness Distribution.	168
77.	Wall Jet Momentum Thickness Distribution.	169
78.	Wall Jet Energy Thickness Distribution.	170
79.	Wall Jet Shape Factor Distribution.	171
80.	Wall Jet Characteristic Thicknesses	172
81.	Wall Jet Displacement Thickness	174
82.	Wall Jet Momentum Thickness	175
83.	Wall Jet Energy Thickness	176
84.	Wall Jet Displacement Thickness	177
85.	Wall Jet Momentum Thickness	178
86.	Wall Jet Momentum Thickness	179

LIST OF ILLUSTRATIONS (Continued)

Figure		Page
87.	Wall Jet Skin Friction.	180
88.	Wall Jet Skin Friction.	181
89.	Wall Jet Skin Friction.	182
90.	Law of the Wall	183
91.	Law of the Wall	184
92.	Wall Sublayer Velocity Profile.	185
93.	Law of the Wall	186
94.	Law of the Wall	187

LIST OF SYMBOLS

C_f	friction coefficient ($C_f = \tau_o/q$)
d	jet orifice diameter; 0.444 inch
h	plane jet slot height
h_{eq}	equivalent jet slot height $\left(\frac{\text{flow area}}{\text{jet span}}\right)$; 0.0567 inch
$\dot{m}$	mass flow rate
P	total pressure, gage
p	static pressure, gage
q	dynamic pressure
r_o	jet radius
Re_s	Reynolds number based on slot height $\left(Re_s = \frac{u_j h_{eq}}{\nu}\right)$
Re_d	Reynolds number based on jet diameter $\left(Re_d = \frac{u_j d}{\nu}\right)$
s	distance between adjacent jets; 2.727 inches
T	temperature
u	velocity
u_j	jet velocity based on ideal expansion to ambient
u_{mid}	maximum velocity at z = 1.363 inches
u_τ	friction velocity
x	cartesian coordinate (streamwise)
Y,y	cartesian coordinate (normal to wall)
Z,z	cartesian coordinate (lateral)
δ	velocity profile thickness parameter
δ_j	jet layer length scale (Figure 44, Chapter IV)

LIST OF SYMBOLS (Continued)

Δ_j	lateral length scale (Figure 55, Chapter IV)
Δ_2	lateral length scale (Figure 55, Chapter IV)
Δ	difference
δ^*	displacement thickness
θ	momentum thickness
δ^{**}	energy thickness
ν	kinematic viscosity
ρ	gas density
τ_w	local skin friction
π	Coles' [36] profile matching parameter
λ	Coles' [36] streamwise decay of shear stress parameter

Subscripts

a	ambient
o	jet exit plane and mainstream reference plane
1	jet peak (Figure 18, Chapter IV)
2	half velocity, jet layer (Figure 18, Chapter IV)
c	revised centerline
e	edge
i	indicated
I.M.	integrated mean
I.P.	integrated profile
j	theoretical jet
max	maximum
min	minimum
t	total

SUMMARY

An experimental study of various three-dimensional wall jet flows was conducted in the Georgia Tech wall jet facility. This investigation was made to obtain data needed on wall jets issuing from multiple circular orifices discharging parallel to the surface. This three-dimensional (3-D) configuration is attractive from both jet persistence and structural considerations. Synthesis and analysis of these three-dimensional data have been conducted in order to compare the behavior of this configuration with the single circular orifice and two-dimensional wall jet results of others and to determine the potential of these techniques for boundary layer control (BLC) applications.

The major areas of investigation were:

1. A geometrically-simple circular orifice wall jet configuration discharging into still air.
2. A circular orifice wall jet incorporating integrational refinements discharging into still air.
3. The "integrated" wall jet configuration under a constant-pressure mainstream flow.

The investigation proceeded systematically from a basic three-dimensional wall jet flow to more complex flows. The studies of the basic and integrated wall jet configurations without mainstream flow established the characteristics of these wall jet flows. The investigation of the integrated wall jet configuration with a mainstream flow provided important

additional data for understanding and using such a configuration in BLC applications.

Detailed velocity profile and skin friction measurements were made. The studies were carried out at two markedly different Reynolds numbers. For the investigation with mainstream flow, a jet-to-mainstream velocity ratio was chosen to provide data in a practical range of wall jet applications. In each of the studies, measurements were made at several streamwise distances from the point of jet injection. Measurements were also made at numerous lateral stations, providing detailed definition of the three-dimensional flow development and interaction.

The growth of the characteristic dimensions of the jet and the decay of the jet velocity are presented for all wall jet studies. In addition, vertical and lateral velocity profile similarity are described. The multiple jet surveys are synthesized and analyzed in order to quantify the flow development. Skin friction laws are demonstrated, and "law of the wall" descriptions are evaluated for the three-dimensional wall jet. Finally, the velocity profile and skin friction measurements are presented in tabular form for those desiring more detail on these wall jet flows.

CHAPTER I

INTRODUCTION AND LITERATURE REVIEW

Introduction

Advanced boundary layer control (BLC) technology offers the means for providing attached flow behavior under aerodynamic conditions which could otherwise cause flow separation. This technology is required since aerodynamic loading on lifting or thrusting surfaces is limited by boundary layer separation; large increases in the aerodynamic loading may be obtained by artificially precluding that separation. Specifically, by either removing or energizing the low velocity boundary layer flow, large adverse pressure gradients are attainable without boundary layer separation. This technology is especially important for STOL aircraft concepts [1] which require high wing loading [2] at low forward speeds in order to reduce the takeoff, approach and landing distances. The use of efficient BLC concepts also offers performance gains for diffusers, as utilized both in thrust augmenting ejectors and aircraft inlets. High performance of thrust augmenting ejectors, an attractive V/STOL propulsion concept [3,4,5], is characterized by large diffuser area ratios with high rates of diffusion [6,7]. However, this performance is limited by flow separation. Suppression of the separation results in more efficient diffusion and increased diffuser expansion rates [8]. Boundary layer control can also be applied to the diffusers of aircraft engine inlets in order to preclude boundary layer separation

and the resulting losses in total pressure recovery and airflow delivery uniformity [9]. These same BLC techniques can also be used to reduce the flow separation losses in the stator passages of rotating turbomachinery [10]. The importance of BLC has been recognized since the advent of boundary layer theory, and it is widely used in critical flows, such as in supersonic inlets. However, more efficient and lightweight BLC designs are essential for many advanced technology applications.

Most previous investigations of BLC methods have concentrated on boundary layer removal by distributed suction and boundary layer energization by blowing. BLC using distributed suction is considered to have limited applicability. Both the structural difficulties [11] and its sensitivity to the potential flow conditions [12] have been prohibitive for aircraft applications.

Boundary layer control by blowing is considered the most promising approach for STOL and aircraft diffuser applications because of the high energy air sources available with each of these devices. In addition, with blowing, the resulting wall jet mixes with the mainstream flow providing potential for a momentum augmentation, rather than the momentum loss incurred with suction BLC.

Numerous fundamental investigations of wall jets generated by blowing from a slot have been reported in the literature [13,14,15,16]. In addition, several investigators have addressed the application of a continuous slot BLC system to wide angle diffusers [8,17]. However, it is structurally preferable to emit the BLC jet from a series of discrete nozzles, rather than from a continuous, uniform slot. Additionally,

both the initial rate of decay of the wall jet velocity and the surface shear losses are expected to be lower for the discrete nozzles than for the continuous slot since the ratio of the jet surface to flow area is smaller. This enhances boundary layer control in the downstream region.

The merits of multiple orifice wall jets are relatively unexplored. Data regarding their growth, decay and behavior after merger are ill-defined, and the modification of these characteristics by the presence of a freestream flow are unknown. The investigation described herein is concerned with providing this information.

This research has consisted of a systematic investigation of two multiple circular orifice wall jet configurations. The first configuration, which is designated the "basic" design, provides a performance baseline against which can be compared a configuration which is more suitable for practical application. The latter configuration is termed the "integrated" design. The specific features of the investigation are detailed in Chapter IV.

Literature Review

Relatively few investigations of single-orifice three-dimensional wall jets and only one investigation of multiple orifice wall jets have been reported in the literature. In addition, one investigation of a multiple orifice free jet has been reported. The results of these studies, which are of particular importance for the present investigation, are summarized in the following paragraphs.

Multiple Circular Orifice Free Jet

In 1964, R. Knystautas [18] reported the results of an experi-

mental and theoretical investigation of flow from a series of closely spaced, uniform, circular free jets in line, discharging into still air. The investigator predicted that these jets merged and yielded two-dimensional turbulent jet flow at some downstream station. The theoretical analysis utilized Reichardt's hypothesis for turbulent shear stress in a free jet to linearize the equation of motion for the mean velocity. This enabled superposition of the mean velocity for multiple interfering jets, and the prediction of both the start of the two-dimensional flow and the location of the hypothetical origin. The experimental investigation, which included three different circular orifice nozzle spacings, showed that the jets indeed merged into an effectively two-dimensional jet at approximately twelve hole spacings downstream of the exit. The theoretical predictions agree reasonably well with the experiments. Of particular interest from a BLC viewpoint was the result that, at any particular position, the downstream velocity is higher for the ultimate two-dimensional jet produced with a series of nozzles than for a continuous slot. For a given jet momentum per unit width, the ultimate velocity increases with the hole spacing. The implication for BLC is that if the three-dimensional wall jet also becomes effectively two-dimensional downstream, analogous results regarding downstream velocity would offer an improvement in jet persistence over comparable two-dimensional wall jet results. In the case of the wall jet, these improvements might be mitigated by surface friction losses and changes in the lateral spreading due to the confinement of the wall.

Single Circular Orifice Wall Jet

In 1968, S. K. A. Naib [19] reported an experimental investigation of a circular air jet exhausted parallel to a wall into quiet air. Experiments were carried out to establish the shape of the velocity profiles, the decay of maximum velocity, and the rate of growth of the jet over a range of 0 to 50 nozzle diameters downstream. From examination of the maximum velocity decay, Naib described four distinct regions of flow: (i) region A of potential core extending about two nozzle diameters from the orifice; (ii) region B of transition flow that extends up to eight diameters; (iii) region C of established flow which extends to about thirty diameters and in which the velocity varies linearly with distance; and (iv) region D of terminal flow in which the residual velocity decays more rapidly as a result of large scale turbulence, and in which the velocity again varies linearly with distance. Naib also reported that in regions C and D there was flow similarity of the non-dimensionalized velocity profiles for the outer half of the jet (taken normal to the plate). By contrast, the non-dimensionalized lateral velocity profiles along the horizontal centerline showed some variation with distance, especially at the outer edges of the jet. The normal velocity profiles for the inner half of the jet were shown to vary appreciably from the Blasius $1/7^{th}$ power law. This variation from the power law is also typical of the wall layers for two-dimensional wall jets. Naib also showed that the jet boundaries increase linearly and confirm the different regions of flow indicated by the decay of maximum velocity. Of particular significance to decay and entrainment consider-

ations is the fact that the rate of spreading parallel to the wall is about six to eight times greater than that normal to it. Due to the broadening effect of the wall on the jet, the increased surface area of the jet becomes available for mixing, which results in greater expansion of the lateral boundaries and slightly faster reduction of velocities than in the case of the free jet. The accuracy of Naib's data presentation is not sufficient to reveal any sensitivity to jet Reynolds number.

In 1971, J. F. Foss and S. J. Kleis [20] reported a theoretical and experimental study of the single round jet/plane wall flow field. This investigation, which was motivated by externally blown flap STOL aircraft considerations, focused on the near field (i.e., within five nozzle diameters) of the jet, for impingement angles between the axisymmetric jet axis and the plane wall of 0 to 15 degrees. Nozzle heights of 0.75, 1.0, 1.5 and 2.0 jet diameters above the wall and two exit flow conditions (fully developed pipe flow and a relatively uniform exit velocity condition) were examined. The authors used the conservation laws and the Reichardt hypothesis to describe the axisymmetric portion of the jet prior to interaction with the wall; good agreement was shown for the short jet development range considered. The velocity measurements before and after impingement were used to define isotach contours giving a graphical representation of the jet development; values of mass, momentum and energy flux were calculated at these same stations to provide a quantitative measure of the three-dimensional jet field. Because of the limited jet development range and the specialized geometry considered in this study, only limited comparisons with the present inves-

tigation are possible.

In 1972, Newman, Patel, Savage and Tjio [21] conducted a theoretical and experimental investigation of an incompressible three-dimensional wall jet originating from a single circular orifice. The jet was exhausted parallel to the plate into quiescent surroundings and was examined over a range of 8 to 200 nozzle diameters downstream. The experimental investigation included measurements of mean velocity and longitudinal turbulence intensity profiles in air and water using hot-wire and hot-film anemometers. An approximate similarity analysis was used to predict that the two transverse length scales and the inverse of the mean velocity scale grow linearly with distance downstream from the orifice; this behavior was experimentally verified. The authors also reported that the longitudinal mean velocity profiles are similar, and, if taken sufficiently far downstream, the non-dimensional mean profiles are in very good agreement both with comparable measurements for two-dimensional wall jets and with the exponential profile widely used in free shear flows. Similarly, it was shown that at 150 nozzle diameters downstream, the non-dimensional velocity profiles for various lateral stations also plot on a single curve. The authors also showed that the distributions of longitudinal maximum mean velocity versus lateral location for various downstream locations plotted on a single curve, the shape of which is in agreement with that of the non-dimensional vertical velocity profiles. While the quantity of data reported was insufficient to verify Naib's "four distinct flow regions," the authors did confirm the former's boundary growth measurements by showing that the rate of

growth of the length scale in the lateral direction was about seven times greater than that of the length scale normal to the wall. The non-dimensional longitudinal turbulence intensities were found to be approximately 50 percent higher than those measured in a two-dimensional wall jet. Insufficient data were reported to reveal any sensitivity of the results to jet Reynolds number.

Multiple Circular Orifice Wall Jet

In 1957, Chesters, Holden and Robertson [22] reported an experimental investigation of protective air curtains created when wall jets are discharged into a still environment. The nozzle configurations used included a single circular nozzle, a single rectangular nozzle, multiple circular nozzles, multiple rectangular nozzles, and a continuous slot nozzle, each of which was located approximately one-sixteenth inch above the wall surface. The authors were concerned with the gross characteristics of the flow. Determination of specific results from their data is difficult. In addition, their multiple circular nozzles yielded highly asymmetrical flow. However, careful replotting of their results reveals that at far downstream stations, a smaller rate of velocity decay exists for the multiple circular orifice wall jet than for the single circular orifice. This provided some support for the suspicion that the individual wall jets merge into an effectively two-dimensional wall jet at some downstream station. However, additional data are required to confirm this result, as well as to identify the specific behavior of multiple circular orifice wall jets.

Purpose of the Present Investigation

An experimental investigation was made to obtain needed data on multiple circular orifice wall jets, a configuration which is attractive from both jet persistence and structural considerations. Synthesis and analysis of these three-dimensional data have been conducted in order to compare the behavior of this configuration with the single circular orifice and two-dimensional wall jet results of others and to determine the potential of these techniques for BLC applications.

CHAPTER II

EQUIPMENT AND INSTRUMENTATION

The experimental portion of this investigation has utilized the Georgia Tech wall jet test facility. A general description of the facility and a specific description of the modifications required for the experimental configurations are included in this chapter. A description of the instrumentation required for test measurements is also included.

General Facility Description

A diagram of the wall jet test facility is shown in Figure 1. This facility consists of separate jet and mainstream air flow systems which are ducted together at the test section where the two flows interact. Downstream of the test section, the mixed flow is discharged through a single control valve. The jet and mainstream flows are supplied by separate compressors capable of continuous, steady flow operation. The following paragraphs briefly describe the features of this facility; a detailed discussion of the facility is contained in reference 13.

Mainstream flow is provided by a single stage centrifugal compressor driven by a 60 HP constant speed motor; the unit will supply an air flow rate in excess of 10,000 SCFM. The air flow from this blower is first discharged through a perforated baffle tube into a large plenum to eliminate the nonuniformities generated by the blower. The flow is

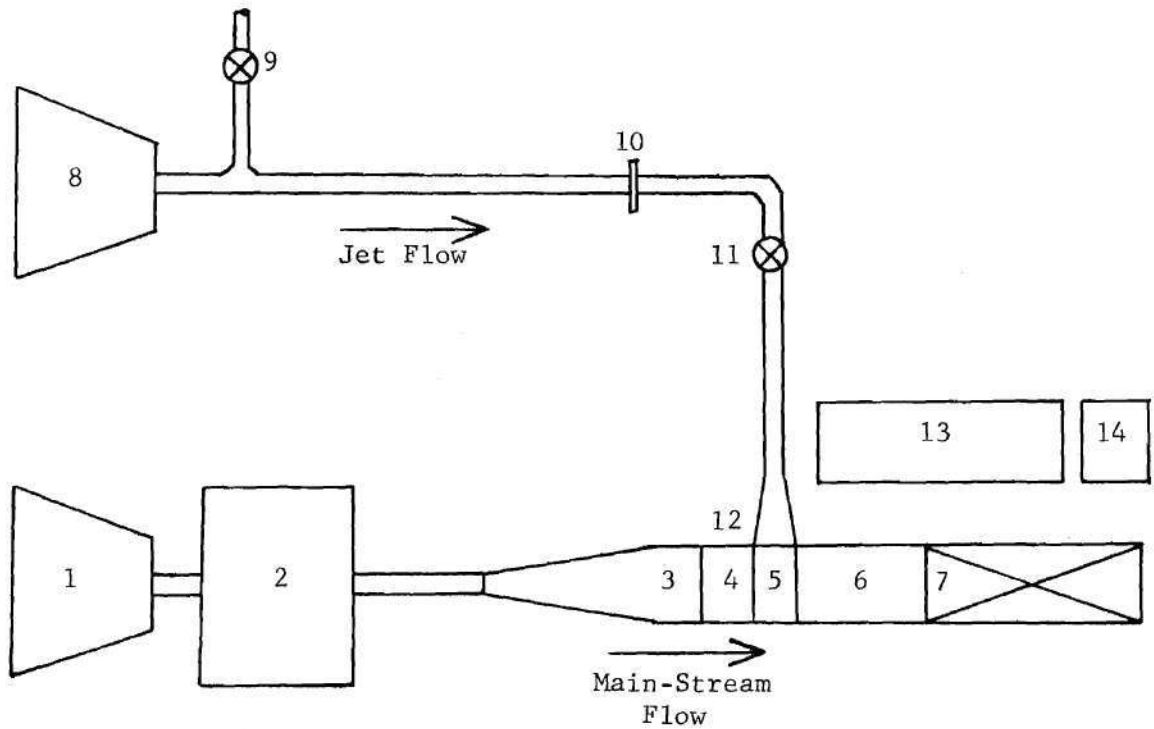

1. Main-stream Blower
2. Main-stream Plenum and Baffle
3. Main-stream Transition and Diffuser Combination
4. Boundary Layer Development Section
5. Jet Slot Section
6. Wall Jet Test Section
7. Main-stream Control Valve
8. Jet Compressor
9. Dump Valve
10. Orifice Meter
11. Jet Control Valve
12. Conical Jet Diffuser
13. Air Supply Control Panel
14. Instrumentation Panel

Figure 1. Wall Jet Test Facility Floor Plan

then accelerated through a circular bellmouth into a duct containing a deep-celled honeycomb flow straightener (cell depth-to-width = 6.5) and lint screen. The mainstream is then brought through a combination transition duct and diffuser to a 16 inch by 30 inch rectangular cross section. At the exit of this transition duct the flow is passed through five separate 36 mesh, 0.0065 inch wire diameter, stainless steel screens to insure uniform flow distribution and to eliminate any large scale turbulence. This mainstream flow is then introduced into the test bed illustrated in Figure 2. The inlet to the test bed is formed by a symmetrical fairing which reduces the cross section from the 16 by 30 inch duct to an 8 by 30 inch test section geometry. After passing through a boundary layer development section, which is 18 inches long, the mainstream flow enters the 36 inch long test section at a velocity of approximately 125 feet per second and interacts with the jet flow. These combined flows then pass through the downstream control valve.

The jet flow is provided by a five stage centrifugal compressor driven by a 75 HP constant speed motor; the unit will supply a flow rate of approximately 1500 SCFM at jet velocities up to approximately 800 feet per second. The jet compressor discharge incorporates a flow dump valve which is operated pneumatically from the control panel; this valve allows controlled discharge of excess flow in order to avoid compressor surge when a low jet flow is needed. The required jet air flow is ducted successively through an orifice run, a throttling valve, a diffuser, a plenum, and a series of screens before entering the test section. A standard flow orifice is located in a six inch diameter seamless aluminum

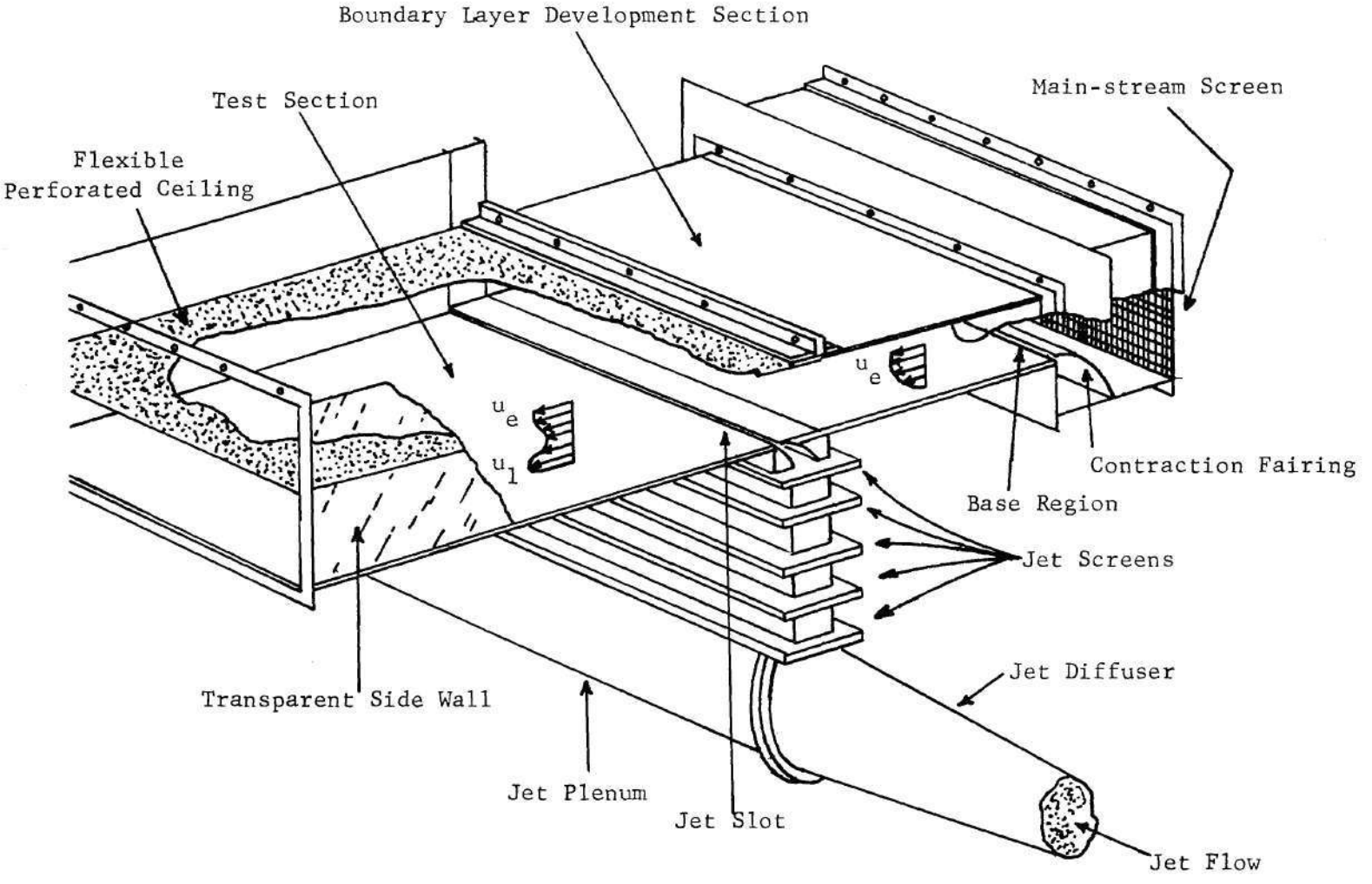

Figure 2. Experimental Test Bed

pipe with 34 and 9 diameters of straight run upstream and downstream of the orifice plate, respectively. This orifice run is equipped with flange pressure taps and a thermocouple probe located five diameters upstream of the plate. Following passage through a throttle valve downstream of the orifice, the flow is ducted through a five degree conical diffuser into a 12 inch diameter by 30 inch long plenum. The diffuser and plenum are shown in Figure 2. The flow from the jet plenum is ducted upward to the jet nozzle through a 2 inch by 30 inch rectangular duct. The flow is then passed through four equally spaced, 24 mesh, 0.0075 inch wire diameter, stainless steel screens to eliminate flow nonuniformities and large scale turbulence. Finally, the jet flow is accelerated and turned parallel to the test section floor by the jet nozzle, and then discharged into the test section, as illustrated in Figure 2.

The test section side walls are constructed of clear plexiglass to facilitate observation of flow visualization studies and to allow precise location of test probes. The precision ground aluminum plate floor incorporates static pressure taps along the test bed centerline and offset 7.5 inches to the right and left of the centerline. The test section also incorporates provision for imposing pressure gradients on the interacting flows with a perforated ceiling, shown in Figure 2, and an adjustable downstream control valve.

Experimental Configurations

Research on the wall jet test facility prior to that reported herein had addressed the characteristics of a two-dimensional (2-D) wall

jet [13], as illustrated in Figure 2. These jets discharged from slots measuring 30 inches in width and having heights of 0.056 inch and 0.155 inch. To examine the performance of multiple circular orifice wall jets, a modification to the jet nozzle was required. This modification was guided by four considerations [23]. First, in order to provide a basis for comparison of the multiple orifice results with the previous 2-D investigations, a common jet discharge area was desired. Second, it was desirable to have an odd number of orifices so that the individual nozzles could be symmetrically spaced about one located at the center of the 30 inch span. Additionally, it was desired that the nozzle spacing be selected to provide approximately 4.5 inches of downstream jet development before merger of the individual jets, assuming a 15° lateral spreading rate [19]. Finally, it was necessary that any rig modifications for the multiple nozzle be reversible, so that, if desired, the 2-D jet could be examined further.

The 2-D jet configuration, shown in Figures 2 and 3, consisted of two 30 inch long, precision machined nozzle blocks attached with transition pieces to the jet plenum. The multiple nozzle designs which satisfied the design criteria in this effort utilized a machined nozzle block which fits as an extension to the 2-D nozzle blocks. The nozzle block was manufactured from aluminum to an overall tolerance of ± 0.004 inch. The 11 circular nozzles were formed by thin-walled, seamless, stainless steel tubing inserts which were interference-fitted in the drilled and radiused orifices of the nozzle block. Each nozzle was 0.444 inch in internal diameter. The 11 nozzles were spaced on 2.727 inch centers

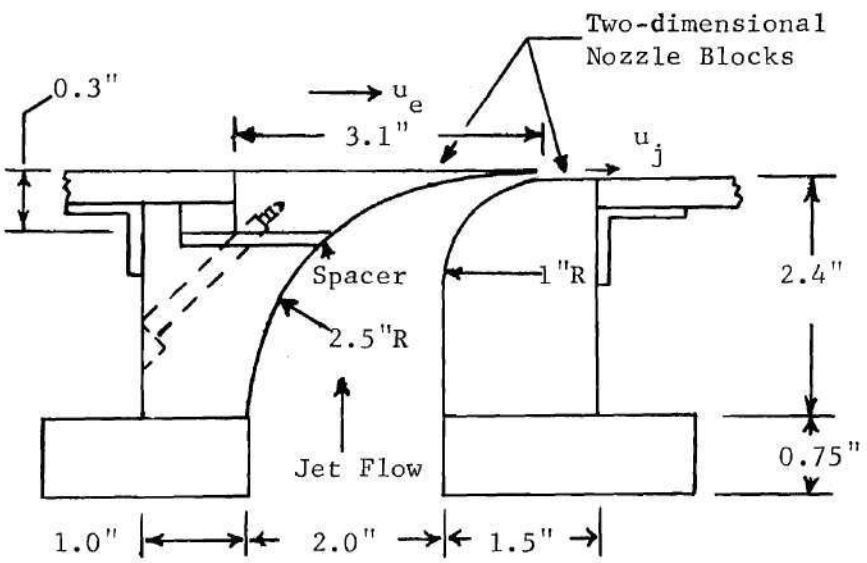

Figure 3. Two-dimensional Jet Nozzle Assembly

across the 30 inch test bed span. The resulting flow area of 1.702 square inches was approximately one percent larger than that of the 0.056 inch 2-D slot.

Two circular orifice wall jet configurations were used in the investigation. The basic configuration features discharge of multiple circular jets parallel to the wall, as shown in Figure 4. A detailed cross section of the nozzle block is shown in Figure 5. The basic configuration was tested to determine its behavior without freestream flow and to provide a performance baseline. Preliminary testing of the basic configuration with freestream flow revealed that flow separation existed between the circular orifices. The integrated configuration incorporates simple, straight geometry fairings or ramps between each nozzle. These provide a reduction in the between-nozzle mainstream flow turning angle from 30° to 13°. This integrated design, shown in Figure 6, provides smooth turning of the freestream flow without flow separation, and is a suitable configuration for integration in a wing or ejector installation. The between-nozzle fairings, which are shown in the nozzle cross section of Figure 7, span the distance between nozzles to within 0.059 inch of each nozzle and extend 1.534 inches downstream of the nozzle exits. The ramps were cast of polyester resin (Ditzler 999) in a precision machined mold and were attached to the nozzle block using silicone rubber adhesive. Accurate positioning of the parts was provided by a precision machined spacing plate.

The multiple orifice nozzle block was joined to the two-dimensional nozzle blocks as shown in Figure 8. The block was aligned and retained

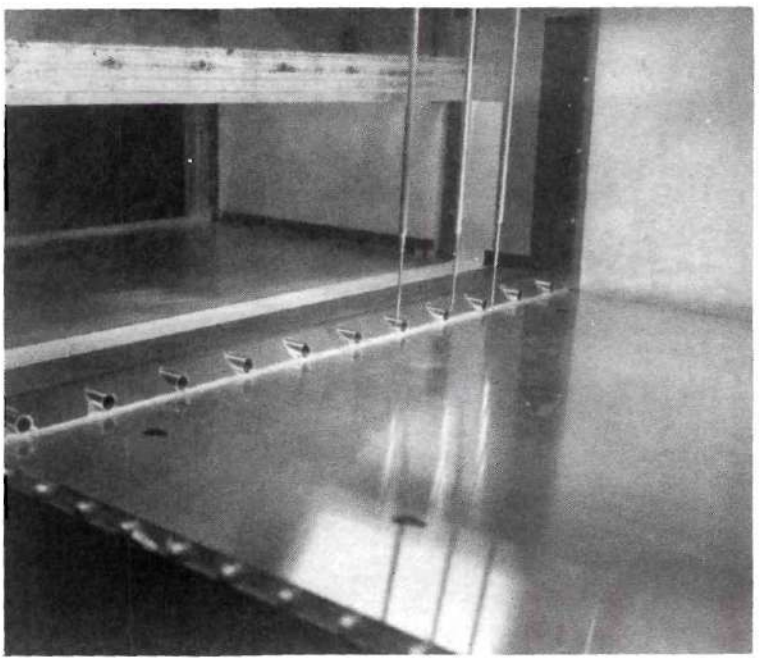

Figure 4. Multiple Orifice Wall Jet, Basic Configuration

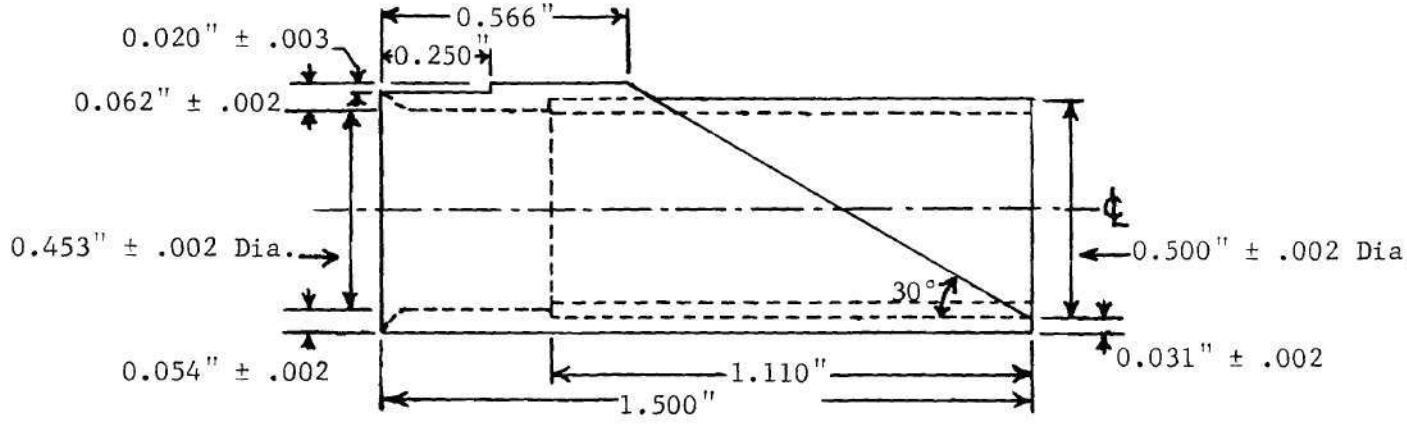

Figure 5. Multiple Orifice Jet Nozzle Block, Basic Configuration

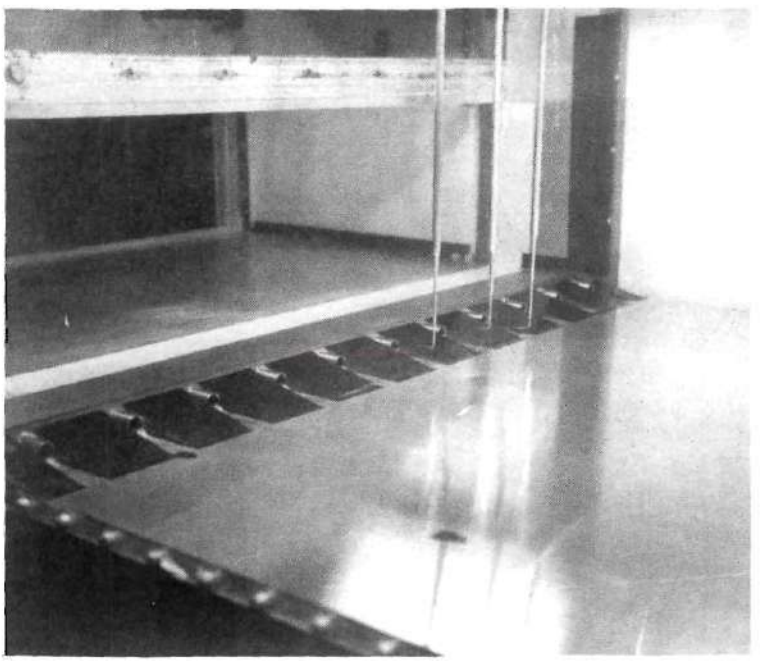

Figure 6. Multiple Orifice Wall Jet, Integrated Configuration

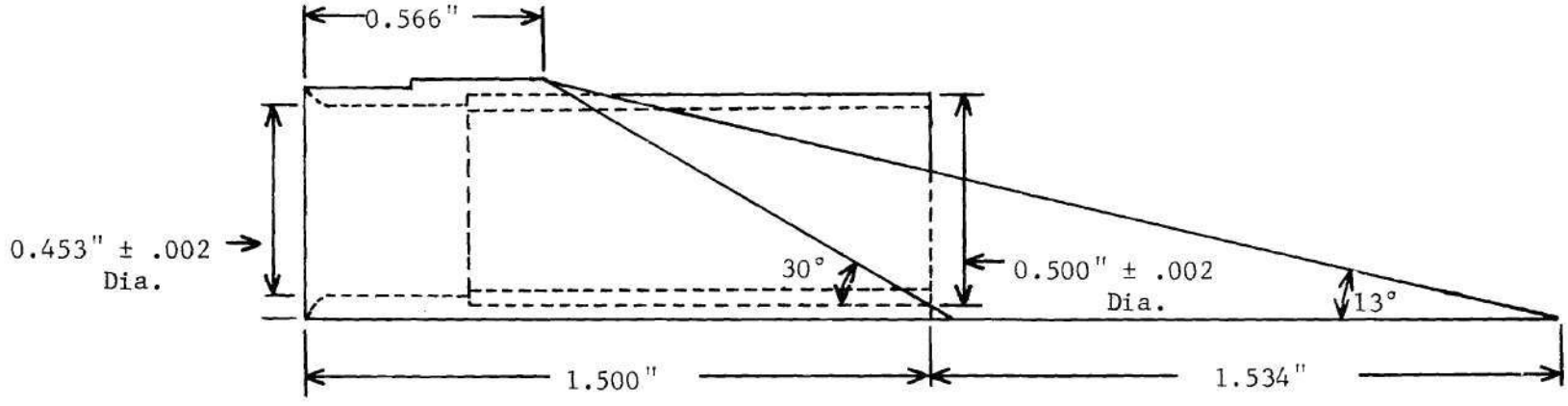

Figure 7. Multiple Orifice Jet Nozzle Block, Integrated Configuration

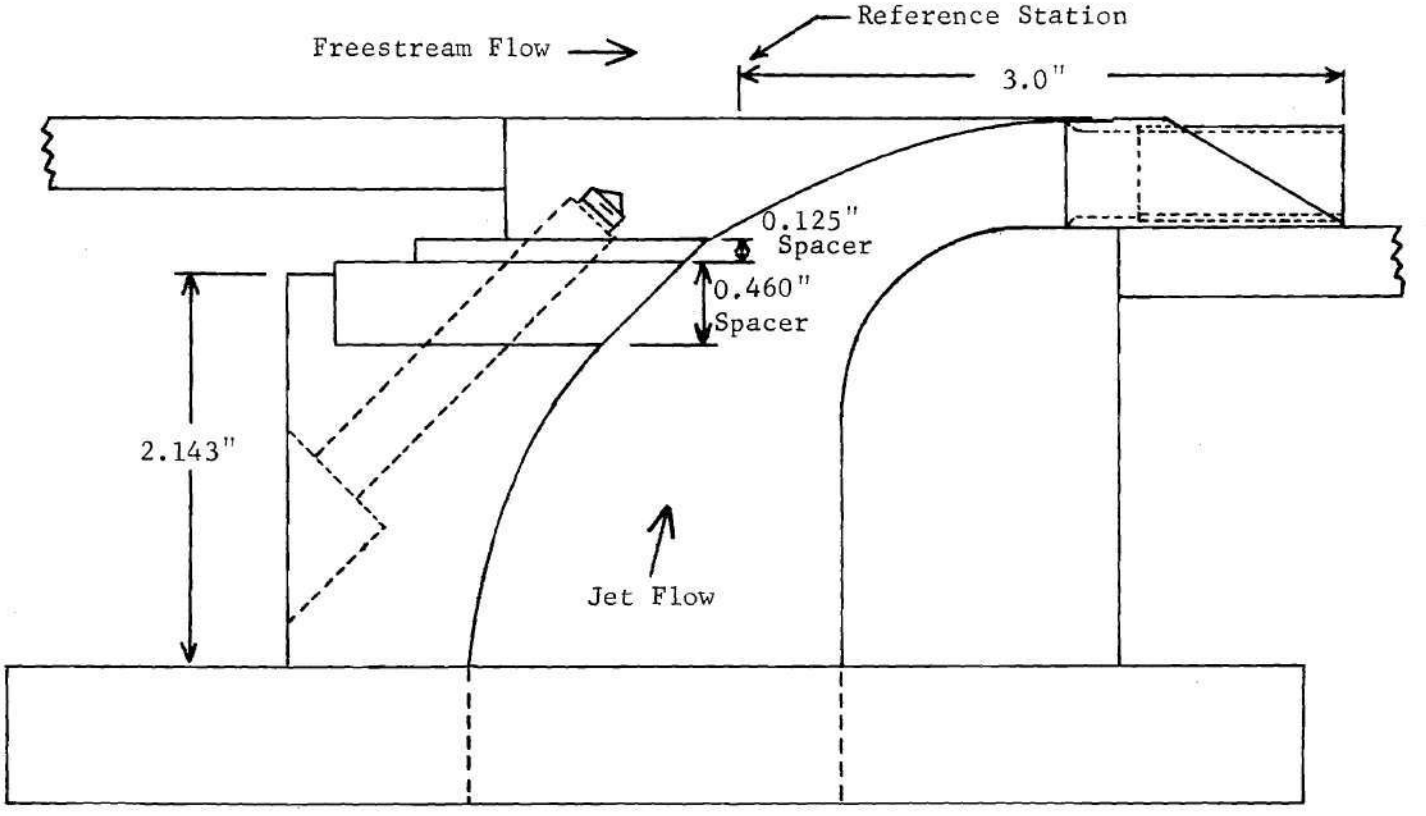

Figure 8. Multiple Orifice Jet Nozzle Assembly

in position by 0.25 inch machine screws in the test bed side walls, and was sealed to the upper and lower two-dimensional nozzle blocks using silicone rubber adhesive. The installed nozzle block positioned the centerline of the individual nozzle exits 0.331 inch above and parallel to the test section floor. The installation used a 24 mesh, 0.0075 inch wire diameter, stainless steel screen across the inlets of the multiple orifice nozzle block to provide uniform flow in the individual nozzles.

Data Acquisition Components

The velocity profile data of this investigation were determined using pressure measurements from flat-tip pitot probes and static probes, in conjunction with temperature measurements from a copper-constantan thermocouple probe. Skin friction measurements were made using a 0.014 inch outside diameter, circular tip Preston tube. Probe geometries are shown in Figures 9, 10, 11 and 12. Jet plenum and orifice conditions were measured using circular-tip pitot probes, orifice flange pressure taps and copper-constantan thermocouples.

The probes were mounted in an actuator located out of the flow field above the test section. The actuator, along with its support and traverse system is shown in Figure 13. The actuator was manually translated, both laterally and longitudinally, parallel to the test bed floor on two horizontal sets of rigid circular guide rods. The actuator was translated vertically along a third set of guide rods, in increments of 0.001 inch, by a remotely controlled stepping motor (Superior Electric Company, Model SLO-SYN-HS25). The motor was coupled to the actuator by an accurate, zero backlash, lead screw drive (Saginaw Ball Nut Model

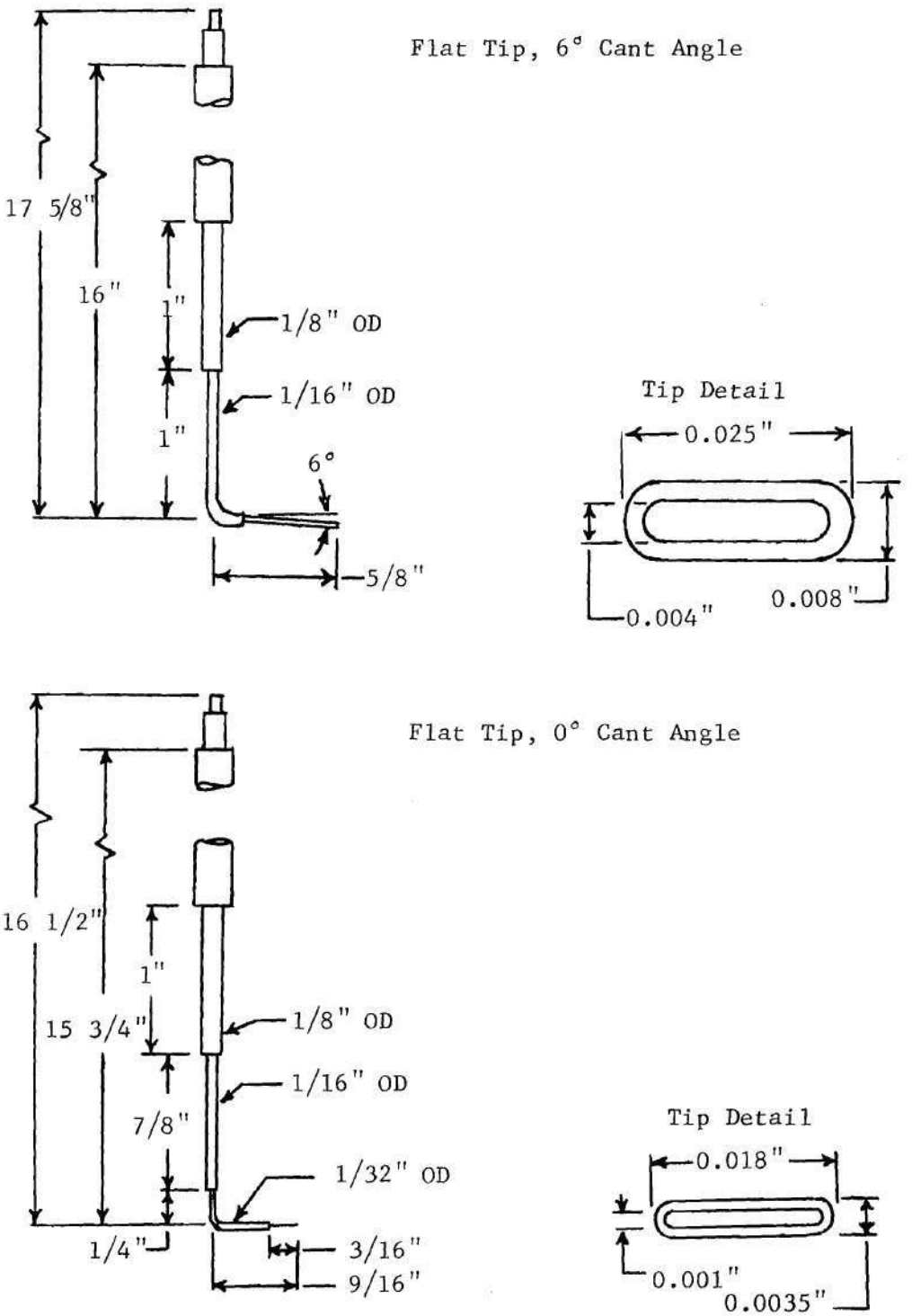

Figure 9. Total Pressure Probe Geometry

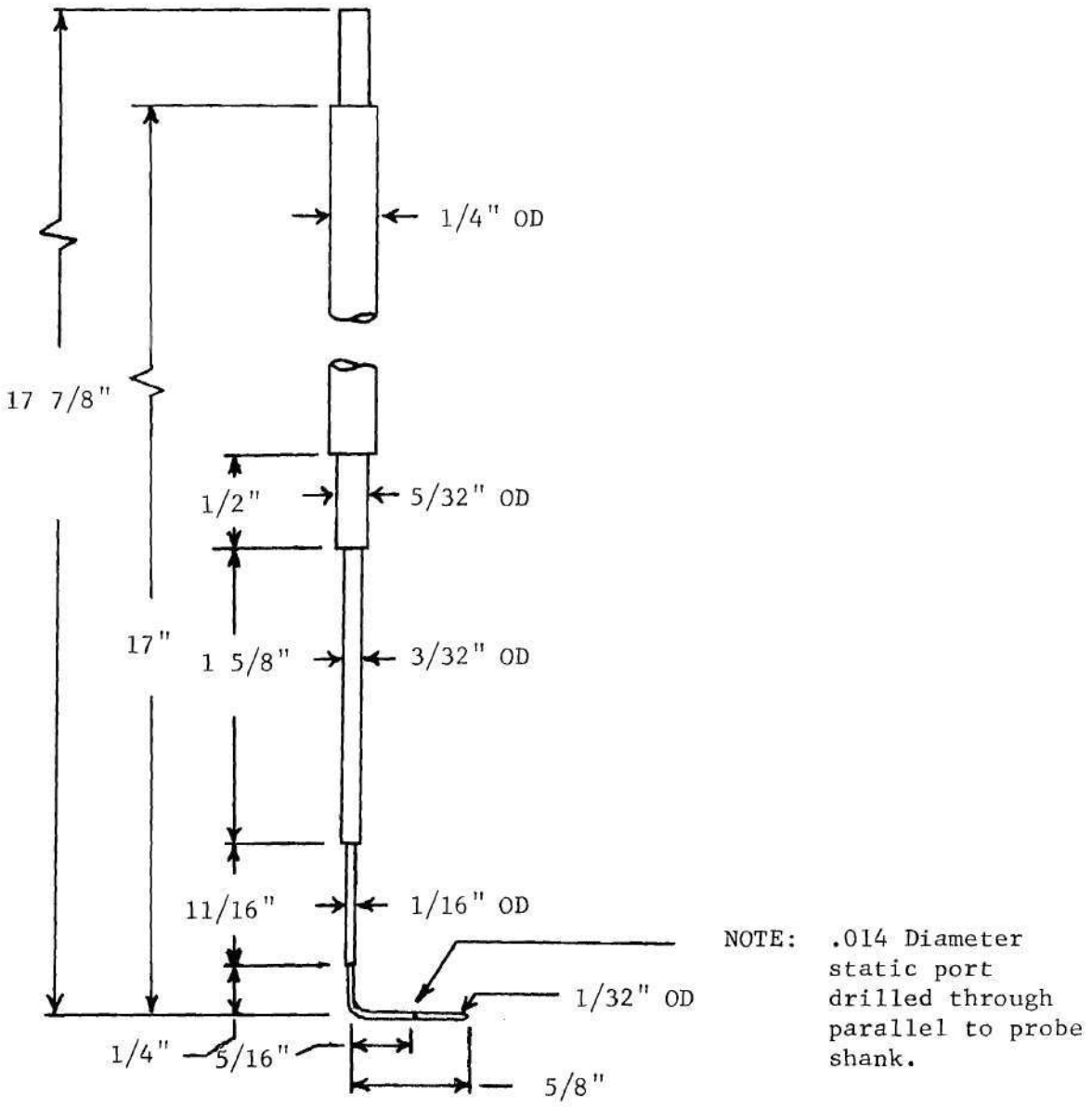

Figure 10. Static Pressure Probe Geometry

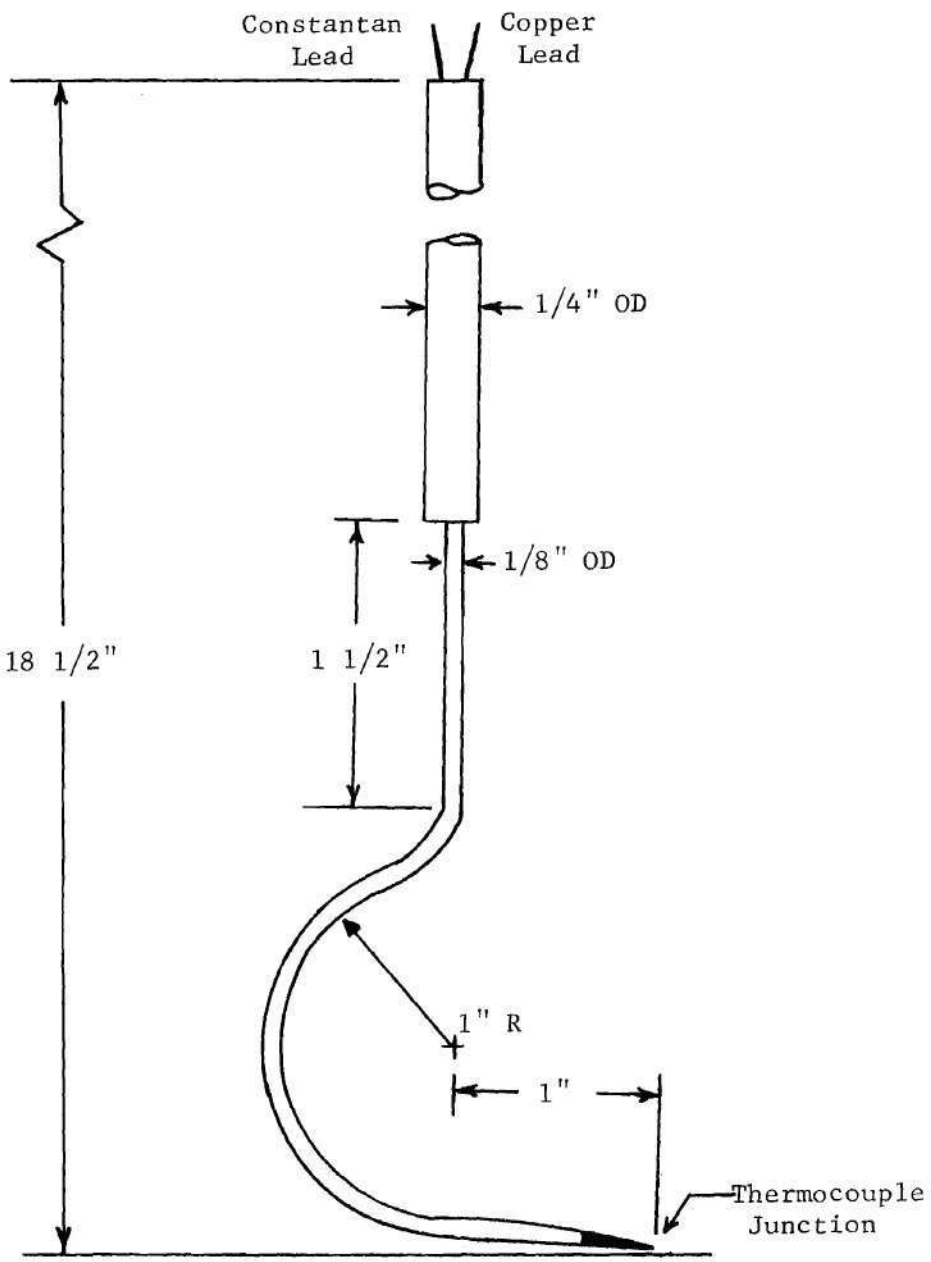

Figure 11. Thermocouple Probe Geometry

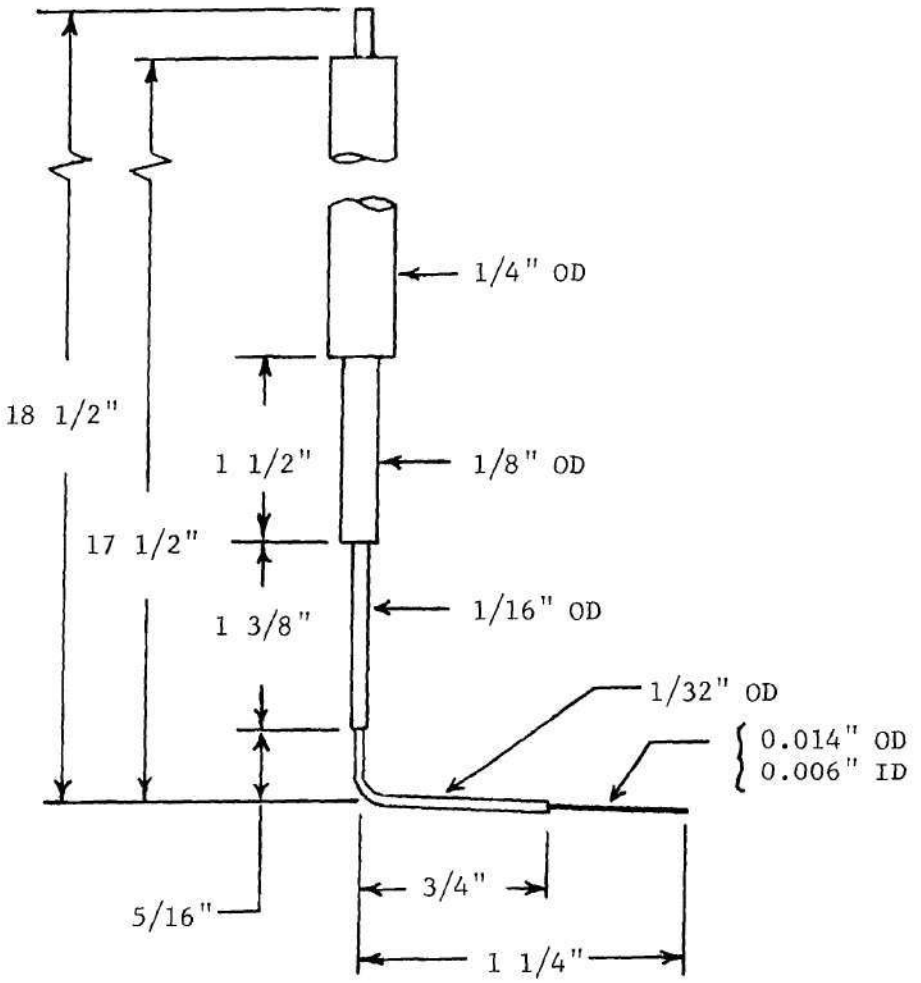

Figure 12. Preston Probe Geometry

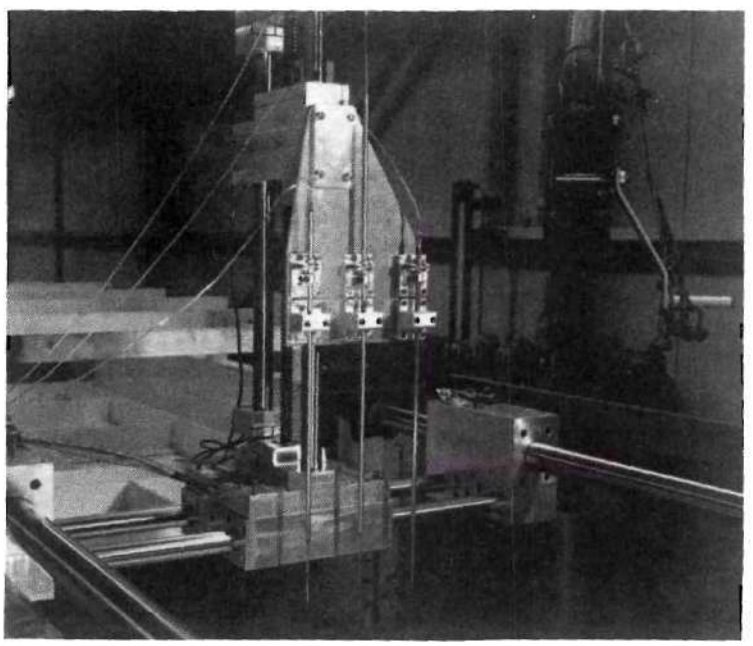

Figure 13. Probe Actuator Assembly

5703039 with Saginaw Ball Bearing Screw Assembly Model 0631-0200 SRT). The position of the probe relative to a datum was monitored using an electronic counter. The actuator could traverse three probes simultaneously, each spaced 2.727 inches apart in the carriage; this spacing corresponds to the individual nozzle centers.

Test pressures were measured with three highly stable and linear, variable capacitance pressure transducers (CGS Scientific, Datametrics Division, Type 501) in conjunction with three Barocel Electronic Manometer signal conditioners (CGS Scientific, Datametrics Division, Type 1015). A 10 mm mercury maximum Δp transducer was employed for measuring the lower pressure differentials, and two 1000 mm Hg maximum Δp transducers were employed for higher differentials. Each transducer output was passed through a separate signal conditioner equipped with an automatic ranging feature to amplify the transducer output; this allowed increased accuracy for small pressure readings. The signal conditioner output was displayed on a digital voltmeter.

Four 48 channel Scanivalve units (Scanivalve Inc., Model 48J4GM) and four Scanivalve fluid switch wafers (Type W1) were used for rapidly sampling all pressures, periodic checks of transducer zero shifts, and periodic comparison of all transducers. The wafer switch provided convenient biasing of the test and ambient pressure. The Scanivalve units were actuated by a five channel solenoid controller (Scanivalve Inc., Model CTLR2/5X54). One Scanivalve unit and wafer switch combination was used to sample static pressure readings; one was used to sample profile and plenum total pressure; and the remaining two units sampled flow

orifice pressures. A typical pressure sensing sequence is shown schematically in Figure 14.

In order to maintain constant jet conditions during testing, an additional pressure read-out channel consisting of a 1000 mm Hg maximum Δp transducer, fluid switch wafer and signal conditioner was used to continuously monitor plenum chamber stagnation pressure. The output was displayed on a digital voltmeter.

Ambient pressure at the test site was measured by a calibrated Bourdon-tube barometer (reading uncertainty of $\pm$ 0.01 inch Hg). Ambient temperature was measured by a mercury thermometer of laboratory quality (reading uncertainty of $\pm$ 0.5°F).

Test temperatures were measured using copper-constantan thermocouples with a precision thermocouple reference junction (Pace Engineering Company, Model BRJR13).

The tests were controlled and the data were recorded using a Hewlett-Packard Automated Data Acquisition System consisting of a Model 2114B computer with 8K words of core storage, a Model 2401C Integrating Digital Voltmeter, featuring automatic ranging and six digit display, a Model 2752A Teletype and Tape Punch and a computer interface for connecting 30 data channels to the digital voltmeter (DVM). A block diagram showing functions of the system is shown in Figure 15. The computer was programmed to step the probe actuator vertically using a translator controller (Superior Electric Company, Model SLO-SYN-STL 800 BV), to cycle the Scanivalves using the solenoid controller, to cycle the data channel scanner (Monsanto, Model 508A), to initiate sampling and to record voltmeter readings for all pressure and temperature input channels, to perform

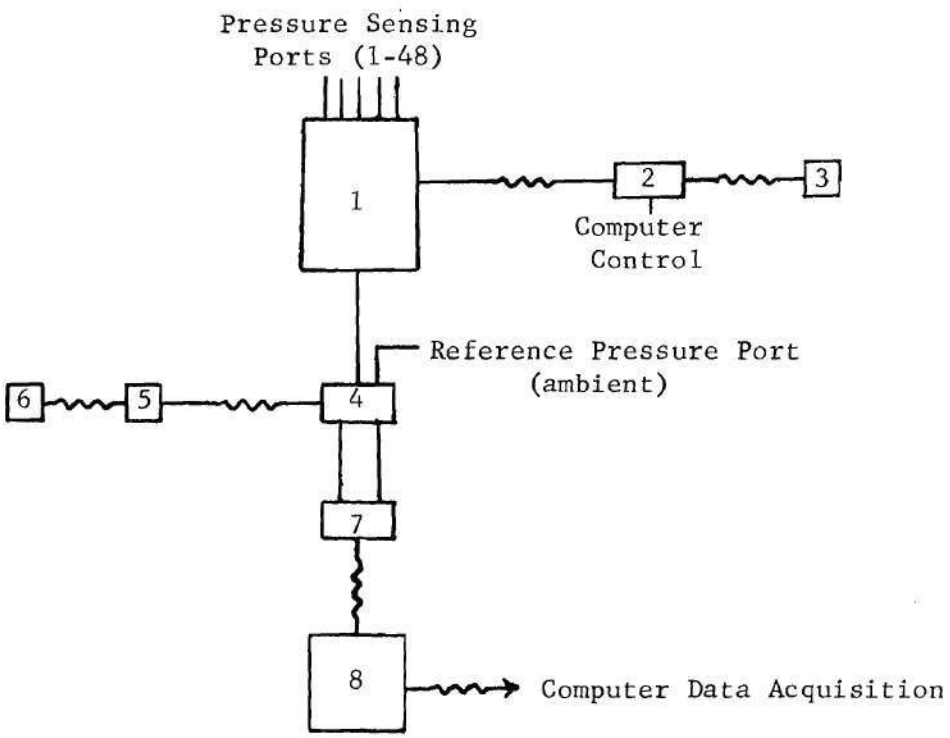

Pneumatic Path

Electrical Path

1. Scanivalve Unit
2. Solenoid Driver
3. Port Indicator
4. Fluid Switch Wafer
5. Solenoid Driver
6. Position Indicator ("Read" or "Null")
7. Pressure Transducer
8. Signal Conditioner

Figure 14. Typical Pressure Sensing Sequence

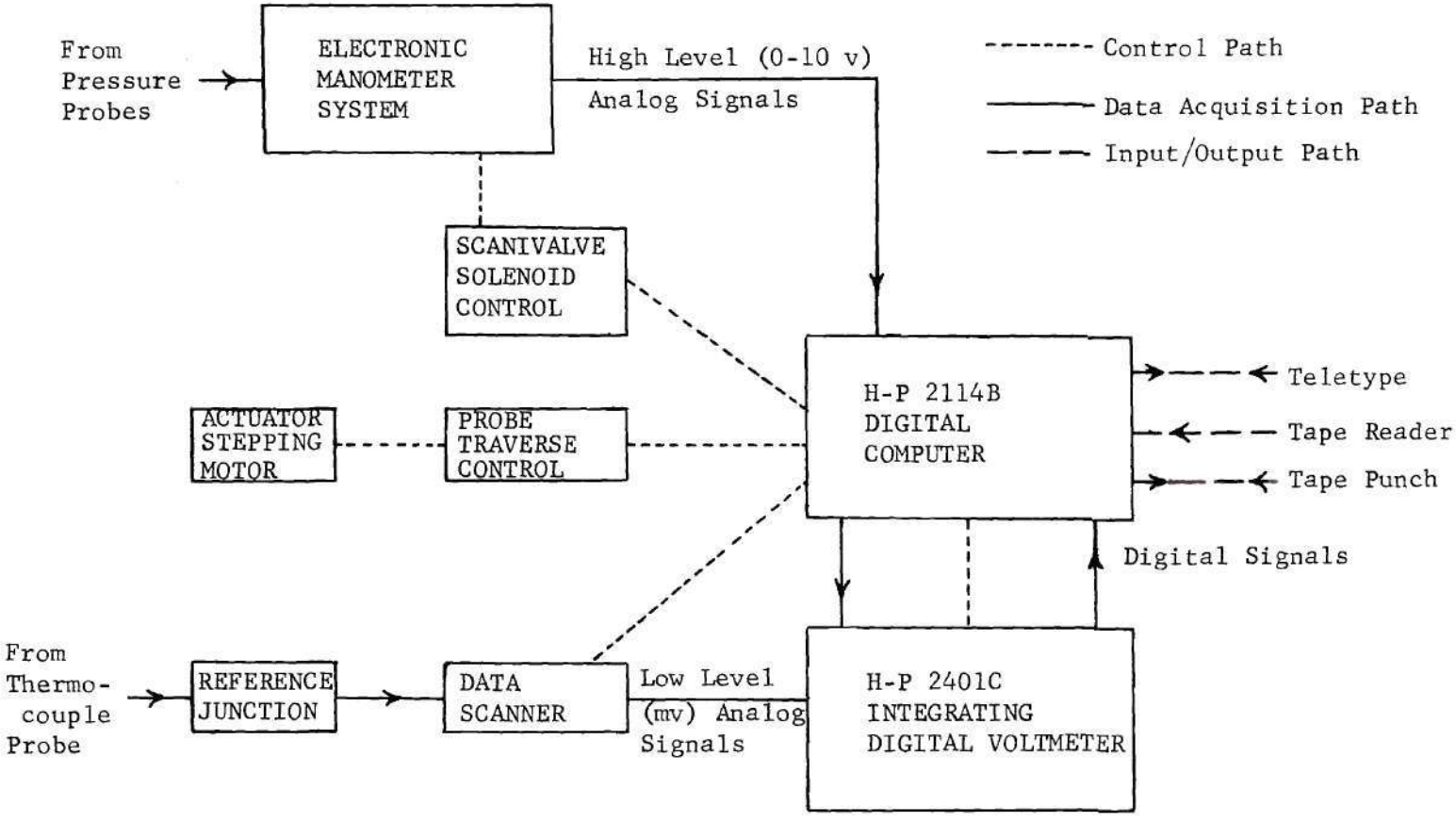

Figure 15. Data Acquisition System

simple on-line data reduction calculations, and to output the data on the teletype and/or tape punch.

The quality of the pressure and temperature data was enhanced considerably by integrating the data input to the DVM over a period of one second. This period is considered of sufficient length to provide a very accurate measurement of the mean value of pressure and temperature. Additionally, this measurement technique allowed determination of the mean value without the need for electronic damping of the signal, as is required for manually recording the value from a non-integrating digital voltmeter. The data quality was further enhanced by computer averaging of five to ten samples from a single source.

CHAPTER III

EXPERIMENTAL PROCEDURE

The techniques used to evaluate the accuracy of the experimental measurements are described in this chapter. The general methods for measuring the jet and mainstream flows and of acquiring and reducing the experimental data are also presented.

Evaluation of Equipment

Temperature Measurement Instrumentation

The four thermocouple probes used for flow temperature measurement were calibrated against a laboratory quality mercury thermometer graduated in 0.5 degree Fahrenheit increments as a standard. The thermometer and probes were placed in a distilled water bath which was heated incrementally through a range of temperatures comparable to those encountered in the test program. (The flows exhibited temperatures of 10-90°F above ambient due to the compression process.) The thermocouple outputs were read by the computer data acquisition system, and were used to define an empirical temperature-emf relation. The incremental heating of the probes and thermometer was then repeated, using the experimentally determined relation to calculate probe temperatures. The two types of instruments differed by no more than one degree Fahrenheit throughout the range of temperatures investigated.

Pressure Measurement Instrumentation

Bourdon-tube Barometer. A precision mercury-column barometer, accurate to ± 0.001 inch of Hg, was used as a standard for calibration of the test site barometer. The comparison was conducted over a period of several weeks in order to establish a significant range of pressures. After an initial adjustment, all readings of the Bourden-tube barometer agreed within 0.01 inch of Hg over the entire range of barometric pressures recorded. Periodic comparisons were made thereafter to assure that this accuracy was maintained.

Pressure Acquisition System. The three independent pressure measuring systems, each composed of a Scanivalve unit, fluid switch wafer, pressure transducer and signal conditioner, were compared using the computer data acquisition system before and after each major segment of research. To accomplish this comparison, each pressure system was used to monitor the same pressurized plenum chamber while using ambient pressure as a reference. The test consisted of incrementally loading and relieving the plenum pressure and recording the output of each system at every plateau. The comparison of the single 10 mm Hg and two 1000 mm Hg transducers was over the complete range of the smaller capacity transducer, and the comparison of the two 1000 mm Hg transducers was over their entire range.

The difference between the 10 mm Hg and the 1000 mm Hg transducer systems was typically less than 0.4% of the reading; the maximum difference ever observed was less than 0.8% of the reading. The 1000 mm Hg transducer systems usually differed by less than 0.2% of the reading;

the maximum disagreement ever observed was less than 0.6% of the reading. These results are within the manufacturer's specifications for these transducer systems.

As a further check on the accuracy of the pressure measurement system, individual Barocel transducers were periodically calibrated using a dead weight tester, an accepted laboratory standard. Comparison over the full range of the 1000 mm Hg transducers was not possible due to limitations of the dead weight tester. However, over the complete range of the 10 mm Hg transducer and up to approximately 250 mm Hg for the 1000 mm Hg transducers, the units were found to measure the impressed pressure with an accuracy of from 0.2 to 0.4% of the reading. This behavior is consistent with the comparisons discussed above. Periodic calibrations were made thereafter to assure that this accuracy was maintained. Additionally, in an investigation of pressure measurement standards, Utterback and Griffith [24] found the variable capacitance pressure transducer to be a highly stable and precise measurement device.

Since the flow under consideration in this investigation was very nearly incompressible, percentage velocity errors vary approximately as the square root of the corresponding dynamic pressure error. For the small magnitude of errors discussed above, the resulting velocity error is roughly one half of the dynamic pressure error and the resulting flow momentum error is roughly proportional to the dynamic pressure error.

The pressure measurement systems were checked frequently for leakage. The ports of each pressure system were sequentially pressurized to approximately mid-range of their respective transducers and were

sealed at that pressure. The pressure decay due to leakage was monitored on a digital voltmeter and was found to be less than 0.25% of the reading per minute. Since the response time of the system was of the order of five seconds, this leakage rate was insignificant.

Probes. Two different flattened-tip pitot probes were used in determination of velocity profiles in the present work. One configuration features a flattened-tip tube canted downwards at a 6° angle to the flow direction, while the other has a flattened-tip tube facing directly into the flow. The latter probe was used in the combined flow studies to minimize the influence of flow pitch angularity. These probes are shown in Figure 9. Neale [13] previously compared the measurements of these two probes with a circular-tip probe in a two-dimensional boundary layer flow; the probes were carefully aligned with the flow. No significant effects of the probe geometry were detected, even in the region near the surface.

Because the spreading of the multiple orifice jets introduced yaw and larger pitch components to the flow sensed by the probes, it was necessary to determine their yaw and pitch sensitivity. Likewise, the sensitivity of the static pressure probe, which was used both in evaluating the velocity profile and in the skin friction measurements, had to be determined. Thus, an investigation was conducted utilizing the computer data acquisition system, the probe actuator, and, in turn, the two flat-tip pitot probes and the static pressure probe. The probes were positioned outside the boundary layer in the mainstream flow. The investigation consisted of orienting the probes both parallel to the flow

and inclined at several angles to the flow, simulating either pitch or yaw flow components. For each orientation, the ratio of the difference between the indicated pressure at the inclined orientation, P_{t_i} or p_i, and the indicated pressure at the parallel orientation, P_t or p, to the mainstream dynamic pressure, q_o, defines the probe pressure error due to a non-parallel flow component. The results of this investigation are shown in Figure 16. They indicate that pitch and yaw affect the probes comparably, and that for yaw or pitch angles less than 5°, a pressure error of less than 1% is measured. It should also be noted that the errors in total and static pressure increase quite rapidly for yaw or pitch angles greater than 5°, but these errors tend to compensate one another in calculations of velocity. This fact is demonstrated in Figure 17, where the velocity error resulting from the combined yaw errors of the 0° cant total pressure probe and the static pressure probe are displayed in terms of the indicated and actual velocities. It is also noted that the asymmetry in the response of the probes to pitch and yaw are the result of probe geometry and, probably, probe imperfections. It was concluded from this study that the influence on the velocity calculation due to flow pitch and yaw components was not significant.

The 0.014 inch diameter Preston-type probe used in skin friction determinations in this investigation was previously calibrated by Neale [13]. The close agreement demonstrated in that calibration with the results of Patel [25] served as justification for using the latter's equation in evaluating skin friction from the measurements in the present work.

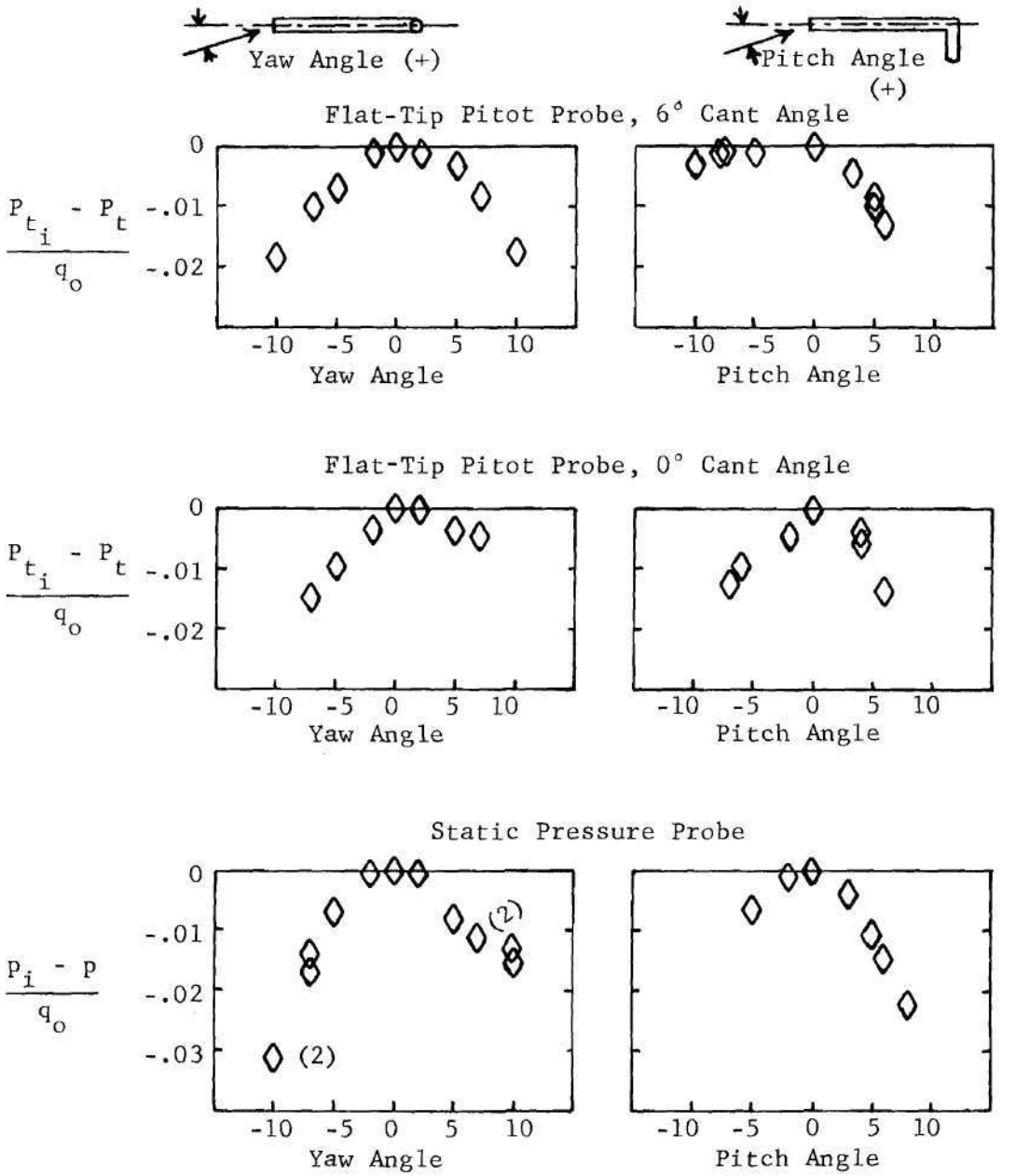

Figure 16. Probe Pitch and Yaw Sensitivity

$$\frac{u_i}{u} = \left[\frac{P_{t_i} - p_i}{P_t - p}\right]^{1/2}$$

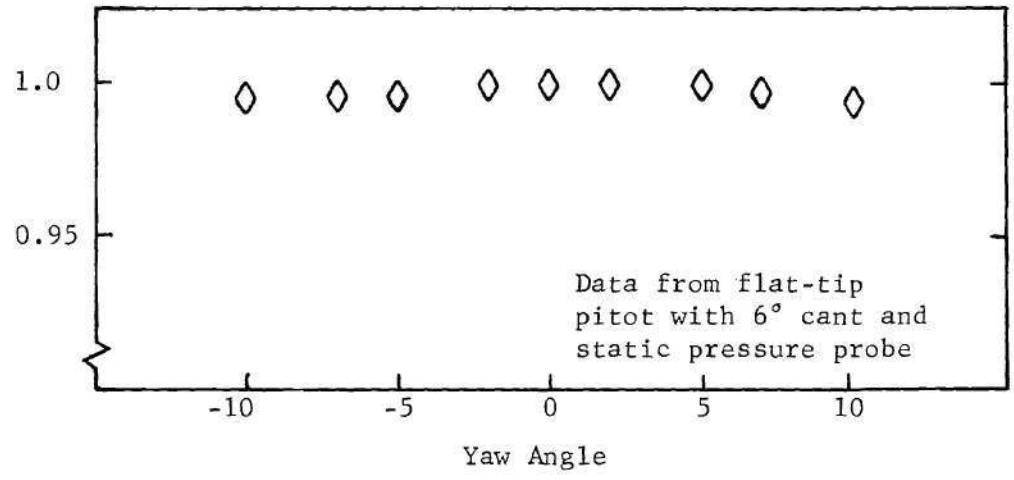

Figure 17. Typical Combined Influence of Yaw Angle

The static pressure probe used in the velocity profile and skin friction determinations of this effort was also previously checked [13] for sensitivity to proximity to solid boundaries. The probe was evaluated by comparing its readings with those of various 1/16 inch diameter floor static taps over a range of typical test pressures. The two results agreed within 1% of the reading for the entire range of pressures, with the probe registering consistently lower values. For the worst case, this difference in reading corresponded to less than 2.2% of the local free-stream dynamic pressure. This difference is probably due, in part, to the size of the floor static pressure taps. (An inside diameter of 1/32 inch is commonly recommended for static taps [26].) It was concluded that the sensitivity of the static probe to solid boundaries was negligible.

The possibility of interaction between the three probes when they were used simultaneously was also checked. With the three probes initially aligned for flow measurement, the static pressure and thermocouple probes were separately, and then simultaneously, raised and lowered relative to the total pressure probe. From monitoring the output of the total pressure probe, it was determined that, within the accuracy of the instrumentation, no pressure effects resulted from the presence of the static pressure and thermocouple probes. A similar check of the effect of the presence of the pitot and thermocouple probes on the static pressure output revealed the same result.

Probe Traverse

To evaluate the accuracy of the probe traverse actuator lead screw

over the span of probe travel, the actuator was mounted on a precision flat reference surface. A steel dowel, mounted in the probe carriage, was raised by the actuator, and its indicated travel was compared with the travel of a standard height gauge. Over the 15 inch span of actuator travel, the indicated travel agreed within ± 0.15% of the actual travel, confirming the manufacturer's specification of .0015 inch variation per inch of travel.

Test Bed Grid

The three-dimensional nature of the wall jet produced with multiple orifices makes accurate lateral positioning especially critical. This consideration was met in the present investigation through the use of a precision machined and scribed spacer plate, which was used to draw lines on the test section floor corresponding to the nozzle centerlines. Symmetrical subdivisions of this grid were then accomplished using a precision ruler. The accuracy of these subdivisions was then rechecked with the spacer plate. A precision ruler was also used to construct and check a grid for stations downstream of the jet exit plane. It is considered that this grid allowed lateral and downstream positioning of the probes to an accuracy within ± 0.03 inch.

Flow Measurement Procedures

Calculation of flow velocity was basic to all portions of this investigation. This calculation, which used the compressible flow relations [27], required determination of the total and static pressure and the temperature. The procedures used to measure these flow properties are described in the following paragraphs.

Mainstream Flow

Measurement of the flow conditions for the two-dimensional mainstream flow were made in the center of the test bed at the exit of the boundary layer development section. The measurement station, hereafter referred to as the "reference station," was located three inches upstream of the nozzle exit plane.

Jet Flow

Jet Plenum Conditions. The jet plenum flow properties were measured by total pressure and temperature probes inserted through each wall of the jet slot section just ahead of the jet nozzle contraction. The total pressure probes revealed identical total pressures at each end of the plenum. The total temperature probes revealed less than a 4°F temperature gradient over the 30 inch plenum width. This small difference in plenum temperature was rendered insignificant by averaging the outputs for velocity calculations.

Jet Profiles. To define a velocity profile in the efflux of the multiple orifice jets required determination of the profiles of static pressure, total pressure and temperature. The possibility of making a survey for each of the three variables at each lateral station (i.e., three separate surveys) was considered. However, an alternate method which substantially reduced the testing time, and hence the period over which the flow conditions had to be maintained fixed, was employed. This method defined the velocity profiles for a chosen nozzle on the basis of the total pressure profile for that nozzle and the static pressure and total temperature profiles of adjacent nozzles. To validate

this method of profile acquisition, the sensitivity of the velocity calculation to temperature and static pressure differences was examined. Then multiple traverses were conducted at the jet exits and at downstream locations to define the typical differences in these flow variables for adjacent nozzles.

The flow velocity is a function of the square root of the absolute temperature; thus, a change of 5°R in total temperature, for the range of jet temperatures considered, yields less than a 0.5% change in jet velocity. Therefore, the velocity calculation was quite insensitive to small variations in the temperature profiles of adjacent nozzles. From centerline surveys of the multiple nozzle exits, it was determined that the typical temperature variations were less than ± 2°F. At approximately 12 nozzle diameters downstream, the typical variations were less than ± 1°F.

The flow velocity is proportional to the square root of $(1-p/P_t)$, where the pressures are absolute values. Thus, a difference between absolute static pressures of 5%, for the range of jet total pressures considered, yields approximately a 0.1% change in jet velocity. Therefore, the velocity calculation was very weakly sensitive to variations of static pressure between adjacent nozzles. Due to the tip length of the probe, static pressure profiles were not determined at the nozzle exits. However, at approximately 12 nozzle diameters downstream of the jet exits, the typical variation in gauge static pressure between adjacent nozzles was less than ± 3%.

Thus, it was concluded that calculation of the velocity profiles

for a given nozzle, based on the total pressure profile for that nozzle and the static pressure and total temperature profiles of adjacent nozzles was valid, and that this calculation yielded values of velocity accurate within ± 0.5%.

Data Acquisition and Reduction

Setting and Stabilization of Flow Conditions

Prior to initiating a test run, a calculation was performed to estimate the jet plenum pressure required to achieve the desired jet velocity. The plenum pressure monitoring channel was then activated, and the jet compressor was started. The jet excess dump valve and control valve were adjusted until the plenum pressure reached the calculated value. The jet was allowed to warm up for at least an hour before initiating a test. For tests involving both flow systems, the mainstream blower was started and allowed to warm up for at least 15 minutes before initiating a test. With these rig warm-up periods, stable test conditions (within ± 0.5%) were maintained for periods exceeding eight hours of continuous testing.

During the initial warm-up the data acquisition system was prepared. The thermocouple reference junction was activated and allowed to stabilize at its reference temperature. The probe traverse control unit and the electronic counter were energized to actuate and display the traverse position. The computer system was then configured for acquisition of the test data.

Final close adjustment to the desired operating condition was made prior to taking data. A period of approximately 10 minutes was

then allowed for the rig conditions to stabilize. In most instances the desired operating point was reached within ± 0.25% accuracy after one cycle of this procedure.

Probe Location

During the jet warm-up period, the test probes were positioned at the desired survey station and lowered to the test section floor for alignment. The total pressure probe was set lower in the carriage so that it contacted the floor before the other probes. A resistance meter was grounded to the test section floor, and the positive lead was attached to the top of the total pressure probe. The carriage was lowered until the meter signaled that the pressure probe had solidly contacted the floor. The carriage was then stepped upward in 0.001 inch increments until the meter indicated that probe contact with the floor was tenuous. The electronic counter was then set to zero. This exercise was repeated twice to verify the zero. With the total pressure probe at the zero location, the positive meter lead was connected to one lead of the thermocouple probe. The latter probe was loosened in its holder and was lowered manually until solid contact with the floor was indicated. The probe was then raised slowly until the meter indicated that the contact with the floor was about to be lost; the probe was fixed in the actuator carriage in this position. The resistance meter was again connected to the total pressure probe, and the zero point was rechecked to insure that the actuator had not been moved. The carriage was then raised 0.001 inch, and the positive meter lead was connected to the top of the static pressure probe. The probe was freed in its holder and was lowered

manually until solid contact with the floor was indicated. The probe was then raised slowly until the meter indicated that contact was about to be lost. The probe was then fixed in the actuator carriage in this position. The carriage was then lowered 0.001 inch, restoring contact of the total pressure and temperature probes with the floor and putting a 0.001 inch compressive deflection on the static pressure probe. Observation of the static probe tip with an optical cathetometer revealed that this extremely light compression did not result in a deflection of the probe tip away from the wall. In these manipulations, all probes were aligned with the flow by comparison with the test bed grid lines on the floor.

Calibration and Checks of Data Acquisition System

Just prior to initiating the test program, several calibrations and checks were made. Calibration and zero point checks were performed on the integrating digital voltmeter. Each Barocel signal conditioner was adjusted in accordance with the manufacturer's operation manual. The computer data acquisition system was used to perform the calibration and zero point checks on each channel of the pressure system.

At least once during a velocity profile survey the Barocel transducers were rechecked to verify that their zeroes had not changed. At the conclusion of a profile, the transducer zeroes were again checked. The initial conditions were maintained for all reported data.

Data Acquisition

For all test programs, the first data input were the ambient conditions. These were read from the barometer and the test stand thermom-

eter, and input to the computer.

For the jet-only testing, the computer data acquisition system was then used to read the jet plenum pressure and temperature, and to calculate the jet velocity. Expansion to ambient conditions was assumed since the test section was open.

The wall jet velocity profile at each axial and lateral station was then evaluated by the computer data acquisition system. For each data point the computer recorded the total pressure, total temperature and probe carriage position and calculated the profile velocity based on ambient static pressure. The probes were repositioned vertically in selected increments ranging from 0.005 inch to 0.080 inch, depending upon the local rate of change of velocity with height. Each profile consisted of approximately 50 points. By monitoring the plenum conditions during the test, the jet velocity was maintained within $\pm$ 0.25%.

For the combined jet and free-stream flow investigation, the probes were raised from the test bed floor and moved forward to the reference position at the exit of the boundary layer development section. The computer data acquisition system was used to read the mainstream and jet plenum pressures and temperatures. It then calculated mainstream and jet velocities and the velocity ratio. Since the test section ceiling was open, the velocities were calculated assuming expansion to ambient conditions. This approach is considered reasonable since measurements on the jet centerline at the closest measurement station ($x/d = 8.2$) gave a gauge static pressure which was less than 2% of the local dynamic head.

The mainstream floor boundary layer just upstream of the nozzle exit plane was recorded next. The probes were lowered to the floor, their alignment was checked, and, then, the computer recorded the boundary layer velocity profile in the same manner as described for the jet profile. Then, the probes were manually moved to each desired downstream location, lowered to the floor and rechecked for proper alignment. Next, while the jet and freestream conditions were held constant, the computer recorded the profile data for the interacting jet and mainstream flow and calculated the velocity profile.

Finally, skin friction measurements were performed with the Preston tube and static pressure probes positioned on the floor at those locations where velocity profiles were obtained. The computer data acquisition system was also used to record these pressures.

Data quality was enhanced in each phase of the testing by utilizing the integrating and averaging capabilities of the computer data acquisition system. While the period of integration of a single reading was varied from 0.1 second to 1 second depending upon reading steadiness, each pressure data point resulted from a simple average of 10 of these integrated readings. Each temperature data point resulted from a simple average of five readings. This integrating and averaging technique requires significant test periods. For example, surveying a single velocity profile for the combined flow field typically required one hour. However, the resulting data quality is considered sufficient justification for the approach.

Data Reduction

During the acquisition of the velocity profile data, the computer simultaneously punched output data on paper tape. The resulting data were then used with several data reduction programs. These programs provided the means for conducting any or all of the following tasks:

1. Numerical integration of the mainstream boundary layer yielding displacement, momentum and energy thicknesses.
2. Numerical integration of the combined flow field yielding displacement, momentum and energy thicknesses.
3. Numerical integration of the nozzle discharge velocity profiles yielding individual nozzle mass flow.
4. Calculation of the local skin friction values.
5. Calculation of "law of the wall" data.
6. Calculation of flow similarity data.

CHAPTER IV

RESULTS AND DISCUSSION

The results of an investigation of a multiple orifice wall jet operating with and without external flow are presented and discussed in this chapter. The specific areas of investigation will be described, followed by a discussion of the flow quality evaluation. Finally, the results of each investigation will be detailed.

Areas of Investigation

This investigation of multiple orifice wall jets was conducted as a three-phase experimental program. The results provided a basis for evaluating the potential of the concept for boundary layer control and for developing and/or assessing methods for applying wall jet flows. The investigation proceeded systematically from a relatively simple 3-D wall jet flow field to the more complex interacting flow fields of the wall jet and the mainstream. Figure 18 presents nomenclature for the most complicated wall jet velocity profile. Where applicable, the specific terminology is the same for all simpler profiles.

Phase 1 consisted of an investigation of the wall jet produced with the basic multiple orifice configuration (Figure 4) without a mainstream flow. This test program provided both a performance baseline for multiple orifice wall jets and an evaluation of the jet Reynolds number sensitivity of this general 3-D wall jet configuration. Then, by referring to this reference case, it was possible to determine changes in

performance due to modifying the design for integration in an application. The jet centerline velocity profile form and a composite of typical streamwise development are shown in Figure 19.

The wall jet produced with the integrated multiple orifice configuration (Figure 6) without a mainstream flow was investigated in Phase 2. This test program provided an assessment of the performance change generated by incorporating typical integrational modifications, as well as more detailed evaluation of the 3-D flow development. Typical streamwise development along the jet centerline is shown in Figure 20.

In Phase 3 the interaction between the wall jet produced with the integrated multiple orifice configuration (Figure 6) and a mainstream flow with a thin boundary layer was investigated. This phase explored the changes in performance which occurred when this typical integrated design was operated under conditions simulating a BLC application. Typical streamwise development along the jet centerline of this combined flow is shown in Figure 21.

Specific test conditions for these three phases are detailed in the following paragraphs.

Phase 1

The wall jet development along the jet centerline and the sensitivity of these results to jet Reynolds number were investigated for the basic multiple orifice configuration without mainstream flow in this phase. The Reynolds number is based on the nozzle diameter. However, to facilitate comparison of the results with two-dimensional wall jets, the Reynolds number was also based on an equivalent 2-D slot height.

This equivalent height, h_{eq}, is defined by the ratio of the flow area to the jet span. Experimental results for this phase were obtained at five stations downstream of the jet exit for an equivalent slot height of 0.0567 inch and for slot Reynolds numbers of 6700 and 13,400 (nominal). These conditions represent Reynolds numbers based on nozzle diameters of 53,400 and 106,800, respectively. Limited horizontal surveys were also conducted to determine the lateral growth of the individual jets. The jet edge was defined to be the point where $P_t = 0$ at the height of δ_1 above the wall.

Table 1 identifies the data collected for this phase. The data are available in Appendix A in tabular form.

Phase 2

The wall jet development along the jet centerline was investigated for the integrated multiple orifice configuration without mainstream flow in the first part of this phase. Comparisons of the results of this investigation with those of Phase 1 define the changes due to fairing (or integrating) the individual nozzles. In the second part, surveys off the jet centerline were conducted to enable the definition of jet lateral characteristics. Experimental results were obtained at nine stations downstream of the jet exit for the equivalent slot height of 0.0567 inch and for a slot Reynolds number of 6700 (nominal). This condition corresponds to a Reynolds number based on nozzle diameter of 53,400. Local skin friction values were also determined at seven downstream locations for jet centerline and off-centerline locations.

A listing of the data secured in this phase is given in Table 2.

The data are tabulated in Appendix B.

Phase 3

This investigation of the integrated multiple orifice configuration considered the interaction of the jet with the mainstream flow. A mainstream boundary layer comparable to that of Neale [13] was used to enable comparisons with 2-D wall jet results. In contrast to the first two phases of this work, which used a jet-to-mainstream velocity ratio of infinity, the testing in this phase was at an initial velocity ratio of two. These choices of velocity ratio provide data at the practical bounds of wall jet applications. A velocity ratio of two is also approximately the lower limit of the primary to secondary ratio for a high performance ejector [7]. Both jet-centerline and off-centerline surveys were conducted. Additionally, local skin friction values were determined for jet-centerline and off-centerline locations.

Table 3 summarizes the data for this phase. The data are tabulated in Appendix C.

Flow Evaluation

The flow quality was carefully evaluated before initiating each phase of the test program. These results are detailed in the following sections.

Phase 1

Velocity profiles were determined at the exit plane of the nine centrally located circular orifices in order to compare the uniformity and magnitude of the efflux from each jet. These surveys were made along the vertical jet centerline of each nozzle, and along the horizontal jet

centerline of three nozzles, while maintaining constant jet plenum conditions. Vertical velocity profiles for the five nozzles which are centrally located about the jet centerline are shown in Figure 22. The theoretical jet velocity, u_j, is based on isentropic expansion of the jet plenum conditions to the ambient; the actual velocity, u, is somewhat lower reflecting the viscous losses experienced in the nozzle block. The horizontal velocity profiles for the three centrally located nozzles are shown in Figure 23. (The nozzles are numbered 1 to 11 from left to right viewing upstream; the centerline nozzle is number 6.) The vertical profiles are typical of those for all nozzles, and excellent repeatability for any nozzle was shown.

Each of the vertical profiles was numerically integrated using Simpson's Rule [28] in order to determine the mass flow of each nozzle. The flow coefficient of each nozzle was defined as the ratio of the integrated mass flow rate, $\dot{m}_{I.P.}$, to the mass flow rate based on the ideal expansion of the jet plenum conditions, $\dot{m}_j$. The momentum coefficient of each nozzle was defined as the ratio of the actual momentum flux of the nozzle (based on $\dot{m}_{I.P.}$ and an equivalent profile velocity), to the ideal momentum flux of the nozzle. The equivalent profile velocity is a mean velocity which reflects the internal losses in the nozzle block due to passage through the flow smoothing screen and to the boundary layer on the interior nozzle wall. From the profiles of Figure 22, a mean value of $0.92\ u_j$ was chosen. As shown in the following tabulation, the five centrally located nozzles exhibited a $\pm$ 1.8% difference in flow and momentum coefficient and a $\pm$ 0.75% difference in maximum velocity.

NOZZLE FLOW DATA
$Re_d = 53,400$

Nozzle	$\dot{m}_j$ slug/sec	$\dot{m}_{I.P.}$ slug/sec	Flow Coefficient	Momentum Coefficient	u_{max} ft/sec
4	6.399×10^{-4}	5.573×10^{-4}	0.871	0.801	282.9
5	6.389×10^{-4}	5.564×10^{-4}	0.871	0.801	279.5
6	6.399×10^{-4}	5.587×10^{-4}	0.873	0.803	278.2
7	6.415×10^{-4}	5.783×10^{-4}	0.901	0.829	279.9
8	6.411×10^{-4}	5.596×10^{-4}	0.873	0.803	279.6

Surveys along the horizontal centerlines, shown in Figure 23, showed that the three centrally located nozzles exhibited only a ± 0.75% difference in maximum velocity. From these measurements it was concluded that the flow through the five centrally located nozzles was acceptably uniform and subsequent measurements were made over this lateral span of the nozzles.

Surveys were made to determine the uniformity of the flow downstream of these same five nozzles. The reader will recall that nozzle six was centered in the 30 inch test bed span; this lateral location was identified z = 0 inches. Hence, the centerline of nozzle four was located at z = -5.454 inches; the centerline of nozzle five, at z = -2.727 inches; the centerline of nozzle seven, at z = 2.727 inches; and the centerline of nozzle eight, at z = 5.454 inches. Velocity profiles were determined from measurements on the centerlines of these five nozzles at x/d of 5.4 and 15.3, and on the centerlines of nozzles five, six and seven at x/d = 8.7. All profiles were measured at $Re_d = 53,400$ (nominal).

In general, since the data scatter was negligibly small, the differences in the velocity profiles were attributed to flow non-uniformities associated with the individual nozzles. As will be described below, the greatest disagreement occurred nearest the nozzle exits. The agreement was significantly improved at downstream stations due to turbulent mixing with the surrounding air.

The individual profiles, shown in Figures 24a and 24b for $x/d = 5.4$, exhibit the same trends in relative magnitude as were shown at the nozzle exits (Figure 22). The wall layers of nozzles five and eight have lower velocities than that of the centerline nozzle, while those for nozzles four and seven are higher. Although the maximum disagreement in this region of the profile is approximately 9%, the peak velocities agree within 1%. The maximum disagreement in velocities in the jet layer portion of the profile is approximately 18% between the profiles of nozzles four and eight. The agreement of the profiles of nozzles five, six and seven is considerably better--approximately 4.3% difference in the region of δ_2.

At $x/d = 8.7$, the differences between the profiles of nozzles five, six and seven are reduced, with good agreement between nozzles six and seven and approximately 7% maximum disagreement in velocity with nozzle five in the wall layer, 0.1% disagreement at the peak, and approximately 5% disagreement in the region of δ_2.

The individual profiles at $x/d = 15.3$, shown in Figure 24c, exhibit a further overall improvement, with approximately 3% maximum disagreement in velocity in the wall layer, approximately 2% disagreement

at the jet peak, and approximately 1% maximum disagreement in the region of δ_2.

An additional check of mean flow uniformity for nozzles five, six and seven at x/d = 15.3 was provided by computing the vertical integral of the velocity over the interval of y = 0 and y = y_e, where y_e is the value of y where $u/u_1 = 0.25$. The integral was evaluated numerically using Simpson's rule. The results revealed 0.04% difference in the velocity integral for nozzles six and seven, and only 0.15% difference for nozzles five and six. Thus, good centerline mean flow uniformity existed for the centrally located nozzles.

From the results of these studies, it was concluded that the centerline flow from the five surveyed nozzles was acceptably uniform. It was also concluded that the flow from nozzle six represented an average of the discharge from the five center nozzles. Therefore, subsequent downstream measurements for this phase were made along the centerline of this nozzle.

Phase 2

The uniformity of the centerline velocity profiles of nozzles five, six and seven was rechecked after installing the integration fairings on the multiple orifice nozzle block. This evaluation was conducted at x/d = 15.3 for Re_d = 53,400 (nominal). These profiles are shown in Figure 25. Excellent agreement exists for the profiles of nozzles five and six. The profile of nozzle seven differs by less than 2% in the wall layer, by 1.2% at the jet peak and by less than 2.3% in the region of δ_2. The repeatability of these profiles was excellent.

It is concluded from these surveys that the placement of the integration fairings did not affect the flow uniformity established in Phase 1, even though the velocity profiles showed somewhat different shapes in the two phases. Subsequent downstream measurements were made along, and laterally about, the vertical centerline of nozzle six.

Phase 3

Surveys of both the mainstream wall boundary layer and the mainstream flow outside the boundary layer were made to evaluate the uniformity of the mainstream flow. These surveys were made in the plane of the upstream reference station.

The results of the dynamic pressure survey of the flow outside the boundary layer are shown in Figure 26. These results show that the dynamic pressure varies by less than ± 1.4% from the mean. The corresponding velocity variations are less than ± 0.7%. Additional confidence in the flow quality is provided by the fact that the typical spanwise velocity differences that could generate three-dimensional flow effects are less than 0.25% of the mean. Also, excellent repeatability was noted.

Velocity profiles in the mainstream boundary layer at the reference plane were determined at 24 spanwise locations about the test bed centerline. The span covered was 12 inches. The profiles at the test bed centerline and 5.5 inches either side of this location are shown in Figure 27. Although excellent agreement was obtained at these stations, profiles at other spanwise locations disagreed. To facilitate evaluation of the possible effects of these differences, the momentum thickness of each profile was computed numerically using the conventional

definition; that is

$$\theta_o = \int_o^\delta \frac{\rho}{\rho_e} \frac{u}{u_e} \left(1 - \frac{u}{u_e}\right) dy \ .$$

The distribution of momentum thicknesses is shown in Figure 28. The values of θ_o vary by ± 15% about the simple mean, with a standard deviation of approximately 8%. These variations are, in part, due to the small magnitude of momentum thickness which exists at the reference plane. To assess the overall mean value of θ_o, an integrated mean momentum thickness can be defined by the following equation:

$$\theta_{I.M._o}(z_1,z_2) = \frac{1}{z_2-z_1} \int_{z_1}^{z_2} \theta_o dz \ .$$

The value of $\theta_{I.M._o}(0,6) = 0.0458$ inch differs by only 0.2% from the value $\theta_{I.M._o}(-6,0) = 0.0457$ inch. Thus, though there are local variations in the small values of momentum thickness, the mean integrated values over the regions to the left and right of the span centerline show excellent agreement.

It is concluded from these studies of the mainstream that the flow is acceptably two-dimensional at the reference station.

An investigation of the flow uniformity was also conducted at $x/d = 12.2$ for a velocity ratio, u_j/u_{e_o}, of two. Velocity profiles were determined at 39 spanwise locations about the test bed centerline. The span covered was approximately 11 inches. These combined flow profiles reflect changes from mainstream boundary layer profiles and jet-only

profiles both due to passage of the mainstream flow over the integrated nozzle block, and the interaction of the two flow fields. The profiles for the jet centerline surveys of the five centrally located nozzles are shown in Figure 29. The profiles exhibit approximately 5% maximum disagreement in the wall layer, 2.5% difference at the jet peak, and a maximum of 1.5% difference in the jet layer at δ_2.

Again, to obtain a more realistic, integrated comparison of the numerous velocity profiles, the momentum thickness, θ, at each location was computed. The previous definition of θ was used, with the upper limit corresponding to the value of y for which $u = .99\ u_e$. These thicknesses are displayed in Figure 30. The values near the jet centerlines are negative, which is characteristic of wall jets, and imply an excess of momentum flux with respect to the freestream. The values for the locations between the nozzles are positive. Their magnitude depends on the local influence of the jet.

Integrated mean momentum thicknesses, $\theta_{I.M.}$ were computed for various distances over the 11 inch span using the previous definition, and the results are displayed in Figure 31. For reference, values of the integrated mean thicknesses for comparable spans at the upstream reference plane are listed in parentheses below the cited values.

The two thickness values for the 5.454 inches to the right and left of the test bed centerline, $\theta_{I.M.}(0,5.454)$ and $\theta_{I.M.}(-5.454,0)$, respectively, indicate considerable differences. However, these differences are magnified by the extremely low values of $\theta_{I.M.}$ under consideration. This is demonstrated by comparing the difference, $\Delta\theta_{I.M.} =$

$\theta_{I.M.}(-5.454,0) - \theta_{I.M.}(0,5.454) = .0043$ to the ideal case of no ramp or nozzle losses. This ideal case provides a baseline performance value against which actual lateral variations can be more exactly assessed. In the ideal case the momentum thickness at the nozzle exit is given by

$$\theta_j = \frac{\rho_j u_j}{\rho_e u_e}\left[1 - \frac{u_j}{u_e}\right] h_{eq} .$$

For these test conditions, $\theta_j = -0.105$ inch. Thus, $\Delta\theta_{I.M.}$ is only 4.1% of θ_j, which reveals the small magnitude of the difference and the acceptable symmetry of the results about the test bed centerline.

The three thickness values for symmetrical regions about the centerlines of nozzles five, six and seven also show differences, but the variations are within those cited above.

The four values of the integrated momentum thickness for spans demarcated by the centerlines of the considered nozzles revealed three regions of comparable $\theta_{I.M.}$ along with one larger value. Again, comparison with θ_j shows only an 8.1% maximum difference.

In total these results reveal differing amounts of change in the mainstream flow in its passage over the nozzle fairings and its interaction with the jets. However, as discussed above, these differences are small in comparison with the ideal performance baseline. In addition, the region downstream of nozzle seven, bounded by the centerlines of nozzles six and eight, have comparable $\theta_{I.M.}$ values for regions which are symmetrical about the nozzle centerline. Also, these values of $\theta_{I.M.}$ are comparable both with the value for this entire 5.454 inch span

and also with that for the 2.727 inch span across the nozzle centerline. Thus, it is concluded that the passage of the mainstream flow over the nozzle and its interaction with the jet flows are comparable for the regions delimited by the centerlines of nozzles six, seven and eight. Therefore, subsequent results for Phase 3 are from measurements made on and about the vertical centerline of nozzle seven.

Results

Typical results for the multiple orifice wall jet investigations conducted in the present work are included in the following paragraphs. The results consist of (1) specific flow development characteristics, such as jet spreading and velocity decay, (2) velocity profile similarity, (3) iso-velocity contours, (4) integrated velocity profiles, (5) skin friction and friction coefficient laws, and (6) "law of the wall" values for this 3-D wall jet flow. Where possible, these results are compared with the findings of other investigators.

Wall Jet Growth

One measure of the growth of wall jets is given by the increase of the half velocity height, δ_2, downstream of the jet exit. The present data indicate that, in the absence of an external stream, the growth of δ_2 for both the basic and integrated multiple orifice configurations is characterized by two regions. The first is a region of near-linear growth during which the jet apparently spreads over the surface due to confinement by the wall and the pressure gradients between the parallel jets. Merging of the individual jets is essentially completed in this region. The second region is also one of near-linear growth, but at a

higher rate which corresponds very nearly to that for the 2-D wall jet. In some cases, there appears to be a detectable zone of transition between these two regions, but its boundaries are not precisely defined by the present data. During the initial portion of the second region, confined lateral spreading continues as a result of turbulent mixing. In the final portion of this region lateral mixing is completed, and the jet develops as a 2-D wall jet with only vertical spreading. These growth data reveal very good agreement with 2-D wall jet results throughout the second region.

The two rates of growth of δ_2 are illustrated for the basic multiple orifice configuration in Figure 32; solid lines through the data are used to emphasize these growth rates. These results, which were extracted from vertical velocity profiles at the indicated stations, are depicted for two values of jet Reynolds number. Limited horizontal surveys were taken at a height $y = \delta_1$ (Figure 18) above the wall in order to locate the lateral edges of the individual jets ($P_t = 0$). Using this technique it was determined that lateral merging of the jets had occurred by station $x/h_{eq} = 121$. Downstream of this station the growth rate undergoes a transition to a rate closely comparable to that of a 2-D wall jet, which is represented by the results of Neale [13]. The lower initial rate of growth is attributable to the rapid lateral spreading of the individual jets.

In comparison with the circular free jet, the circular wall jet exhibits an initial region of comparable growth followed by a region of slower growth. This latter behavior is comparable to that of the 2-D

wall jet which exhibits less rapid spreading than the 2-D free jet due to the suppression of turbulence by the wall. These comparisons are illustrated by the axially symmetric free jet results of Trupel and the 2-D free jet results of Forthmann, both of which were compiled by Abramovich [29]. (The axially symmetric results were converted for the present comparison using the ratio r_o/h_{eq}, where r_o is the jet radius.) At the jet exit the 2-D and 3-D results are separated by the difference between their physical heights.

The growth in δ_2 for the multiple orifice configuration displays the same Reynolds number trend that is evident in 2-D wall jet results [13,30,31]. Specifically, an increase in jet Reynolds number results in a decrease in the growth of the half velocity height. However, a significantly more dependent relationship is demonstrated by the circular wall jet than by the 2-D wall jet. For example, doubling the jet Reynolds number for the circular configuration reduces the growth rate in the initial region by approximately one half, while the same increase for the 2-D configuration reduces the growth rate by approximately five percent. The cause of this vast difference in behavior is not evident, and further testing over a wider range of Reynolds numbers is needed.

The half-velocity heights for the basic and integrated multiple orifice configurations are contrasted in Figure 33. The growth for the integrated nozzles also exhibits two linear regions. However, in the region near the jet, this configuration produces a slower vertical growth rate than the basic configuration. This behavior is attributed to increased lateral dispersion of the jet which results from spreading of

the flow over the edges of the between-nozzle ramps. This increased lateral spreading reduces the vertical growth. Yet, near station $x/h_{eq} = 300$, both configurations exhibit the same vertical heights and closely comparable growth rates. Downstream of station $x/h_{eq} = 166$, the integrated configuration displays a linear growth rate very comparable to the 2-D wall jet, as represented by the results of Neale [13]. This implies that the jet merger is completed, and the jet is developing as a 2-D wall jet. The axially symmetric and plane free jet results from Abramovich [29] are also included in Figure 33; the integrated wall jet configuration exhibits the same performance with respect to these free jet results as was indicated for the basic wall jet above.

The jet growth for the integrated configuration is repeated in Figure 34 along with the single, circular nozzle, wall jet results of Newman, et al. [21] and Naib [19]. Both the present results and those of Naib exhibit two regions of linear growth. The results for the integrated configuration indicate that the angle of divergence of δ_2/d (i.e., $d\delta_2/dx$) is 1.7° for $x/d < 21$, while downstream of this station, the divergence angle is 4.3°. The results of Naib are similar, showing a divergence angle of 2.3° for $x/d < 27$ and 3.5° downstream of that point. The greater divergence angle for the multiple circular jet is attributable to lateral confinement of the jet by adjacent jets. In contrast, Newman, et al. report a growth rate which is characterized by a single linear curve having a divergence angle of 2.8°. The reason for this difference is not apparent. The two regions of growth for the axisymmetric free jet from Abramovich [29] are also included in the figure.

While the initial region exhibits growth which is closely comparable to the multiple orifice results, the divergence in the downstream region (5.5°) is greater than the wall jet due to greater turbulent mixing in the free jet and the lack of axisymmetric spreading in the wall jet.

The addition of an external stream to the jet flows of the integrated nozzle configuration (Phase 3) resulted in a decreased rate of growth of the half velocity. Figure 35 illustrates this growth for a velocity ratio (jet velocity to external velocity) of two, contrasted with previous results from Phase 2, at a velocity ratio of infinity. The data show the same effect of velocity ratio that is evident not only for 2-D wall jets, but for 2-D and axisymmetric free jets as well. Specifically, a decrease in velocity ratio results in a decrease in the rate of growth of δ_2. Velocity surveys made at several downstream off-centerline locations revealed that the same is true for jet lateral growth; for the velocity ratio of two, the individual jet flows did not spread sufficiently to merge. The growth of δ_2 for axisymmetric free jets at a velocity ratio of infinity is represented by the data of Trumpel, while the results for the same configuration at a velocity ratio of approximately two are from the data of Landis and Shapiro; both results are compiled by Abramovich [29]. As discussed previously for both the circular and 2-D configurations, the wall jet growth for infinite velocity ratio is less than that for the free jet because of jet spreading and the subsequent suppression of mixing due to the wall. However, for the velocity ratio of two, the integrated circular wall jet growth rate is very nearly the same as for the free jet. As was mentioned above and

as will be demonstrated in a subsequent section, the multiple circular jets did not merge and, in fact, the initial spreading was almost completely eliminated. For the plane jets at a velocity ratio of two, it is noted that the growth for the wall jet, as represented by the results of Neale [13], is also closely comparable to that of the plane free jet, as presented by the data of Weinstein, Osterle and Forstall [32]. Thus, it appears that the vertical spreading rate for a velocity ratio of two for both the multiple circular and 2-D wall jets is very close to those for an axisymmetric free jet and plane free jet, respectively.

The growth of the multiple circular orifice wall jet has been detailed by the discussion and data of this section; in summary, the results indicate a strong dependence on jet Reynolds number and jet-to-freestream velocity ratio. For a velocity ratio of infinity, the circular wall jets, like a circular free jet, exhibit two linear regions of growth of half velocity height. The growth in the initial region is slower than that of a comparable 2-D wall jet, due to the rapid lateral spreading of the individual jets. However, following merger and lateral mixing of the individual streams, the jet flow develops as a 2-D wall jet. The growth rate for the circular wall jets is much more strongly dependent on jet Reynolds number than the 2-D wall jet, and further testing is warranted to explore the significant decrease in growth that results from increases in jet Reynolds number. Introducing between-nozzle fairings for the integrated configuration produces a slight decrease in initial growth; however, two linear regions of δ_2 growth are again displayed, the second region matching that of the basic configuration in

both extent and rate of growth. These two linear growth regions confirm the finding by Naib [19] of similar regions for the single circular wall jet; yet the multiple orifice unit exhibits more rapid growth, due to the lateral confinement of individual jets by adjacent ones. Testing of the integrated circular wall jets at velocity ratios of two and infinity provides growth data at practical bounds for analytical treatment of this three-dimensional wall jet. The decrease in growth of δ_2 which results from a decrease in velocity ratio is consistent with the behavior of 2-D wall jets, as well as of 2-D and axisymmetric free jets. Surprisingly, the growth rate for the integrated configuration closely matches that for the axisymmetric free jet at a velocity ratio of two.

Wall Jet Velocity Decay

The persistence of a wall jet is an important characteristic for determining its potential applications. One measure of the persistence is provided by the decay of the peak centerline velocity, u_1, downstream of the jet exit. This section provides documentation of the decay characteristics of the multiple circular orifice wall jet, and compares its performance with other jet configurations. In general, these results reveal that the decay rate of the basic multiple orifice configuration is reduced by an increase in jet Reynolds number. Closely comparable decay characteristics are exhibited by the integrated multiple orifice configuration. The multiple orifice decay results are very similar in the initial spreading region to those for single circular orifice wall jets; however, further downstream, the multiple orifice decay rate is significantly less due to the merger, and hence, the confinement of the

individual jets. The addition of an external stream significantly reduces the decay of the centerline velocity due to the reduced spreading of the jet into the coflowing stream. These results are discussed further in the following paragraphs.

The decay of the peak centerline velocity for the basic multiple orifice configuration is displayed in Figure 36. These results, which are depicted for two values of jet Reynolds number, show that an increase in Re_s results in a decrease in the decay of u_1. This is the same trend exhibited by two-dimensional (2-D) wall jets [13,30,31]. This behavior results because an increase in Re_s produces a decrease in the ratio of the wall shear stress to momentum flux; this decreases the amount of jet momentum which must be transferred to the wall layer and increases the persistence of the wall jet.

The effect on velocity decay of converting the basic multiple orifice wall jet to the integrated configuration is shown in Figure 37. The interaction of the individual jets with the between-nozzle fairings results in a slight increase in jet decay in the region near the jet exit. However, the difference in decay decreases with downstream distance until the values of u_1/u_j are closely comparable at $x/h_{eq} = 283$ ($x/d = 35.7$). Also included in the figure are decay data for comparable test conditions on a 2-D wall jet, as reported by Neale [13]. Due to the greater length of the jet core of the axisymmetric nozzles, this configuration exhibits a velocity decay which is initially less than the 2-D wall jet. However, downstream of $x/h_{eq} = 200$, the decay rate becomes greater than the trend exhibited by the 2-D wall jet data.

Figure 37 also displays centerline velocity decay results for the axisymmetric and 2-D free jets; these results are from Abramovich's compilation [29] of the axisymmetric jet experiments of Albertson, et al. and from the plane jet results of Knystantas [18]. In both cases, the free jets exhibit more rapid decay than their corresponding wall jet configurations, with the 2-D jets showing the most significant differences. The superior persistence of the wall jets is attributable to their confinement by the wall, to the suppression of turbulence by the wall, and hence reduced mixing in the outer layer, and also to the lower shear stresses at the wall compared with those in the free shear layer of the free jet configurations, as shown in the results of Liaw [33].

The jet decay results for the integrated configuration are repeated in Figure 38 to compare the current multiple orifice results with the single orifice wall jet data of Newman, et al. [21], Naib [19], and Chesters, et al. [22]. The axially symmetric free jet results of Albertson are also repeated as a reference line. The initial decay rates of the present results are very similar to those of Naib and Newman, et al. The results of Chesters, et al. show a stronger initial persistence than the other results, which is probably due to lower nozzle losses. However, further downstream all single orifice decay rates are greater than that of the present multiple orifice configuration.

In Figure 39, these decay results are emphasized using a log-log plot; in addition, the multiple orifice wall jet results of Chesters, et al. [22] are presented. Although this plotting format emphasizes the variation in the initial decay rates, which is attributable to differ-

ences in the individual jet velocity profiles and nozzle wall boundary layer thicknesses, the slopes of the decay curves are closely comparable. Yet, downstream of approximately station $x/d = 35$ both multiple orifice cases display a marked reduction in decay rate. These results are emphasized by the solid lines, while the slope of the single orifice results is represented by the dashed line. The decrease in the decay rate for the multiple jet configuration is ascribed to the merger of the individual jet streams, with a consequent reduction in the lateral spreading of the jets. The downstream travel of the jets before merger of the individual plumes is expected to be strongly influenced by the jet spacing-to-diameter ratio, s/d, as is the case for multiple free jets [18]. The value of s/d for both the present investigation and for that of Chesters, et al. is approximately six.

Figure 40 shows the effect of an external stream on the decay of the jet peak centerline velocity. Exhausting the jets in an external stream at a jet-to-freestream velocity ratio, u_j/u_{e_o}, of two results in a significant reduction of the decay. This decreased decay is the result of the reduced spreading of the jet into the coflowing stream. Also shown on the figure are comparable results from the two-dimensional (2-D) wall jet investigation of Neale. The greater jet core length of the axisymmetric nozzles produces a velocity decay which is initially less than that of the 2-D wall jet. However, due to the rapid lateral spreading of the circular jets, this difference is diminished downstream.

Figure 41 emphasizes the persistence of the jet centerline velocity for the present three-dimensional (3-D) wall jet configuration

compared to that for the 2-D wall jet. At a given downstream location, the difference $u_l - u_e$, as a fraction of the initial difference, $u_j - u_e$, is a measure of the excess energy remaining in the jet. Over the range of $x/h_{eq} = 97$ to $x/h_{eq} = 194$, these results show that the ratio of these velocity differences is typically 25-30% greater for the 3-D wall jet. This superior persistence of the centerline velocity of the 3-D configuration is an important consideration in selecting a wall jet scheme for boundary layer control on surfaces well downstream of the jet nozzle.

Figure 41 also includes velocity decay data for the present 3-D configuration without internal nozzle losses (i.e., $u_l = u_j$ at $x = 0$). These corrected results are based on full recovery of the approximately 8% nozzle internal velocity loss, which was described in the Flow Evaluation section of this chapter. A nozzle which is optimized for performance in an actual BLC installation is expected to show decay performance that is somewhat better than the current data, but less than the ideal results.

Figure 42 contains a comparison of the jet centerline velocity decay for wall jets and free jets. Like Figure 41, these results are referenced to the freestream velocity; however, the results are segregated according to the two- or three-dimensional geometry of the jets. Figure 42a contains the Phase 2 and 3 results for the multiple circular orifice wall jet, while Figure 42b includes data at comparable flow conditions from the 2-D wall jet investigation of Neale [13]. Included in each figure are corresponding results for axially symmetric and plane free jets. For the axially symmetric free jet, the results at a velocity

ratio of approximately two are from the experiments of Landis and Shapiro, which are tabulated by Abramovich [29]. For the plane free jet, the velocity-ratio-of-two results are from the data of Weinstein, et al., as tabulated by Abramovich [29].

For an infinite velocity ratio, both the 2-D and 3-D wall jets decay less rapidly than the equivalent free jets. This slower decay rate is, in part, a result of the suppression of turbulence level in the outer layer due to the wall. This yields decreased mixing with the surrounding fluid, and, in turn, decreased vertical growth of the jet boundaries (Figure 35) and reduced jet decay. This decreased decay is also the result of the lower values of shear stress at the wall, compared with those in the free shear layer of the free jet configuration [33]. The difference in decay rates between the free and wall jet configurations is smaller for the 3-D geometry, which is attributable to the increased lateral growth of the individual jets due to confinement by the wall.

For both the 2-D and 3-D configurations, Figure 42 shows that the wall jet decay, expressed in terms of the ratio of u_1-u_e to u_j-u_e is more rapid for a velocity ratio of two than was the case for an infinite velocity ratio. This behavior is the result of the wall shear stress becoming more predominant at lower values of velocity ratio. This causes a greater rate of decrease of the difference u_1-u_e due to the momentum transfer to the wall layer. By contrast, the 2-D and 3-D free jet results show less rapid decay at a velocity ratio of two than at an infinite velocity ratio. This behavior reflects the absence of a boundary surface and the effect of the velocity difference, u_1-u_e, on mixing with the free stream, as noted by Weinstein, Osterle and Forstall [32].

The off-centerline decay of the multiple orifice jets is addressed in Figure 43. These results display the downstream development of the centerline maximum velocity, u_1, with that of the maximum velocity, u_{mid}, at a lateral station halfway between nozzle exits, z = 1.363 inches. This presentation shows the initial increase of u_{mid}, due to the lateral spreading of the individual jets, accompanied by the decay of u_1. The merger of these values in the neighborhood of station x/d = 35 signals the complete mixing of the individual jets and the establishment of a two-dimensional wall jet flow. This merger location is the same as that noted in Figure 39 associated with the pronounced change in centerline velocity decay.

The decay characteristics of the multiple orifice wall jet have been documented by the data, comparisons and discussion of this section. In summary, the decay behavior of the basic and integrated multiple orifice configurations is closely comparable. The decay rate is a function of both the jet Reynolds number and the jet-to-freestream velocity ratio. Specifically, an increase in Re_s results in a significant decrease in the decay of jet centerline velocity, while a decrease in u_j/u_{e_o} has the same effect. Testing of the integrated circular wall jets at velocity ratios of two and infinity has provided decay data at extremely practical limits for the present analysis, as well as for future analytical treatments of this three-dimensional wall jet.

In the initial spreading region, the multiple orifice decay results are very similar to those for single circular orifice wall jets. Further downstream, the multiple orifice decay rate decreases signifi-

cantly due to the merger of the individual jets. The downstream travel of the jets before merger of the individual plumes is expected to be strongly influenced by the jet spacing-to-diameter ratio. It was also noted in the initial spreading region that the multiple orifice configuration exhibits a velocity decay which is initially less than the two-dimensional (2-D) wall jet, due to the greater core length of the axisymmetric nozzles. However, due to the rapid lateral spreading of the circular jet, its decay rate becomes slightly greater than that of the plane wall jet downstream of station $x/h_{eq} = 200$.

The addition of an external stream significantly reduces the decay of the centerline velocity due to the reduced growth of the jet into the coflowing stream. For a jet-to-freestream velocity ratio of two, the axisymmetric nozzles produce a velocity decay which is initially less than that of the 2-D wall jet. However, this advantage is diminished somewhat at downstream locations.

All of these decay comparisons provide the designer with important considerations and guidelines for selecting a wall jet scheme for boundary layer control.

Wall Jet Velocity Profile Similarity

The analysis and prediction of three-dimensional wall jet behavior will be greatly aided by the establishment of velocity profile similarity. This section presents the degree of similarity identified for the multiple circular orifice wall jet. In general, similarity of the vertical velocity profile is established, both for the jet centerline and off the centerline. This result is shown for the multiple orifice jets operated

both with and without a freestream velocity. Additionally, horizontal similarity is demonstrated for both the lateral peak velocity profiles and the lateral velocity profiles taken in planes y = constant (between $y = \delta_1$ and $y = \delta_2$ at $z = 0$). This result is also shown to be valid for the jets operated with or without a freestream velocity. Moreover, in each case good agreement is demonstrated with several different analytical profile descriptions, yielding good predictive tools for design and analysis of three-dimensional wall jets.

Various length and velocity scales are used to characterize the vertical velocity profiles of wall jets. Figure 44 depicts those used for the wall jet operated without a freestream velocity, $u_j/u_{e_o} = \infty$. The length scale δ_2 is defined as the value of y at which $u = u_{1/2}$, where u_1 is the peak profile velocity. The slope of the profile at δ_2 determines another length scale δ_j, the jet layer length scale. Physically, δ_j represents the thickness of linear jet layer velocity profile with the same values of u_1 and u_e, and with a velocity gradient equal to the maximum velocity gradient. Variations of these definitions will also be used for characterizing the lateral velocity profiles; these will be defined later in this section.

The centerline velocity profiles for the basic nozzle configuration at $u_j/u_{e_o} = \infty$ are shown on a non-dimensional basis in Figure 45. These results are presented for two streamwise stations (one before jet merger and one approximately at merger) and for two values of jet Reynolds number. The plot reveals that the velocity profiles have a high degree of similarity. For comparison, Verhoff's analytical representa-

tion [30] of the velocity profile for a two-dimensional wall jet at infinite velocity ratio is also included. Verhoff has matched this functional form with his own data, as well as with data from numerous other two-dimensional (2-D) investigations. In addition, Neale [13] has shown that this expression agrees well with his 2-D wall jet data. The present three-dimensional results are also in very good agreement with Verhoff's equation; therefore, its use in an approximate integral analysis is expected to yield good results.

Comparable results for the integrated nozzle configuration are shown in Figure 46. These non-dimensionalized centerline velocity profiles are presented for five streamwise stations (two before jet merger and three after merger) for a single value of jet Reynolds number. With the exception of $x/d = 15.3$, these results also show that the velocity profiles are highly similar and agree well with Verhoff's analytical representation. The results at $x/d = 15.3$ are in the transition zone between the potential core region (close to the jet) and the fully developed region.

The choice of an alternate length scale for normalizing the same data is shown in Figure 47. Normalization by the jet layer length scale also yields highly similar behavior for these centerline velocity profiles, except in the inner layer (near the wall) which, as is well known, involves multiple length scales. These data are compared with a numerical representation formulated by Liaw [33] using least square fitting of two-dimensional wall jet data. These data show good agreement with Liaw's formulation.

Downstream of the jet starting region ($x/d > 15.3$), vertical velocity profiles at locations either side of the jet centerline are also similar. Figure 48 includes the non-dimensionalized velocity profiles for the centerline station and four lateral stations for a single streamwise position, $x/d = 20.9$. In each case the characteristic velocity is the local maximum velocity, u_{max}, while the characteristic dimension is the local value of δ_2. These results show a high degree of similarity and also compare very well with Verhoff's analytical representation. Figure 49 repeats the profile at the centerline location and adds the profiles at lateral stations halfway between the nozzle exits, for the same streamwise station, $x/d = 20.9$. These results also show both similarity and good agreement with Verhoff's profile; by treating both positive and negative values of z/d, they also illustrate the general symmetry of the jet profile.

These same data are replotted in Figure 50 with δ_j as the characteristic length scale. These results, which reveal somewhat greater data spread in this plotting format, are also compared with the formulation of Liaw [33]. While showing good agreement with this analytical form near the jet outer edge and near $y = \delta_2$, these results do not agree as well near the maximum velocity region, particularly for the profiles at the mid-nozzle stations. The results also reveal multiple length scales near the wall. However, the results reveal that similarity does exist, and a more exact choice of δ_j (based on least square fitting of the velocity profile data) should yield better agreement with Liaw's formulation.

Figure 51 displays comparable velocity profile data at streamwise station $x/d = 35.7$. These results also demonstrate the similar nature of the vertical velocity profiles and the utility of Verhoff's analytical representation for their description. Comparison of these same results with the analytic form of Liaw in Figure 52 also confirms the similarity of these results, and indicates the potential value of this analytic description for treatment of downstream off-centerline locations.

These demonstrations of similarity are extremely important because they allow a designer who is utilizing a similar wall jet configuration to predict the centerline velocity profiles downstream of the jet development region. For example, for a given jet Reynolds number, one can enter the u_1/u_j versus x/d curve (Figure 38) to extract, for a given downstream station, a value of u_1. One can also enter the δ_2/d versus x/d curve (Figure 34) to obtain a corresponding value of δ_2. Then, since Verhoff's analytical form for 2-D wall jets gives an excellent prediction of circular wall jet vertical velocity profile shape, both for jet centerline and off-centerline locations, one can use this form to construct the u versus y centerline velocity profile. As noted earlier, somewhat less precise prediction is provided by Liaw's analytical form at $x/d = 20.9$; however, good centerline and off-centerline profile prediction are provided at $x/d = 35.7$, and this analytical form could also be used.

In order to treat lateral similarity of the multiple jets, it is necessary to examine further the symmetry of the velocity distribution about the geometrical jet centerline ($z = 0$). Figure 53 presents the

lateral distribution of the peak velocities, u_{max}, at $x/h_{eq} = 20.9$. It is evident that the peak velocity distribution is not symmetrical about the geometric centerline, but instead, due to lateral drifting of the jet, is more nearly symmetrical about $z = -0.093$. A smooth curve through these results is the basis for defining the new centerline and a new peak centerline velocity, u_1. It is noted that in terms of the jet velocity, u_j, the definition of a new peak centerline velocity results in only a 0.5% change in the value of u_1/u_j. Thus, the previous results for jet growth, decay and vertical similarity are not significantly affected by this redefinition of the centerline location and velocity.

Figure 54 confirms the validity of this revised centerline ($z_c = 0$) by the close agreement of the peak velocity results for both positive and negative z_c locations. A faired curve also passes smoothly through these data illustrating the symmetry of the results. This plot also yields the values of Δ_2 and Δ_j. These characteristic lateral length scales are similar to those defined in the vertical direction; their basis of definition is shown in Figure 55. Now, having redefined the jet centerline to account for an experimental discrepancy, one can then examine the lateral velocity profiles for similarity.

A non-dimensionalized lateral distribution of the local maximum velocities at $x/d = 20.9$ is shown in Figure 56. This figure, which uses the value of Δ_2 as the characteristic length scale and $u_1 - u_{min}$ as the characteristic velocity, includes values either side of the jet centerline, $z_c = 0$. An exponential profile which is widely used for describing free shear flows is also included. The present results show excellent

agreement with this analytical form, except near the minimum value (where $u_{max}-u_{min} = 0$ and $|z_c| = 1.27$ inches).

The choice of an alternate length scale and the same velocity scale is illustrated in Figure 57. This form of the previous result compares favorably with the analytical description formulated by Liaw [33] from least square fitting of two-dimensional wall jet data. This analytical form shows good agreement over the outer portion of the lateral profile, as well as in the vicinity of Δ_2, but is less useful in the region of the maximum velocity. Also shown is an exponential function which is generally used for describing a two-dimensional wake. This form also shows good agreement over the outer and mid-portion of the profile, and offers a somewhat improved description in the region near the maximum velocity. For comparison, the exponential form used in the previous figure is also included by utilizing the value of Δ_2/Δ_j. Again, this form adequately describes the velocity profile everywhere except over the outer portion near the minimum value.

In addition to the lateral profile similarity which exists for the maximum velocities, there also exists lateral similarity in planes, y = constant, located between $y = \delta_1$ and $y = \delta_2$. This is illustrated in Figure 58, which includes both positive and negative values of z_c. Also shown is the analytical form presented by Liaw for characterizing two-dimensional wall jet profiles. Good agreement with this curve is displayed over the entire profile.

In summary, both vertical and horizontal velocity profile similarity have been demonstrated for the Phase 2 test results. For both

the centerline and off-centerline vertical velocity profiles, not only was excellent profile similarity demonstrated, but also, good agreement with the analytical form of Verhoff was shown. Good agreement with Liaw's two-dimensional profile was also demonstrated for $x/d = 35.7$. Additionally, the lateral maximum velocity profile was shown to be in very good agreement with a free shear layer exponential profile. Lateral velocity profiles taken in planes y = constant between $y = \delta_1$ and $y = \delta_2$ were also shown to be similar, exhibiting close agreement with Liaw's analytical profile.

The characteristic length and velocity scales used in treating the Phase 3 vertical velocity profile data ($u_j/u_{e_o} = 2$) are defined in Figure 59. Because of the very thin upstream boundary layer, the velocity profiles exhibited no u_{min}, and the definitions of δ_2 and δ_j are based on u_1 and u_e.

The normalized plot of the centerline velocity profiles for Phase 3 is shown in Figure 60. The results display excellent similarity. The analytic function derived by Liaw for the two-dimensional wall jet data of Neale is also included; this form provides an excellent description of the current three-dimensional wall jet results. For comparison, an exponential function, which results from the constant eddy viscosity solution for a two-dimensional wake (with small differences between the free-stream velocity and the minimum velocity in the profile), is also included. Like Liaw's form, this exponential form is matched to the data at the half-velocity height. While yielding only fair agreement in the outer portion of the profile, the exponential form also provides an

excellent description of the data from the region of the half-velocity height to the jet peak.

Consideration of the vertical velocity profiles at off-centerline stations also reveals similarity. Figures 61 and 62 display normalized centerline and lateral station velocity profiles for two streamwise stations, at $x/d = 12.2$ and at $x/d = 24.5$. Both results exhibit excellent profile similarity. Again, the results are in very good agreement with Liaw's results from 2-D wall jets.

The Phase 3 results, like those of Phase 2, reveal a slight drifting of the jet centerline from the geometrical centerline. This behavior is illustrated in the lateral distribution of maximum velocities shown in Figure 63; the velocity distributions at both $x/d = 12.2$ and 24.5 reveal this slight drift. As before, in order to make allowance for this experimental difficulty, a redefined jet centerline was selected, based on a faired curve through the data, for each of the downstream stations. This corrected centerline, $z_c = 0$, is identified by a dashed line for both stations. Faired curves through the data are also shown for both downstream stations; these smooth curves through the results are the bases for defining a new peak centerline velocity, u_1. In terms of the jet velocity, u_j, the definition of a new peak centerline velocity results in less than a 2% change in the value of u_1/u_j. Thus, the previous results for jet growth, decay and vertical similarity are not significantly affected by this redefinition of the centerline location and velocity.

The validity of these revised centerlines is shown in Figures 64

and 65; close agreement of these peak velocity results is shown for both positive and negative z_c locations. A faired curve passes smoothly through the data of each x/d location illustrating the symmetry of the results. These plots also yield the value of Δ_2 at each location; this characteristic lateral length scale is defined in Figure 55. Once again, having redefined the jet centerline to account for an experimental discrepancy, one can examine the lateral velocity profiles for similarity.

Figure 66 displays a non-dimensionalized lateral distribution of the local maximum velocities at both x/d = 12.2 and 24.5. This figure, which uses Δ_2 as the normalizing length scale and the velocity difference, u_1-u_{min} as the characteristic velocity, includes both positive and negative z_c values and displays good similarity. Also included in the figure is an exponential profile which is widely used for describing free shear flows and which shows good agreement with the present results, except near the minimum velocity. It is expected that additional data in the region of interaction between the jet and the between-jet boundary layer would improve the definition of u_{min} and the agreement in this region.

In addition to the lateral profile similarity which exists for the maximum velocities, there also exists lateral similarity in planes y = constant located between values of $y = \delta_1$ and $y = \delta_2$ at z = 0. Figure 67 displays the distribution of velocities in three planes of constant height for downstream station x/d = 12.3. These distributions, which contain data for both positive and negative values of z_c, allow determination of the normalizing length, Δ_2, for each value of y/d.

Figure 68 contains normalized plots of these velocity profiles. The results reveal good profile similarity for the three values of y/d. Also included is an exponential profile which is widely used for describing free shear flows. The present results show good agreement with this analytical form, except in approaching the region of the minimum value.

Similar results for downstream station x/d = 24.5 are shown in Figures 69 and 70. Again, the results for three lateral velocity profiles at various constant heights (between $y = \delta_1$ and $y = \delta_2$ at $z = 0$) reveal good similarity and very good agreement with the free shear exponential form.

In summary, both vertical and horizontal velocity profile similarity has also been demonstrated for the Phase 3 test results. For both the centerline and off-centerline vertical velocity profiles, not only was profile similarity demonstrated, but also excellent agreement with the analytical form of Liaw was shown. Moreover, lateral peak velocity profiles and lateral velocity profiles taken in planes y = constant (between $y = \delta_1$ and $y = \delta_2$ at $z = 0$) were shown to be similar for two downstream stations. In general, good agreement between these horizontal profiles and a free shear layer exponential profile was also shown.

Wall Jet Iso-velocity Profiles

Plots of constant velocity contours (i.e., iso-velocity profiles or isotachs) for the three-dimensional wall jet flow fields are presented in Figures 71, 72, 74 and 75 as an additional aid in visualizing and interpreting the flow development. These four sets of data are the result of multiple vertical velocity surveys conducted at four downstream stations

with the integrated nozzle configuration. Two downstream locations are presented for jet flow only (Phase 2), and the other two are for a jet-to-freestream velocity ratio of two (Phase 3). This synthesizing of the individual vertical velocity profiles provides both a representation of the flow at a given location, and also, for several locations, provides a format for showing the response of the jet to a given external condition. The plots specifically show contours of constant local-to-jet peak velocity ratio, u/u_1, in a plane normal to the jet flow looking upstream. The lateral and vertical distances are non-dimensionalized by the jet nozzle diameter.

The iso-velocity contours in Figure 71 represent interpolated data from 14 vertical surveys at station x/d = 20.9. The lateral distances extend on both sides of the nozzle centerline to the line of symmetry between adjacent nozzles (i.e., z = ± 1.363 inches). The results reveal that the contours which are approximately circular at the jet exit, become flattened ovals in shape, with the major axis oriented parallel to the wall; this feature was also reported by Newman, et al. [21]. This is considered to be a result of jet spreading due to lateral pressure gradients created by flow entrainment in the confined space near the wall. The profiles also reveal the slight drift from the geometrical centerline, with the corrected centerline at approximately z/d = -0.209, or z = -0.093 inch. Also presented in Figure 71 are lines connecting the local values of δ_1 and δ_2. These results reveal that though the jet profile is three-dimensional, the confined lateral spreading has produced approximately horizontal lines of δ_1 and δ_2. The lateral mixing continues downstream of this station.

As shown in Figure 72, horizontal jet spreading and mixing is essentially completed at x/d = 50. At this station, the wall jet flow is nearly two-dimensional. These results are obtained from data of 10 vertical profiles over a horizontal and vertical distance twice that of the previous figure. The approximately horizontal contours of δ_1 and δ_2 are also shown. The completion of jet spreading and mixing is also illustrated by the variation of δ_2 with downstream distance, shown plotted using normalized coordinates in Figure 73. This figure, which displays the growth of the half-velocity height both on the jet centerline and on both sides of the nozzle centerline at the line of symmetry between adjacent nozzles, further confirms that an essentially two-dimensional flow exists downstream of station x/d = 50.

The iso-velocity contours in Figure 74 are the result of interpolated data from 15 vertical profiles surveyed at station x/d = 12.2 for a jet-to-freestream velocity ratio, u_j/u_{e_o}, of two. Also shown are the lateral variations of δ_1 and δ_2, along with the previously discussed slight drift from the geometric centerline. These results display contours for both the wall jet flow and the wall boundary layer between jets. The jet flow contours again show flattening near the wall in the wall layer and a slightly oval character due to spreading over the wall. The contours indicate that the influence of the jet extends laterally to the centerline between nozzles, as evidenced by the slopes of the contours, and approximately two nozzle diameters above the wall.

Figure 75, which details the results of 15 vertical profiles at x/d = 24.5, shows similar limits on the vertical extent of jet influence;

however, the lateral influence has increased, as shown by the slopes of the contours in this region. The extent of jet spreading into the wall layer is strongly controlled by the jet momentum excess, a factor which is discussed in the next section.

This method of data treatment is a valuable aid in visualizing and interpreting the wall jet flow development. Synthesizing the individual vertical velocity profiles provides both a representation of the flow at a given location, and, for several locations, provides a format for showing the response of the jet to a chosen external condition. The resulting representation is valuable for indicating flow development trends and flow regions requiring additional analysis.

Wall Jet Integrated Velocity Profiles

An additional means of synthesizing the velocity profile data is provided by integrals of the velocity data for a fixed streamwise position. In contrast to the semi-quantitative results of the iso-velocity contours, profile integrals yield a quantitative measure of the averaged flow characteristics. This characterization of the wall jet flow is useful for assessing the three-dimensional development as well as providing a basis for comparing 3-D and 2-D wall jet results. The integral parameters computed for this approach are the displacement, momentum and energy thicknesses. They are applicable only for the data of Phase 3. For wall jets these characteristic thicknesses are generally negative, implying excesses of mass, momentum and mechanical energy flux with respect to the freestream. A comparison of the rate of change of these characteristic thicknesses with corresponding 2-D results provides a

relative measure of these BLC concepts. In addition, an evaluation of wall jet momentum deficit for constant pressure flow provides a measure of the frictional losses at the wall.

Characteristic thicknesses at selected lateral stations for several downstream locations will be considered first. These thicknesses are defined as follows [34]:

$$\delta^* = \int_o^\delta \left(1 - \frac{\rho u}{\rho_e u_e}\right) dy$$

$$\theta = \int_o^\delta \frac{\rho u}{\rho_e u_e}\left(1 - \frac{u}{u_e}\right) dy$$

$$\delta^{**} = \int_o^\delta \frac{\rho u}{\rho_e u_e}\left(1 - \frac{u^2}{u_e^2}\right) dy \ .$$

These integrals are evaluated numerically using Simpson's rule [28]. Figures 76, 77 and 78 display the distribution of δ^*, θ and δ^{**} at downstream station $x/d = 12.25$. These results are from the vertical velocity profiles at 39 lateral stations located over an 11 inch span of the test section. The data format is the view depicted looking upstream. The "thickness profiles" show the characteristic negative values about the jet centerlines. In the regions between the nozzles, where a boundary layer exists and the jet has not yet penetrated, the thicknesses are positive. In general, the thickness profiles reveal good symmetry about the jet centerlines, although the slight lateral drift of the jet centerline discussed previously is evident.

Further information about the flowfield is provided by area integrals of the velocity data for fixed streamwise planes. Again, the quantities determined are the characteristic thicknesses. However, in this case they are integrated mean values over a particular lateral span. Since these quantities depend on all the velocity data for a given streamwise plane, they provide an excellent means for synthesizing the numerous profile data. Just as iso-velocity contours, instead of a single profile, are necessary to characterize the 3-D flow, an area integration, rather than a single direction integration, is required to compute these characteristic thicknesses. For this analysis, the integrated mean (I.M.) thicknesses are defined by

$$\delta^*_{I.M.} = \frac{1}{\Delta z} \int_{z_1}^{z_n} \int_o^{\delta} \left(1 - \frac{\rho u}{\rho_e u_e}\right) dydz$$

$$\theta_{I.M.} = \frac{1}{\Delta z} \int_{z_1}^{z_n} \int_o^{\delta} \frac{\rho u}{\rho_e u_e} \left(1 - \frac{u}{u_e}\right) dydz$$

$$\delta^{**}_{I.M.} = \frac{1}{\Delta z} \int_{z_1}^{z_n} \int_o^{\delta} \frac{\rho u}{\rho_e u_e} \left(1 - \frac{u^2}{u_e^2}\right) dydz$$

where the integration over z extends over the lateral span from z_1 to z_n, and $\Delta z = z_n - z_1$. These forms of the thickness relations are derived in Appendix D. The method of cubature is used for the numerical integrations [28].

The integrated mean values of the displacement, momentum and

energy thickness in the freestream flow at the reference station immediately upstream of the nozzles are

$$\delta^{*}_{I.M._o} = 0.0578 \text{ inch}$$

$$\theta_{I.M._o} = 0.0458 \text{ inch}$$

$$\delta^{**}_{I.M._o} = 0.0789 \text{ inch}$$

These positive values reflect the boundary layer growth in the flow development section. These data are included as horizontal lines in Figures 76, 77 and 78. The much larger values of thicknesses between nozzles indicate both the considerable losses which occur over the nozzle ramps and the losses due to the action of wall skin friction on the flow.

Figure 79 displays the distribution of the shape factor, $H = \delta^{*}/\theta$, as derived from the data of Figures 76 and 77. The shape factor for the freestream flow at the reference station is also shown. For comparison, it is noted that the data of Nikuradse, Gruschwitz and Kehl, as tabulated by Schlicting [34], show that separation of a turbulent boundary layer with pressure gradient occurs for $H \approx 1.8 - 2.4$. The values of H for the between-nozzle stations reveal the increase from $(\delta^{*}/\theta)_{I.M._o}$ that results from the adverse pressure gradients due to flow over the ramps. By contrast, the low values of shape factor exhibited in the jet centerline regions imply excess momentum, which can be utilized for BLC.

As discussed in the Flow Evaluation section of this chapter, the

nozzle flow centered at z = 2.727 inches was chosen for further analysis because of the good flow symmetry in this region. This symmetry is illustrated by the values of the integrated mean momentum thickness at x/d = 12.2 for several regions about this selected centerline.

$$\theta_{I.M.}\ (0,\ 5.454) = 0.0055 \text{ inch}$$

$$\theta_{I.M.}\ (0,\ 2.727) = 0.0051 \text{ inch}$$

$$\theta_{I.M.}\ (2.727,\ 5.454) = 0.0059 \text{ inch}$$

$$\theta_{I.M.}\ (1.363,\ 4.090) = 0.0053 \text{ inch}$$

The good agreement of these values for regions about the selected centerline (z = 2.727 inches) gave good confidence for further studies of the jet and freestream flow interactions in this region.

Figure 80 displays the distributions of δ^*, θ and δ^{**} about the jet centerline, z = 2.727 inches, at the streamwise stations x/d = 12.2 and 24.5. These results, which are from 15 vertical velocity profiles over a 2.73 inch span, illustrate the development of the thicknesses due to the mixing of the jet with the freestream boundary layer. The results on, and in the vicinity of, the jet centerline display an increase in characteristic thickness with axial distance. This increase is due to the velocity decay which results from mixing of the jet with the boundary layer and freestream flow and from wall shear. By contrast, the values near the between-nozzles centerline reveal a decrease in characteristic thickness with axial distance due to energization of the boundary layer by the jet. The values of the integrated mean thicknesses

at the freestream reference station are also included in the figure to illustrate the increase in characteristic thicknesses which occurs due to passage of the freestream flow over the nozzle ramps and to wall shear.

Further information on streamwise flow development is given in Table 4 which documents the change in displacement thickness, momentum thickness, energy thickness and shape factor for both the jet centerline, $z = 2.727$ inches, and the centerlines between nozzles, $z = 1.363$ inches and $z = 4.090$ inches. At the initial station, $x/d = 8.198$, the jet centerline thicknesses are relatively large negative values, indicative of the mass, momentum and energy excesses which exist, relative to the freestream. At the same streamwise location, the values at the between-nozzle centerlines are relatively large positive values, indicative of the deficit in the wall boundary layer flow, relative to the freestream. The large increase in between-nozzle values over the values at the freestream reference (i.e., the $(\ )_{I.M._o}$ values) indicates a considerable loss over the between-nozzle ramps. At downstream stations, the centerline values are increasing as a result of the jet spreading and mixing with the surrounding flow. Correspondingly, the excesses in mass, momentum and mechanical energy have decreased. On the other hand, at the locations between the nozzles, the thicknesses generally decrease as the jet spreads, energizing the boundary layer and reducing the deficits. This tabulation also reveals that the wall jet has additional capacity for energization of the boundary layer downstream of the final station at $x/d = 35.68$. Additionally, the fact that the shape factor is decreas-

ing with downstream distance portends greater resistance of the between-nozzle boundary layer to flow separation [34]. This trend is very important to the designer who wishes to use three-dimensional wall jets in a BLC application.

The data of Figure 80 were used to calculate the area integrals (i.e., the $\delta^*_{I.M.}$, $\theta_{I.M.}$, and $\delta^{**}_{I.M.}$) at x/d = 12.2 and 24.5. These results are plotted in Figures 81, 82 and 83 in terms of the differences between characteristic thicknesses at a particular downstream station and the values at the free stream reference station; these differences are normalized by the equivalent slot height. This plotting format allows comparison both with different wall jet configurations, as exemplified by Neale's two-dimensional wall jet results, and with different freestream boundary layer thicknesses. Furthermore, in the ideal case of no ramp or nozzle losses, these normalized variables become simply $\frac{\delta^*_j}{h_{eq}}$, $\frac{\theta_j}{h_{eq}}$ and $\frac{\delta^{**}_j}{h_{eq}}$ at x = 0 inches, where

$$\frac{\delta^*_j}{h_{eq}} = 1 - \frac{\rho_j u_j}{\rho_e u_e}$$

$$\frac{\theta_j}{h_{eq}} = \frac{\rho_j u_j}{\rho_e u_e}\left[1 - \frac{u_j}{u_e}\right]$$

$$\frac{\delta^{**}_j}{h_{eq}} = \frac{\rho_j u_j}{\rho_e u_e}\left[1 - \left(\frac{u_j}{u_e}\right)^2\right]$$

Because these variables represent an idealized design, comparison of

their values with the test values reveals the efficiency of an actual nozzle integration. The ideal values for the three-dimensional wall jet are shown as dashed lines in the three figures.

Relative to the ideal values, the higher values of displacement, momentum and energy thicknesses at $x/h_{eq} = 97$ demonstrate both the losses due to the present nozzle/ramp integration design, as well as the wall losses due to skin friction. The increase of momentum thickness due to mixing with the freestream boundary layer is also included. In fact, the loss of momentum across the ramp as indicated by the results in Figure 82 is approximately equivalent to one half of the momentum injected. Thus, additional research to seek more efficient integrated nozzle designs is warranted.

Figure 81 reveals the change in the normalized displacement thickness for both the present jet configuration and the two-dimensional wall jet results of Neale. The data trends are emphasized with a solid line. The thickness value for the three-dimensional configuration unexpectedly decreases slightly, while it shows the expected increase for the two-dimensional results. This latter behavior reflects the decay of the injected momentum due to wall friction and mixing with the lower-momentum freestream. The unexpected behavior of the three-dimensional result is explained by reference to Figure 80 and Table 4. First, the data of Figure 80 reveal that over the downstream distance of $x/d = 12.2$ to $x/d = 24.5$, significantly larger decreases of θ and δ^{**} occur on the jet centerline than is exhibited by δ^{*}. The momentum thickness increases approximately 60%, and the energy thickness increases approximately 71%,

while the displacement thickness increases by only 45%. Interestingly, the relative mixing and decay of the two-dimensional jet over the same downstream distance is almost identical; δ^* increases by 48%, θ increases by 60%, and δ^{**} increases by 67%. By contrast, the change in the characteristic thicknesses over the lateral edges of the jet show greater percentage decreases of δ^* than those exhibited by θ and δ^{**}. This trend is illustrated by the results for $z = 1.363$ inches, whereas δ^* decreases by 9%, θ and δ^{**} decrease by 3% and 0.5%, respectively, over the same downstream distance. This trend is typical of the changes in thicknesses which occur over the lateral edges of the three-dimensional jet. The net effect of these contrasting behaviors is the decrease of integrated displacement thickness over the indicated downstream distance, while the integrated momentum and energy thicknesses increase, as shown in Figures 82 and 83.

It is significant that the three-dimensional wall jet reveals an integrated momentum thickness increase which is less than for the two-dimensional wall jet. This result is shown in Figure 82. Over the same downstream lengths, the momentum thickness of the three-dimensional wall jet increases approximately 21%, while the two-dimensional results reveal an approximately 38% increase. This is apparently an indication of the relatively smaller wall friction effect on the three-dimensional wall jet, and indicates potentially superior jet persistence for this type of flow field.

In summary, these results indicate that the three-dimensional wall jet seems to offer advantages over two-dimensional configurations, especially if the losses due to the integration of the nozzles can be

eliminated or minimized by proper design. It is very important that such a design avoid flow separation over the between-nozzle ramps, though this is somewhat controllable by higher jet momentum. The behavior of the displacement and momentum thicknesses at between-nozzle and centerline locations is summarized in Figures 84 and 85. The mid-nozzle results reveal a very gradual decrease in value when referenced to the integrated mean values at the reference station. By contrast, the centerline values reveal a rapid increase when similarly referenced. A larger value of between-nozzle loss could yield even more rapid increases of centerline displacement and momentum thickness, as the centerline momentum would be consumed in controlling the between-nozzle deficit.

An additional measure of the boundary layer control potential of the multiple orifice jets is shown in Figure 86, where the variation of between-nozzle momentum thickness for the present configuration is compared with the momentum thickness variation for a turbulent boundary layer on a flat plate [34]. A one-seventh power velocity distribution is assumed for the flat plate boundary layer. For this comparison, the two cases are matched at the data station, x = 3.64 inches. Again, the decreasing values of for the present configuration are the result of the energization of the freestream and between-nozzle boundary layers by the multiple jets, and the results confirm the BLC potential of this configuration.

Wall Jet Skin Friction

Friction Coefficient. The wall jet skin friction coefficients, which were determined using a Preston-type probe, are shown in Figures 87

and 88. The probe used was previously calibrated by Neale [13] and compared with the results of Patel [25]. The friction coefficients are plotted versus the local Reynolds number based on the maximum velocity, u_1, and the wall layer thickness, δ_1. Values are presented for the jet centerline location, z = 0 inches, and the centerlines between nozzles, z = 1.363 inches for various downstream stations. Figure 87 displays the results from the integrated nozzle configuration for jet flow only (i.e., Phase 2); Figure 88 contains the results from the same configuration operated at a velocity ratio of two (i.e., Phase 3).

The friction coefficients shown in Figure 87 compare well with the experimental, 2-D wall jet results of both Bradshaw and Gee [35] and Neale [13]. Both of these results were also obtained using Preston tubes. The values for both the jet centerline and the between-nozzle locations show good agreement with the previous results.

In Figure 88 the values of friction coefficient for the Phase 3 tests are compared with the experimental values of Neale at the same velocity ratio, and with Coles' computation of Wieghardt's constant pressure boundary layer [36]. Along the jet centerline (z = 0), the value of the friction coefficient near the jet exit (x/h_{eq} = 65) is very near the flat plate boundary layer value, reflecting the fact that the near-wall portion of the jet flow resembles a boundary layer in some "starting region." In this region the influence of the outer layer has not yet penetrated through the jet. Further downstream, the influence of the outer layer is felt by the wall layer, and the values of the friction coefficient increase rapidly, showing good agreement with Neale's two-dimensional wall

jet data. This same trend in friction coefficient values was evident in Neale's data, though more rapid transition to the higher values of friction coefficient was demonstrated; this behavior was the result of the smaller nozzle height, and, hence, more rapid establishment of true wall-jet flow. These differences are also evident in the law of the wall plots to be discussed in the next section.

Along the between-nozzle centerline (z = 1.363 inches) the value of the friction coefficient near the jet exit (x/h_{eq} = 65) is also very near the flat plate boundary layer value, but the values increase with downstream location, reflecting the jet's increasing influence on this region with downstream distance. However, the values never reach the higher levels demonstrated along the line z = 0 inches because of the weaker influence of the jet in the off-centerline locations. Nevertheless, a significant influence of the jet is apparent.

H. Ludwieg and W. Tillman showed that the wall shearing stress for a two-dimensional turbulent boundary layer depends strongly on the shape factor H. Their results, which are tabulated by Schlichting [34], are well approximated by the empirical formula

$$\frac{\tau_w}{\rho U^2} = 0.123 \times 10^{-.678H} \, Re_\theta^{-.268}$$

The present results along the between-nozzle centerline (z = 1.363 inches) have been compared with this empirical form in Figure 89. This comparison reveals that the measured friction coefficient is consistently lower than that predicted by the empirical result. It is concluded that the

Ludwieg-Tillman formula based on shape factor has only limited applicability to a three-dimensional wall jet, with the empirical form perhaps being used as an upper limit for estimating wall shear stress.

In summary, the measurements of wall friction coefficients for a 3-D wall jet operating without external flow reveal values which agree well with 2-D wall jet results. When operated with a freestream flow, the jet centerline measurements display agreement with the 2-D turbulent boundary layer results in the "starting region," and agree well with 2-D wall jet results downstream of this region. The between-nozzle measurements display the same trend; however, the maximum values are lower than the jet centerline values due to the limited influence of the jet in this flow region.

Law of the Wall. Semi-logarithmic plots of velocity profiles in the wall layer of the 3-D wall jet for the integrated configuration (Phase 2) at an infinite velocity ratio are presented in Figures 90 and 91. The results from measurements along the jet centerline and along the mid-nozzle centerline are plotted in Figures 90 and 91, respectively. Both plots include the straight lines corresponding to Coles' "law of the wall" [36] and Neale's 2-D wall jet results [13]. In contrast with turbulent boundary layer results, these wall jet data exhibit the usual behavior of falling below the linear law in the outer region of the wall layer, reflecting the influence of the jet layer. However, as expected, the data nearest the jet exit at $x/h_{eq} = 43$ show little divergence from the linear equation since the wall and jet layers are in the initial stages of interaction (i.e., the wall layer is nearly a typical boundary

layer). The data appear to agree better with Coles' "law of the wall" in the region around $\log_{10}(u_\tau y/\nu) = 2$, where the linear law usually holds, than with Neale's linear equation. However, the differences are relatively small.

Liaw [33] has recently shown that Neale's data for this region near the wall agree well with an analytical relationship based on the boundary layer equations, a modified mixing length formula and similarity requirements. According to this formulation, the velocity profiles in the near-wall region depend upon the streamwise decay of the wall shear stress (or the friction velocity, u_τ). A comparison of two velocity profiles from the present data with the analytical predictions of Liaw is presented in Figure 92. The parameter λ is a measure of the rate of streamwise decay of wall shear stress. The data for both $x/h_{eq} = 166$ and 396.5 exhibit linear regions from $\log_{10}(u_\tau y/\nu) = 1.6$ to 2.25. Additionally, the values for $x/h_{eq} = 166$ are lower than the theory of Liaw predicts, while a value slightly higher than predicted is exhibited for $x/h_{eq} = 396.5$. However, the theory correctly predicts the trends and provides a valuable representation of the sublayer. This is important since an analytical expression for this layer when coupled with expressions for the outer flow may be used to evaluate the wall shear stress [33].

Figures 93 and 94 display velocity profiles in the wall sublayer for the velocity ratio of two investigation (Phase 3). The results along the jet centerline ($z = 0$) are shown in Figure 93. The data display linear behavior for $30 < (u_\tau y/\nu) < 500$, and generally agree well with Coles'

linear form. However, the u/u_τ result for $x/h_{eq} = 65$ diverges above Coles' law of the wall at large values of $u_\tau y/\nu$; this behavior is typical of a wall boundary layer and illustrates that the outer shear layer has not yet merged with the wall layer. Further downstream, the results are typical of 2-D wall jet results, in which the wall layer is retarded by the outer jet layer. These results give excellent agreement with Coles' linear equation in the region around $\log_{10} (u_\tau y/\nu) = 2$.

The results along the between-nozzle centerline ($z = 1.363$) are shown in Figure 94. These data exhibit a range of turbulent boundary layer behavior. As expected, for very low values of $u_\tau y/\nu$, the data fall below Coles' linear result, while at values above about 400, the typical trend of values greater than the linear description is observed. The values of λ for each profile are indicated; their very low magnitudes show good agreement with Coles' result ($\lambda = 0$) over the linear portion of the velocity profiles. Also, at large values of $\log_{10} u_\tau y/\nu$, the results reveal values of Coles' profile matching parameter, π, that describe the downstream flow development. At $x/h_{eq} = 65$ the outer profile has a π value of 1.14 which Coles showed is indicative of a turbulent boundary layer subjected to a mild positive pressure gradient [36]. In this case, the positive pressure gradient is imposed on the freestream boundary layer by the between-nozzle fairings. The value of π decreases rapidly downstream due to constant pressure flow. However, the results display a pronounced effect due to the spreading influence of the jet. The value of π of 0.22 at $x/h_{eq} = 283$ is a good indicator of the jets' influence on the profile, since Coles showed a typical constant pressure boundary

layer has a π of about 0.6 and a typical negative pressure gradient boundary layer has a π value of about 0.2. Thus, these experimental values of π for this 3-D wall jet show the development of the between-nozzle boundary layer, and are consistent with the δ^*/θ trends shown earlier.

In summary, the wall sublayer velocity profiles for the 3-D wall jet show good agreement over the linear portion with Coles' empirical "law of the wall" result. The jet centerline results show typical wall boundary layer profiles at the near-jet station, illustrating no outer shear layer influence on the wall layer. Further downstream, the wall layer is retarded by the outer jet layer, and the typical wall jet profile is demonstrated. The profiles for the between-nozzle centerline exhibit a typical range of turbulent boundary layer behavior. Coles' linear portion of the profile, and the outer layer's influence on downstream development are well described by Coles' profile matching parameter, π.

Table 1. Phase 1 Data Index
(Appendix A)

Re_d	x/d	x/h_{eq}	z	Measurements*		Summary Index
				Velocity Profile	Skin Friction	
53,400	5.4	43	0	X		194
	8.7	69	0	X		194
	15.3	121	0	X		194
	25.	198	0	X		194
	35.7	283	0	X		194
106,800	5.4	43	0	X		194
	8.7	69	0	X		194
	15.3	121	0	X		194
	25.	198	0	X		194
	35.7	283	0	X		194

* "X" denotes measurements made.

Table 2. Phase 2 Data Index (Appendix B)

Re_d	x/d	x/h_{eq}	z	Measurements*		Summary Index
				Velocity Profile	Skin Friction	
53,400	5.4	43	0	X	X	206
	15.3	121	0	X	X	206
			± 2.727	X		206
	20.9	166	0	X	X	206
			- 0.062	X		206
			± 0.125	X		206
			± 0.250	X		206
			± 0.500	X		207
			± 0.750	X		207
			± 1.000	X		207
			± 1.363	X	X	207
	30	238	0	X		207
	35.7	283	0	X	X	208
			± 1.363	X	X	208
	40	317	0	X		208
	50	396.5	0	X	X	208
			- 0.062	X		208
			± 0.125	X		208
			± 0.500	X		208
			± 1.363	X	X	209
			± 2.727	X		209
	60	476	0	X	X	209
			± 1.363	X	X	209
	70	555	0	X	X	209
			± 1.363	X	X	209

*"X" denotes measurements made.

Table 3. Phase 3 Data Index (Appendix C)

u_j/u_{e_o}	x/d	x/h_{eq}	z	Measurements*		Summary Index
				Velocity Profile	Skin Friction	
2.0	8.2	65	0	X	X	250
			± 1.363	X	X	250
	12.2	97	0	X	X	250
			± 0.125	X		250
			± 0.250	X		250
			± 0.312	X		250
			± 0.437	X		251
			± 0.500	X		251
			± 0.937	X		251
			± 1.363	X	X	251
	16.3	129	0	X	X	251
			± 1.363	X	X	251
	24.5	194	0	X	X	252
			± 0.125	X		252
			± 0.250	X		252
			± 0.312	X		252
			± 0.437	X		252
			± 0.500	X		252
			± 0.937	X		253
			± 1.363	X	X	253
	35.7	283	0	X	X	253
			± 1.363	X	X	253

*"X" denotes measurements made.

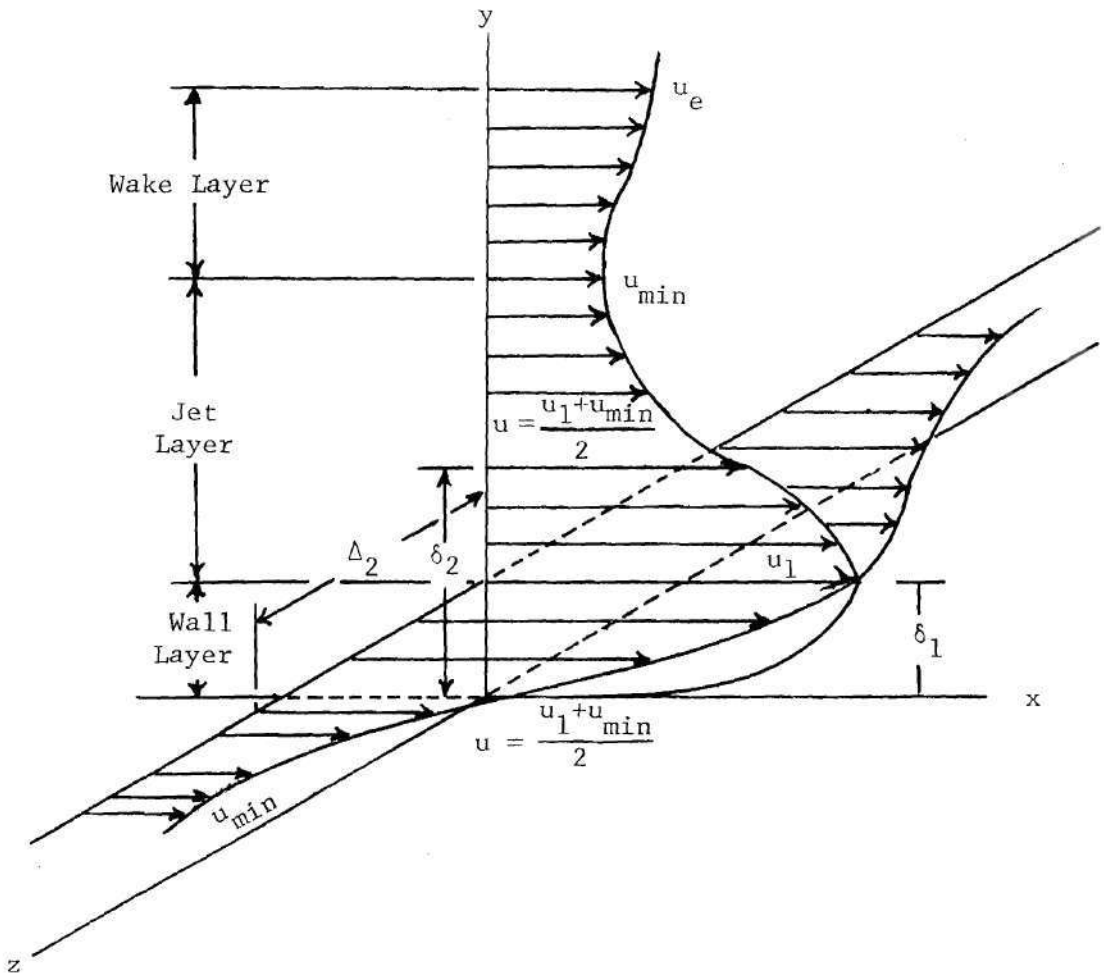

Figure 18. Wall Jet Velocity Profile Nomenclature

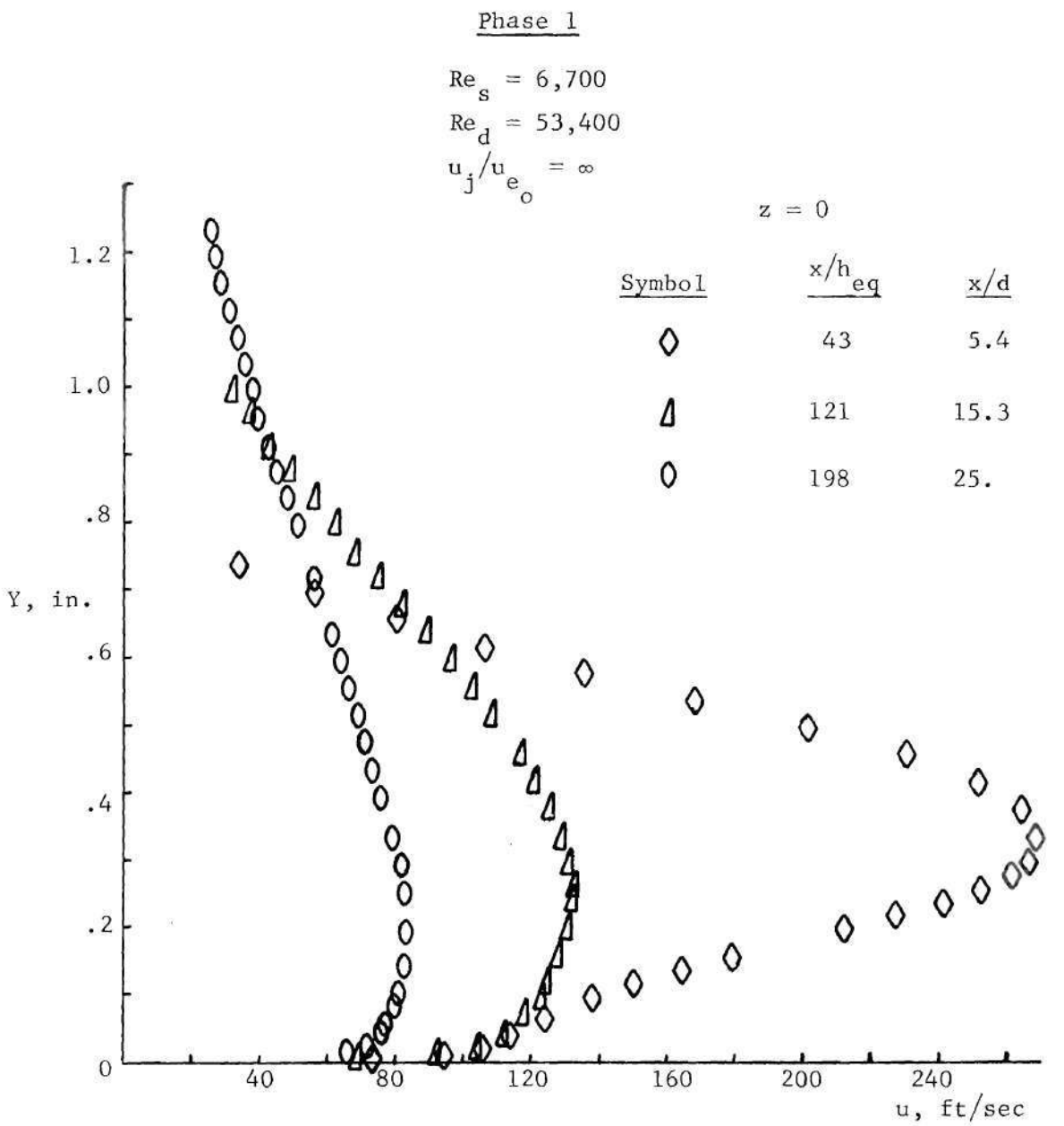

Figure 19. Phase 1 Composite Wall Jet Development for the Basic Multiple Orifice Configuration

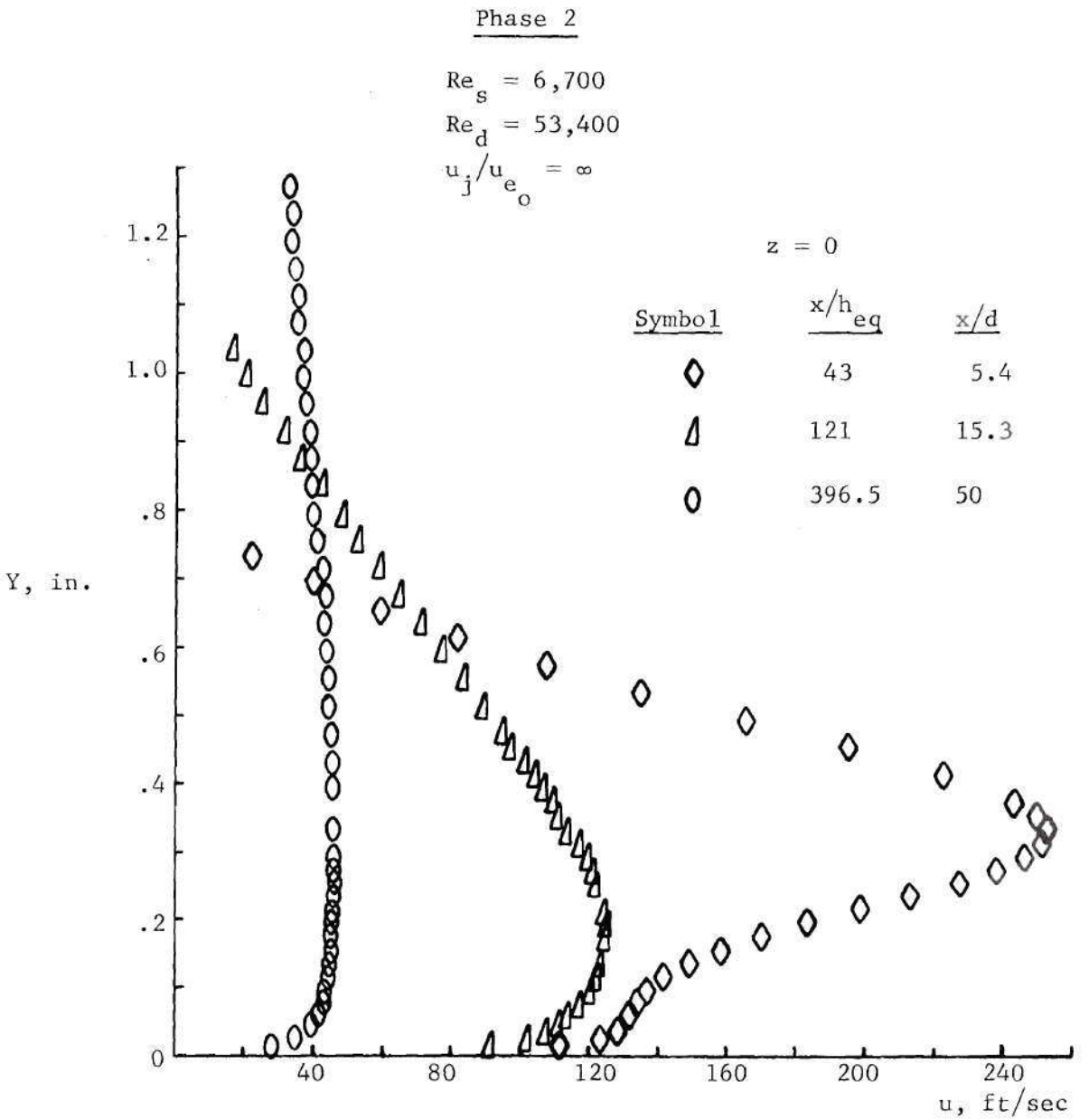

Figure 20. Phase 2 Composite Wall Jet Development for the Integrated Multiple Orifice Configuration

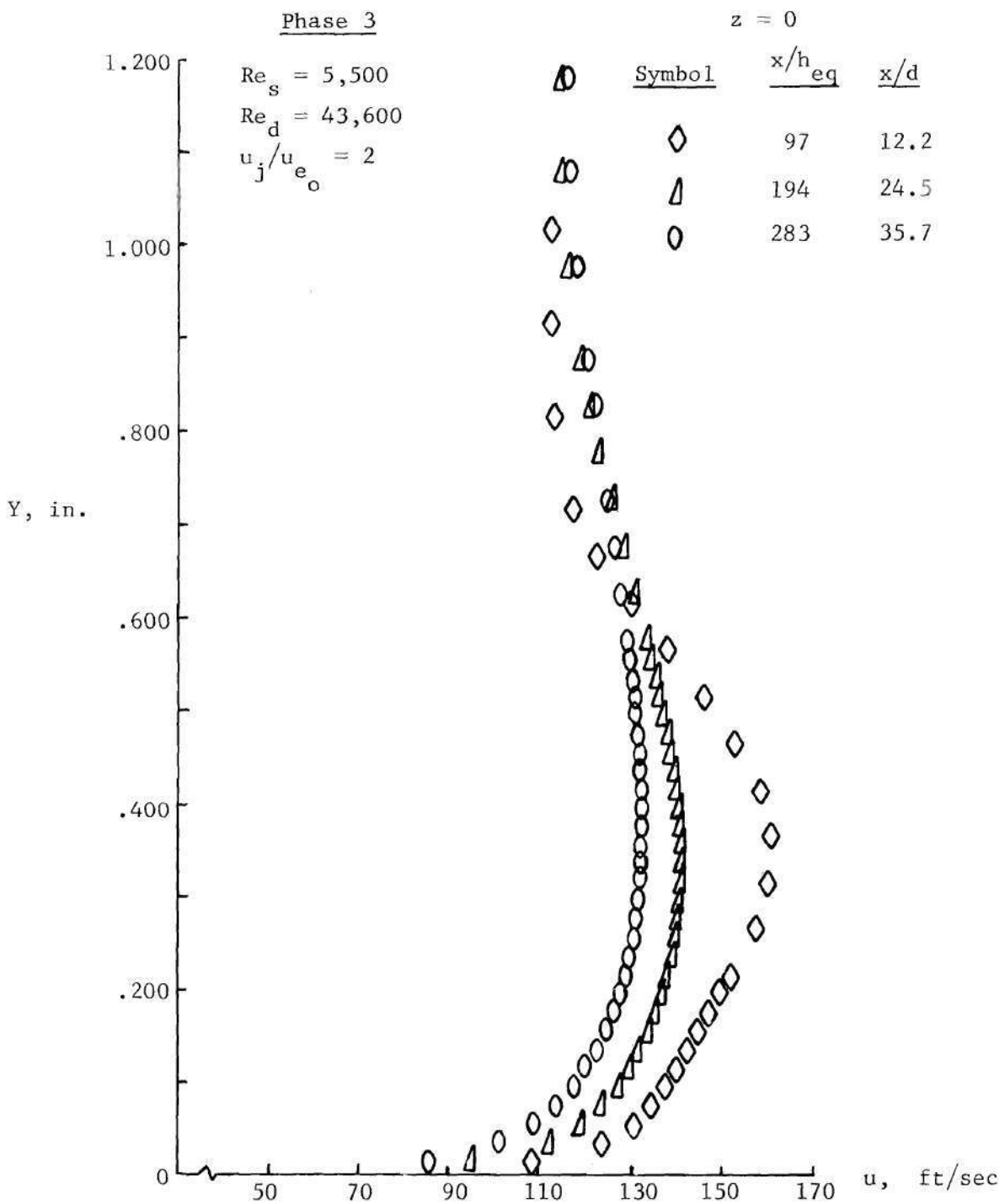

Figure 21. Phase 3 Composite Wall Jet Development for the Integrated Multiple Orifice Configuration

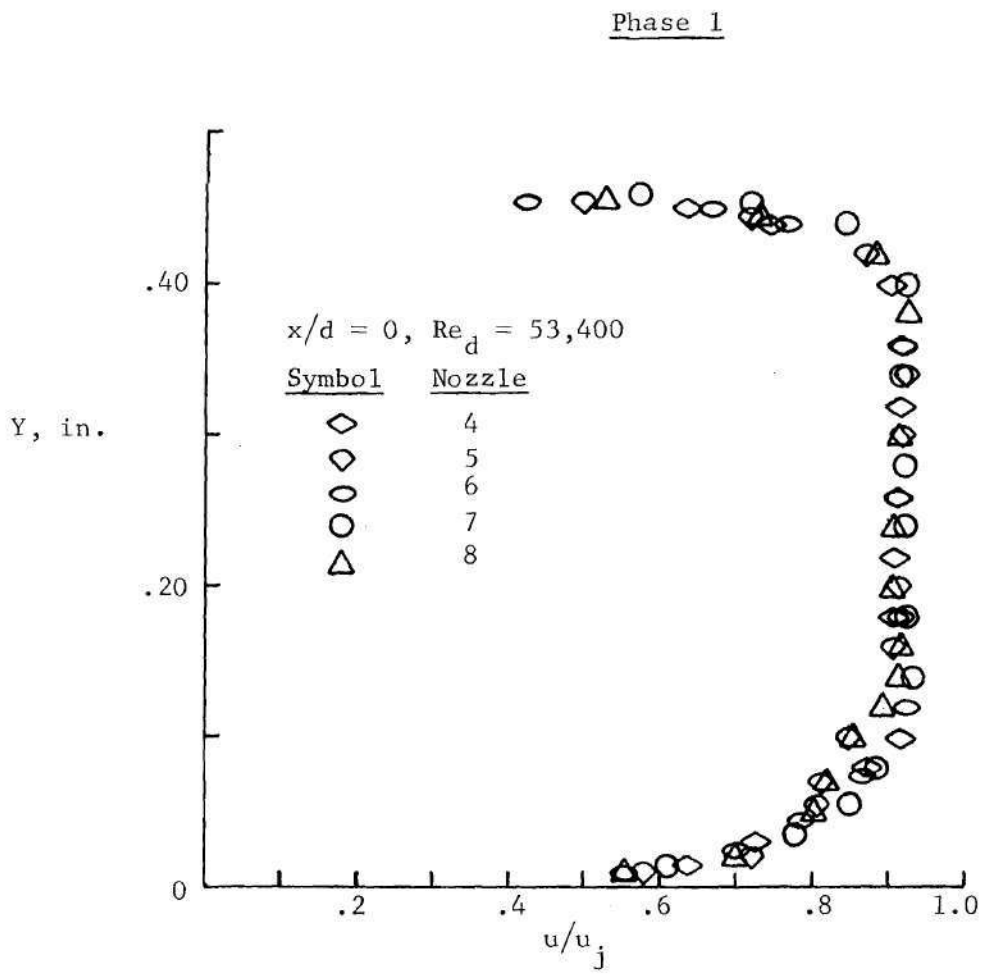

Figure 22. Jet Vertical Velocity Profile at the Exit

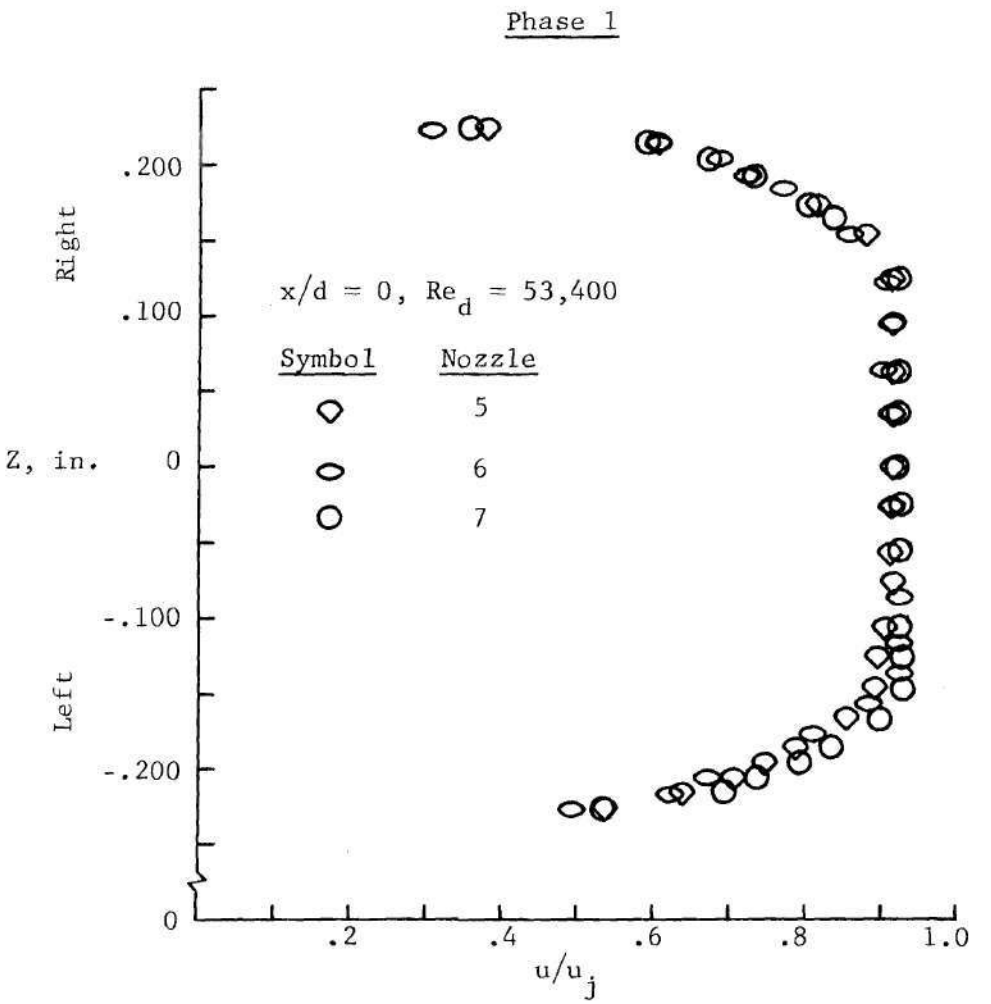

Figure 23. Jet Horizontal Velocity Profile at the Exit

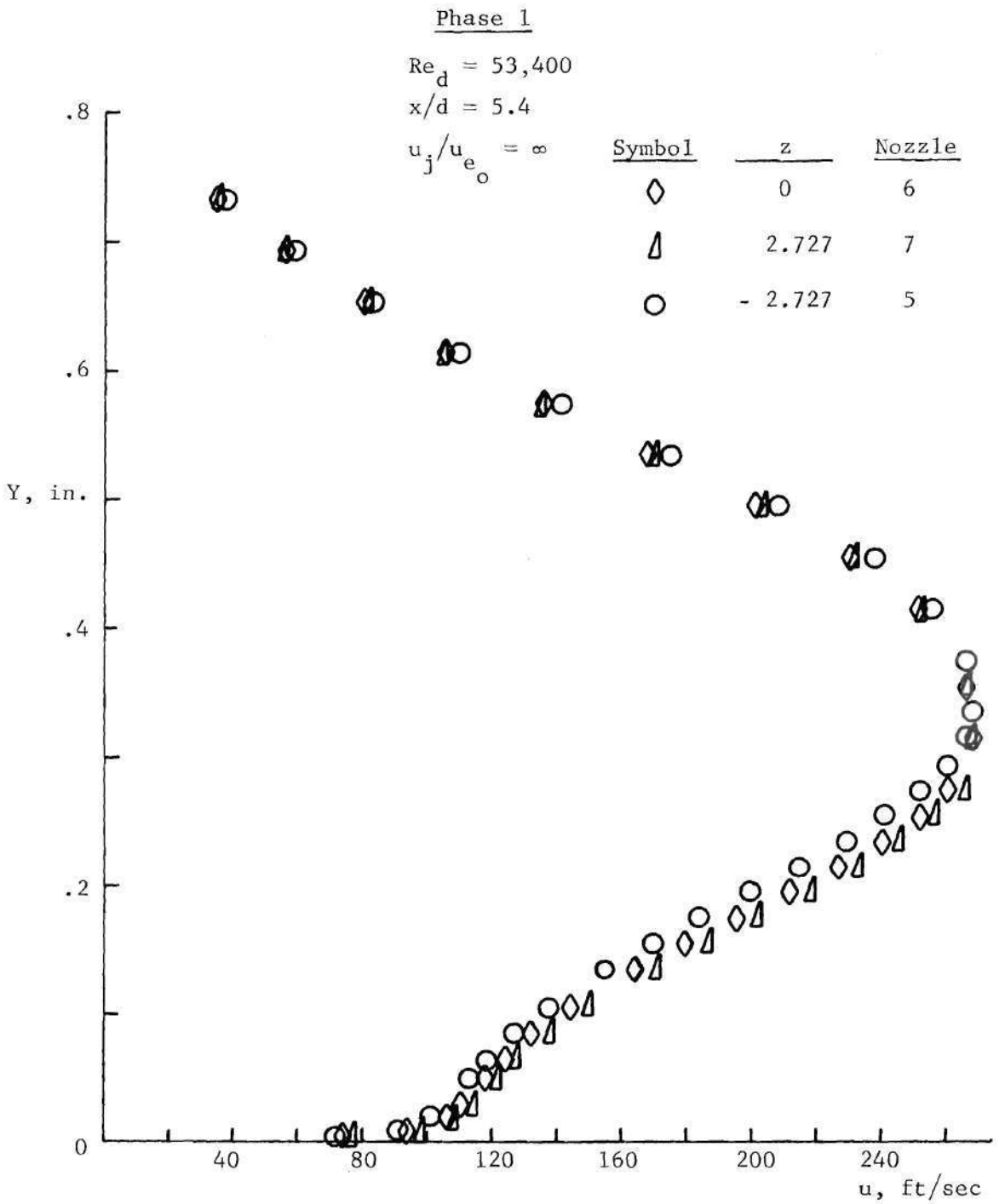

Figure 24a. Phase 1 Downstream Flow Evaluation

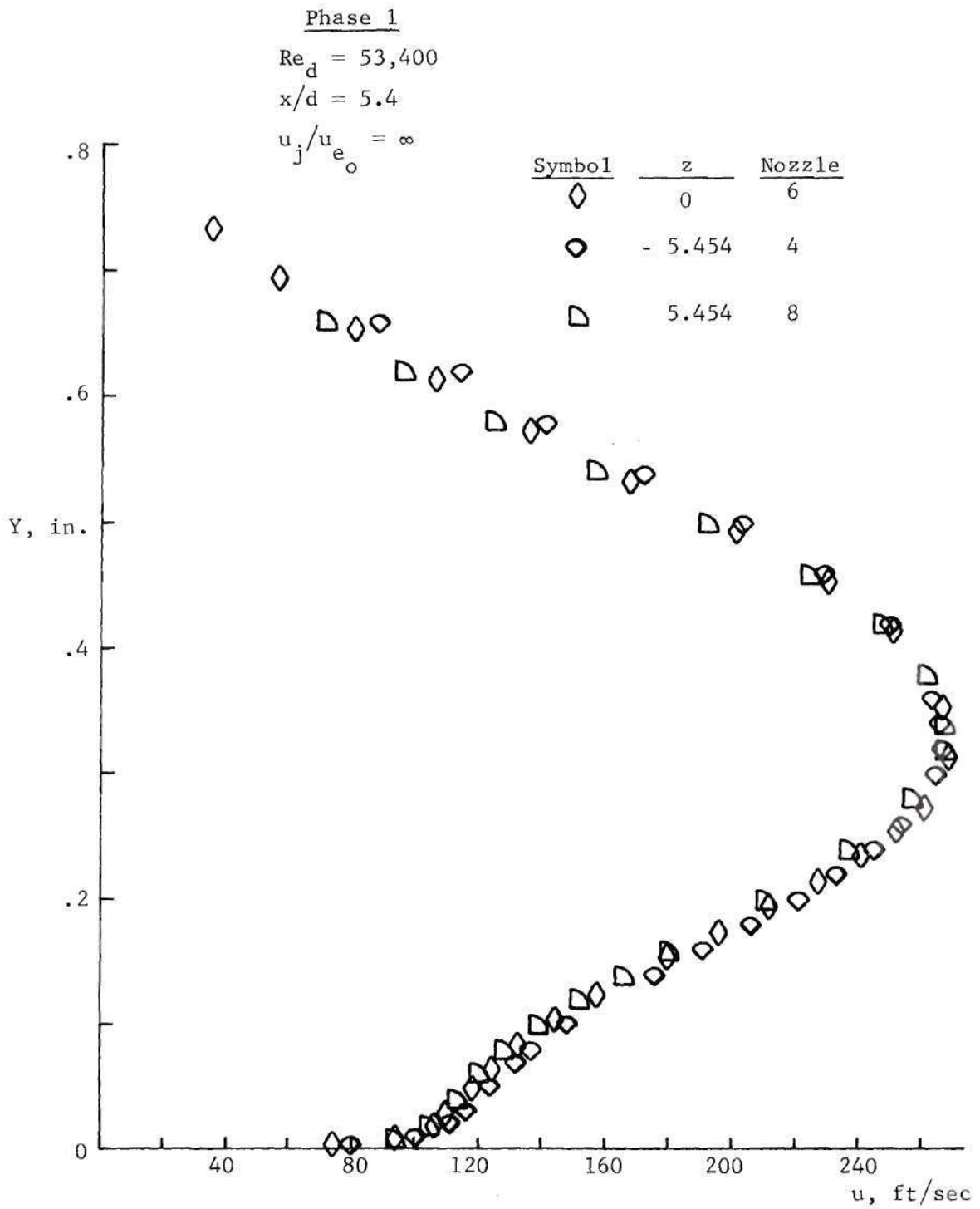

Figure 24b. Phase 1 Downstream Flow Evaluation

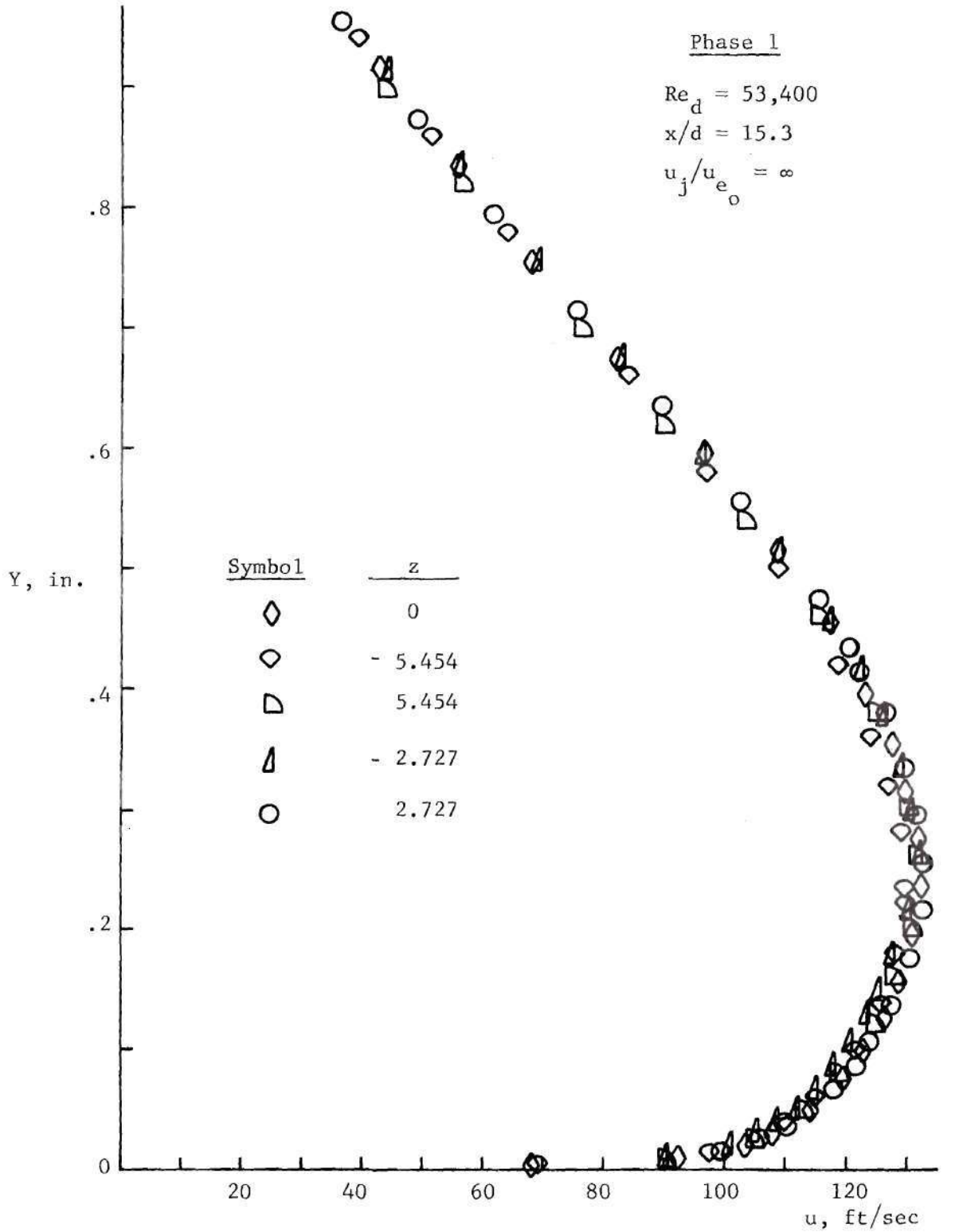

Figure 24c. Phase 1 Downstream Flow Evaluation

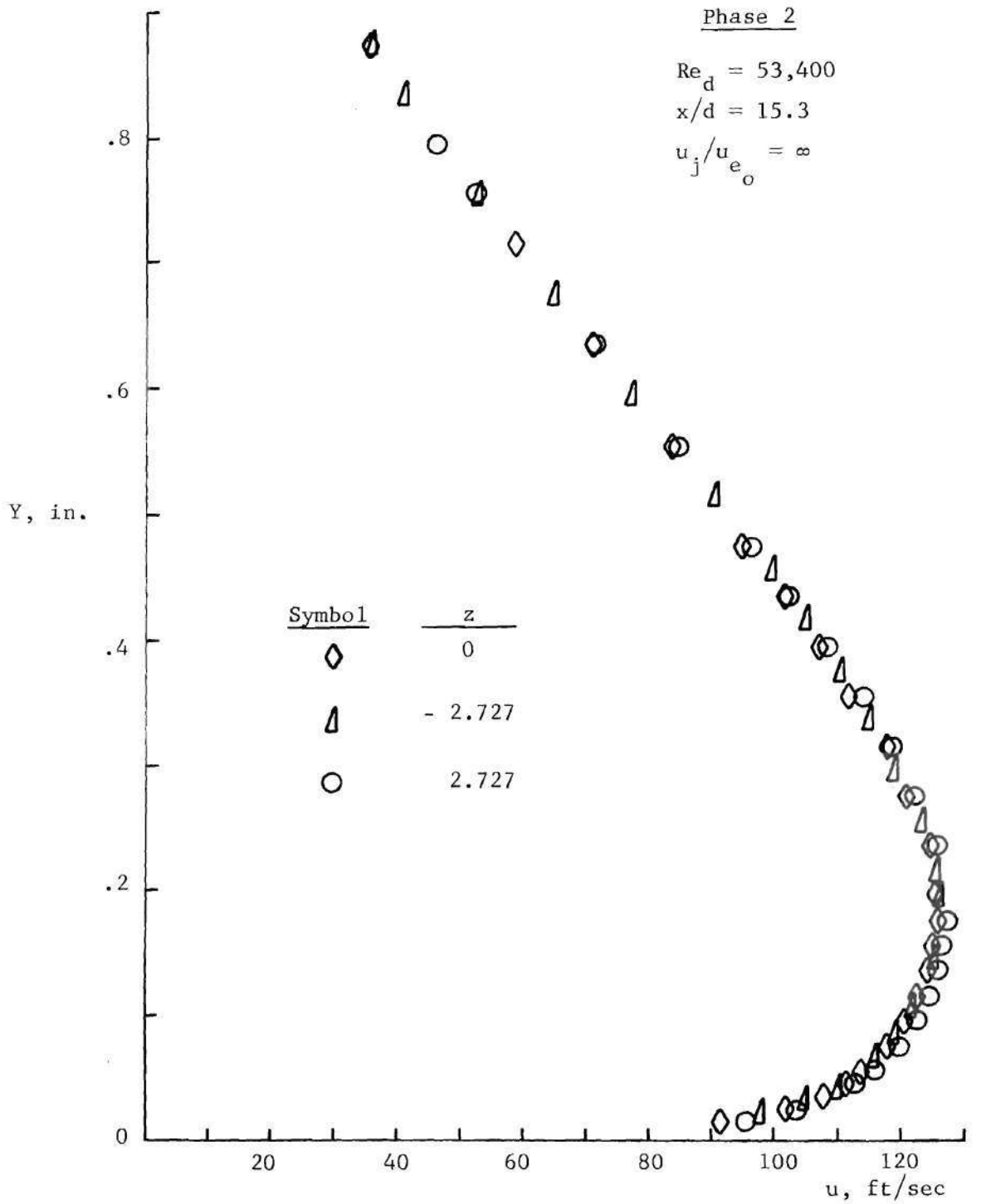

Figure 25. Phase 2 Downstream Flow Evaluation

Phase 3

NOTES:

1. Numbers represent percentage deviation from mean dynamic pressure.
2. View looking upstream at plane of reference station (Figure 8).

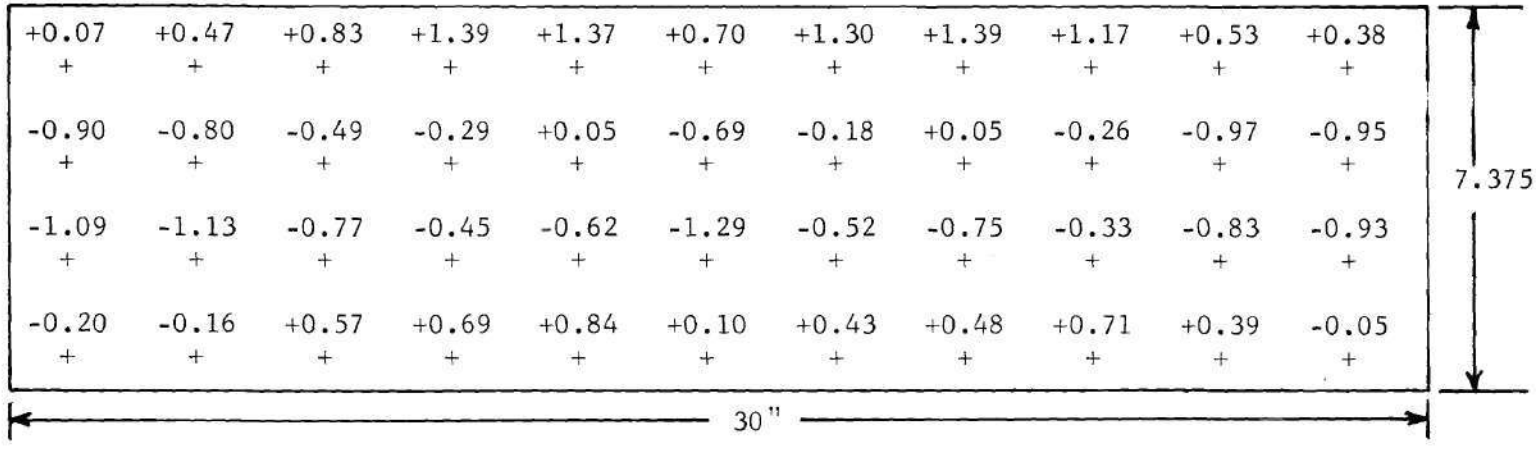

Figure 26. Phase 3 Mainstream Dynamic Pressure Survey

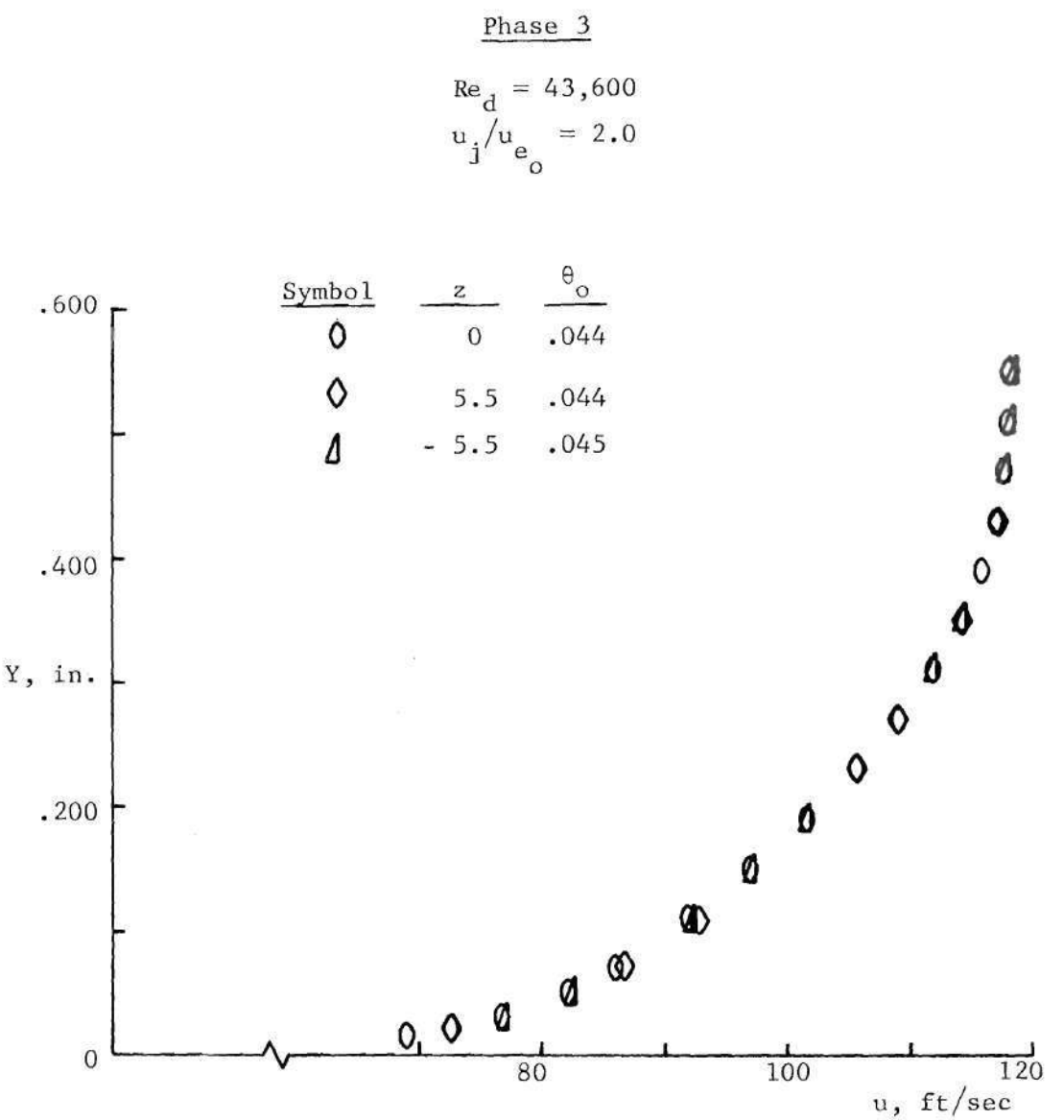

Figure 27. Phase 3 Mainstream Boundary Layer Evaluation

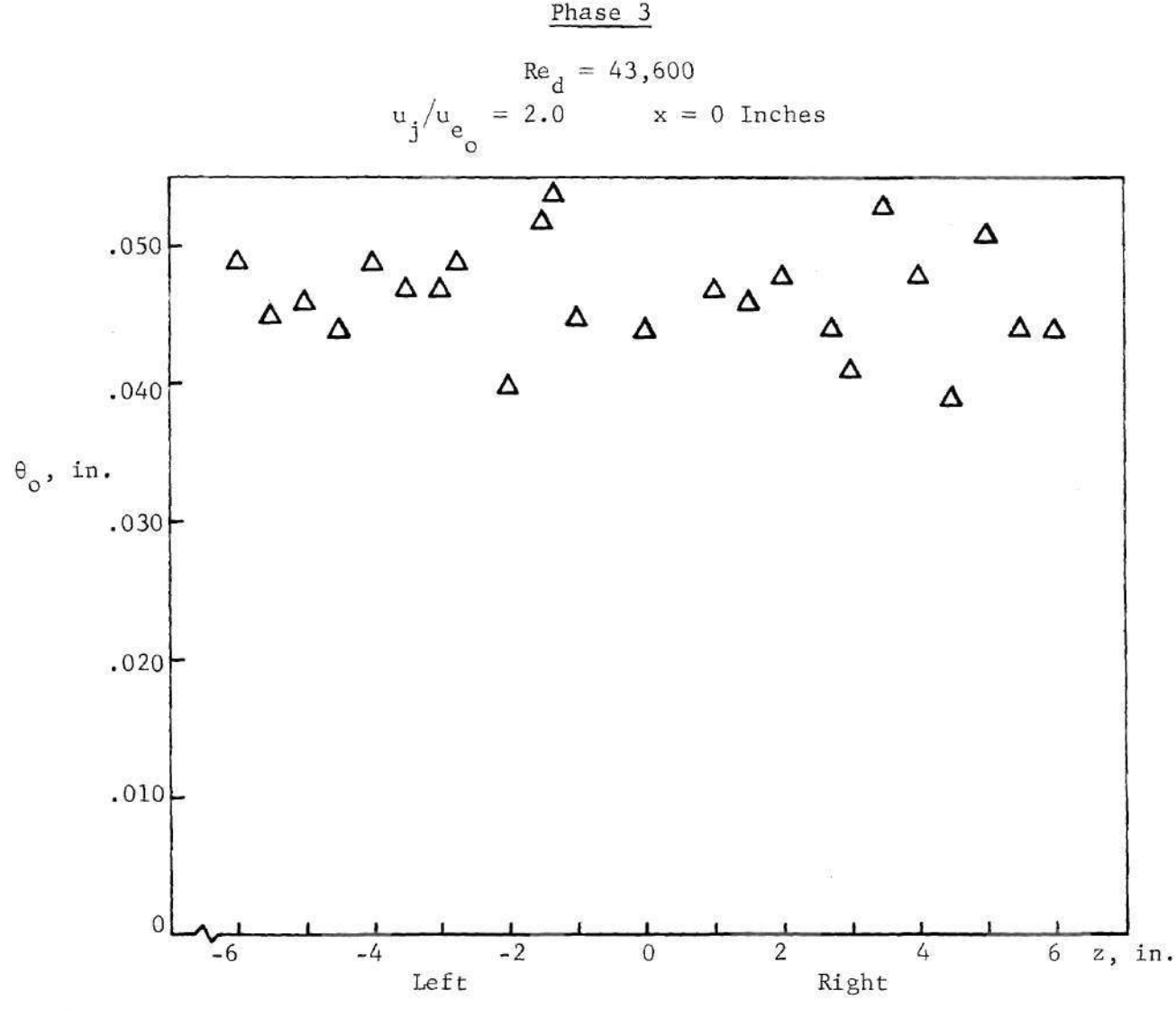

Figure 28. Phase 3 Mainstream Boundary Layer Momentum Thicknesses; View Looking Upstream

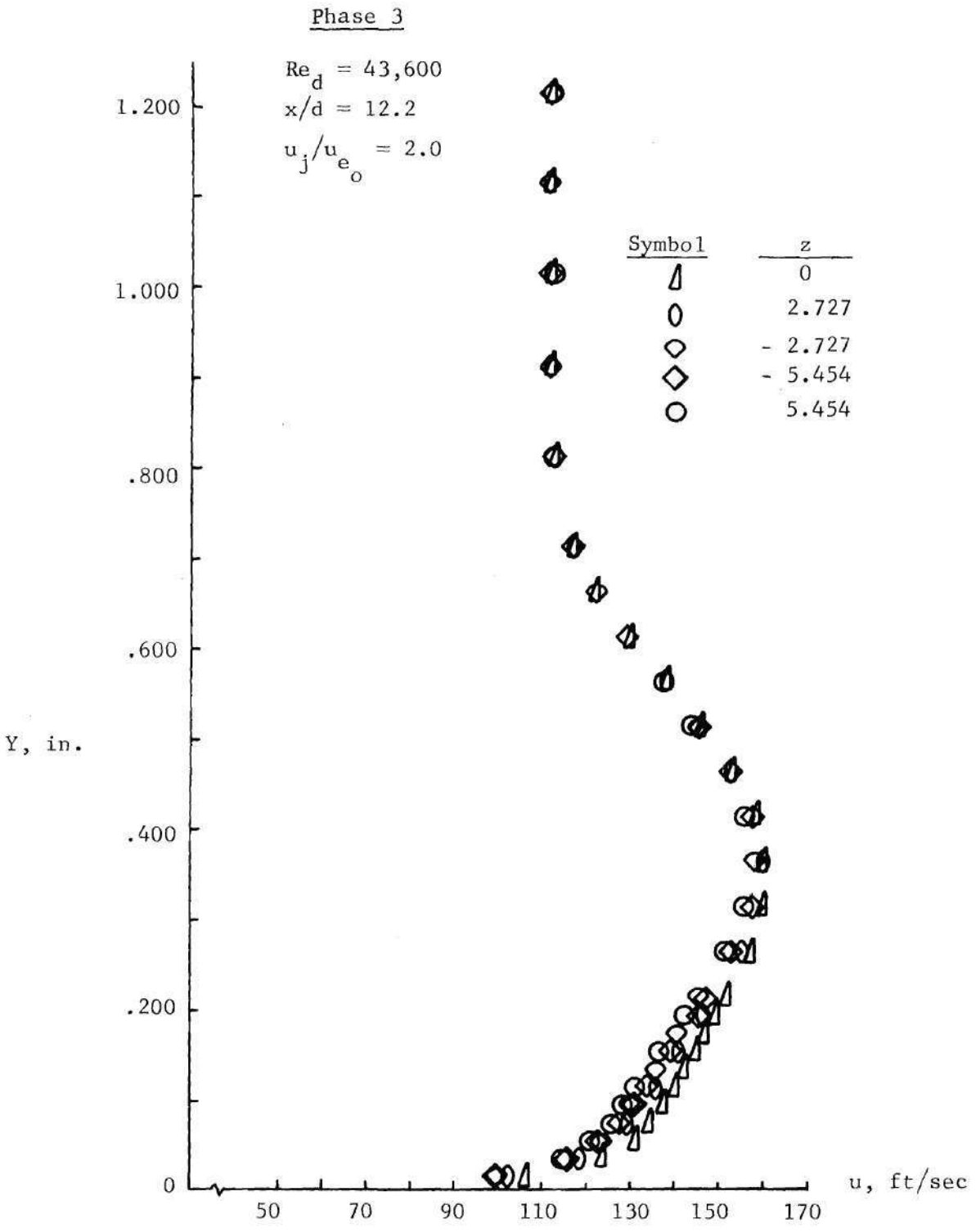

Figure 29. Phase 3 Downstream Flow Evaluation

Phase 3

$Re_d = 43{,}600$ $x/d = 12.2$

$u_j/u_{e_o} = 2.0$

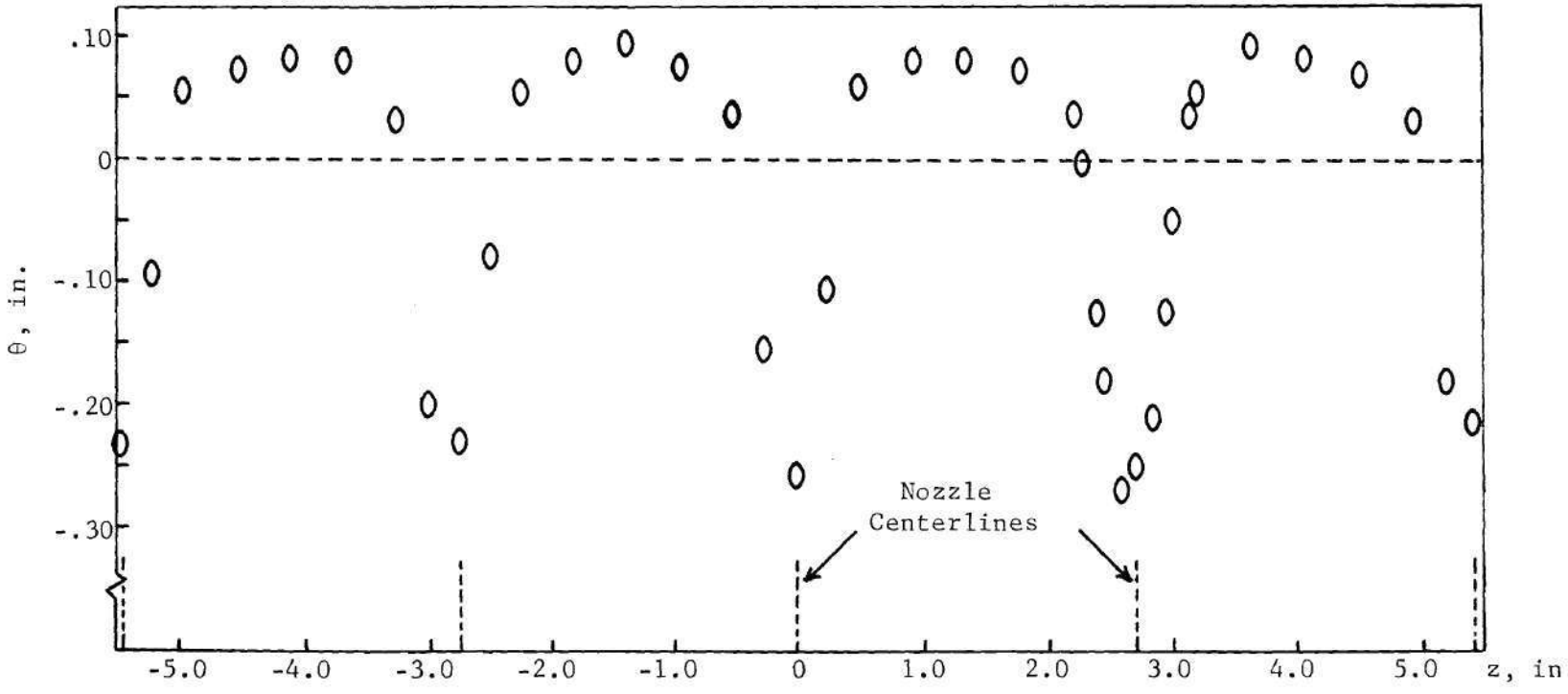

Figure 30. Phase 3 Downstream Momentum Thicknesses

Phase 3

$Re_d = 43,600 \qquad x/d = 12.2$

$u_j/u_{e_o} = 2.0$

NOTES:

1. Values without parentheses are $\theta_{I.M.}$ at $x/d = 12.2$ over the indicated span.
2. Values in parentheses are $\theta_{I.M.}$ at the reference station over the indicated span.
3. View is looking upstream.

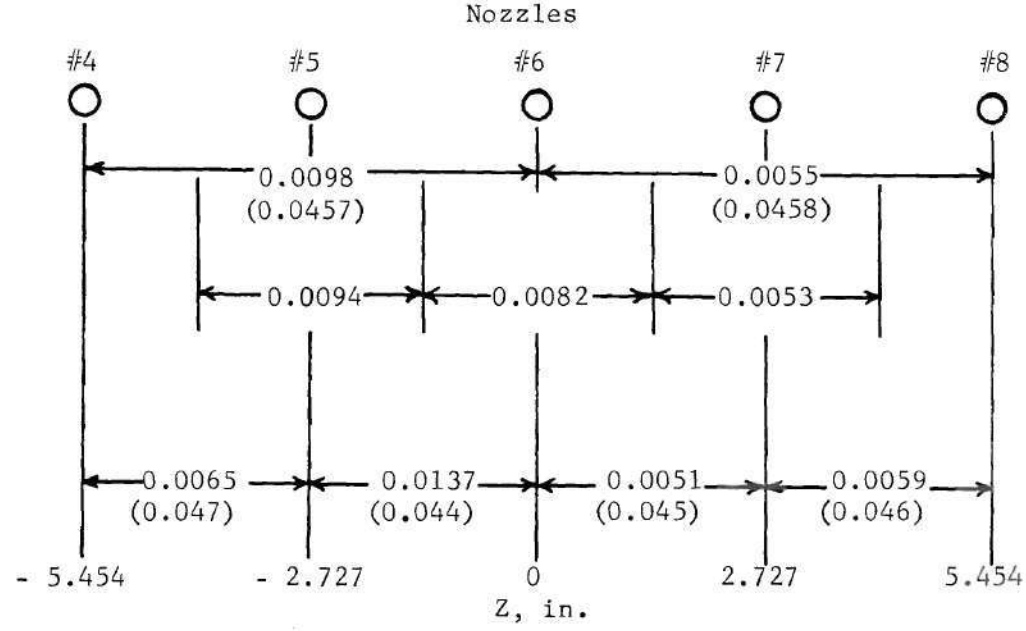

Figure 31. Phase 3 Downstream Integrated Momentum Thicknesses

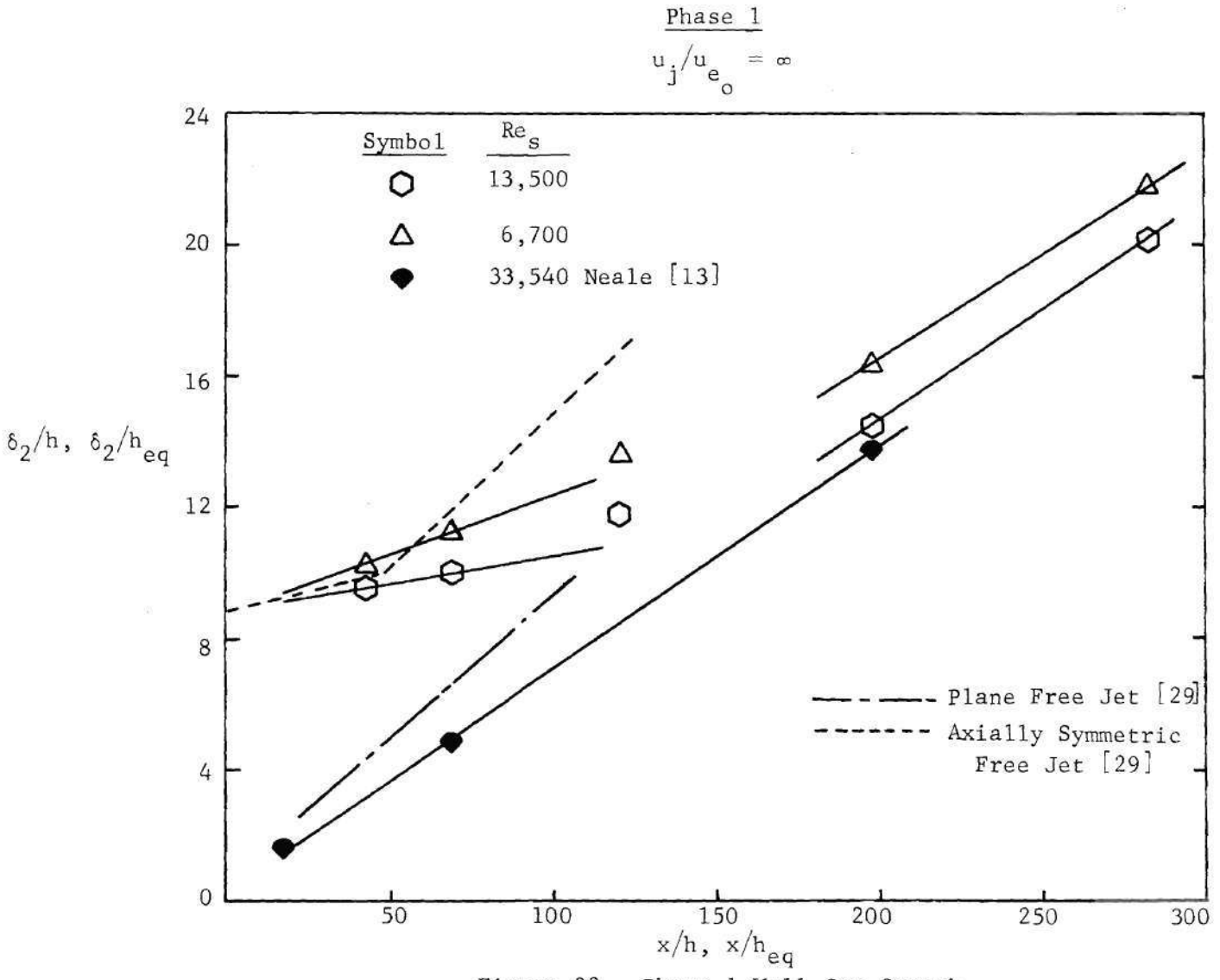

Figure 32. Phase 1 Wall Jet Growth

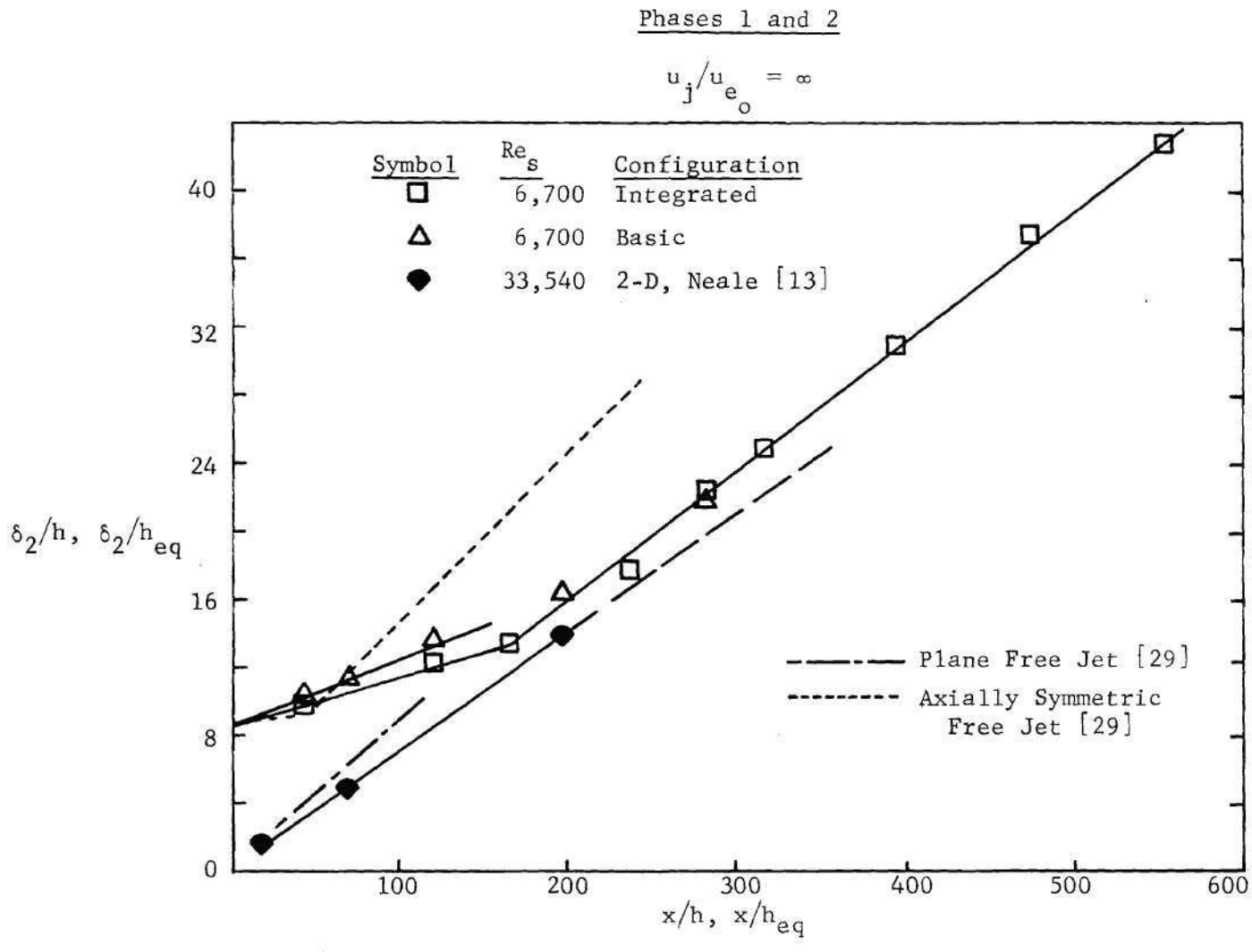

Figure 33. Phases 1 and 2 Wall Jet Growth

Phase 2

$u_j/u_{e_o} = \infty$

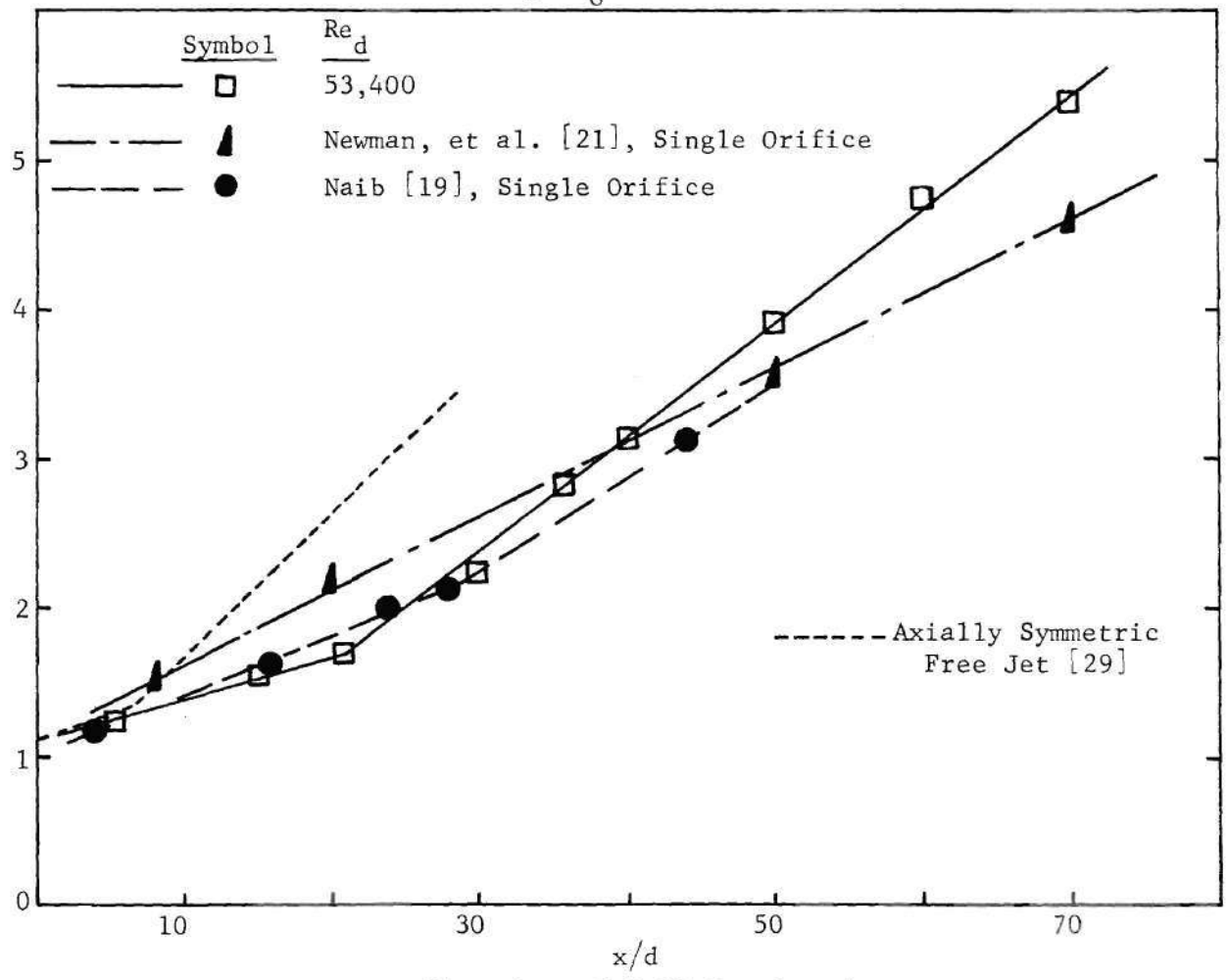

Figure 34. Phase 2 Wall Jet Growth

Phases 2 and 3

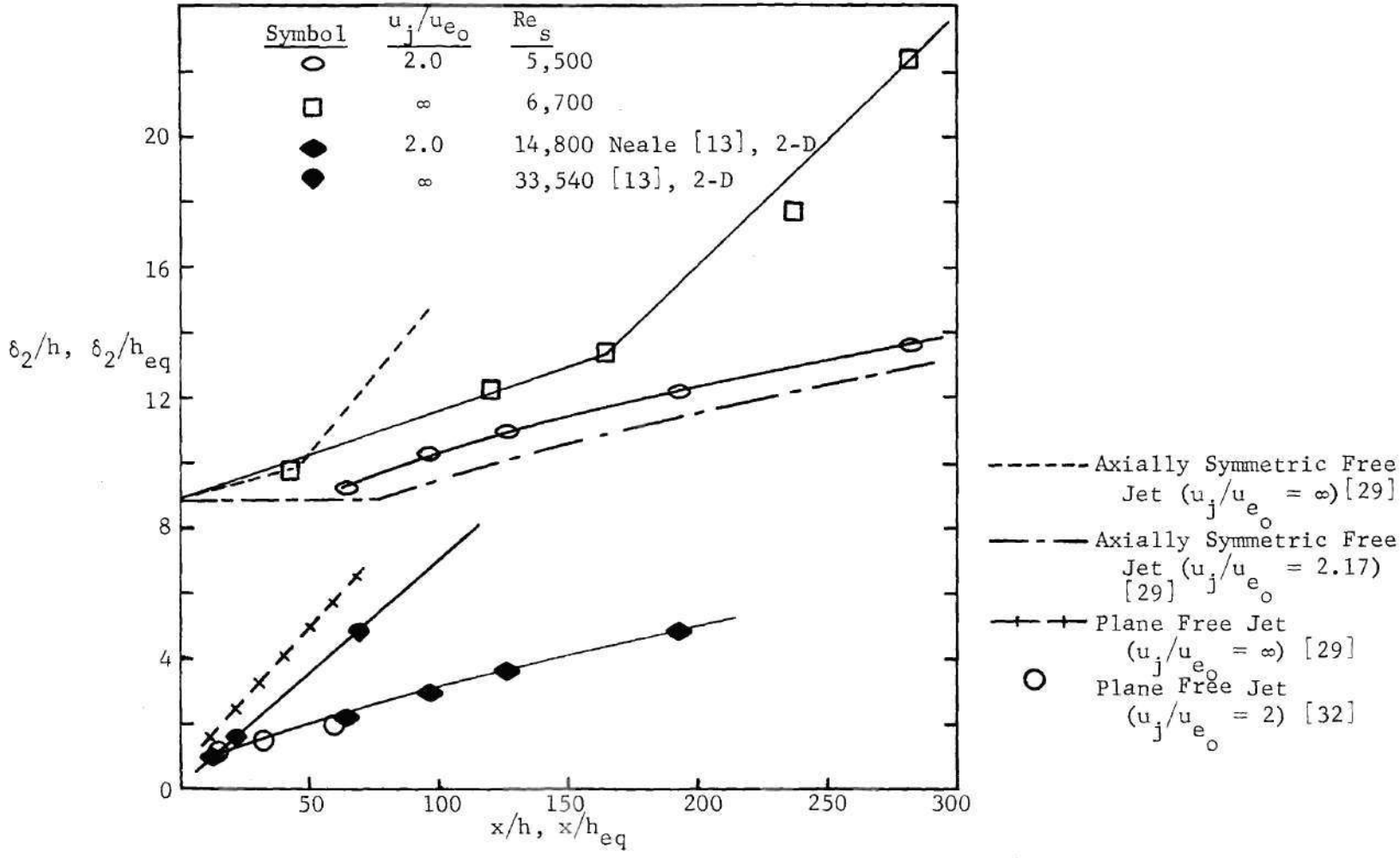

Figure 35. Phases 2 and 3 Wall Jet Growth

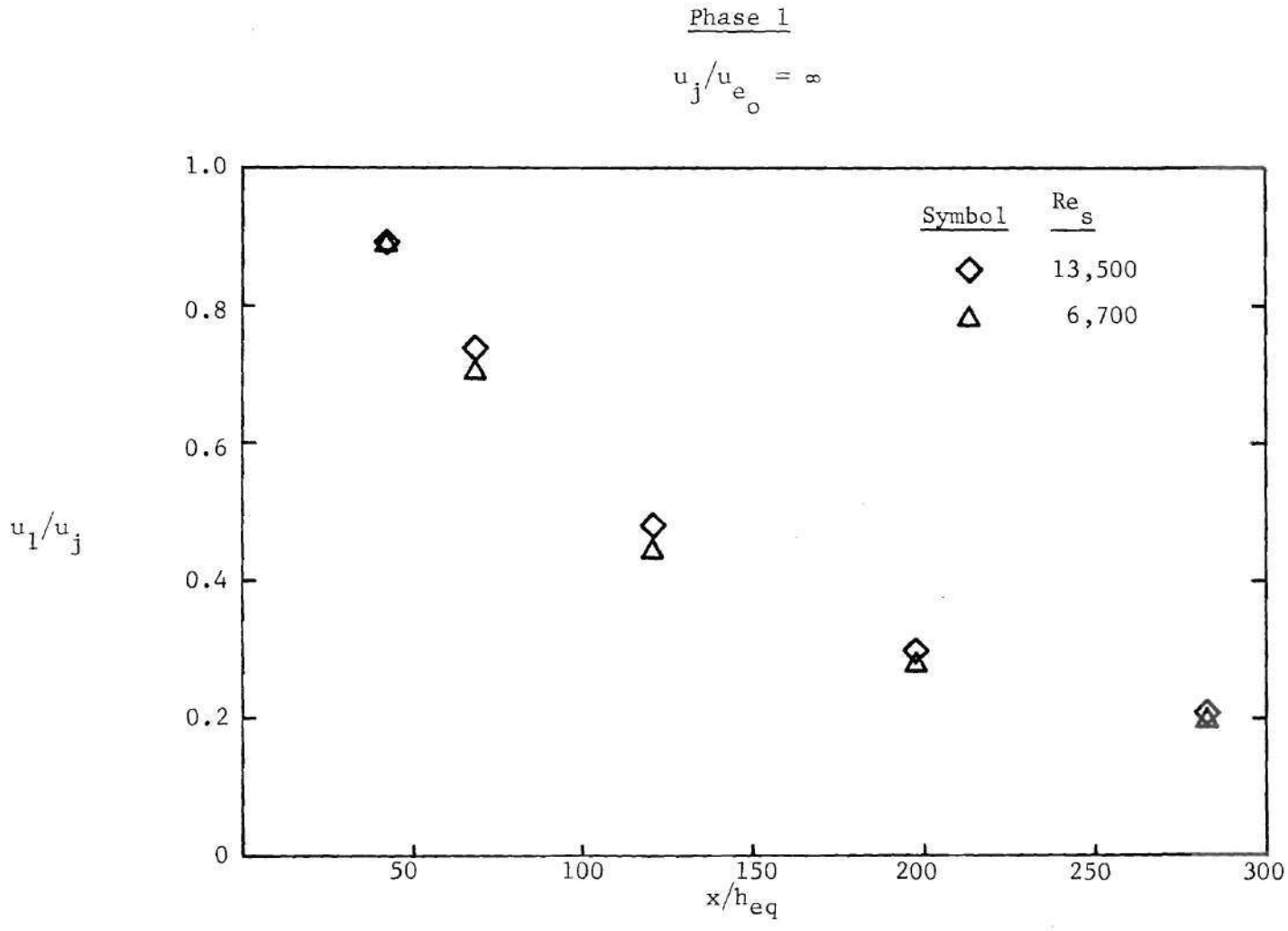

Figure 36. Phase 1 Wall Jet Velocity Decay

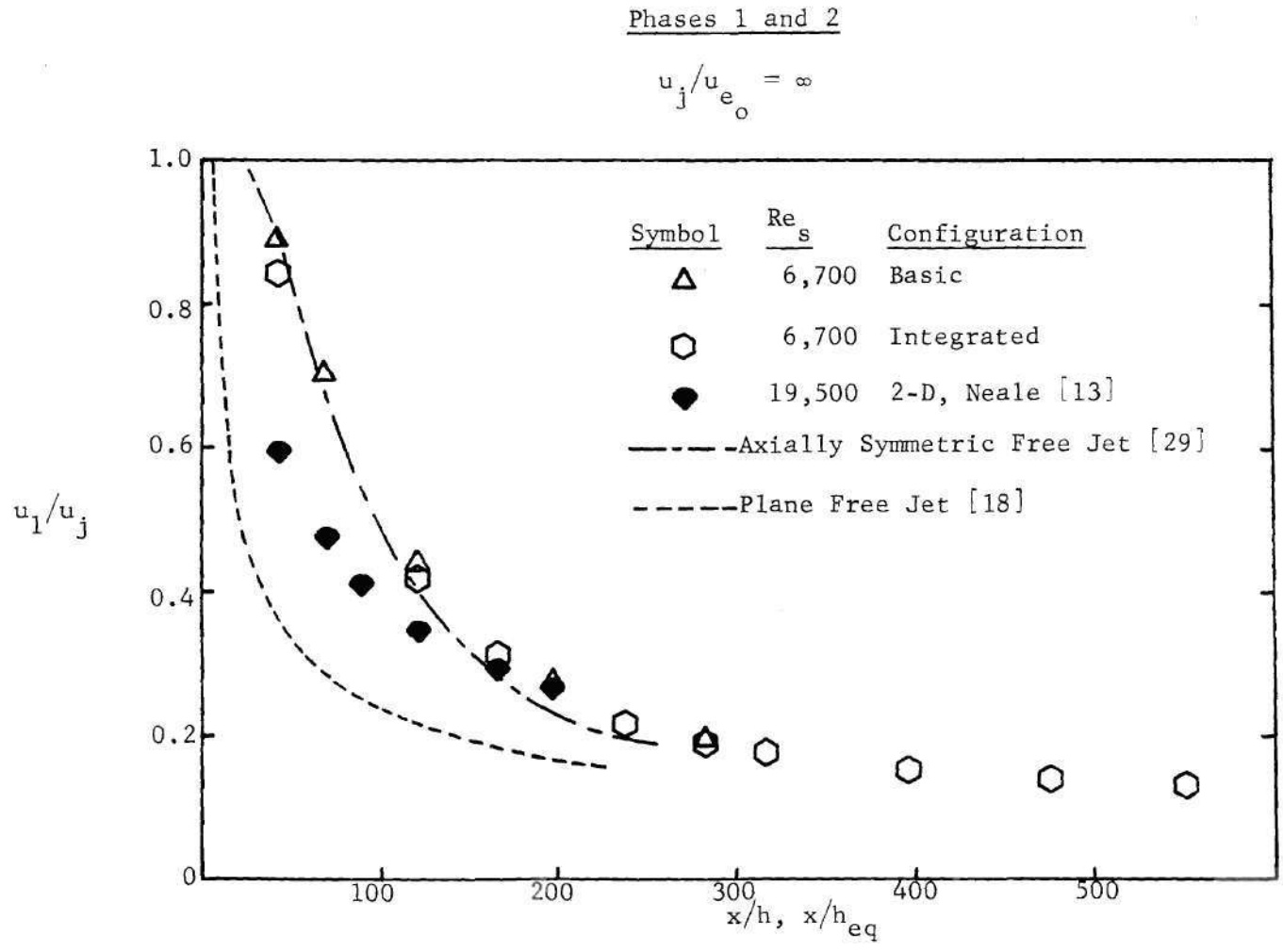

Figure 37. Phases 1 and 2 Wall Jet Velocity Decay

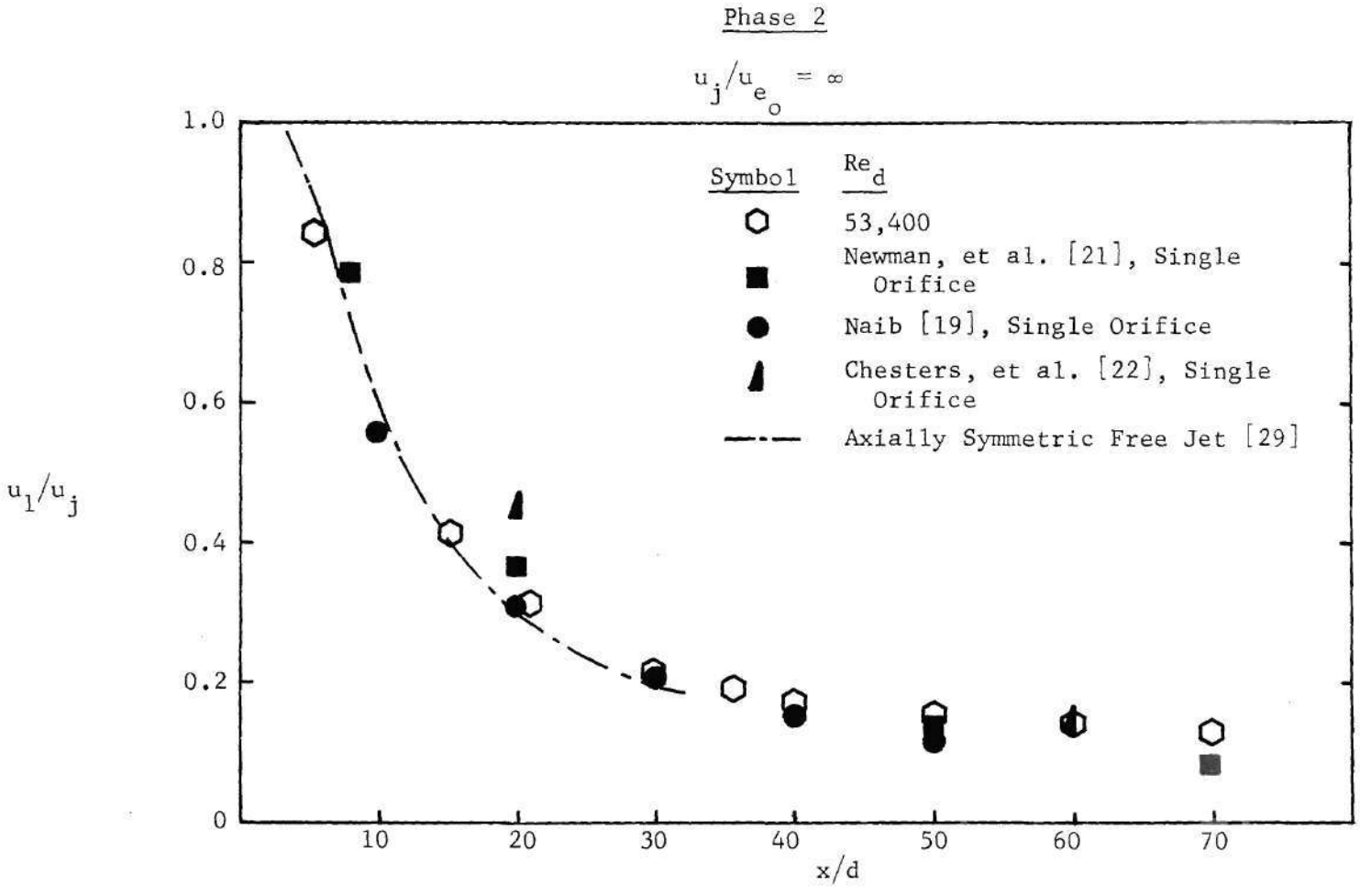

Figure 38. Phase 2 Wall Jet Velocity Decay

Phase 2

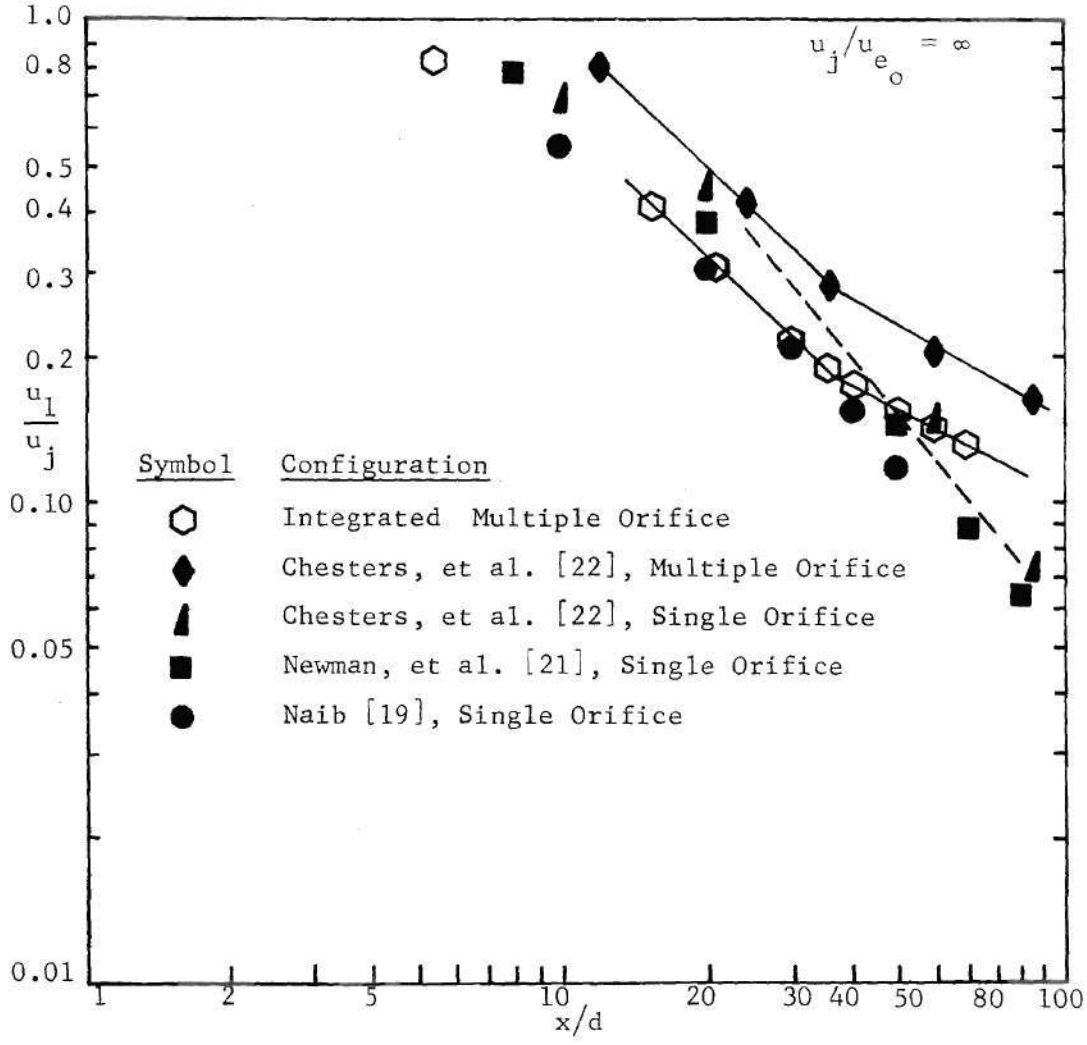

Figure 39. Phase 2 Wall Jet Velocity Decay

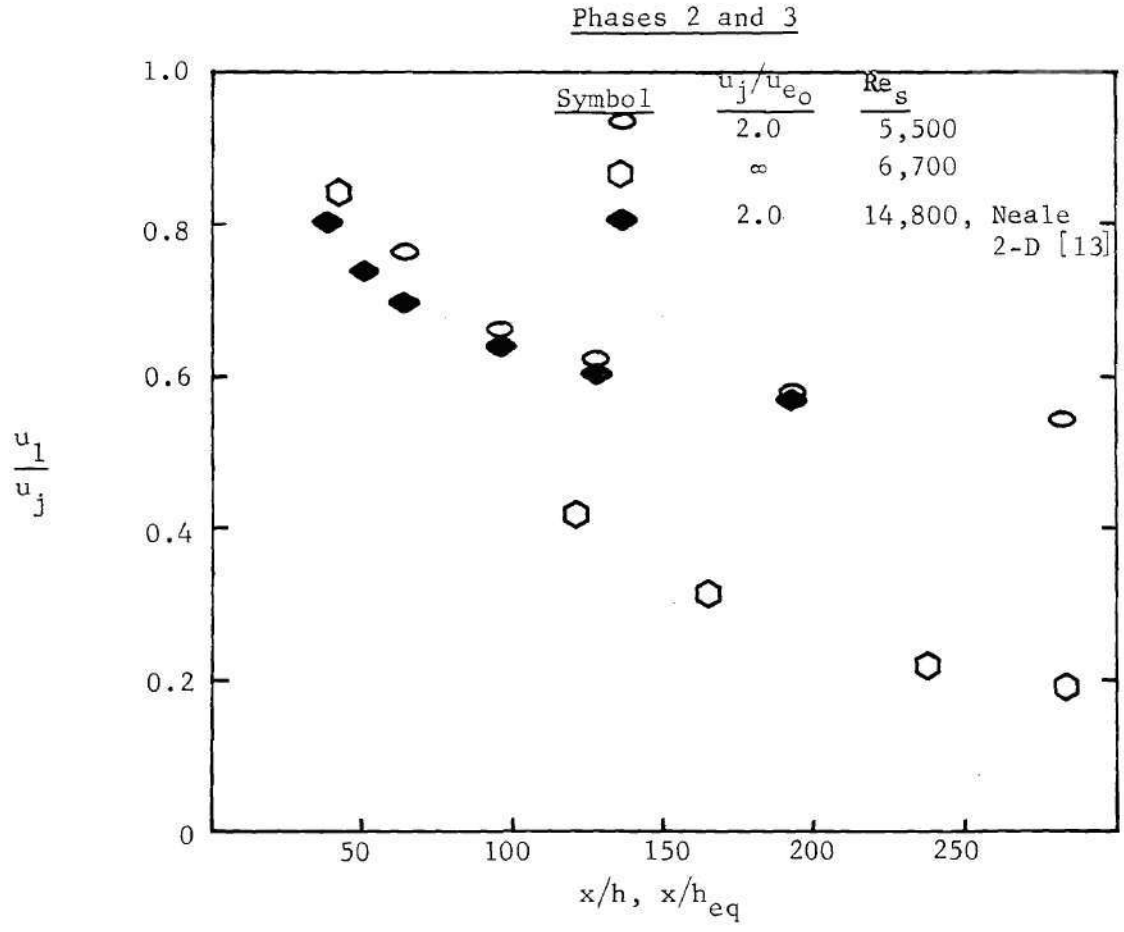

Figure 40. Phases 2 and 3 Wall Jet Velocity Decay

Phase 3

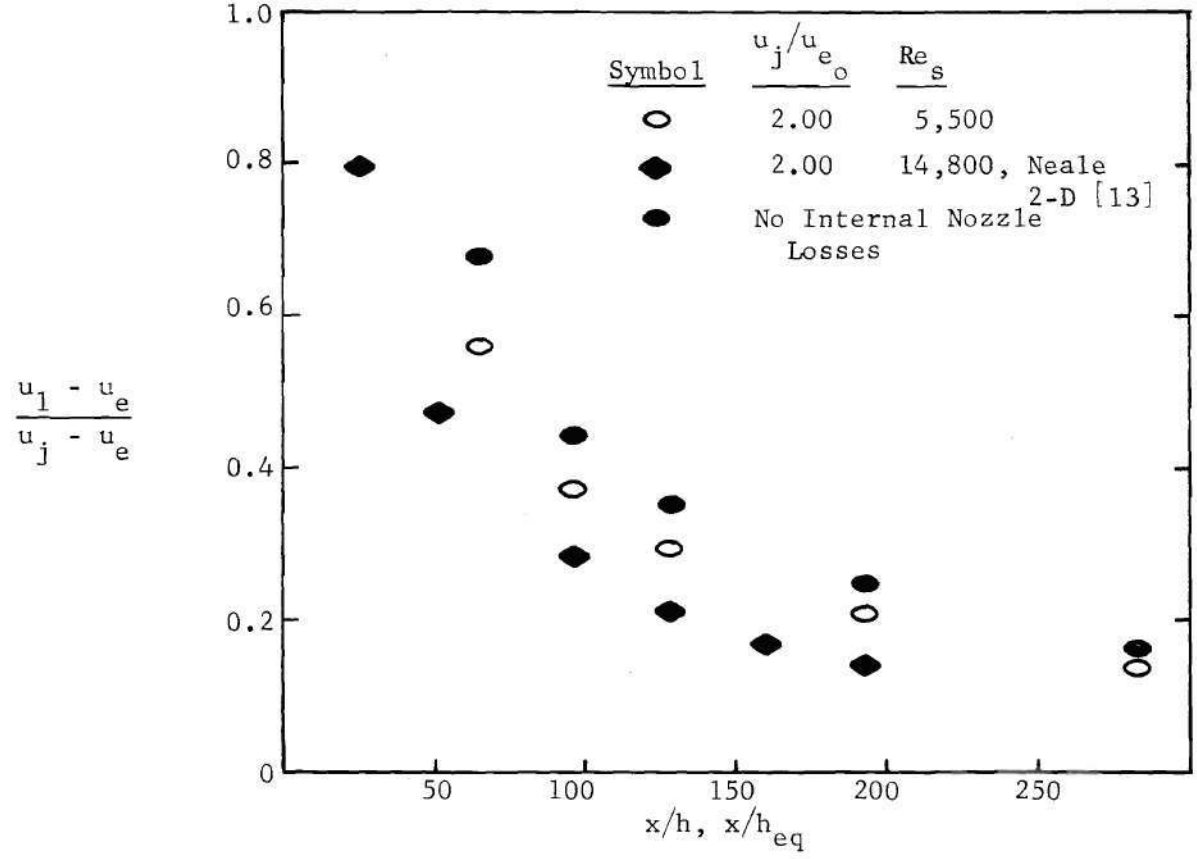

Figure 41. Phase 3 Wall Jet Velocity Decay

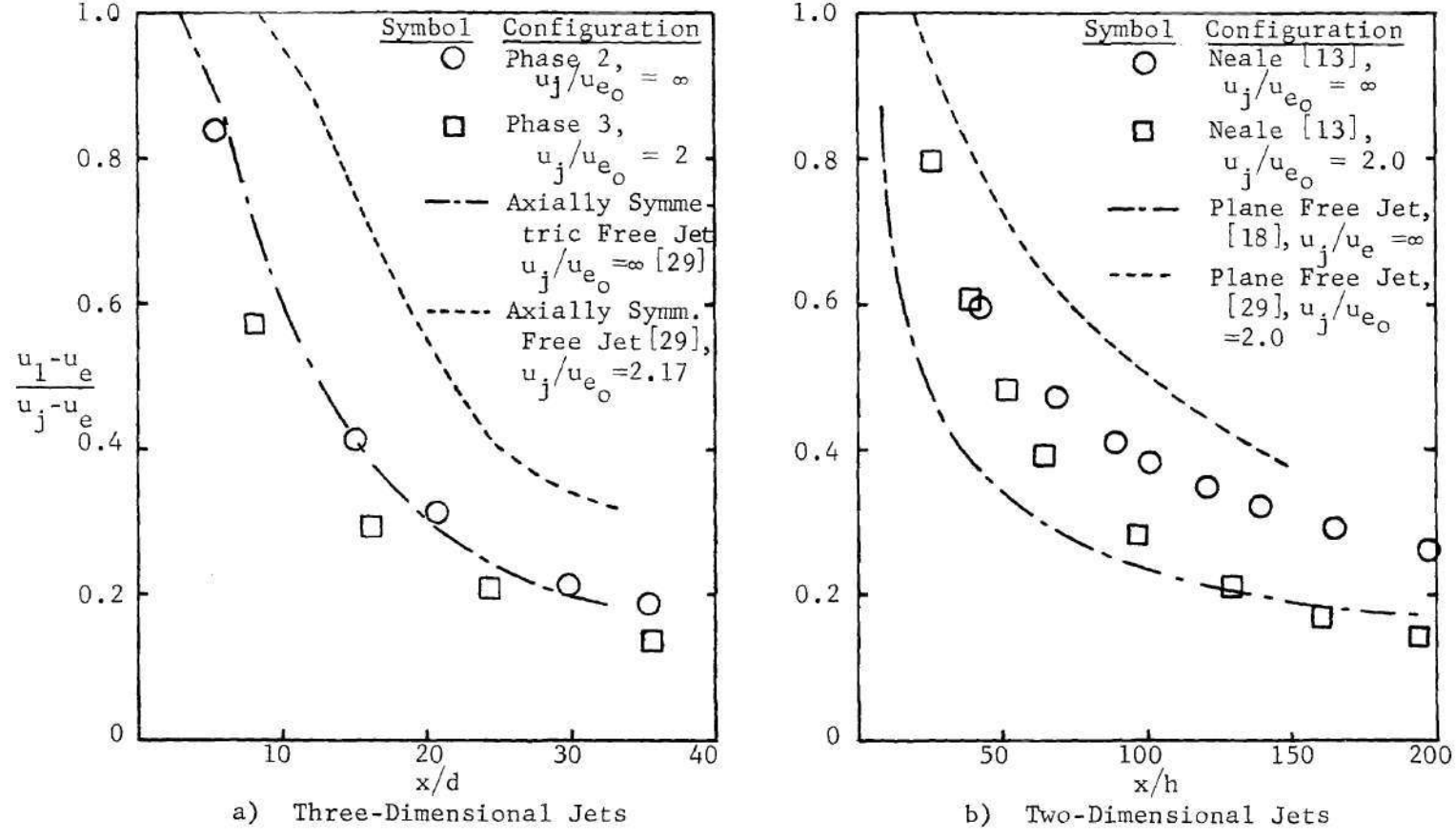

Figure 42. Comparisons of Wall Jet and Free Jet Velocity Decay

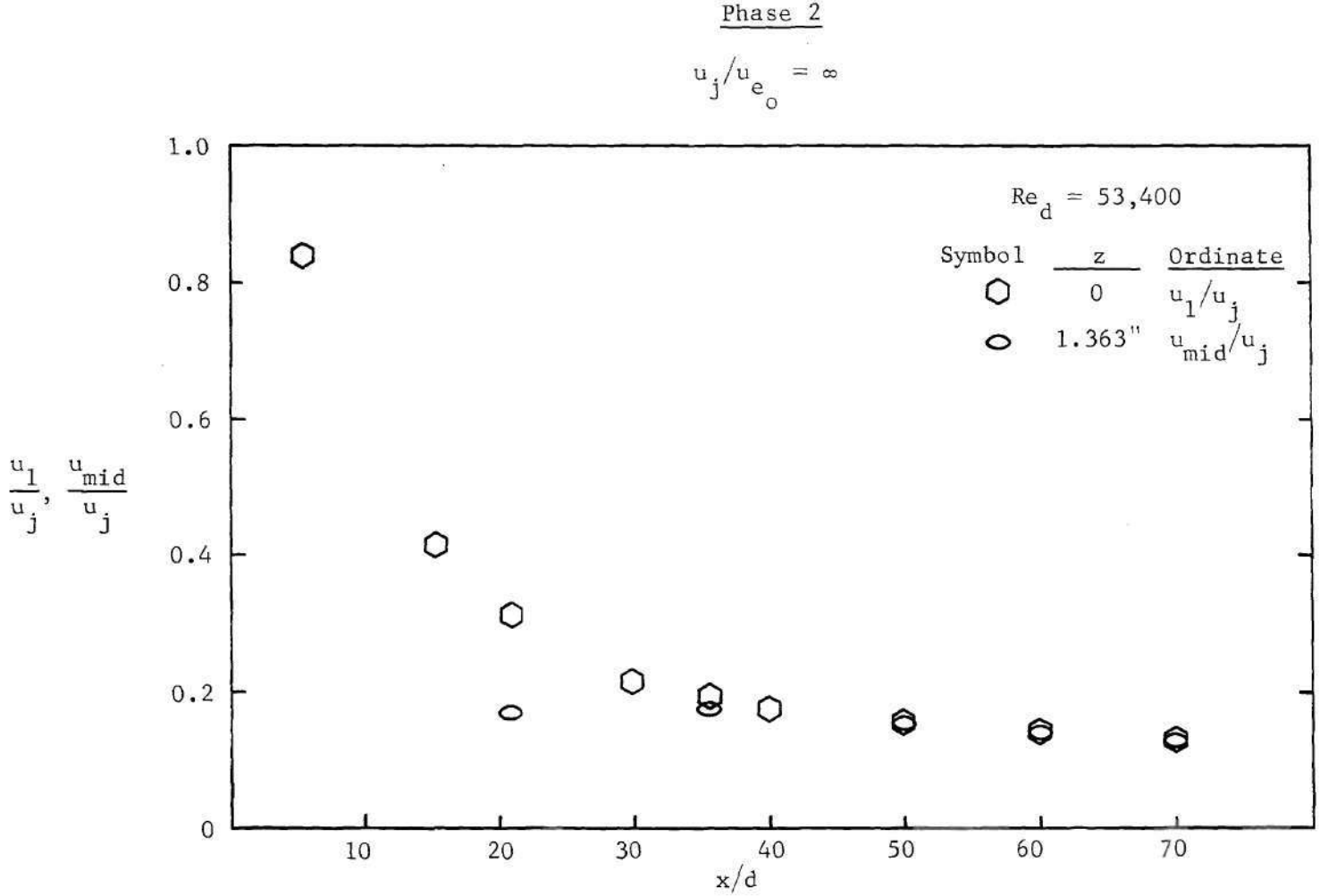

Figure 43. Phase 2 Wall Jet Velocity Decay

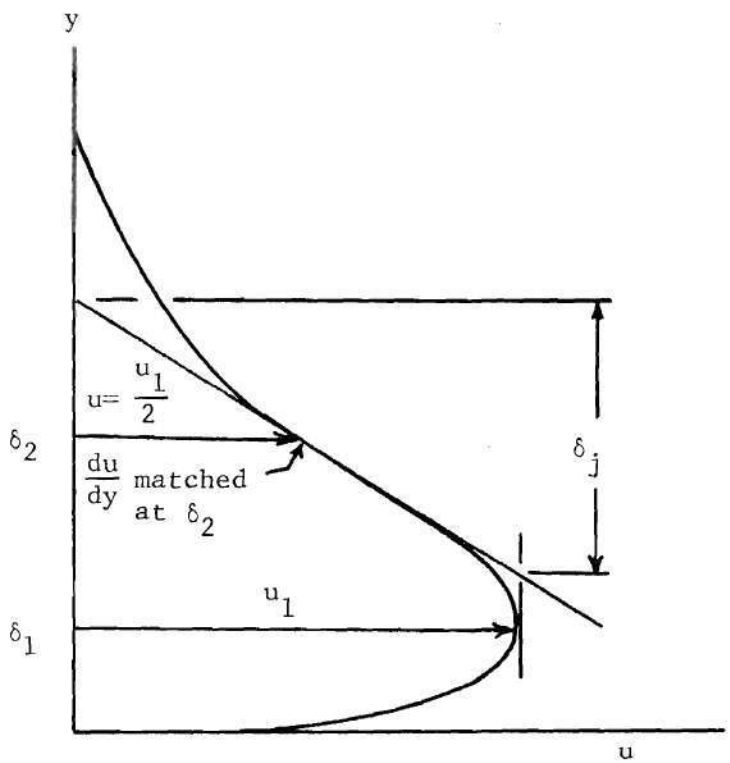

Figure 44. Profile Similarity Parameter

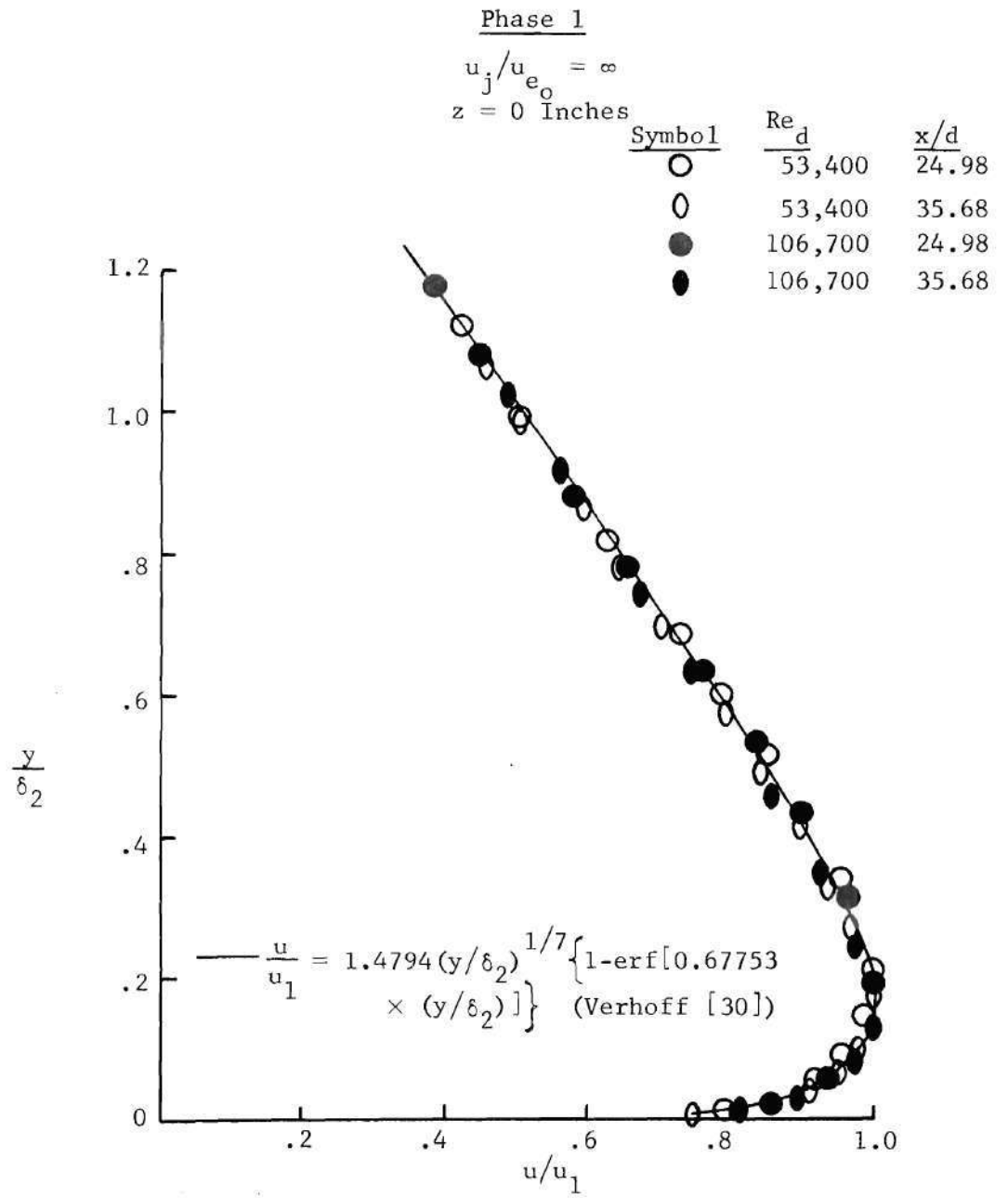

Figure 45. Phase 1 Wall Jet Velocity Profile

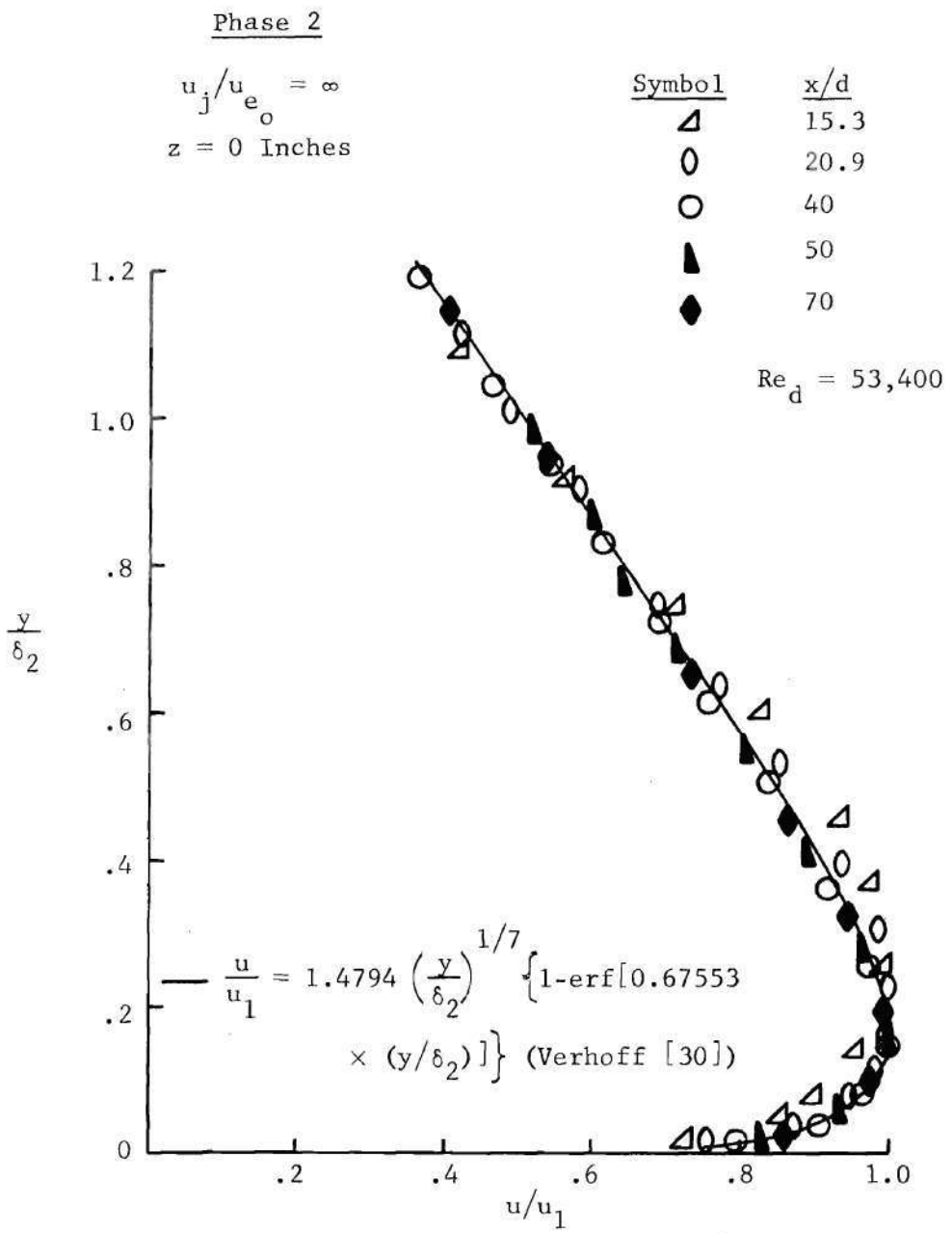

Figure 46. Phase 2 Wall Jet Velocity Profile

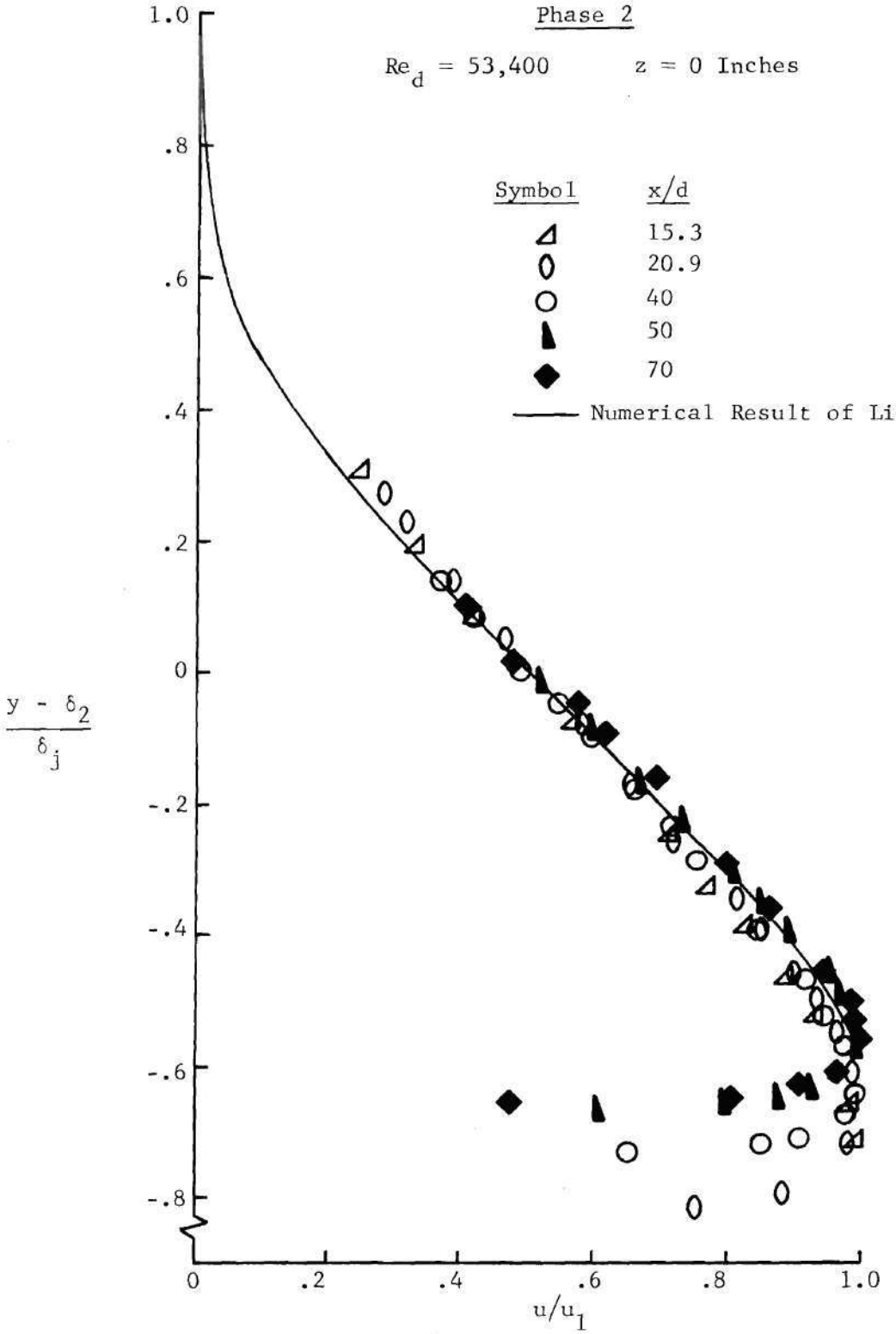

Figure 47. Phase 2 Wall Jet Velocity Profile

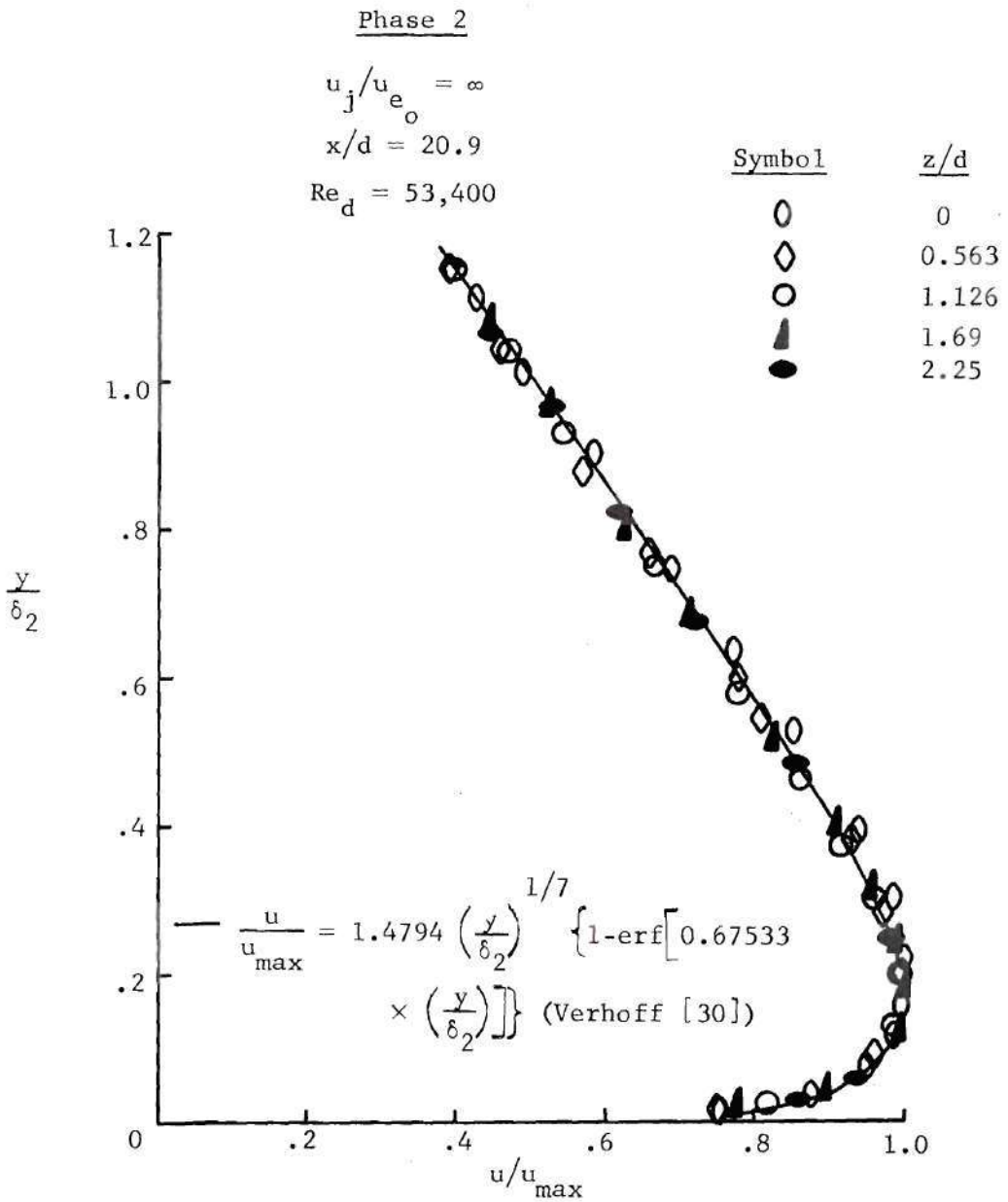

Figure 48. Phase 2 Wall Jet Velocity Profile

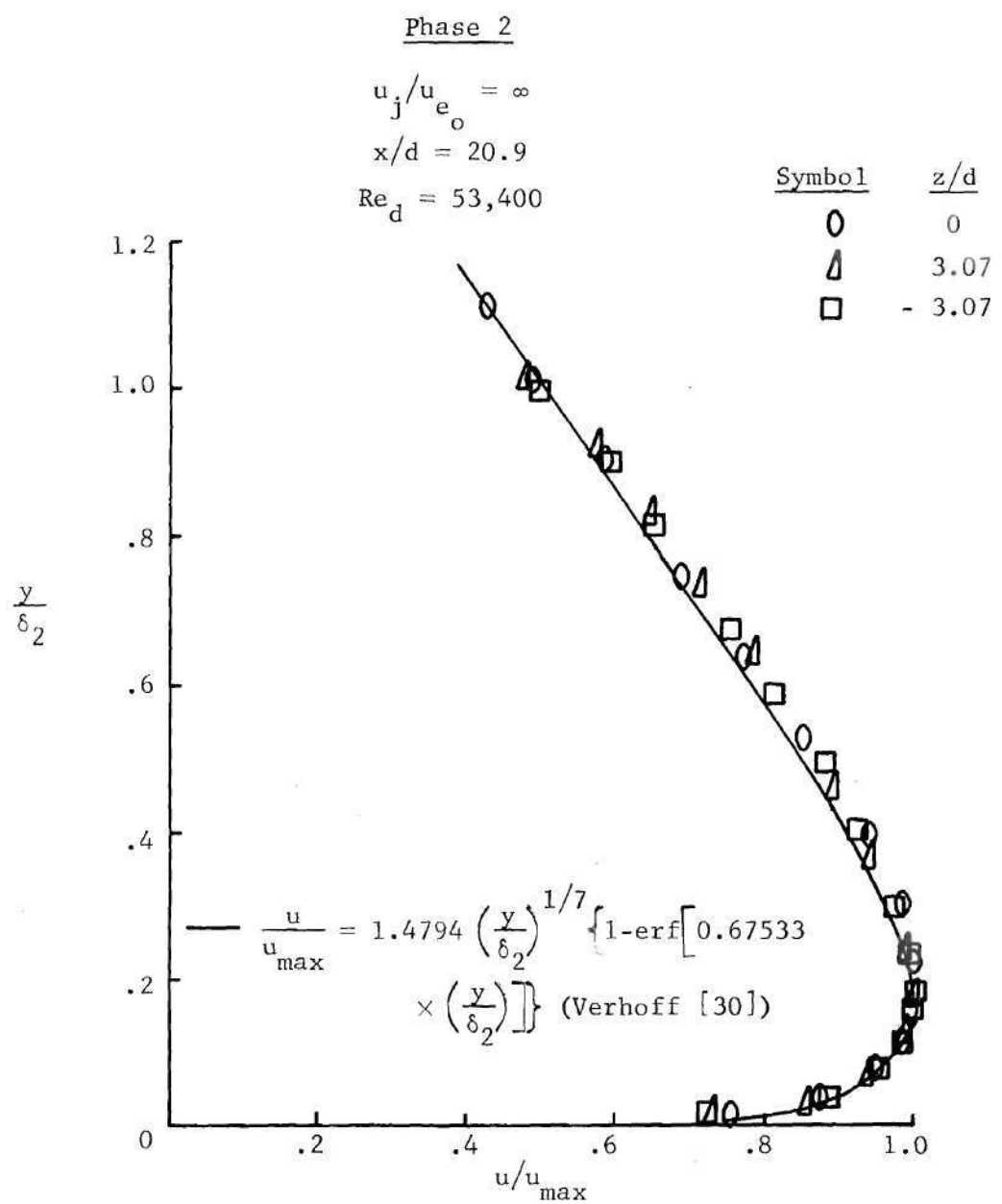

Figure 49. Phase 2 Wall Jet Velocity Profile

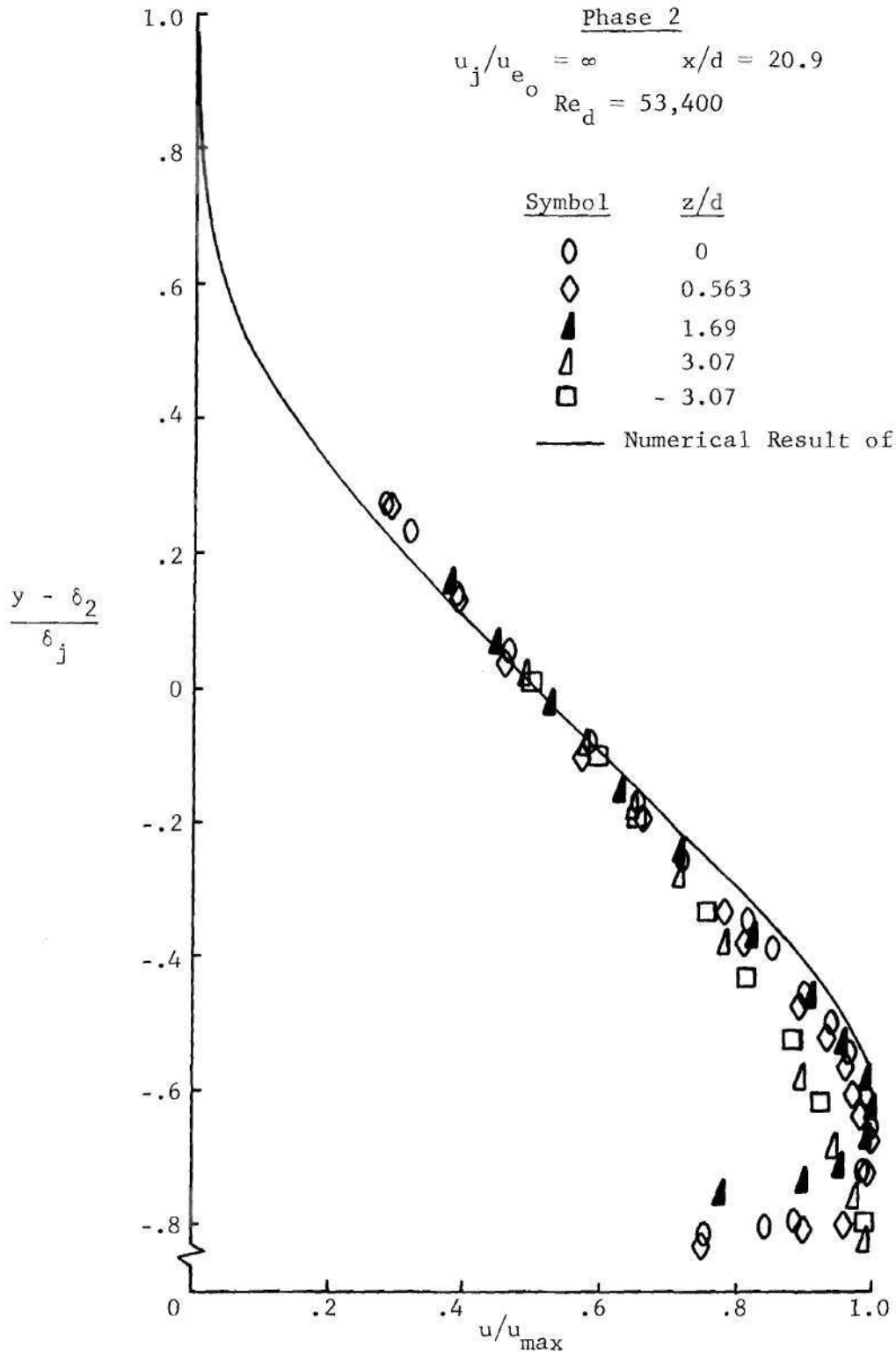

Figure 50. Phase 2 Wall Jet Velocity Profile

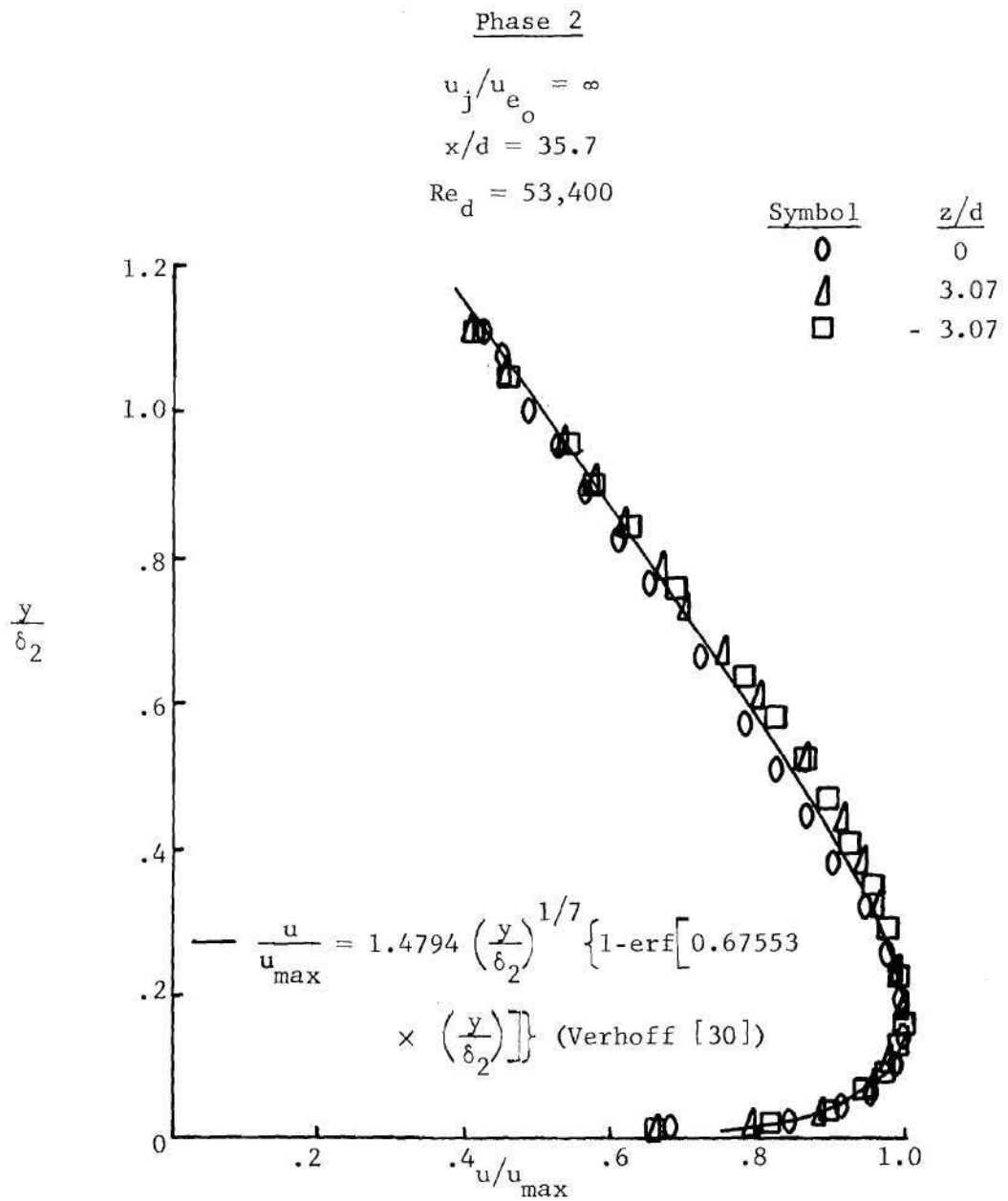

Figure 51. Phase 2 Wall Jet Velocity Profile

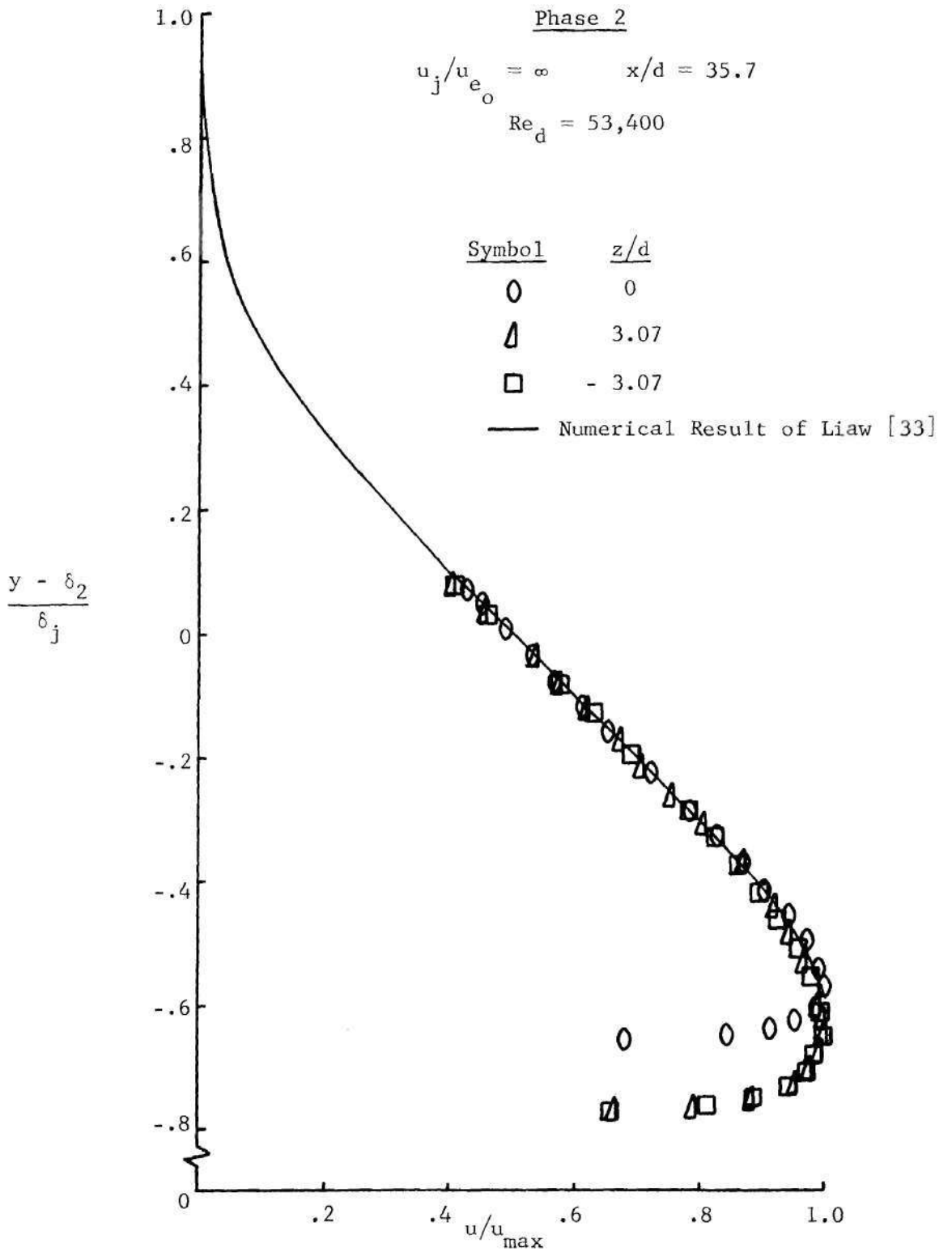

Figure 52. Phase 2 Wall Jet Velocity Profile

Phase 2

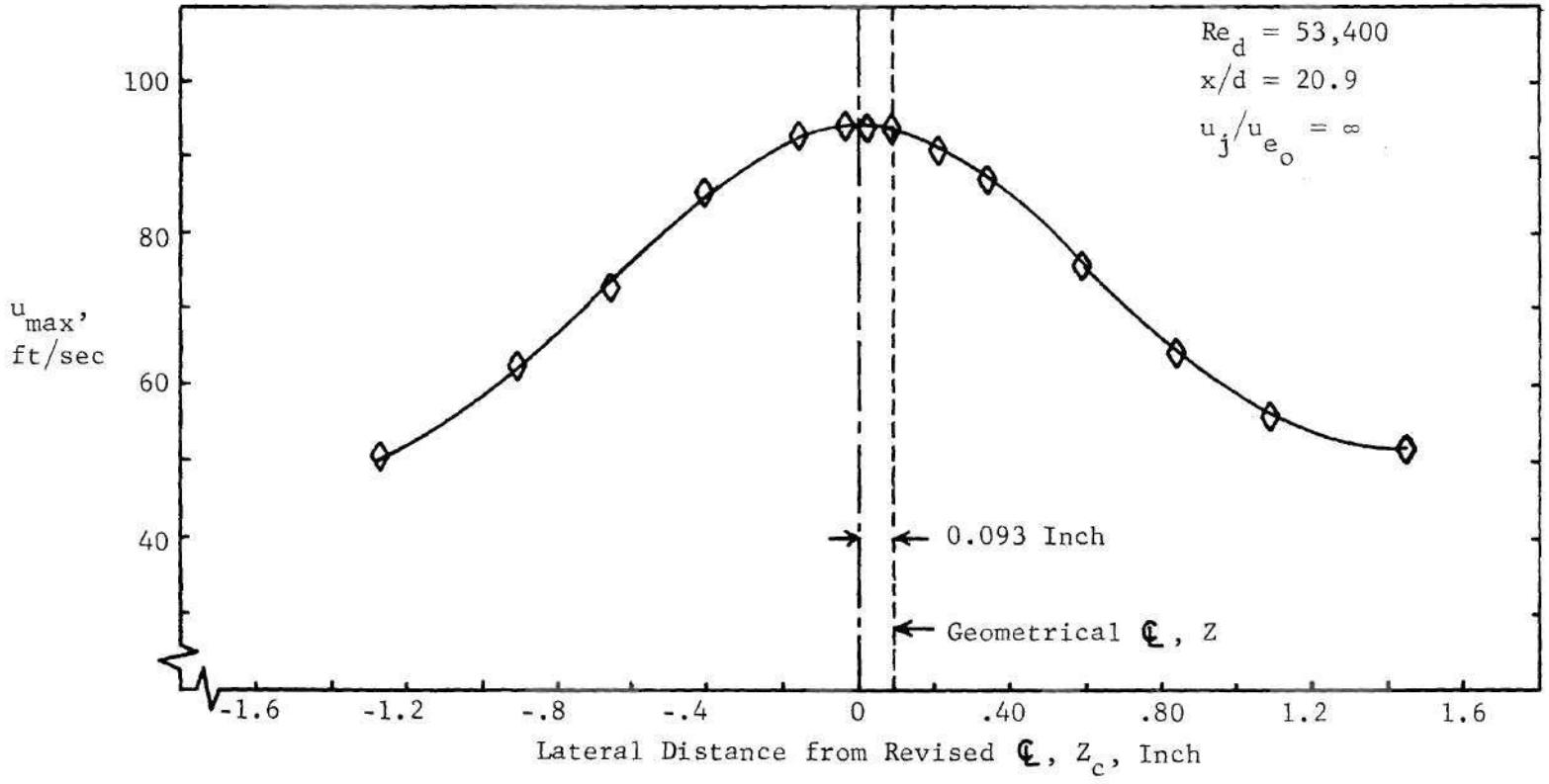

Figure 53. Phase 2 Wall Jet Velocity Profile

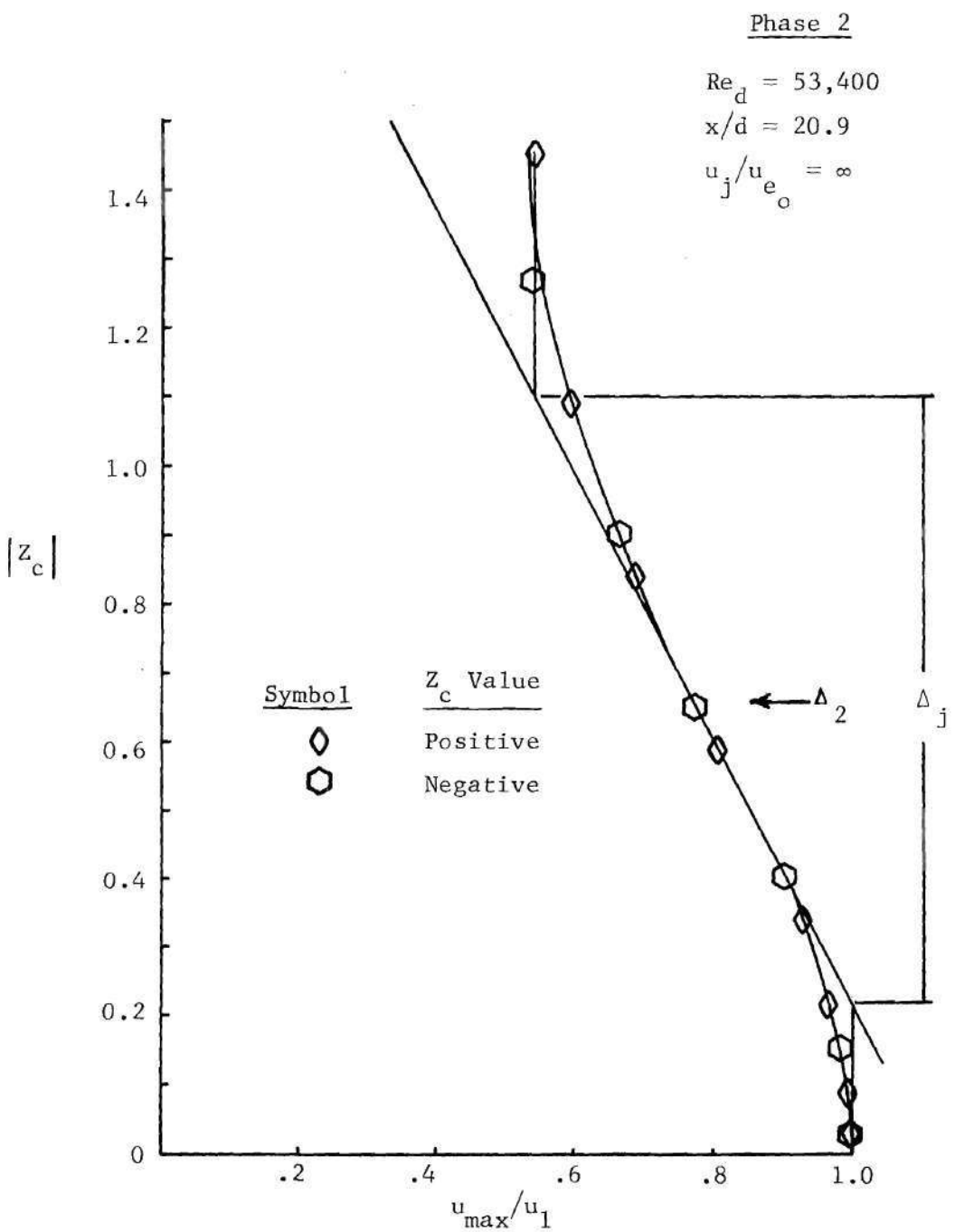

Figure 54. Phase 2 Wall Jet Velocity Profile

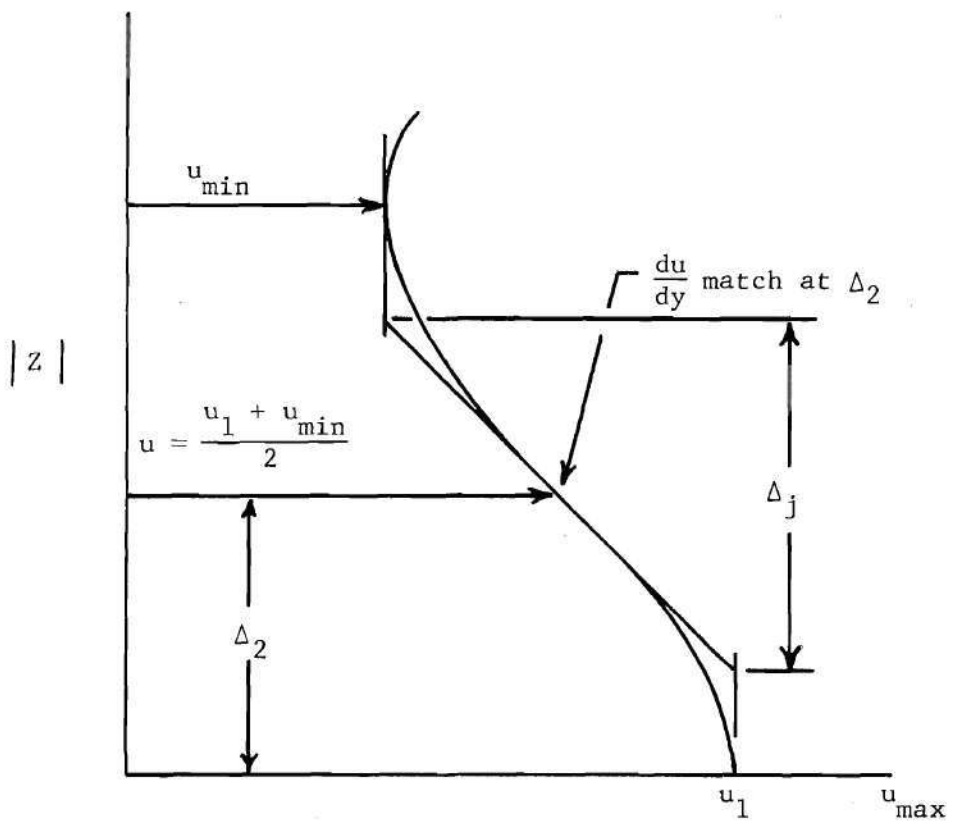

Figure 55. Wall Jet Velocity Profile; Definition of Δ_2 and Δ_j

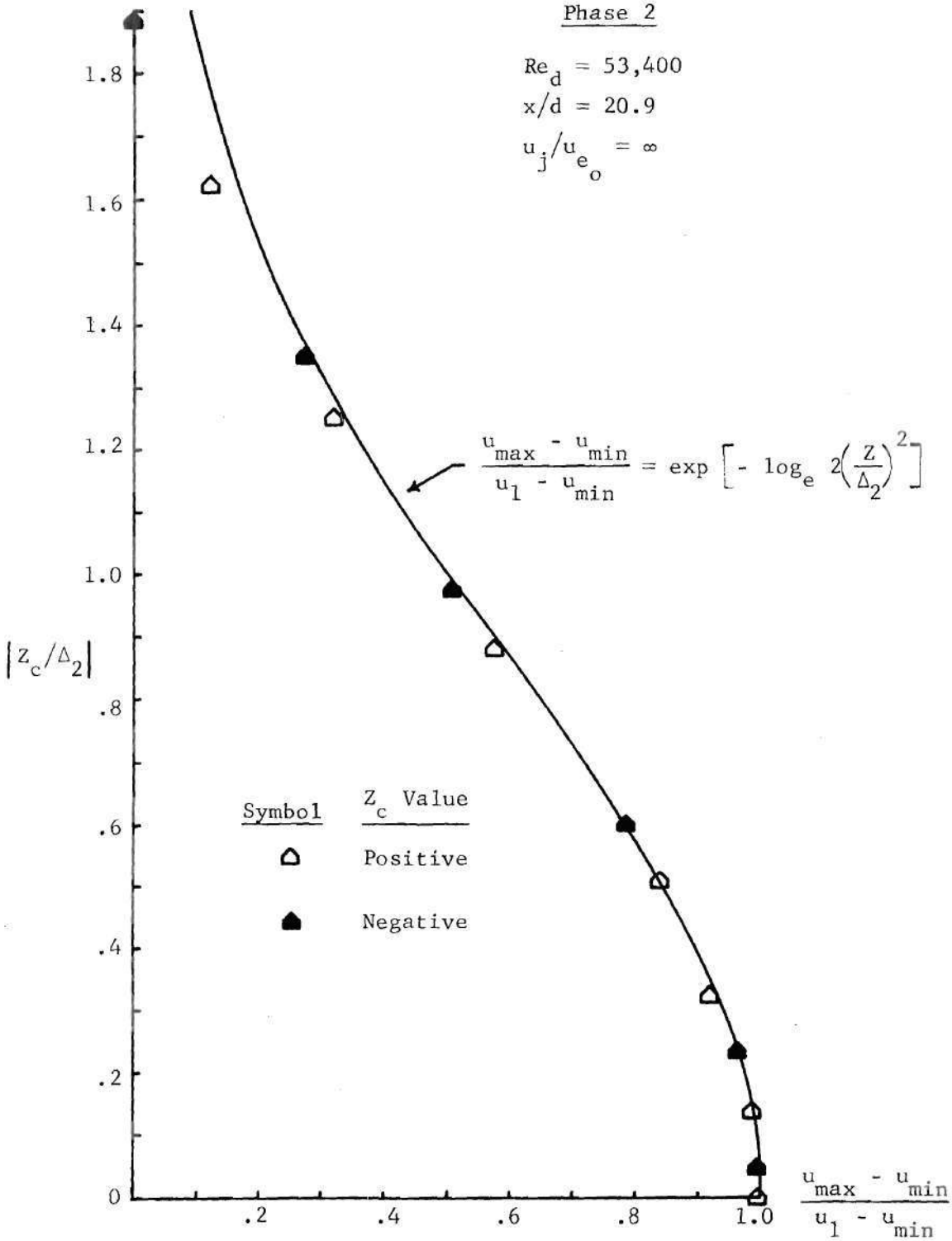

Figure 56. Phase 2 Wall Jet Velocity Profile

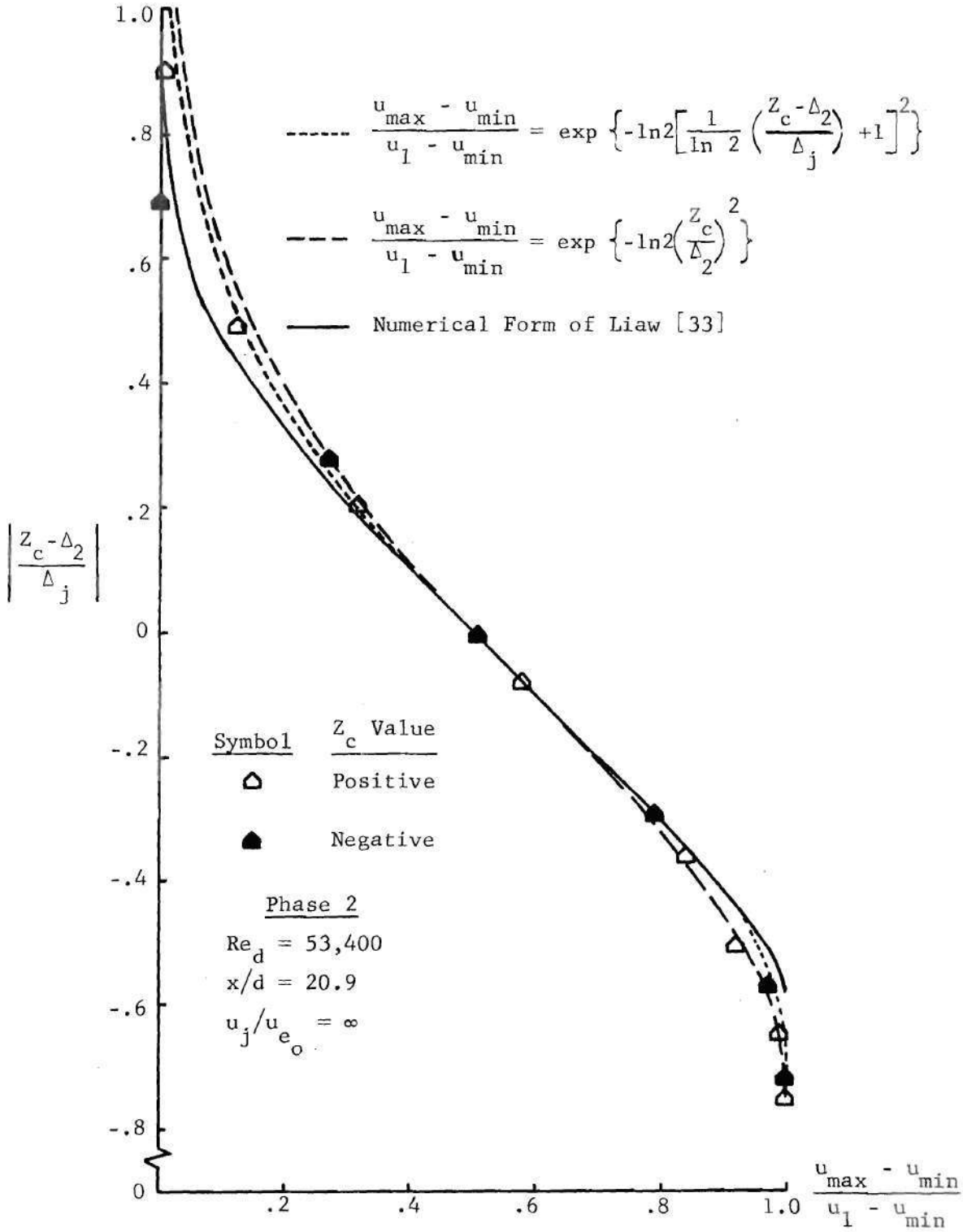

Figure 57. Phase 2 Wall Jet Velocity Profile

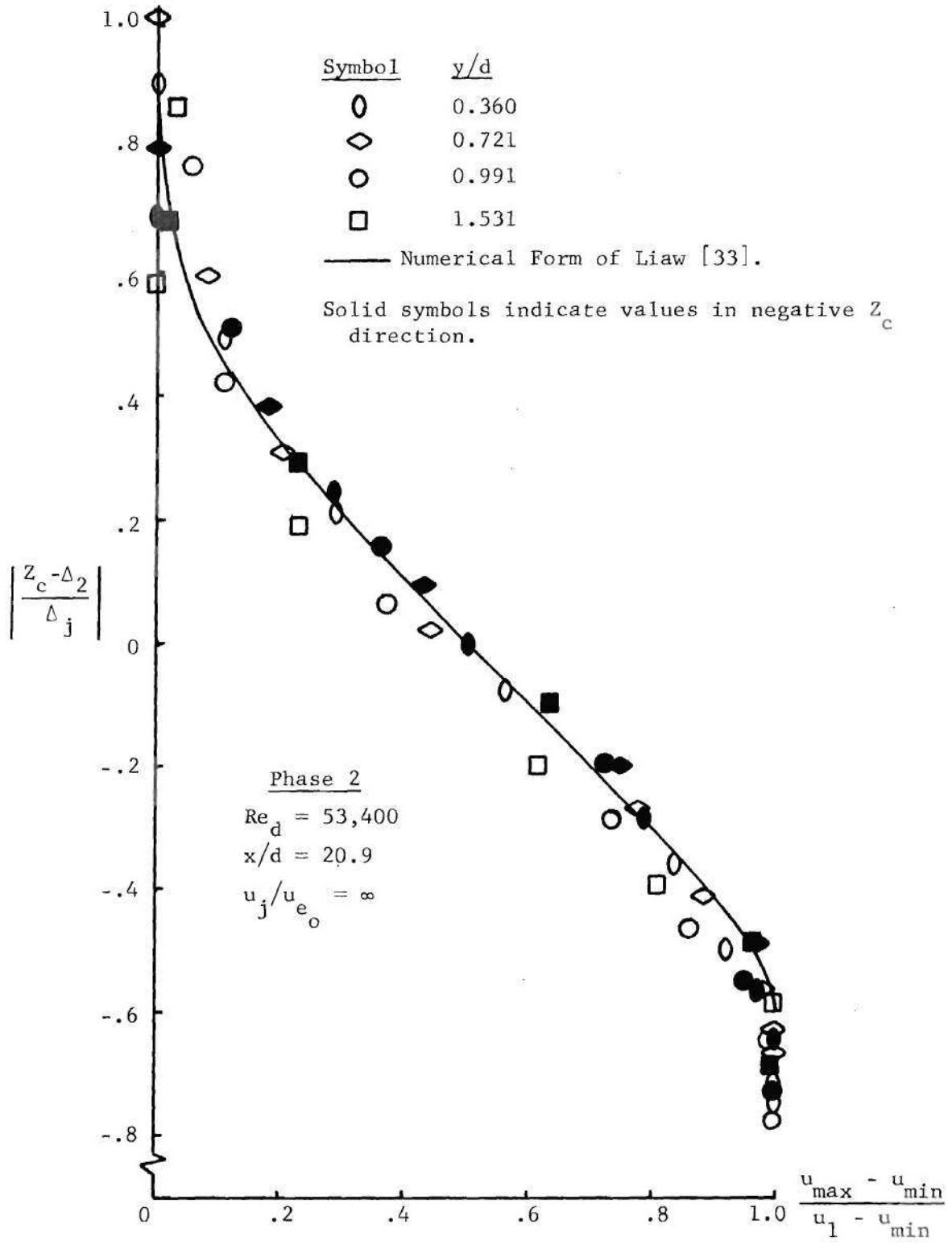

Figure 58. Phase 2 Wall Jet Velocity Profile

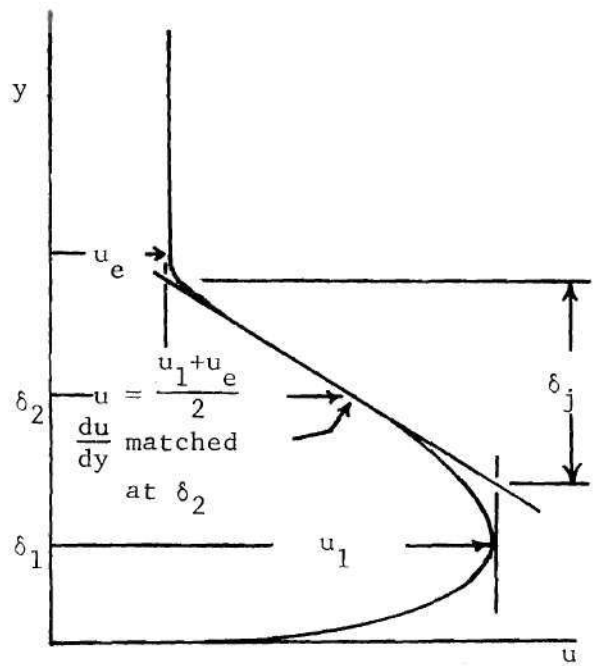

Figure 59. Profile Similarity Parameter

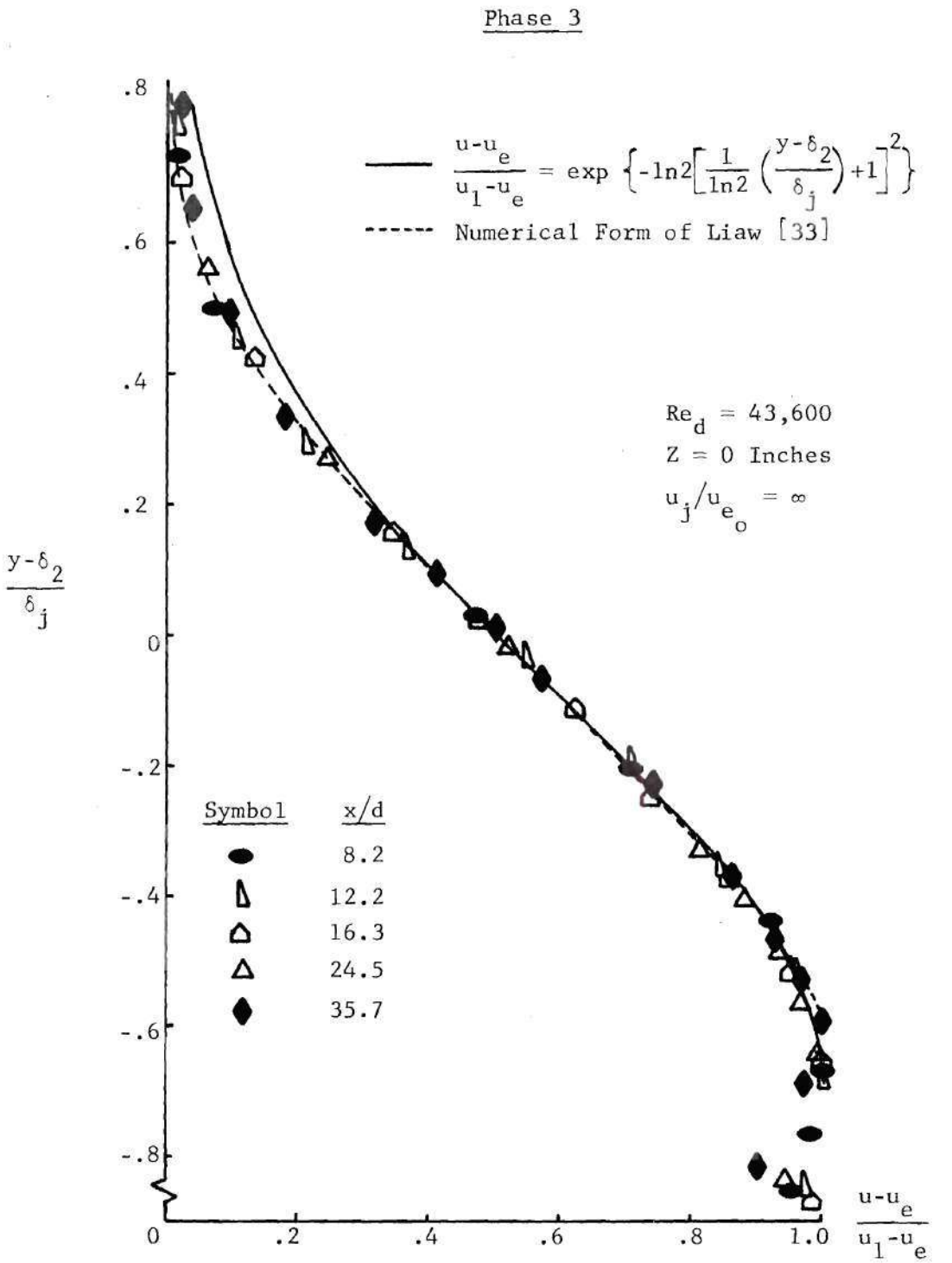

Figure 60. Phase 3 Wall Jet Velocity Profile

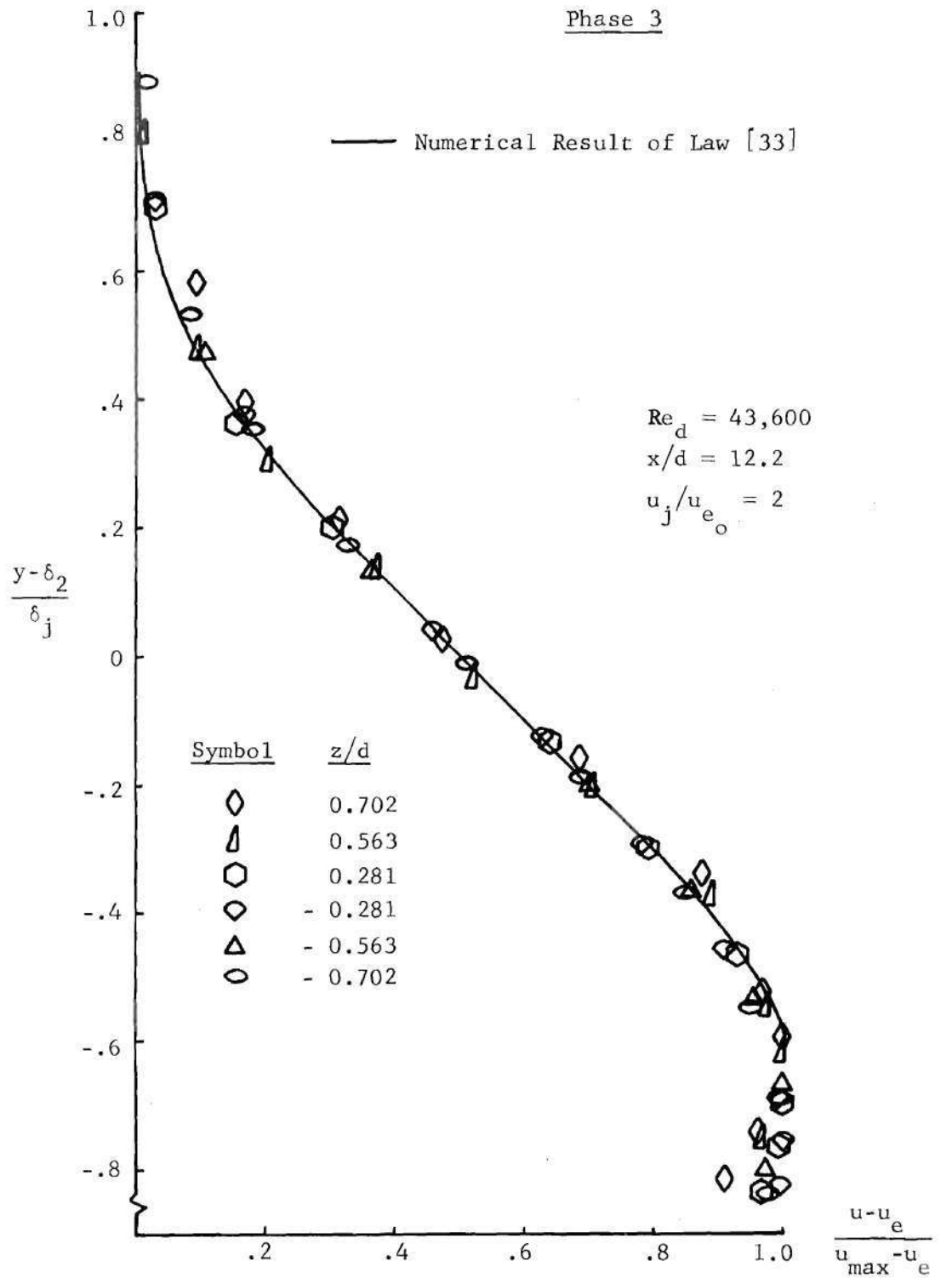

Figure 61. Phase 3 Wall Jet Velocity Profile

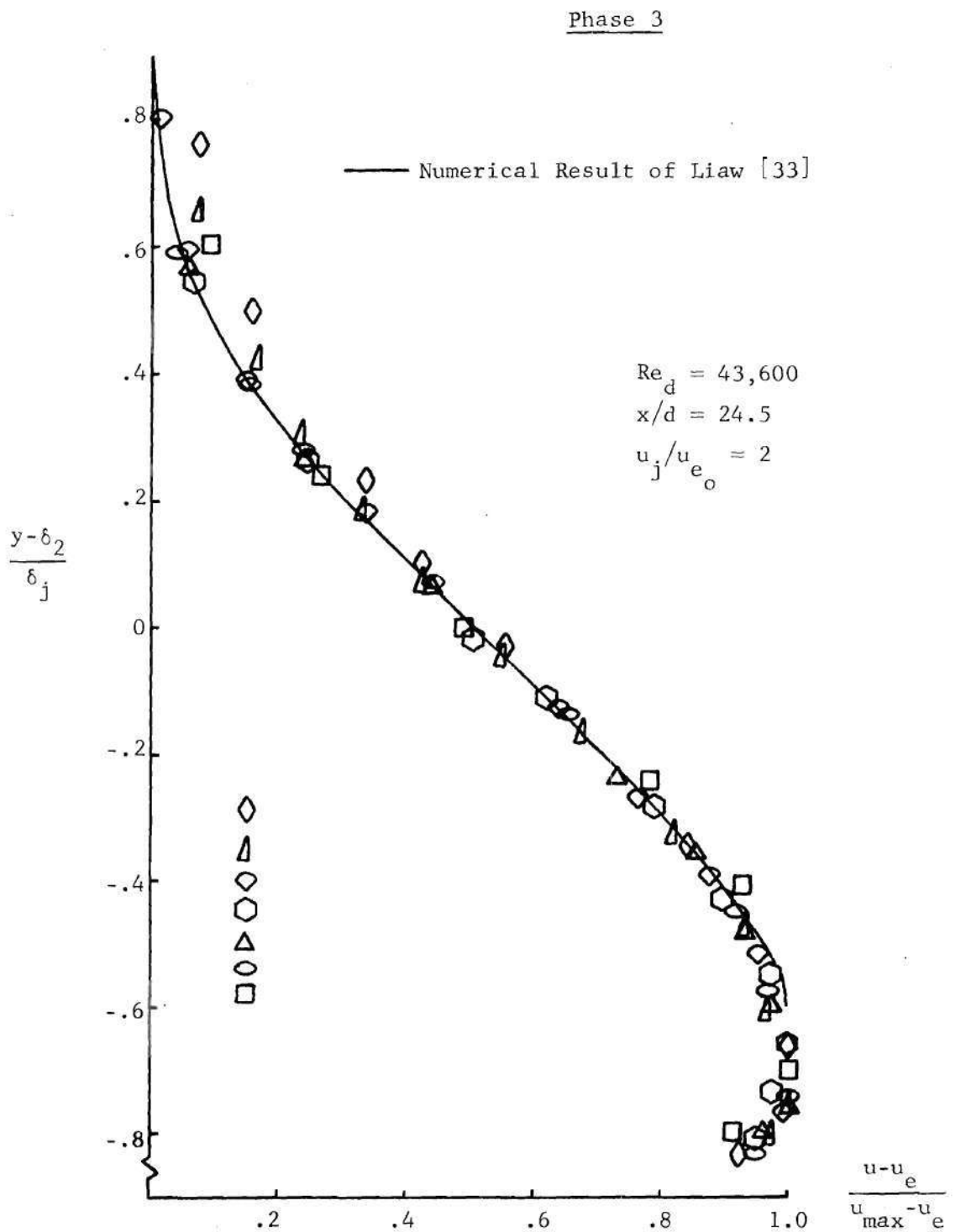

Figure 62. Phase 3 Wall Jet Velocity Profile

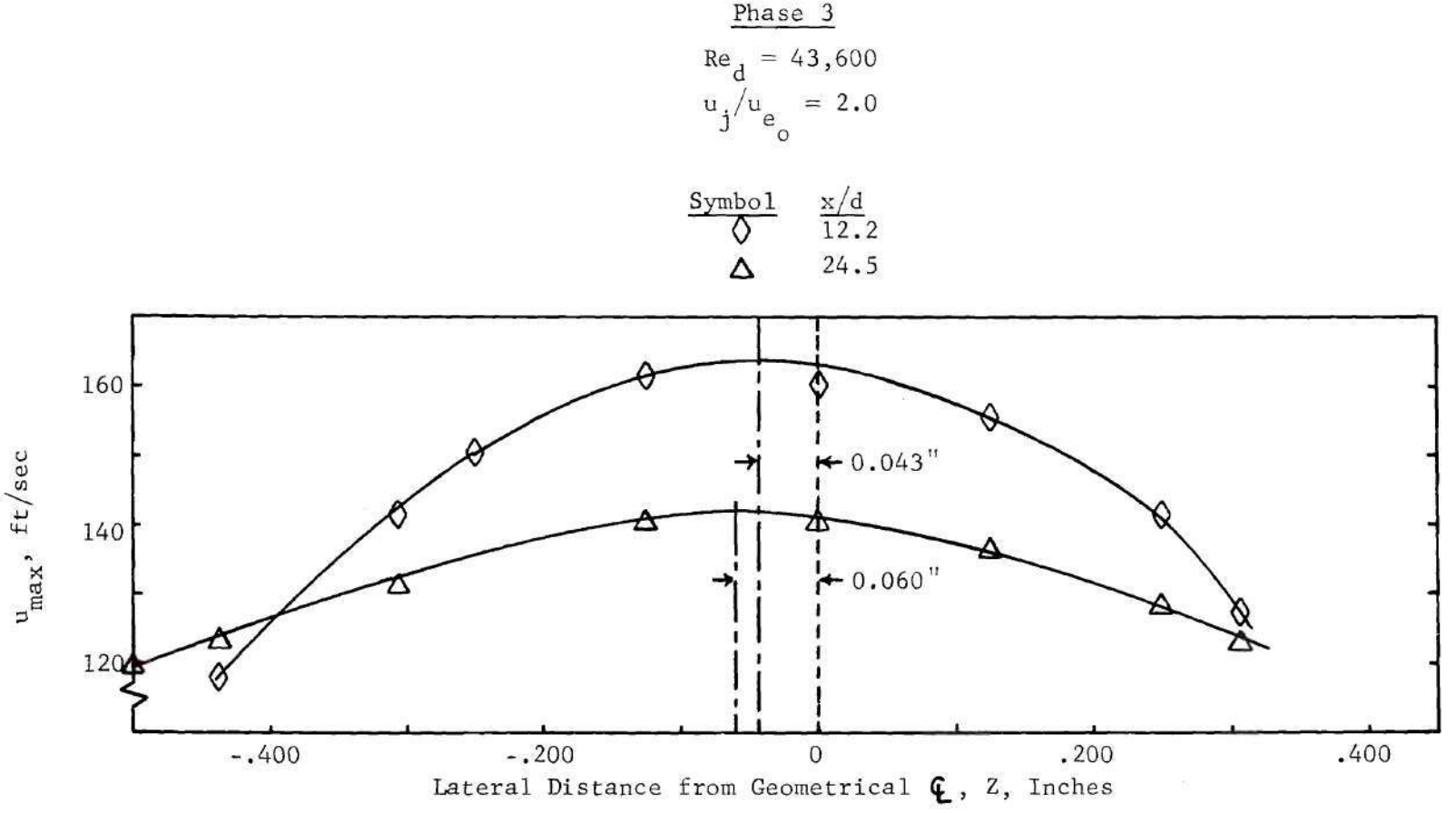

Figure 63. Phase 3 Wall Jet Velocity Profile

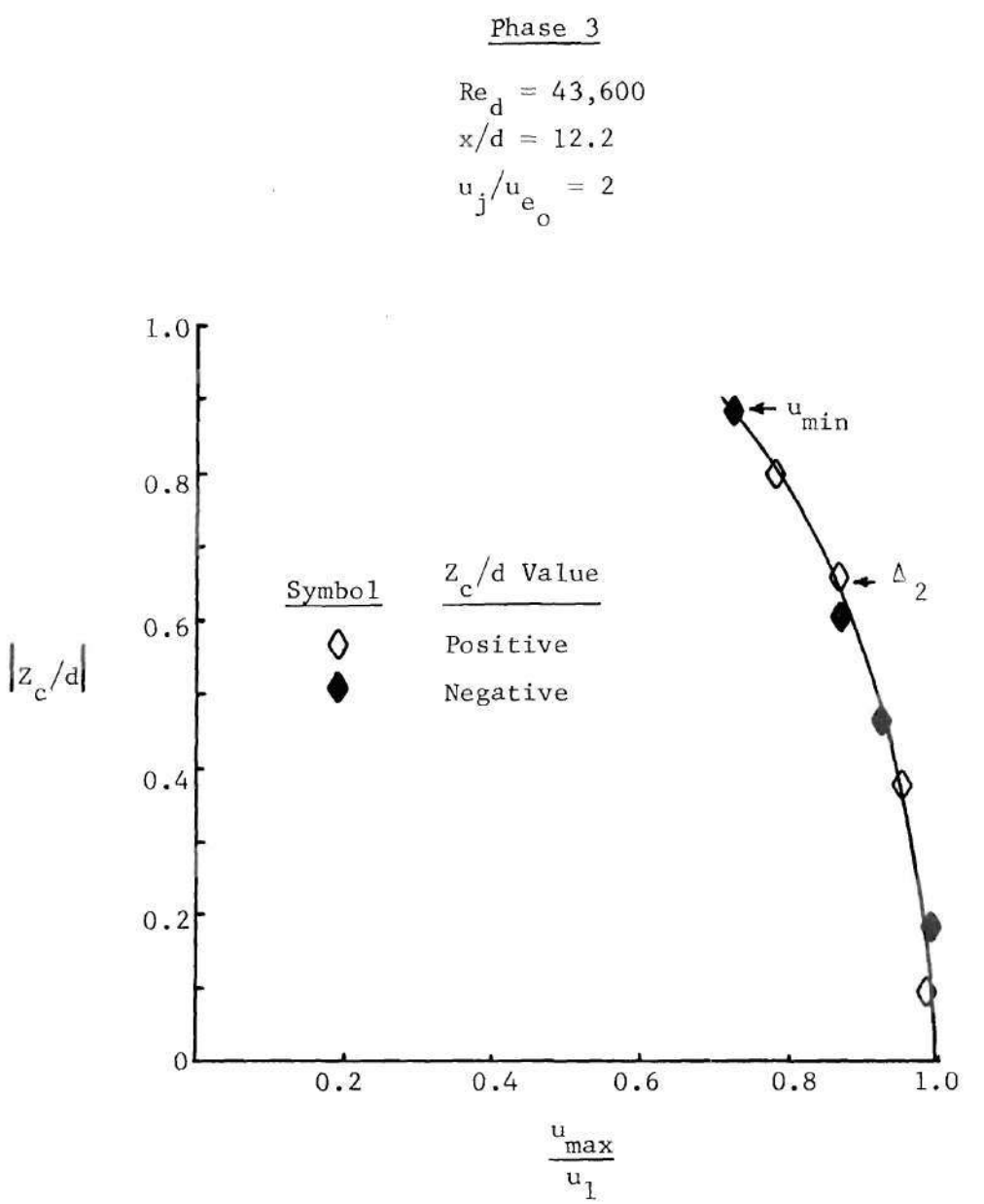

Figure 64. Phase 3 Wall Jet Velocity Profile

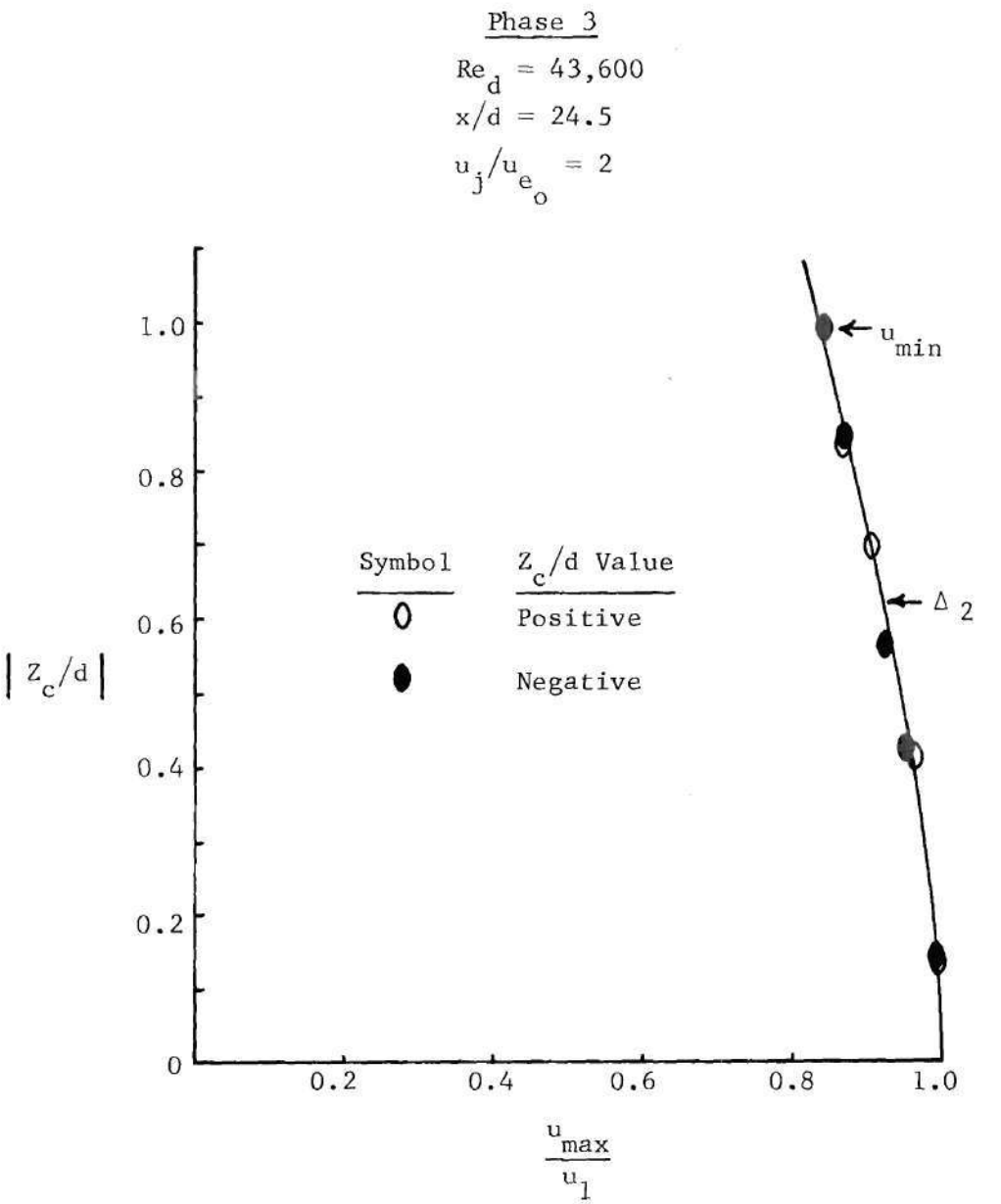

Figure 65. Phase 3 Wall Jet Velocity Profile

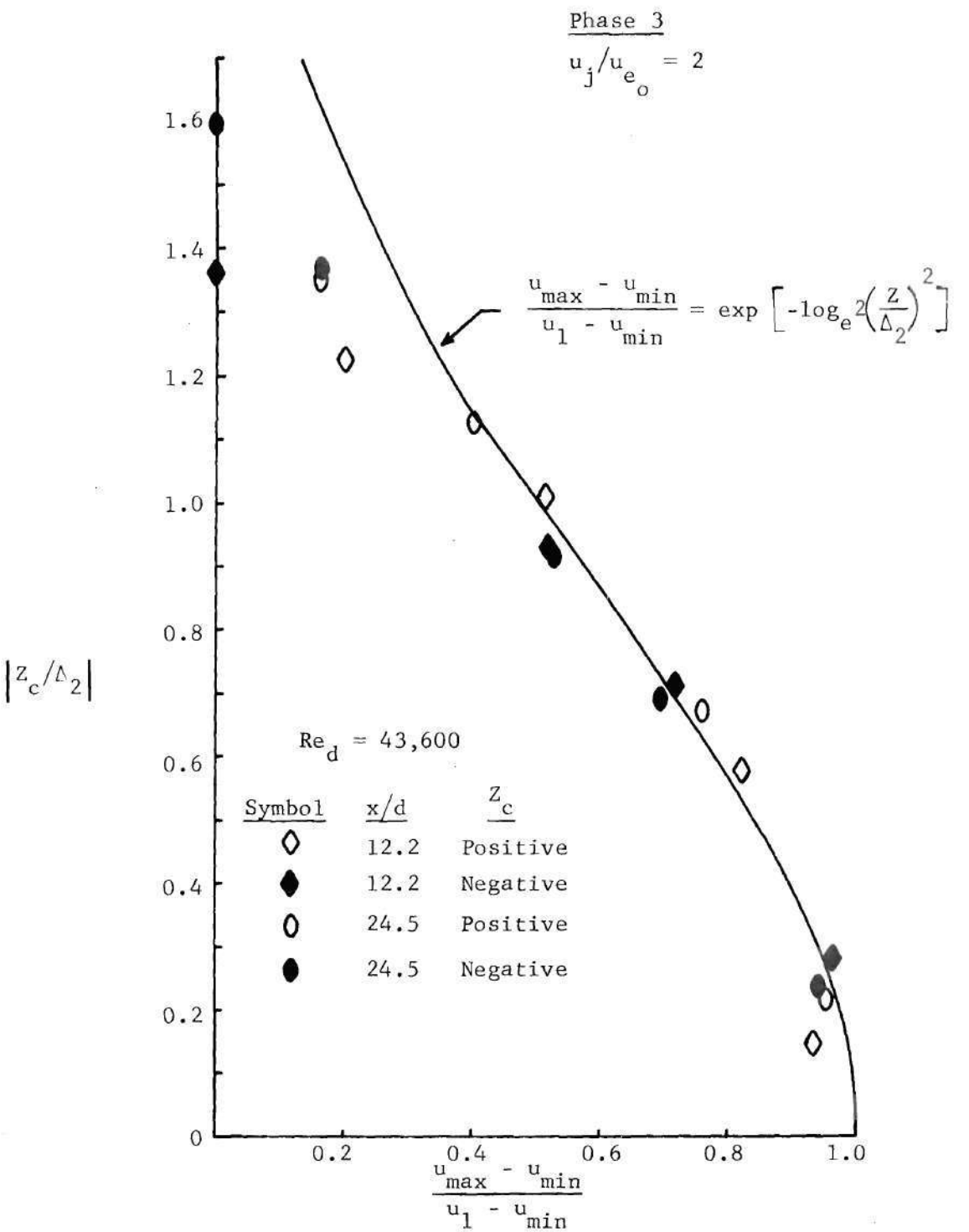

Figure 66. Phase 3 Wall Jet Velocity Profile

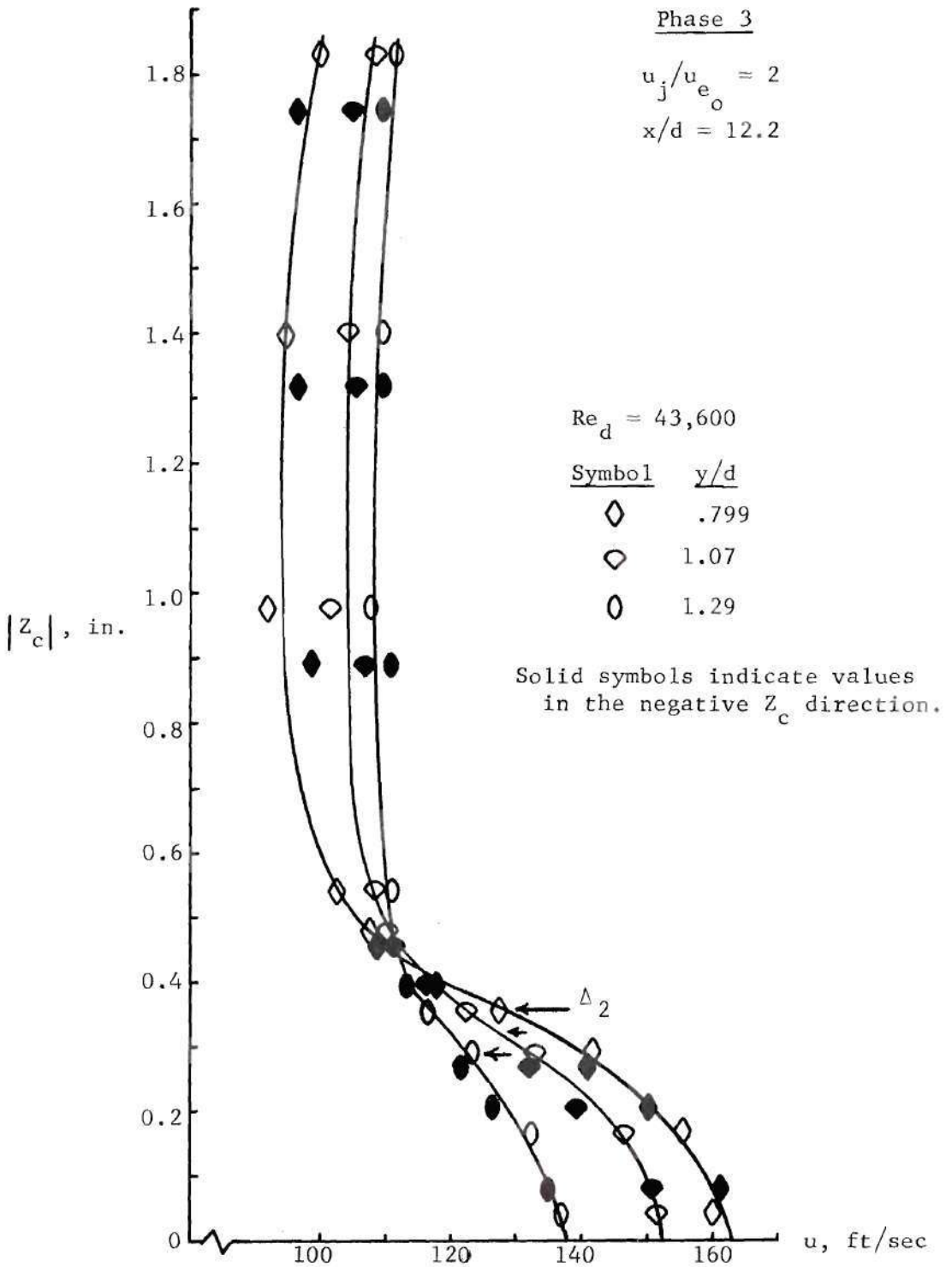

Figure 67. Phase 3 Wall Jet Velocity Profile

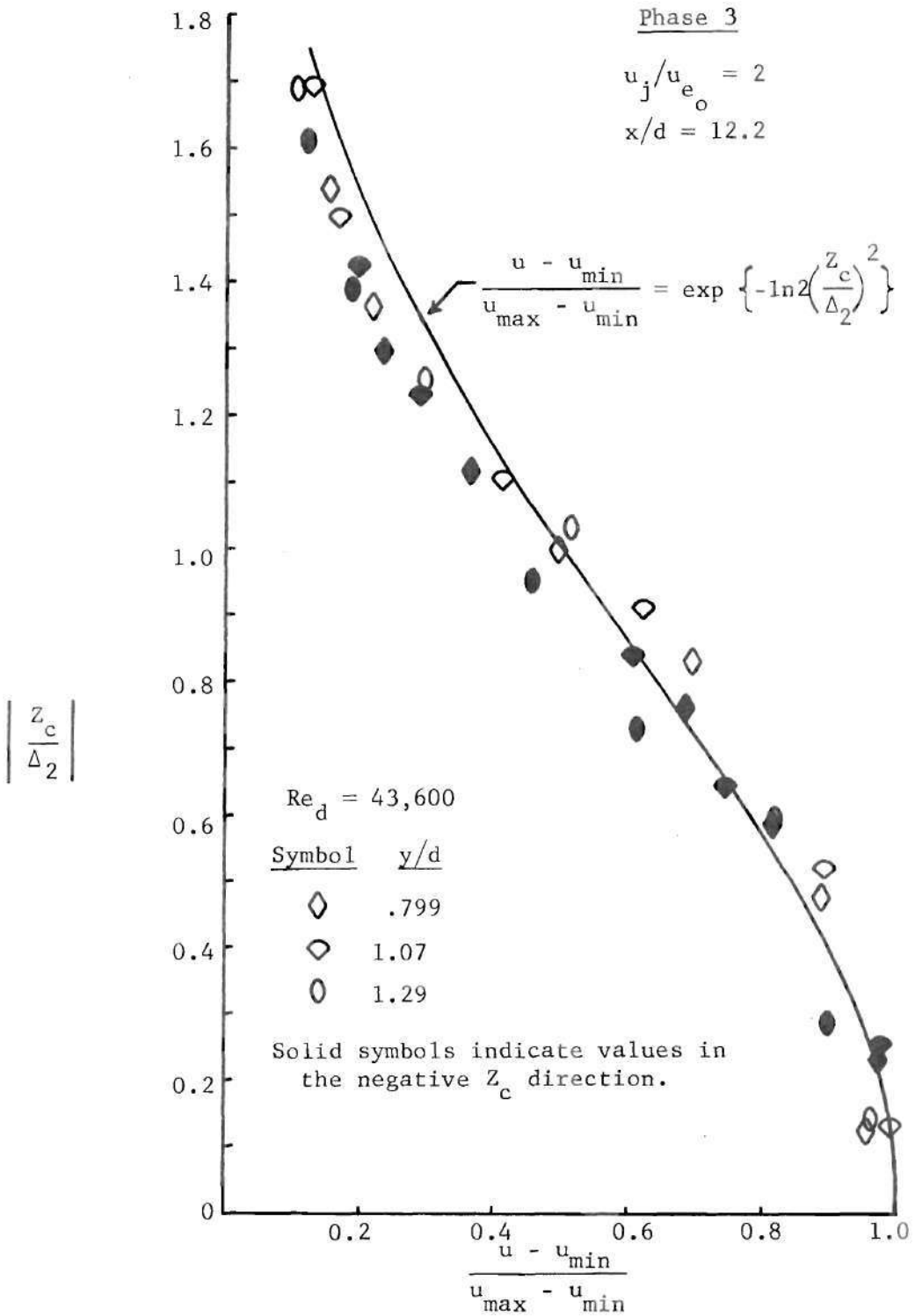

Figure 68. Phase 3 Wall Jet Velocity Profile

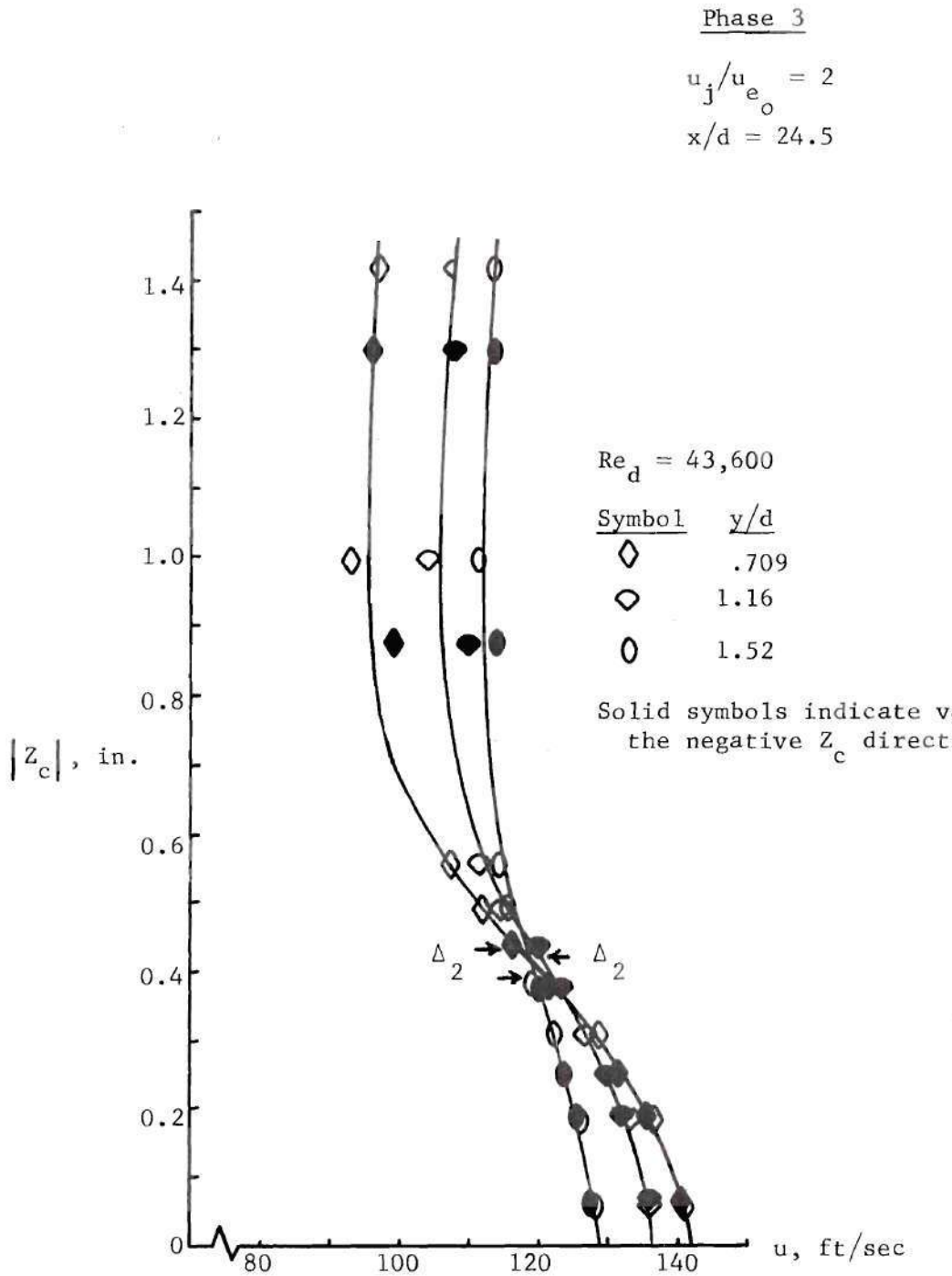

Figure 69. Phase 3 Wall Jet Velocity Profile

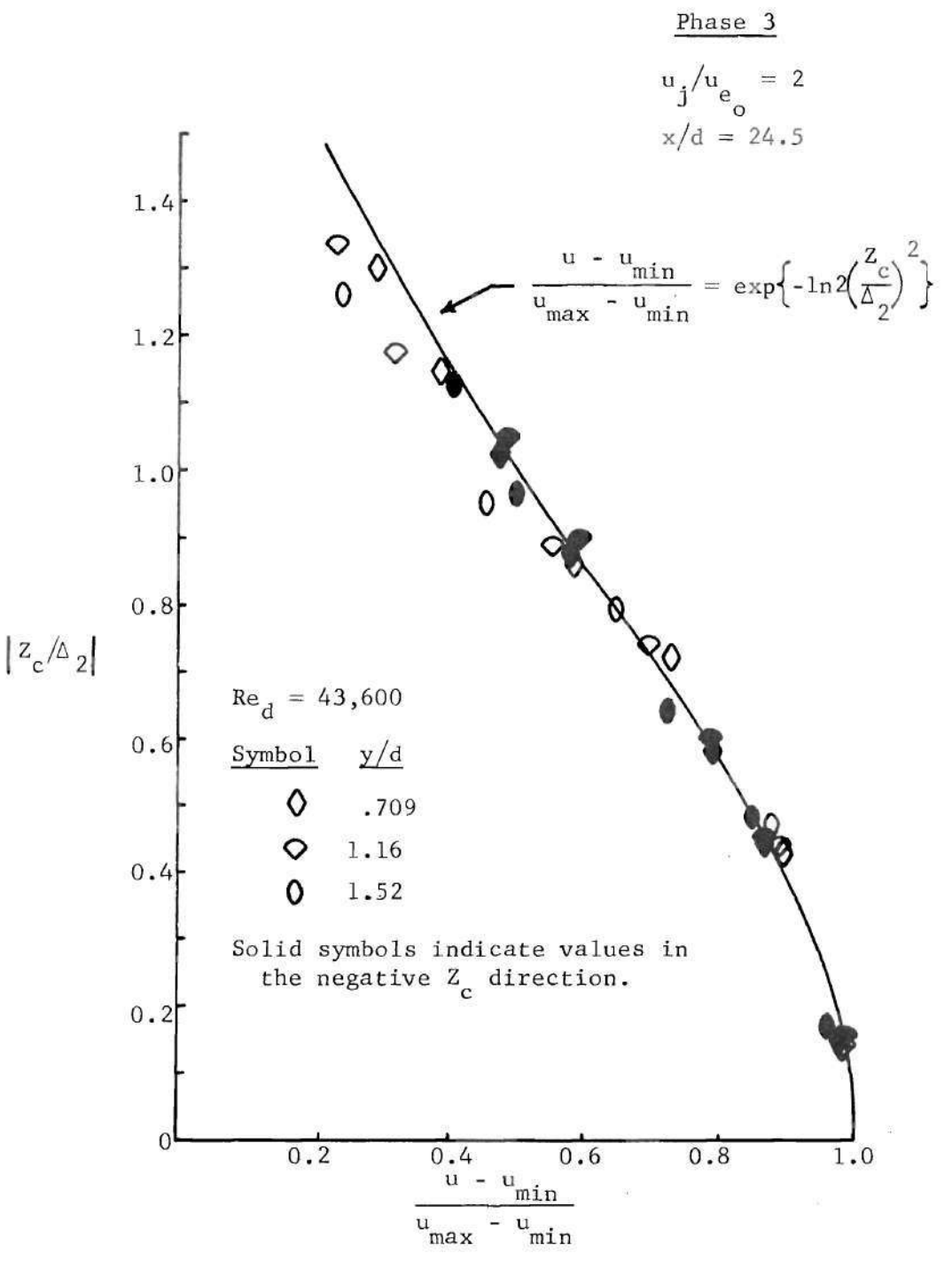

Figure 70. Phase 3 Wall Jet Velocity Profile

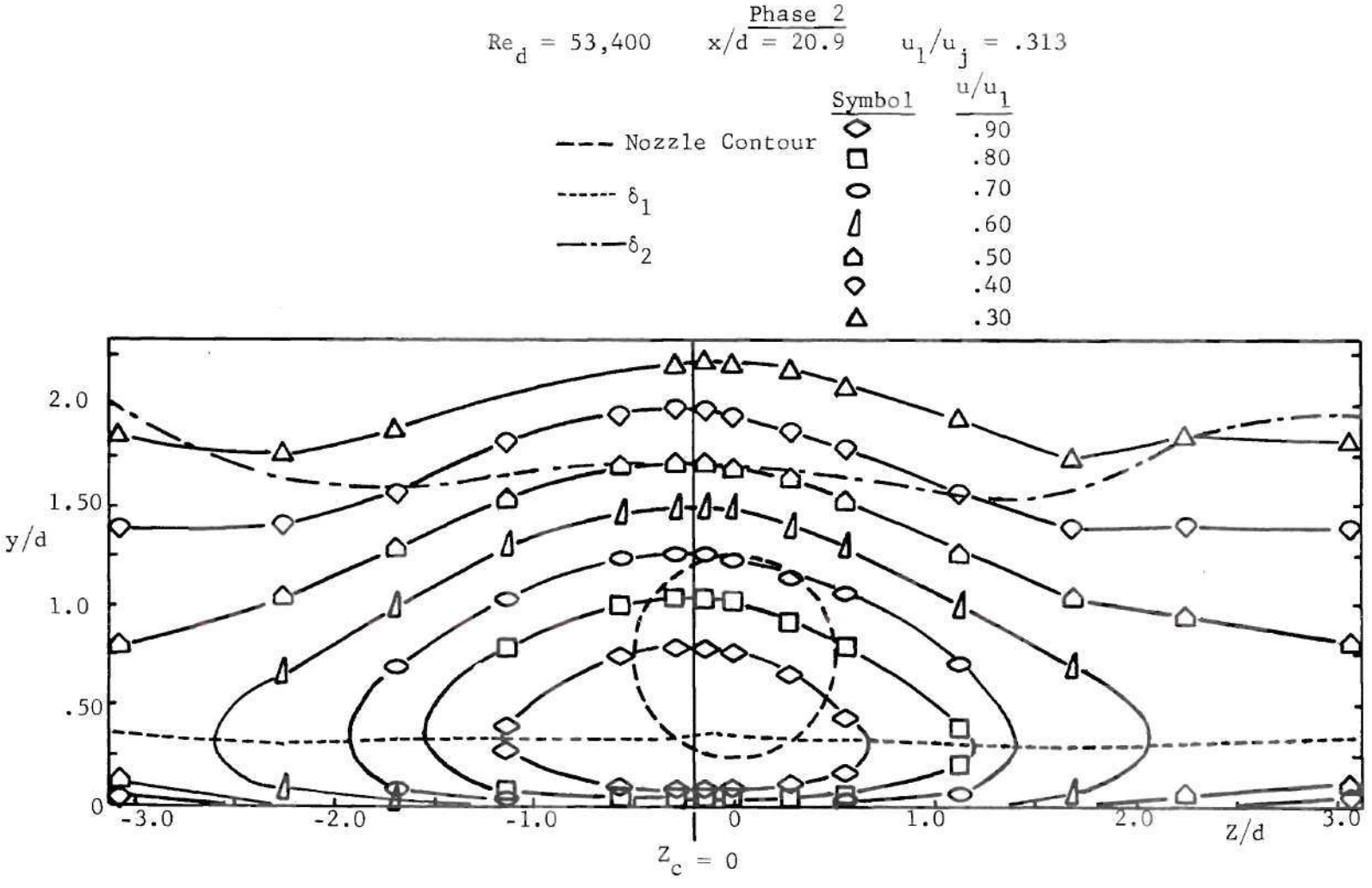

Figure 71. Phase 2 Iso-velocity Profiles

Phase 2

Re_d = 53,400
x/d = 50
u_1/u_j = .155

δ_1
δ_2
Nozzle contours

Symbol	u/u_1
◇	.90
□	.80
○	.70
◁	.60
⌂	.50

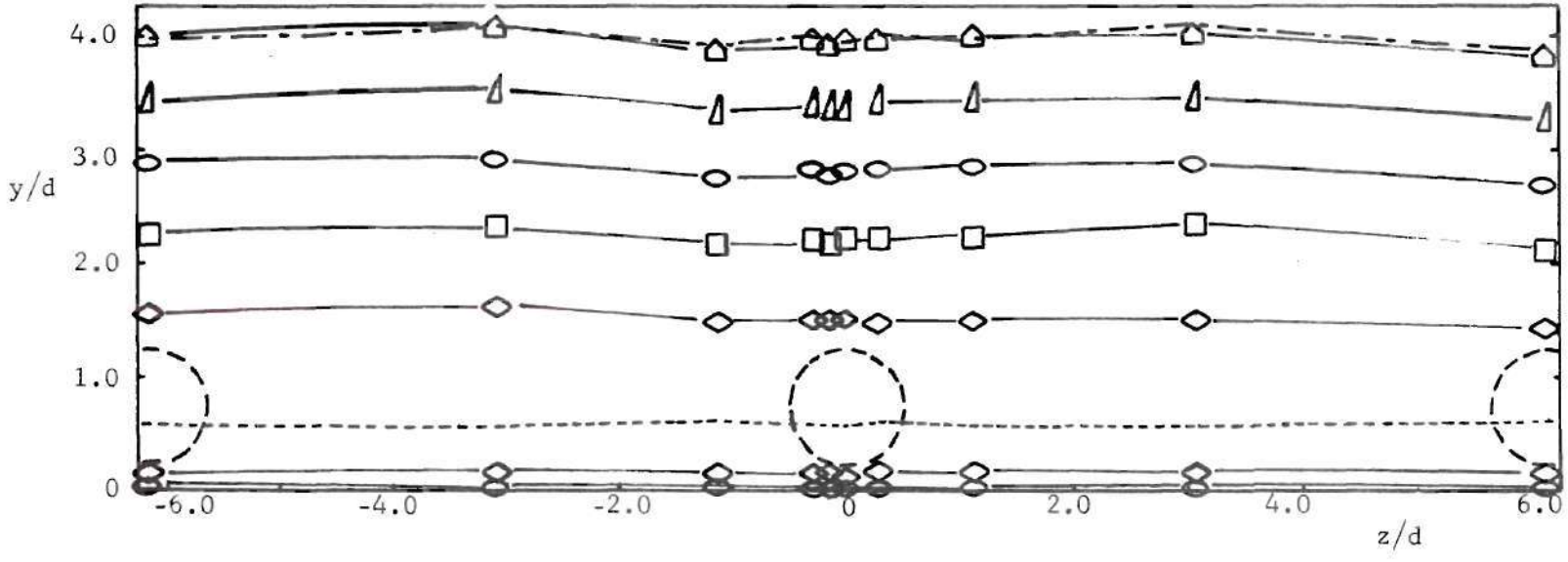

Figure 72. Phase 2 Iso-velocity Profiles

Phase 2

$Re_d = 53,400$ $u_j/u_{e_o} = \infty$

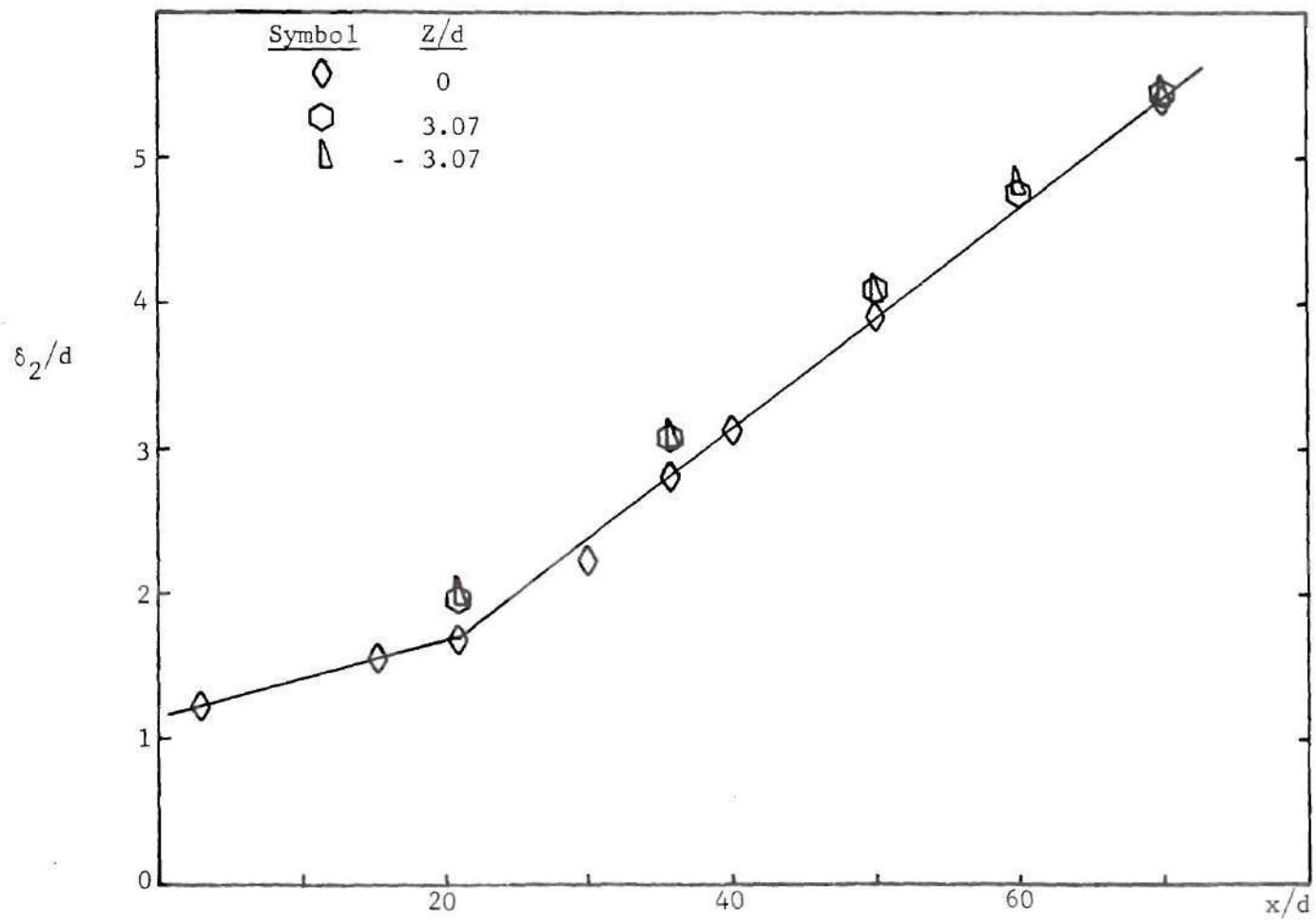

Figure 73. Phase 2 Half-Velocity Growth

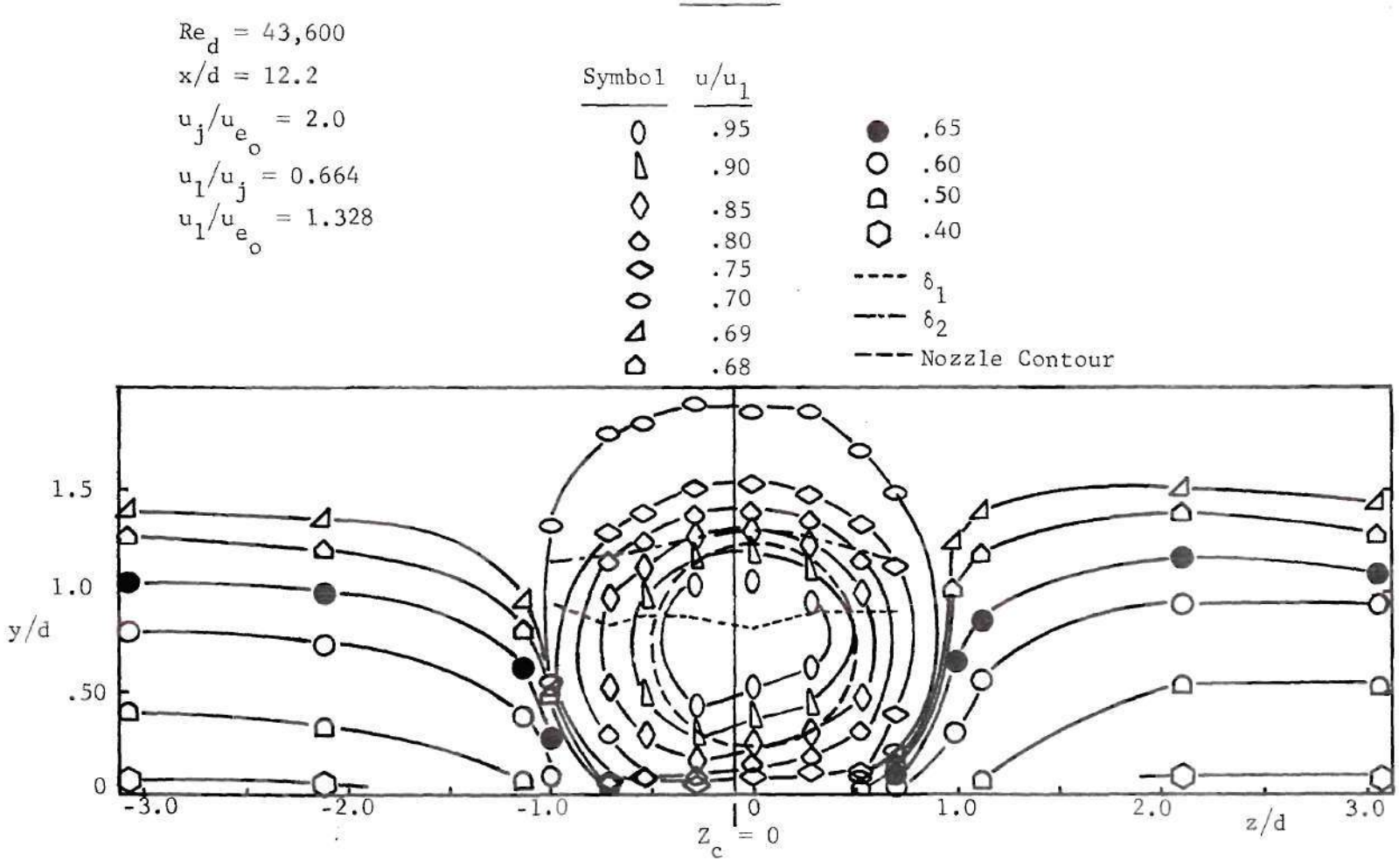

Figure 74. Phase 3 Iso-velocity Profiles

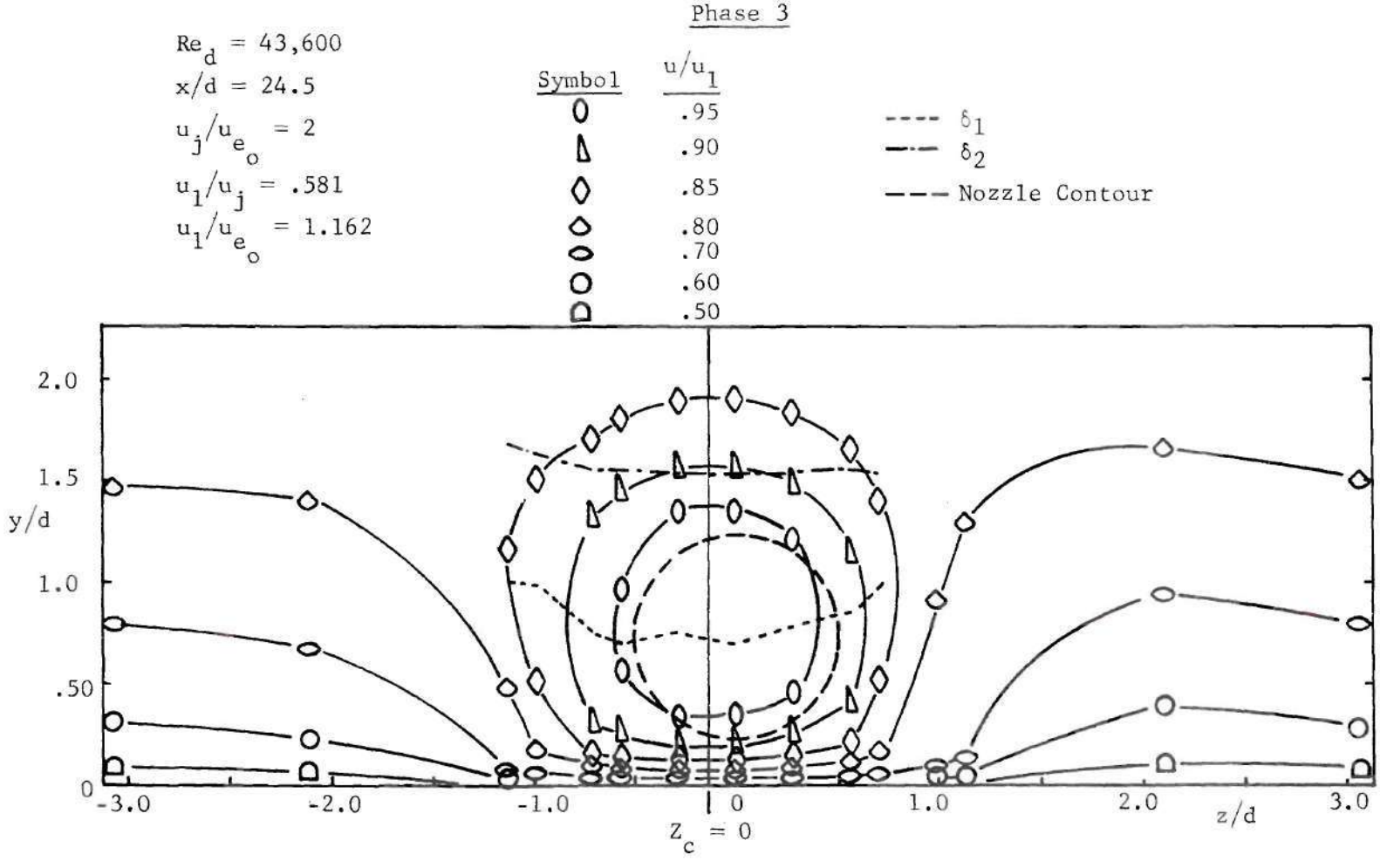

Figure 75. Phase 3 Iso-velocity Profiles

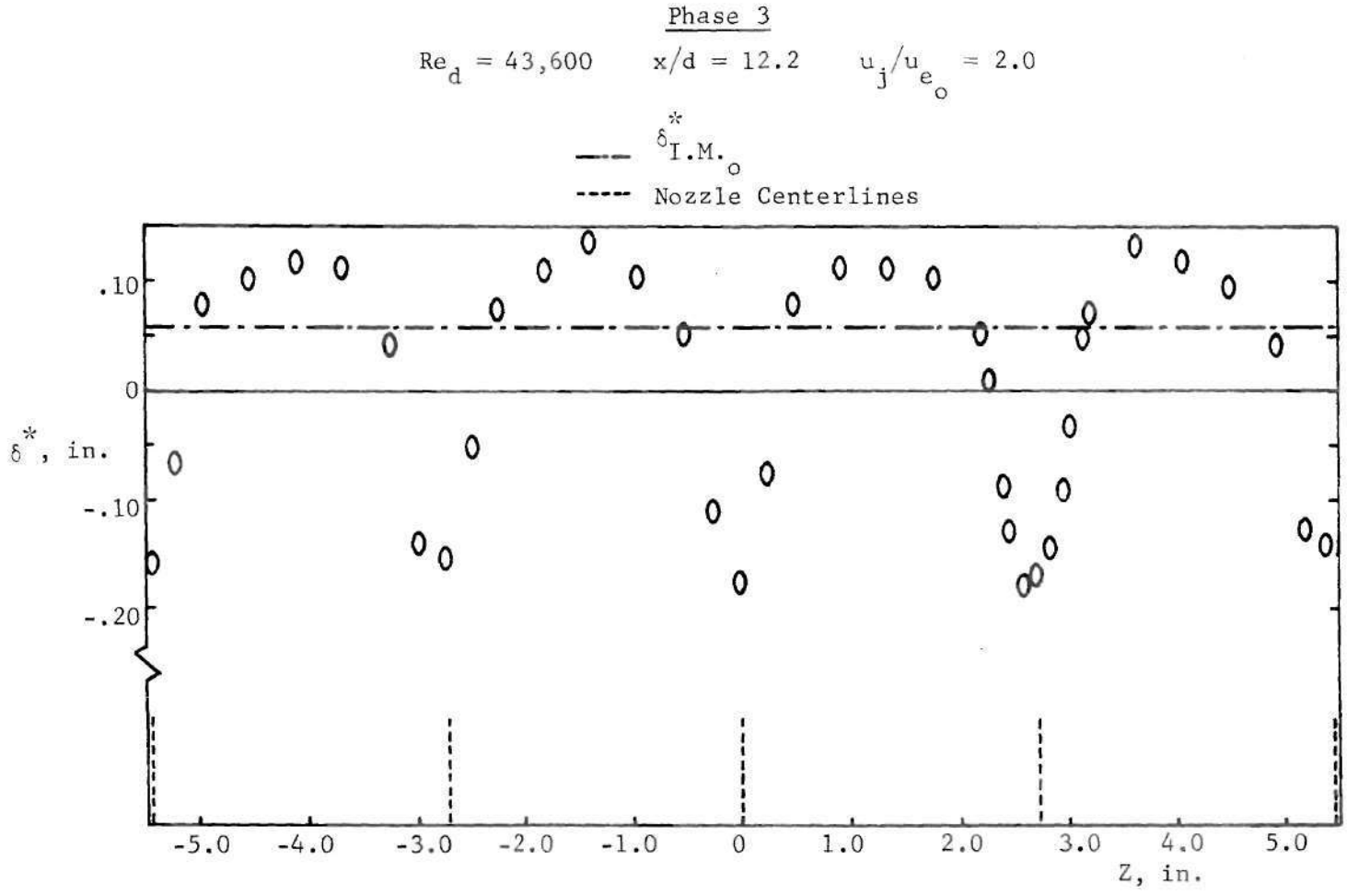

Figure 76. Wall Jet Displacement Thickness Distribution

Phase 3

$Re_d = 43,600$ $x/d = 12.2$ $u_j/u_{e_o} = 2.0$

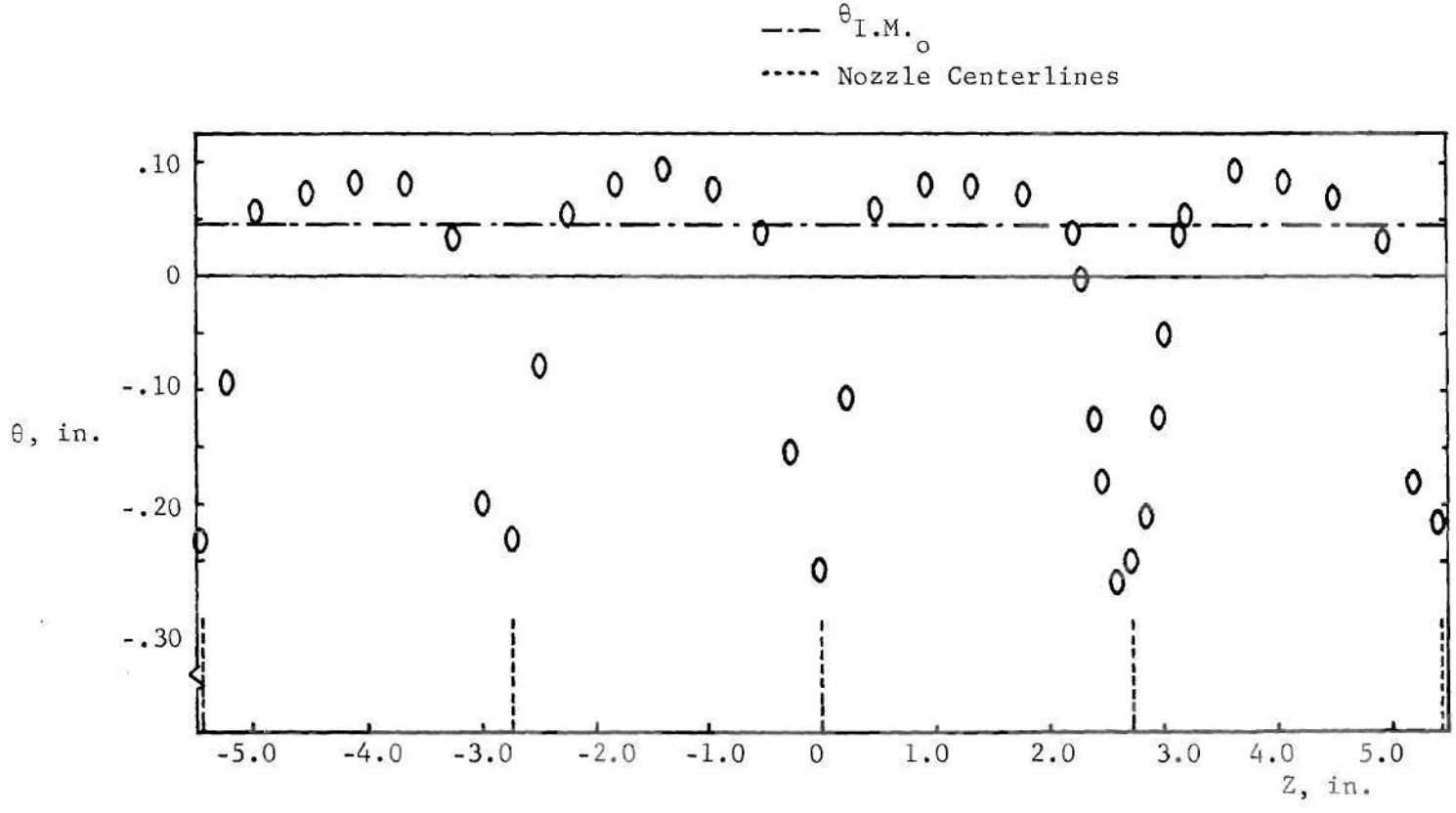

Figure 77. Wall Jet Momentum Thickness Distribution

Phase 3

$Re_d = 43{,}600$ $x/d = 12.2$ $u_j/u_{e_o} = 2.0$

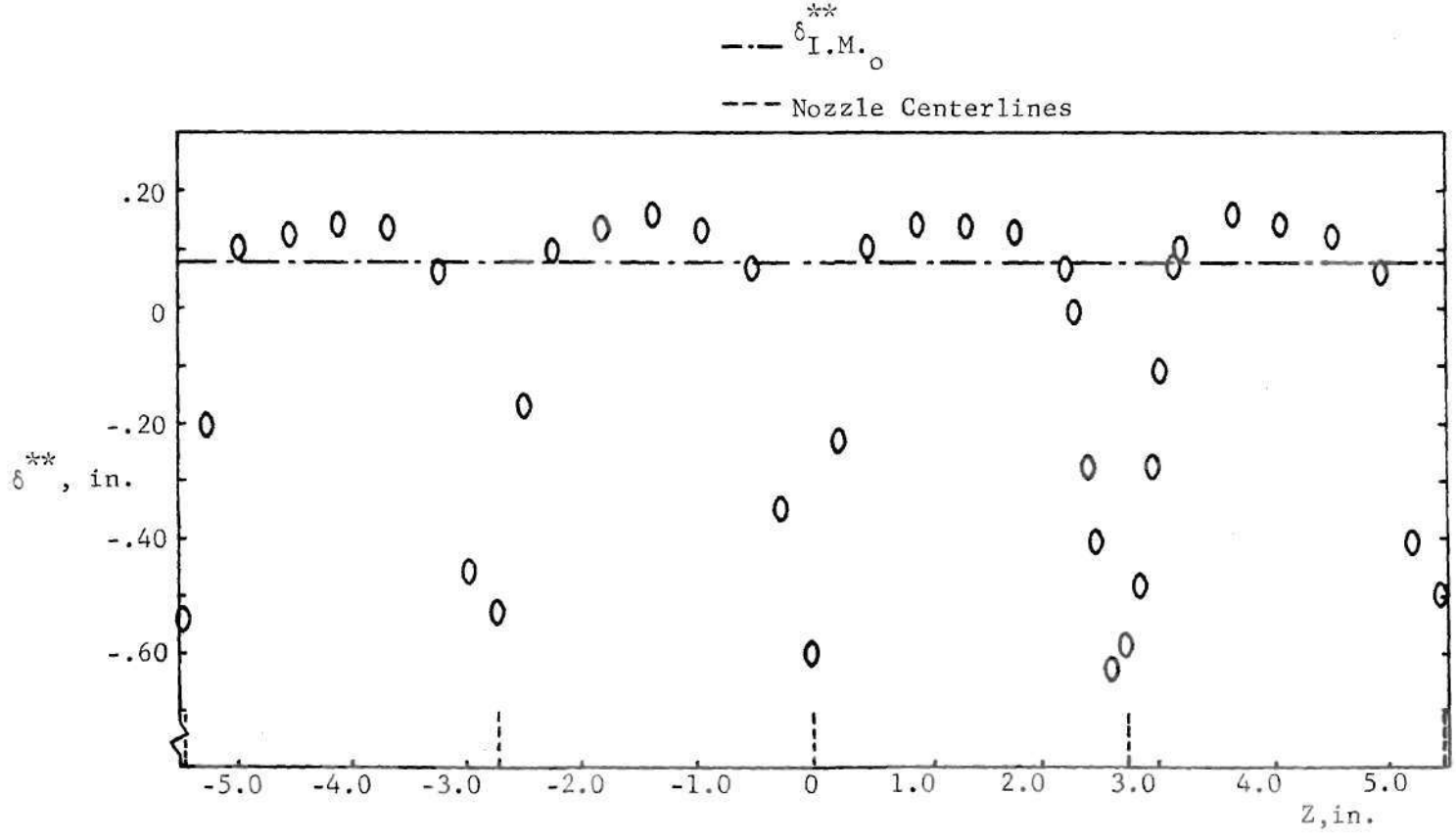

Figure 78. Wall Jet Energy Thickness Distribution

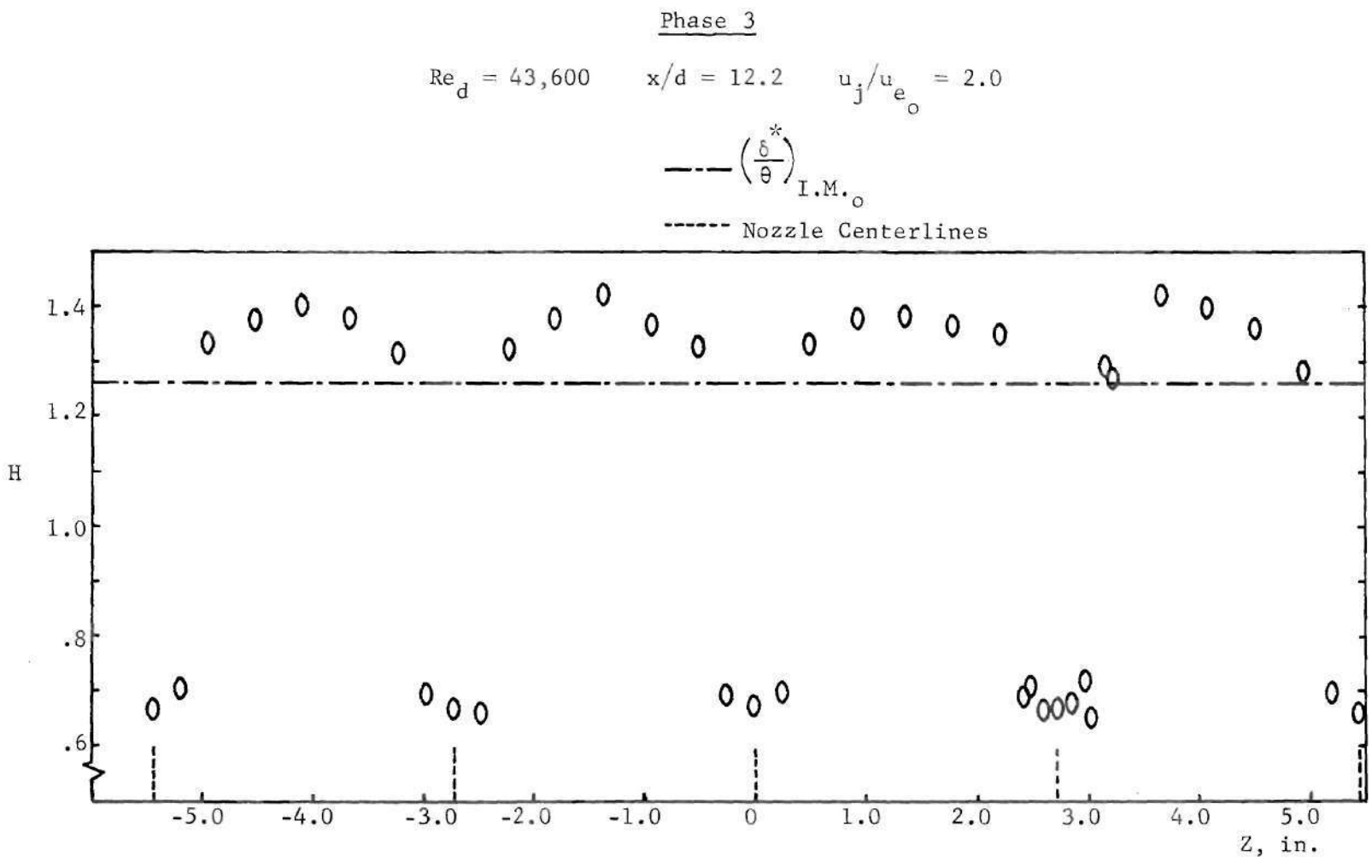

Figure 79. Wall Jet Shape Factor Distribution

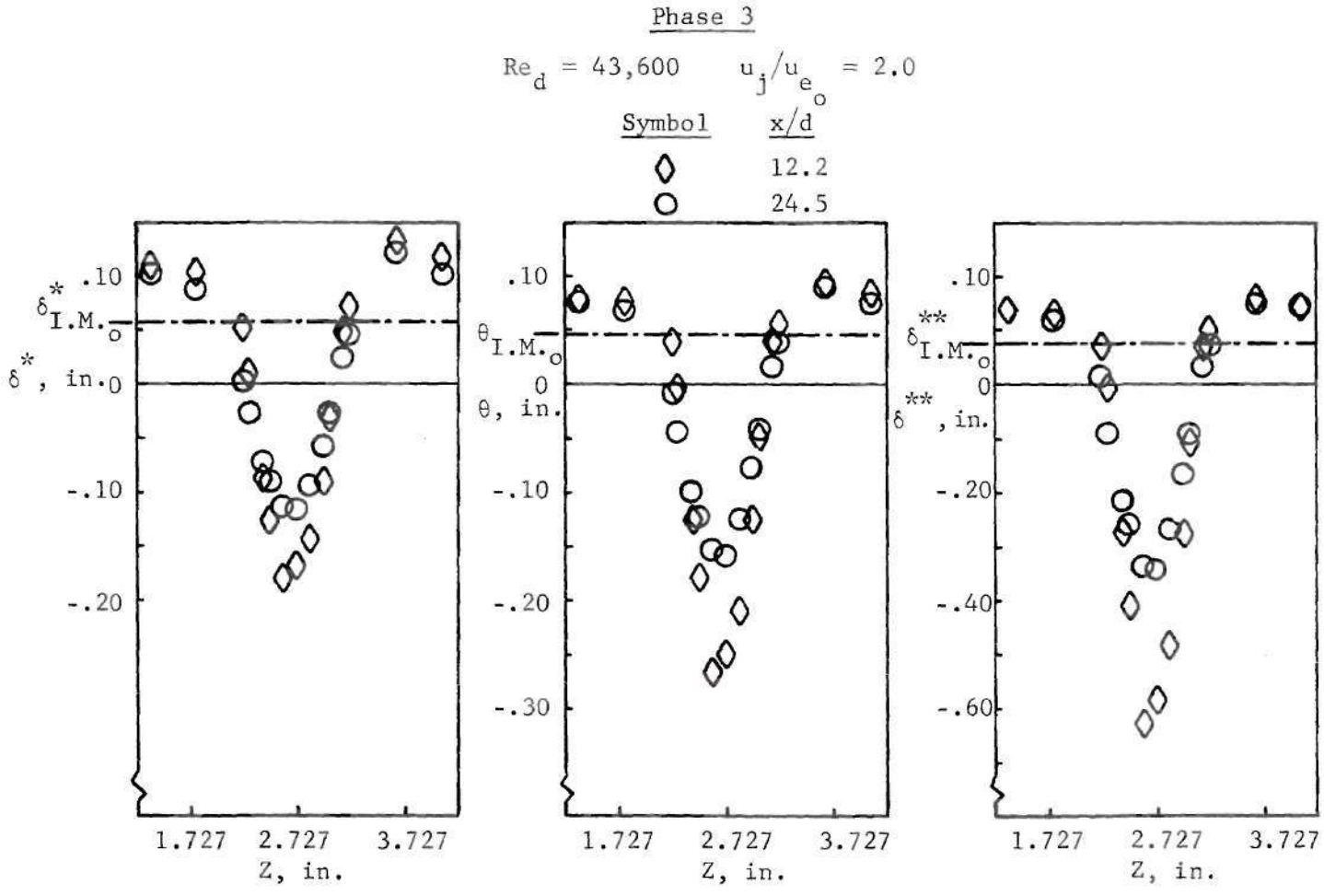

Figure 80. Wall Jet Characteristic Thicknesses

Table 4. Wall Jet Characteristic Thicknesses, Phase 3

$\delta^{*}_{I.M._o}$ = 0.0578 Inch $\quad \theta_{I.M._o}$ = 0.0458 Inch $\quad \delta^{**}_{I.M._o}$ = 0.0789 Inch

x/d	Z = 1.363"				Centerline				z = 4.090"			
	δ^{*}, in.	θ, in.	δ^{**}, in.	H	δ^{*}, in.	θ, in.	δ^{**}, in.	H	δ^{*}, in.	θ, in.	δ^{**}, in.	H
8.198	.1306	.0883	.1506	1.479	-.2003	-.3305	-.8289	.606	.1323	.0888	.1509	1.490
12.25	.1115	.0804	.1401	1.387	-.1673	-.2493	-.5824	.671	.1190	.0848	.1473	1.403
16.3	.1063	.0787	.1386	1.351	-.1492	-.2147	-.4878	.695	.1046	.0779	.1374	1.343
24.46	.1023	.0782	.1394	1.300	-.1152	-.1556	-.3401	.740	.1012	.0784	.1405	1.291
35.68	.0999	.0776	.1395	1.281	-.0731	-.1001	-.2133	.730	.0939	.0741	.1341	1.267

Phase 3

$u_j/u_{e_o} = 2.0$

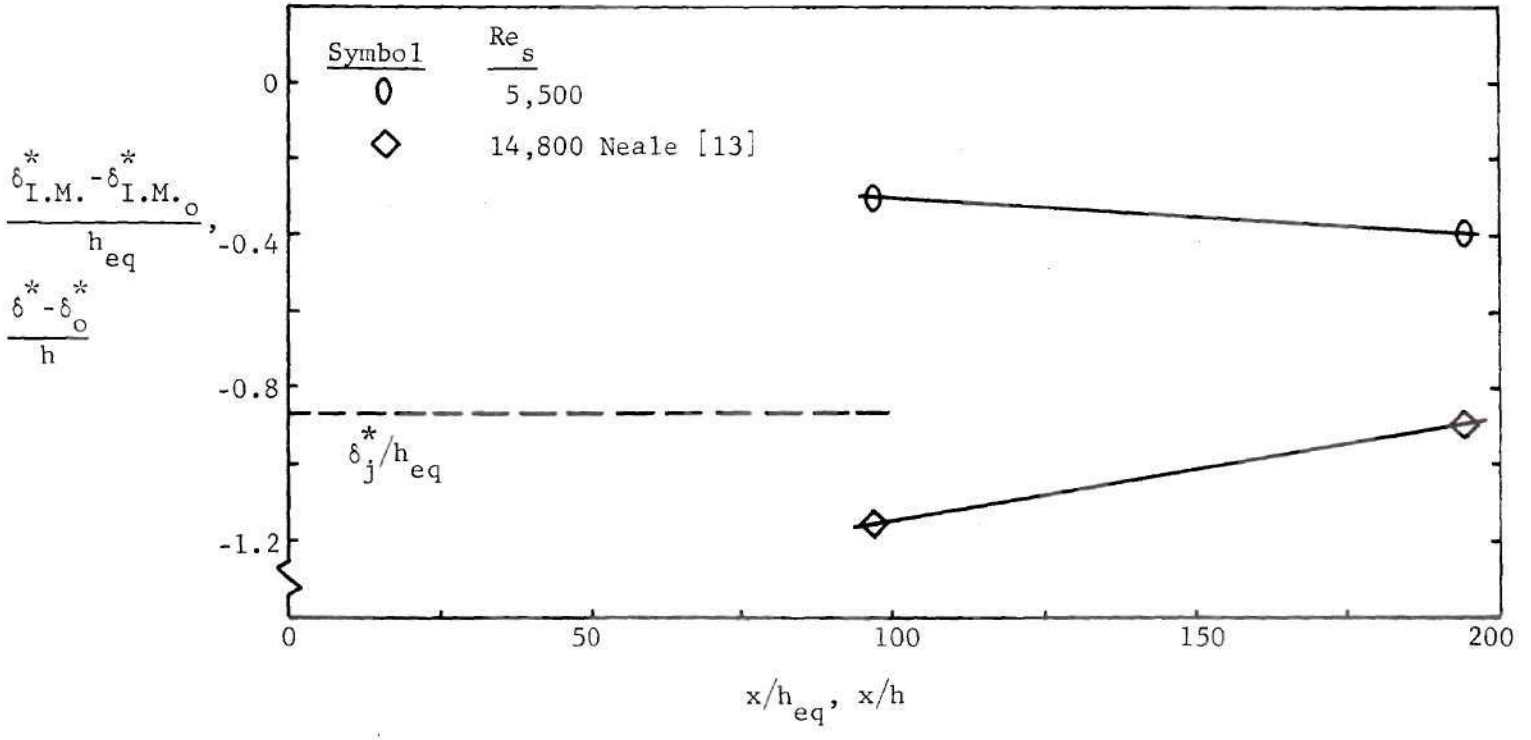

Figure 81. Wall Jet Displacement Thickness

Phase 3

$u_j/u_{e_o} = 2.0$

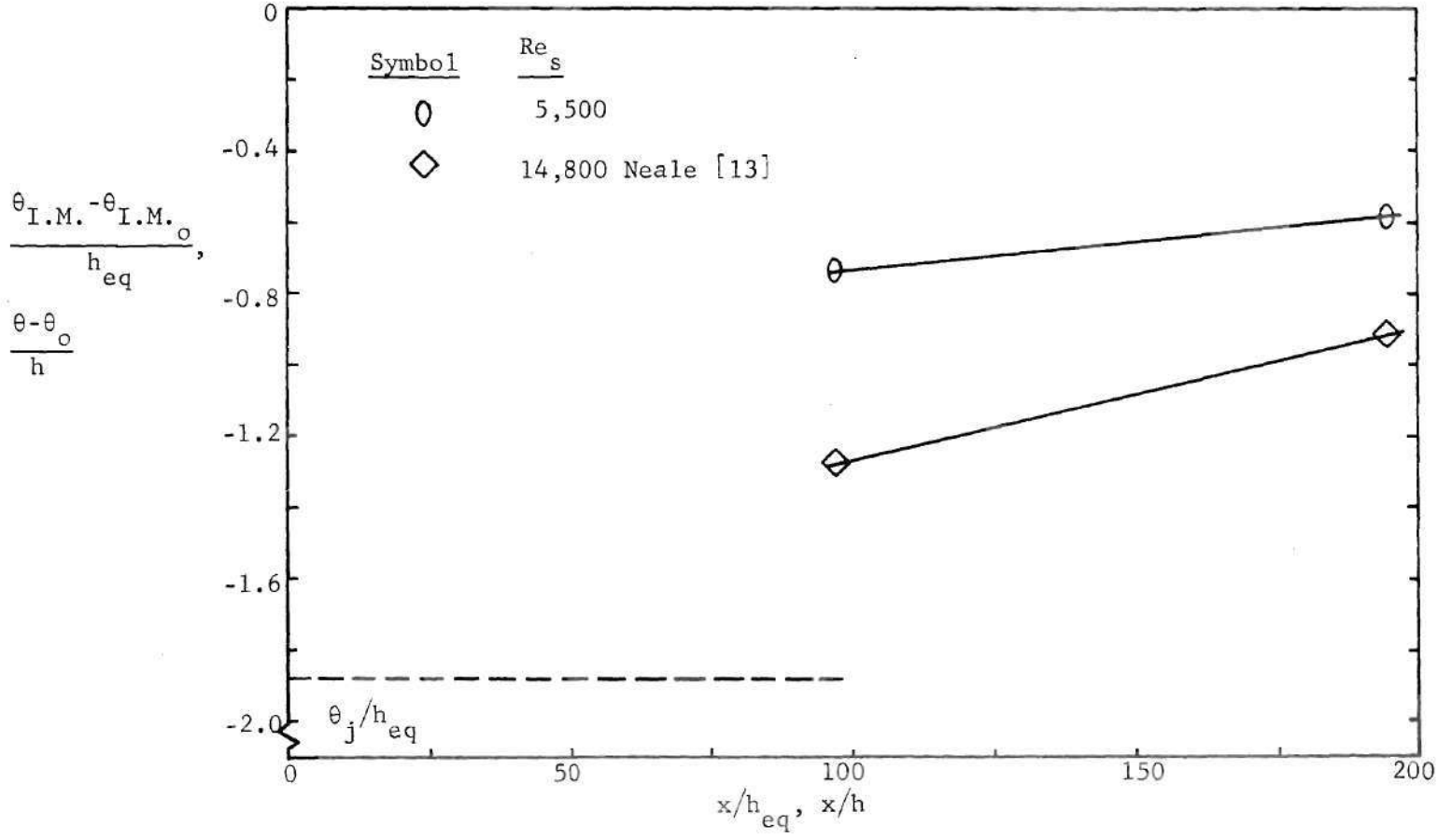

Figure 82. Wall Jet Momentum Thickness

Phase 3

$u_j/u_{e_o} = 2.0$

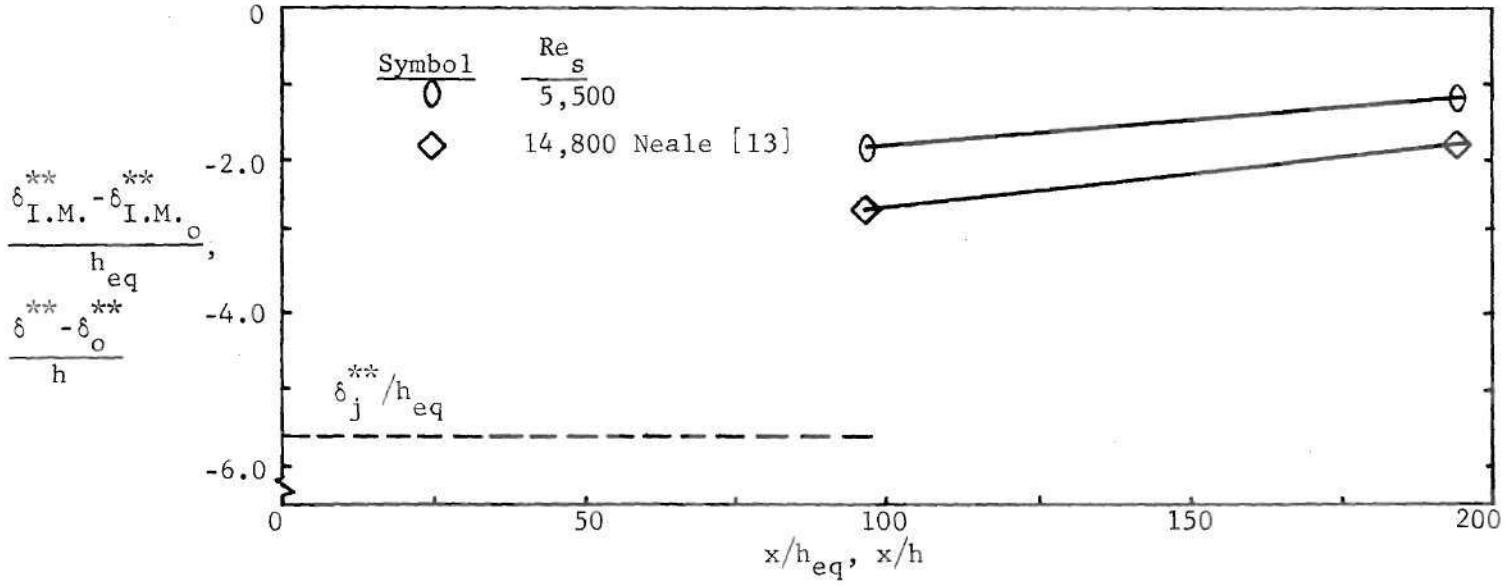

Figure 83. Wall Jet Energy Thickness

Phase 3

$u_j/u_{e_o} = 2.0$

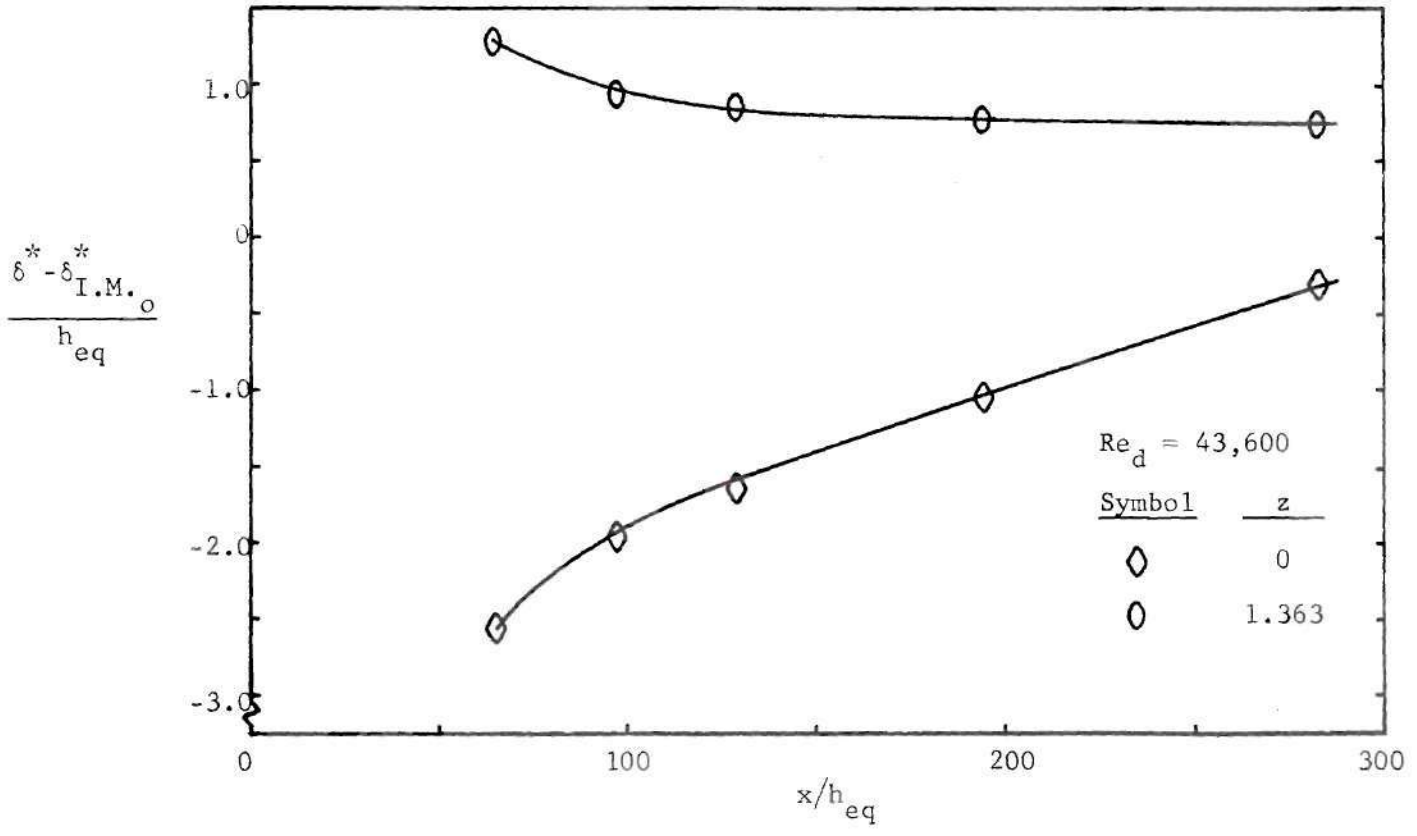

Figure 84. Wall Jet Displacement Thickness

Phase 3

$u_j/u_{e_o} = 2.0$

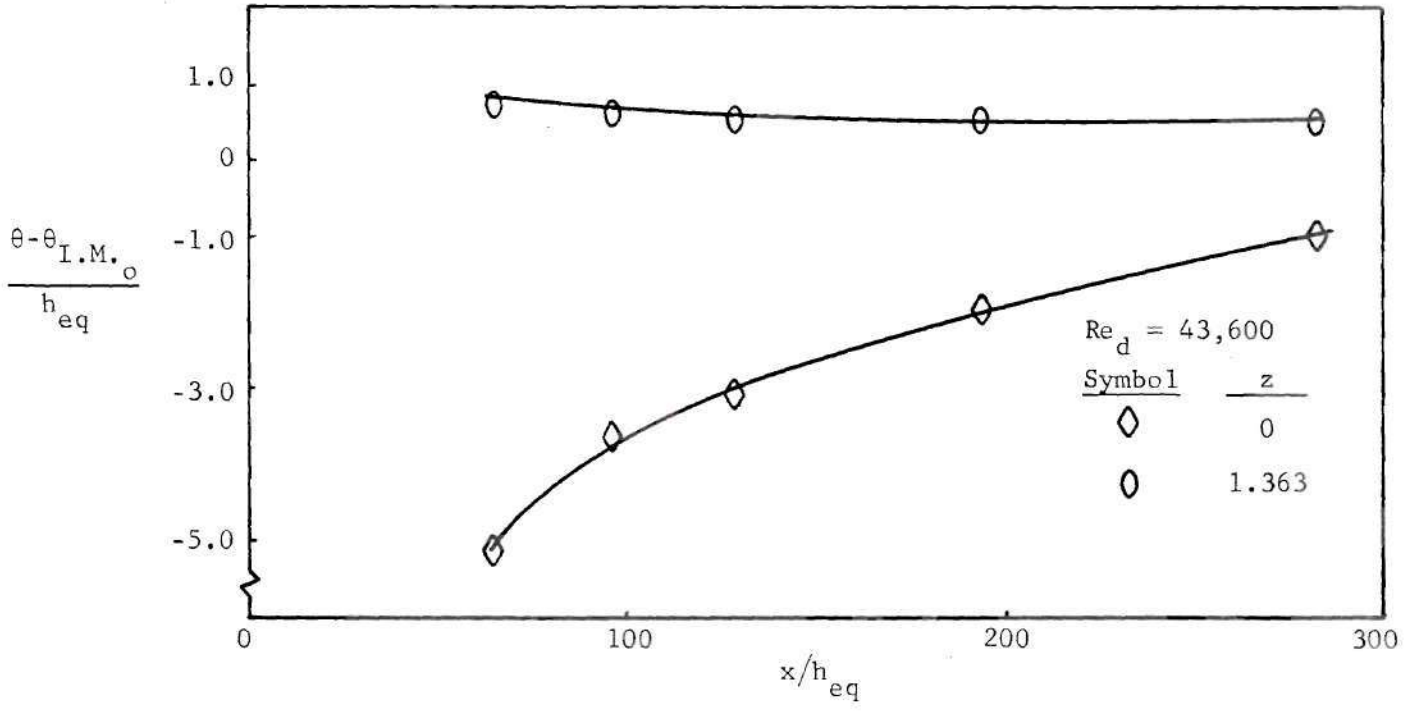

Figure 85. Wall Jet Momentum Thickness

Phase 3

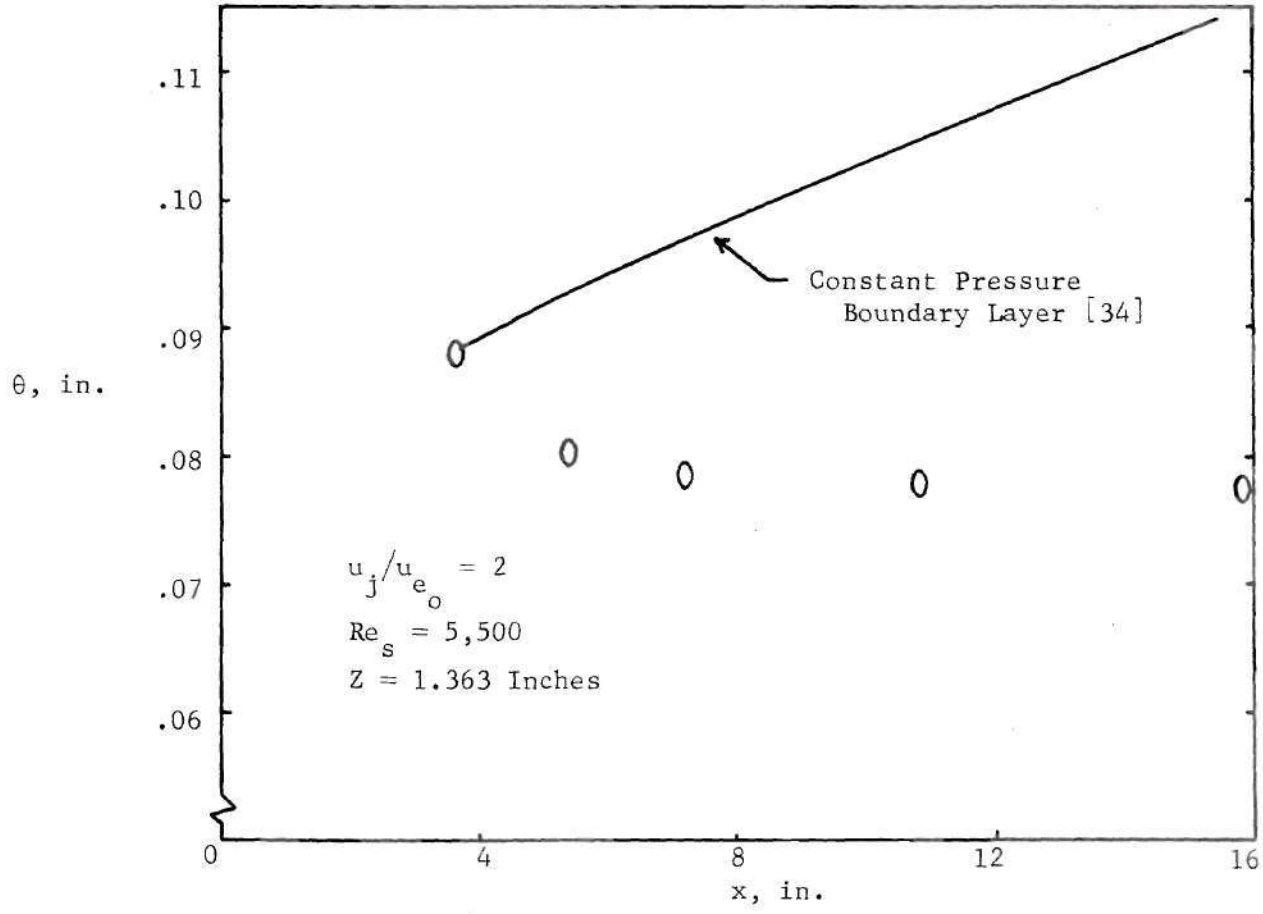

Figure 86. Wall Jet Momentum Thickness

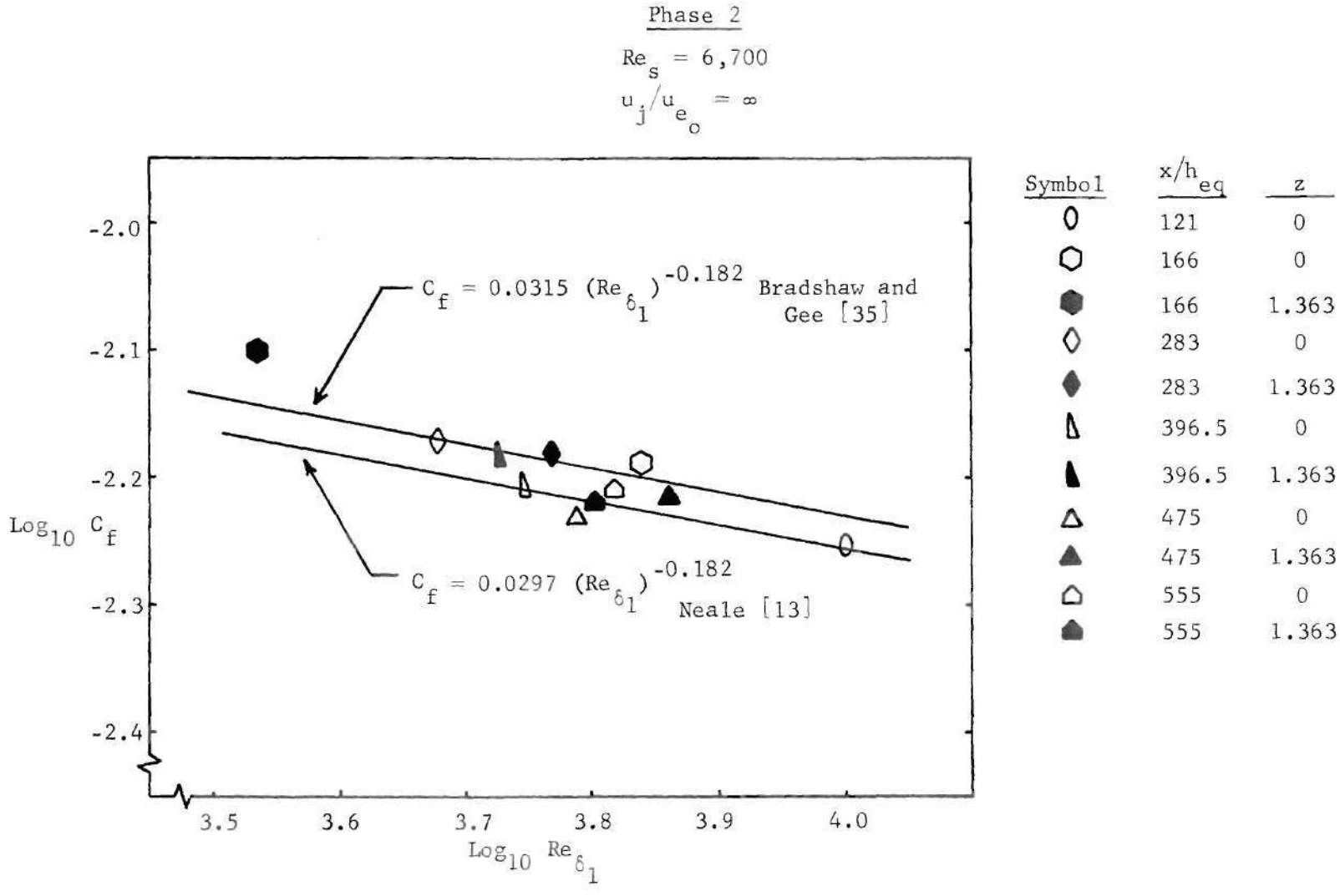

Figure 87. Wall Jet Skin Friction

Phase 3

$Re_s = 5{,}500$ $u_j/u_{e_o} = 2.0$

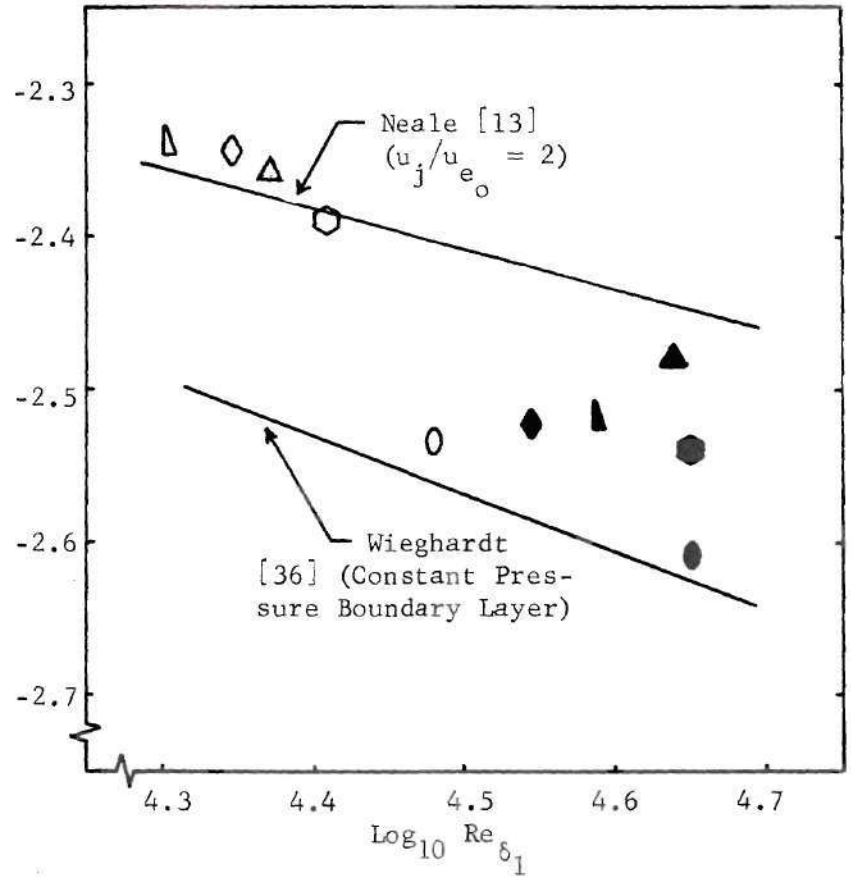

Symbol	x/h_{eq}	z
○	65	0
●	65	1.363
⬡	97	0
⬢	97	1.363
◇	129	0
◆	129	1.363
◺	194	0
◭	194	1.363
△	283	0
▲	283	1.363

Figure 88. Wall Jet Skin Friction

Phase 3

$Re_s = 5{,}500$ $\quad u_j/u_{e_o} = 2.0$

$Z = 1.363$

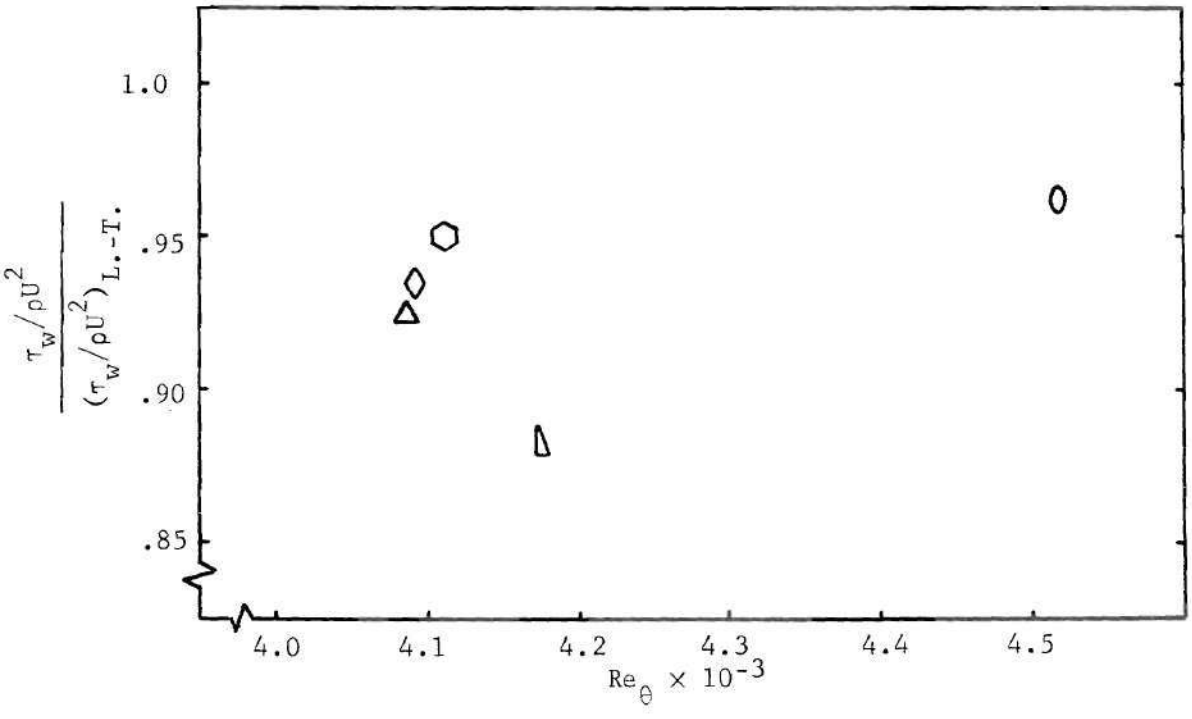

Symbol	x/h_{eq}	H
○	65	1.48
⬡	97	1.39
◇	129	1.35
◺	194	1.3
△	283	1.28

The results are normalized by the Ludwieg and Tillman result:

$$\frac{\tau_w}{\rho U^2} = 0.123 \times 10^{-.678H} \times Re_\theta^{-.268} \quad [34]$$

Figure 89. Wall Jet Skin Friction

Phase 2

$Re_s = 6,700$

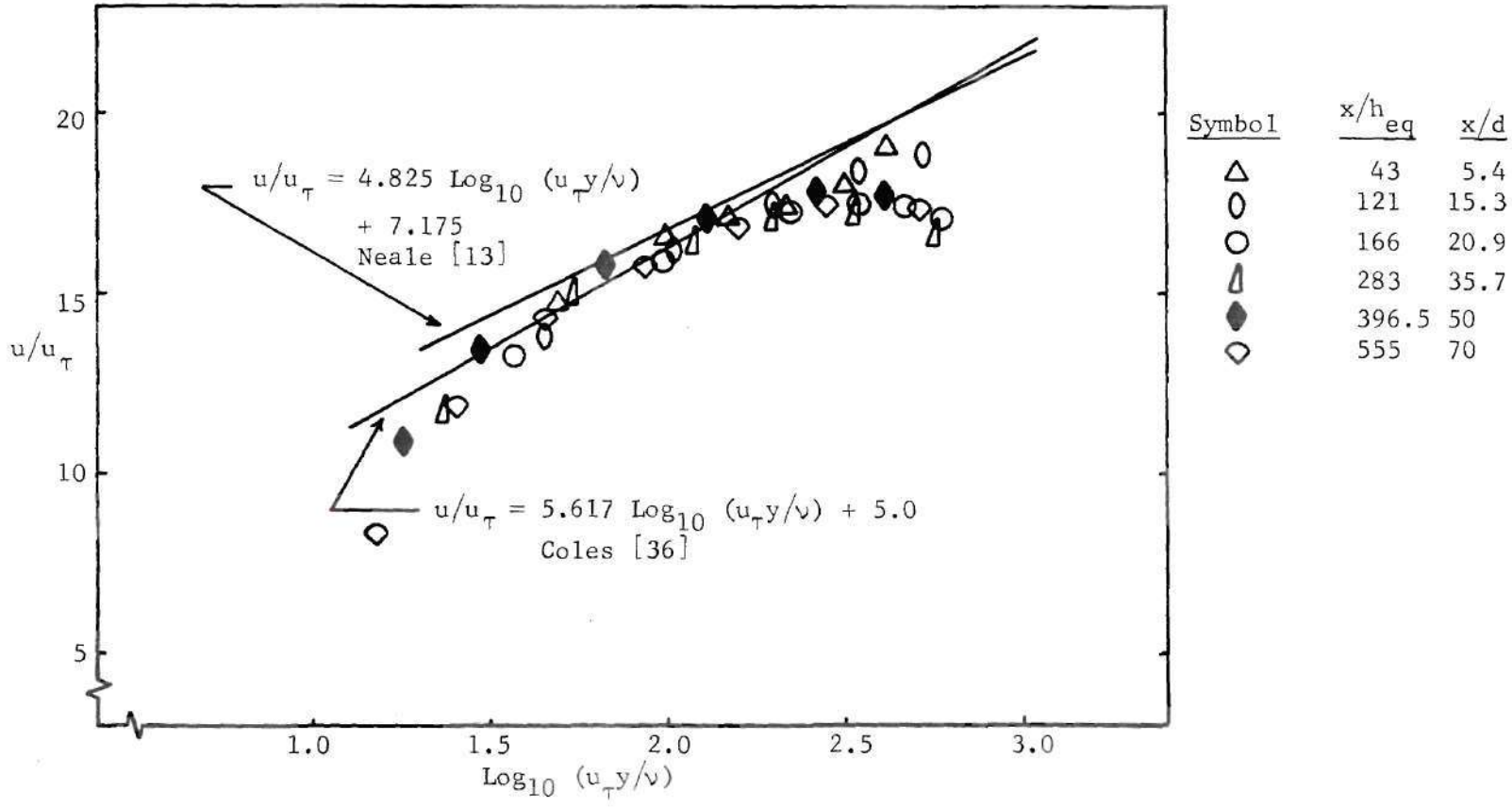

Figure 90. Law of the Wall

Phase 2

$Re_s = 6,700$

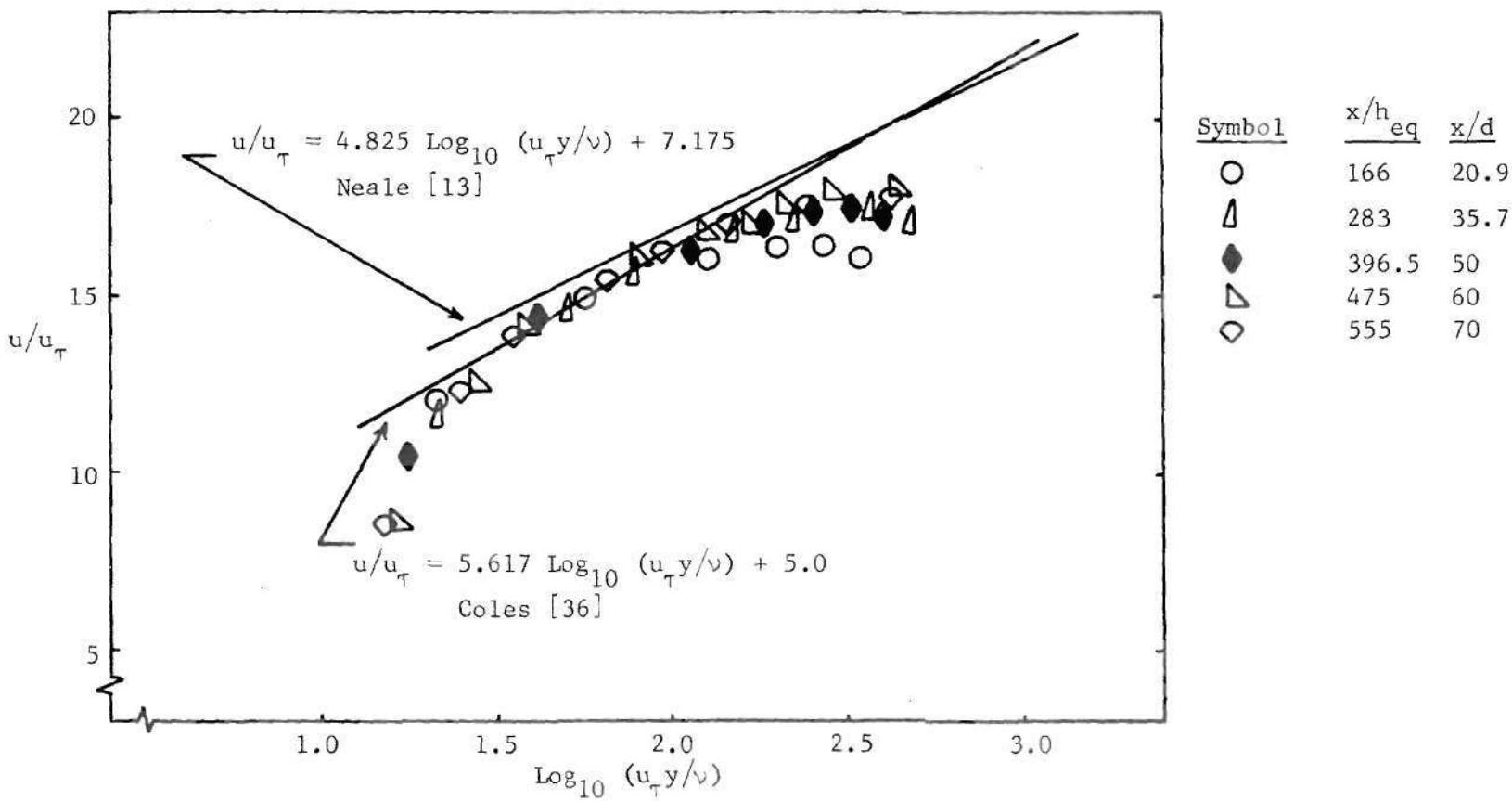

Figure 91. Law of the Wall

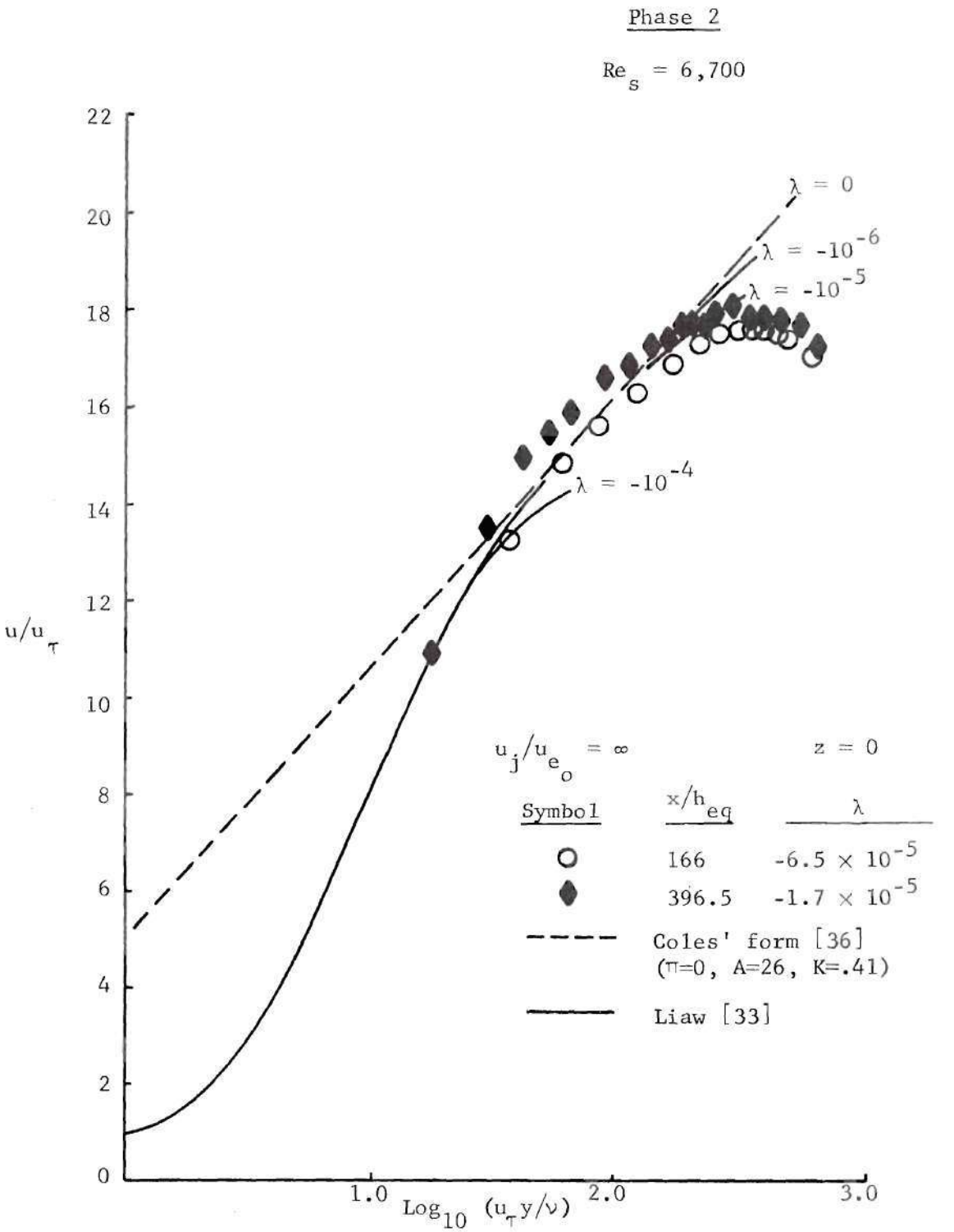

Figure 92. Wall Sublayer Velocity Profile

Phase 3

$u_j/u_{e_o} = 2$

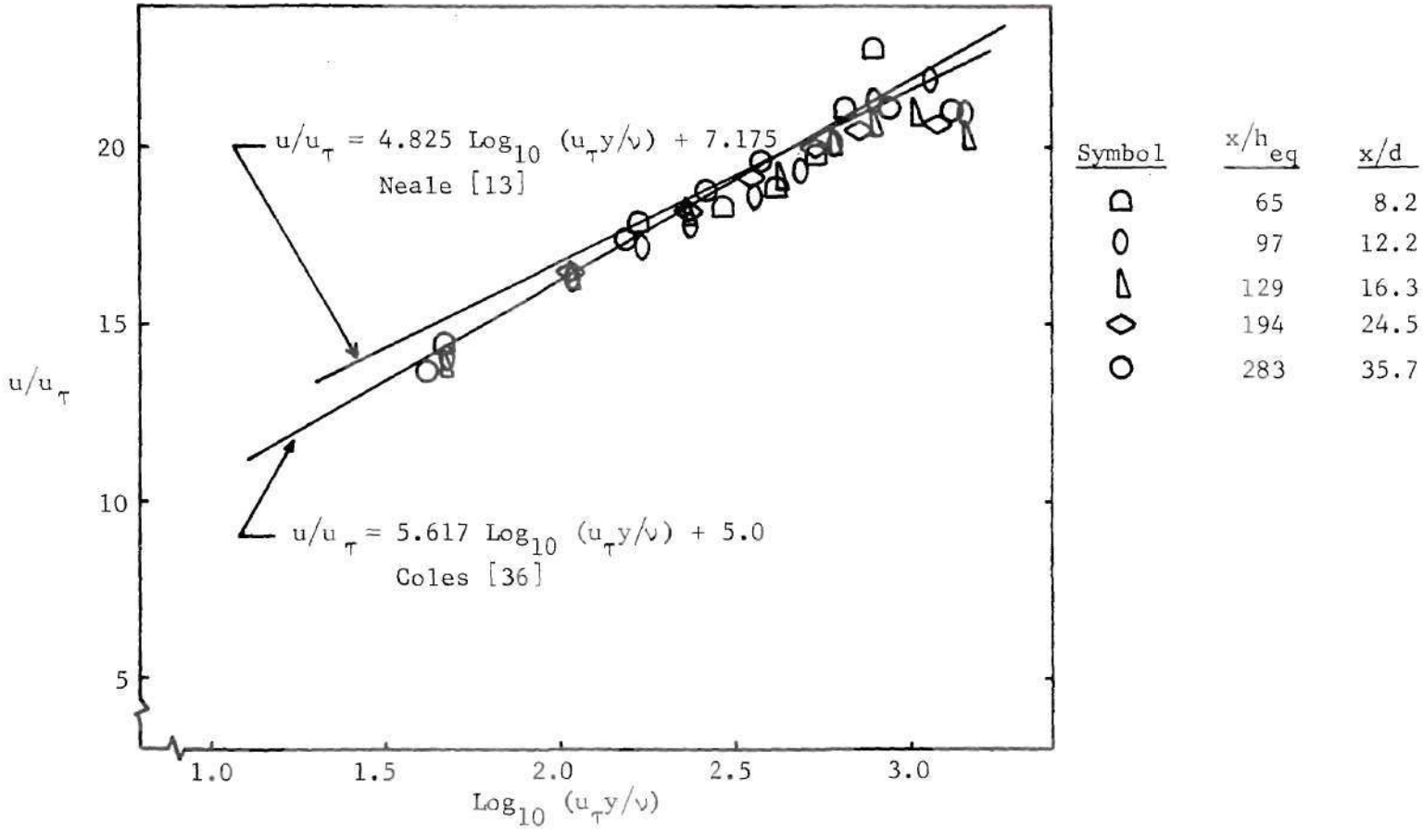

Symbol	x/h_{eq}	x/d
	65	8.2
	97	12.2
	129	16.3
	194	24.5
	283	35.7

Figure 93. Law of the Wall

Phase 3

$u_j/u_{e_o} = 2$

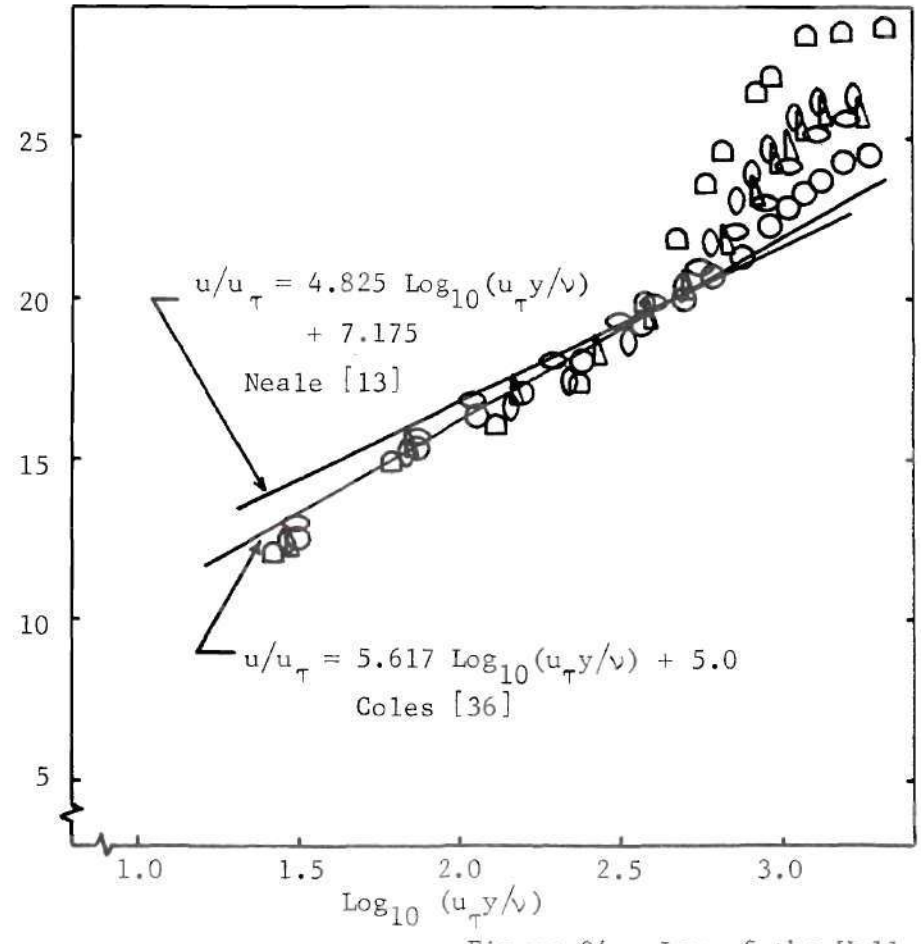

$z = 1.363$

Symbol	x/h_{eq}	$\lambda \times 10^6$	π
	65	1.80	1.14
	97	1.67	.79
	129	1.62	.66
	194	1.60	.55
	283	1.55	.22

Figure 94. Law of the Wall

CHAPTER V

CONCLUSIONS

An analysis of the data collected in this experimental program has led to the following major conclusions concerning wall jets produced from multiple, circular nozzles:

1. For a jet-to-freestream velocity ratio of infinity, there are two well-defined regions of linear growth in the half-velocity height, δ_2. Rapid lateral spreading of the individual streams, leading to jet merger, occurs in the initial region of linear δ_2 growth. This region of growth is strongly dependent upon the jet Reynolds number. A doubling of the Reynolds number results in approximately a 50% decrease in the growth rate. Two-dimensional wall jet behavior occurs in the final region of linear δ_2 growth. This 2-D flow is exhibited after approximately seven nozzle spacings downstream of the jet exit plane.
2. The growth rate in δ_2 is strongly dependent upon the jet-to-freestream velocity ratio. For a velocity ratio of two lateral spreading is small, and the growth rate is comparable with that for axisymmetric free jets.
3. The decay in the maximum velocity for the basic (geometrically simple) and integrated (incorporating aerodynamic fair-

ings between nozzles) multiple orifice configurations at a velocity ratio of infinity are comparable. In the initial region, which is dominated by lateral spreading, the decay rates agree well with those for a single circular orifice wall jet. Further downstream in the regions where the jets have merged, the decay rate decreases significantly.

4. The centerline velocity decay is a weak function of the jet Reynolds number, but has a strong dependence on the jet-to-freestream velocity ratio. For a velocity ratio of two the decay rate is small due to the low rate of spreading of the jet into the coflowing stream.
5. The velocity profiles normal to the surface exhibit similarity and the similarity forms are in excellent agreement with those for 2-D wall jets. Furthermore, velocity profile similarity exists along lines parallel to the surface. These similar profiles compare well with analytical forms proposed in the literature.
6. This investigation has shown that plots of constant velocity contours provide a qualitative means for visualizing and interpreting the 3-D flow development. By contrast, calculation of area integrals of the velocity profile data yields a quantitative measure of the averaged flow characteristics.
7. The momentum integral at $x/d = 35.7$ for a jet-to-freestream velocity ratio of two indicates that excess momentum is available for BLC for a thin mainstream boundary layer. These

limited results also reveal that the mean displacement, momentum and energy thicknesses increase more slowly with downstream location for the 3-D wall jet than for a comparable 2-D configuration.

8. The wall friction coefficients for the 3-D wall jet at a jet-to-freestream velocity ratio of infinity agree well with 2-D wall jet results. For a velocity ratio of two the friction coefficients are comparable with 2-D turbulent boundary layer results in the initial potential core region. In the wall jet development region downstream of the potential core, the friction coefficients are comparable with 2-D wall jet results.

9. The wall layer velocity profiles for the 3-D wall jet have a linear logarithmic region which matches Coles' empirical "law of the wall."

CHAPTER VI

RECOMMENDATIONS

The results presented herein for wall jets produced from multiple nozzles are sufficiently promising to warrant additional studies. The following specific areas of investigation are recommended.

1. Further testing should be conducted to evaluate and interpret the significant changes in vertical and horizontal growth rates that result from changes in the jet Reynolds number.
2. Tests should be conducted to determine the effect of the nozzle diameter-to-spacing ratio on the decay and merging of the individual plumes.
3. In this research the selection of jet-to-freestream velocity ratios of infinity and two was based on providing information at practical limits of BLC applications. Additional testing at intermediate velocity ratios is needed to aid in optimization of this wall jet scheme for BLC installations.
4. Tests with various streamwise pressure gradients are needed to fully evaluate the potential of the 3-D wall jets for BLC.
5. In this research significant flow losses were experienced due to the ramps between the nozzles. Additional development and optimization of the nozzle integration are needed.
6. Other non-circular jet nozzles should be tested to determine if the jet geometry can be used to advantage in controlling

the spreading and decay rates. Rectangular jets of varying height-to-width ratios are of primary interest.

APPENDIX A

PHASE 1 EXPERIMENTAL DATA

Phase 1 Data Summary

Initial Velocity Ratio = ∞

d = 0.444 Inch

h_{eq} = 0.056 Inch

x/d	x/h_{eq}	z in.	Re_d	u_j ft/sec	T_j °F	u_1 ft/sec	Velocity Profile Index
5.42	42.96	0	53,400	300.42	144.8	268.31	195
8.69	68.91	0	53,400	300.42	144.8	212.06	196
15.27	121.09	0	53,400	300.42	144.8	132.35	197
24.98	198.09	0	53,400	300.42	144.8	83.86	198
35.68	282.91	0	53,400	300.42	144.8	59.66	199
5.42	42.96	0	106,800	600.54	168.9	538.70	200
8.69	68.91	0	106,800	600.54	168.9	444.35	201
15.27	121.09	0	106,800	600.54	168.9	289.28	202
24.98	198.09	0	106,800	600.54	168.9	179.01	203
35.68	282.91	0	106,800	600.54	168.9	124.05	204

Velocity Profile

$u_j/u_{e_o} = \infty$

z = 0 Inches

Re_d = 53,400 x/d = 5.42

Y, in.	u/u_1	T, °F	Y, in.	u/u_1	T, °F
.004	.278	106.9	.194	.789	126.3
.009	.351	109.7	.214	.846	128.3
.014	.378	110.4	.234	.898	130.7
.019	.396	110.3	.254	.938	132.4
.024	.406	111.6	.274	.971	134.7
.029	.412	111.9	.294	.991	136.3
.034	.419	112.4	.314	1.000	136.9
.039	.426	112.3	.334	.999	136.3
.044	.435	112.9	.354	.992	134.9
.049	.439	113.5	.374	.982	132.8
.054	.447	113.6	.414	.937	127.1
.064	.464	114.6	.454	.859	120.6
.074	.480	115.4	.494	.750	114.1
.084	.495	116.5	.534	.625	107.9
.094	.516	116.9	.574	.506	102.3
.104	.539	117.9	.614	.394	96.3
.114	.560	119.1	.654	.299	91.7
.124	.588	119.7	.694	.209	87.7
.134	.612	120.7	.734	.130	82.7
.144	.642	121.6			
.154	.669	122.7			
.174	.729	124.5			

Velocity Profile

$u_j/u_{e_o} = \infty$

z = 0 Inches

Re_d = 53,400 x/d = 8.69

Y, in.	u/u_1	T, °F	Y, in.	u/u_1	T, °F
.004	.413	106.7	.214	.914	118.
.009	.529	109.5	.234	.938	118.4
.014	.564	110.3	.254	.963	118.
.019	.584	110.6	.274	.981	118.3
.024	.598	110.5	.294	.994	118.4
.029	.611	111.1	.314	1.000	117.5
.034	.621	110.5	.334	.987	115.8
.039	.629	111.1	.354	.983	115.5
.044	.636	112.1	.374	.967	114.3
.049	.646	111.5	.394	.947	113.7
.054	.654	111.0	.414	.923	112.2
.064	.666	112.7	.434	.888	110.9
.074	.681	112.6	.454	.855	108.9
.084	.695	113.3	.474	.819	107.7
.094	.712	113.3	.514	.738	103.9
.104	.725	114.1	.554	.656	101.2
.114	.744	114.6	.594	.578	97.9
.124	.762	115.2	.634	.496	94.2
.134	.777	115.3	.674	.413	91.0
.144	.794	115.5	.714	.351	87.4
.154	.813	115.6	.754	.282	85.3
.174	.847	117.1	.794	.221	82.2
.194	.88	117.3	.834	.165	79.7

Velocity Profile

$u_j/u_{e_o} = \infty$

z = 0 Inches

Re_d = 53,400 x/d = 15.27

Y, in.	u/u_1	T, °F	Y, in.	u/u_1	T, °F
.004	.519	97.1	.274	.997	99.7
.009	.698	98.7	.294	.991	99.3
.014	.749	98.9	.314	.980	98.3
.019	.783	99.0	.334	.973	98.3
.024	.795	99.3	.354	.962	98.1
.029	.817	99.7	.374	.948	97.8
.034	.827	99.8	.394	.931	97.1
.039	.846	99.9	.414	.914	96.4
.044	.854	99.8	.434	.890	95.9
.049	.864	99.9	.454	.885	95.3
.054	.872	100.3	.474	.858	94.7
.064	.892	101.1	.514	.820	93.8
.074	.903	99.8	.554	.778	92.4
.084	.914	100.0	.594	.728	90.9
.094	.927	100.5	.634	.673	89.4
.104	.928	100.3	.674	.619	88.2
.114	.946	101.0	.714	.567	86.5
.124	.953	100.7	.754	.513	85.1
.134	.960	100.1	.794	.471	84.2
.144	.964	100.6	.834	.422	82.9
.154	.970	100.7	.874	.373	81.4
.174	.987	100.5	.914	.324	80.5
.194	.988	99.9	.954	.279	79.5
.214	.996	100.1	.994	.239	77.9
.234	1.000	99.5			
.254	.995	100.0			

Velocity Profile

$u_j/u_{e_o} = \infty$

z = 0 Inches

Re_d = 53,400 x/d = 24.98

Y, in.	u/u_1	T, °F	Y, in.	u/u_1	T, °F
.004	.514	89.1	.274	.977	88.7
.007	.629	90.1	.294	.976	88.5
.014	.792	89.7	.314	.956	88.2
.019	.825	90.0	.334	.944	88.0
.024	.854	89.8	.354	.941	88.1
.029	.870	89.8	.394	.900	86.9
.034	.882	89.8	.434	.875	86.8
.039	.897	89.6	.474	.851	86.4
.044	.904	89.7	.514	.825	86.0
.049	.910	89.5	.554	.789	85.5
.054	.917	89.5	.594	.761	84.7
.064	.931	89.8	.634	.731	84.3
.074	.955	89.8	.674	.693	83.7
.084	.954	89.6	.714	.670	83.4
.094	.971	89.9	.754	.627	83.0
.104	.972	89.5	.794	.605	82.3
.114	.981	89.6	.834	.573	81.8
.124	.987	89.8	.874	.540	81.2
.134	.988	89.8	.914	.505	80.7
.144	.991	89.3	.954	.466	79.9
.154	.991	89.7	.994	.456	79.6
.174	.994	89.5	1.034	.423	79.2
.194	1.000	89.5	1.074	.400	78.5
.214	.998	89.1	1.114	.372	78.3
.234	.993	89.2	1.154	.339	77.9
.254	.986	88.6	1.194	.324	77.3
			1.234	.305	76.8

Velocity Profile

$u_j/u_{e_o} = \infty$

z = 0 Inches

Re_d = 53,400 x/d = 35.68

Y, in.	u/u_1	T, °F	Y, in.	u/u_1	T, °F
.004	.453	86.4	.354	.957	84.9
.009	.653	86.2	.404	.935	84.8
.014	.749	86.2	.454	.905	84.1
.019	.808	86.0	.504	.896	84.5
.024	.835	86.3	.554	.873	84.7
.029	.854	86.1	.604	.841	85.4
.034	.869	86.3	.654	.815	85.7
.039	.893	86.2	.704	.793	85.7
.044	.900	86.2	.754	.744	85.2
.049	.912	86.1	.804	.731	84.6
.054	.913	86.2	.854	.701	83.8
.064	.938	86.0	.904	.664	83.2
.074	.942	85.8	.954	.641	82.7
.084	.951	86.1	1.004	.621	82.3
.094	.965	85.7	1.054	.593	81.7
.104	.967	86.1	1.104	.562	81.4
.114	.984	85.9	1.154	.542	81.1
.124	.978	85.8	1.204	.505	80.7
.134	.973	85.9	1.254	.488	80.3
.144	.984	86.1	1.304	.459	80.2
.154	.991	85.9	1.354	.439	79.8
.174	.989	85.8	1.404	.397	79.2
.194	.990	85.8	1.454	.373	78.8
.214	1.000	85.7	1.504	.345	78.7
.234	.985	85.5	1.554	.324	78.4
.254	.983	85.4	1.604	.311	78.1
.274	.977	85.3	1.654	.275	77.9
.294	.972	85.4	1.704	.245	77.6
.314	.964	85.3	1.754	.245	77.3
.334	.963	85.0	1.804	.178	76.9

Velocity Profile

$u_j/u_{e_o} = \infty$

z = 0 Inches

Re_d = 106,800 x/d = 5.42

Y, in.	u/u_1	T, °F	Y, in.	u/u_1	T, °F
.004	.360	123.8	.174	.818	146.1
.009	.431	126.1	.194	.869	148.4
.014	.452	126.9	.214	.916	151.3
.019	.467	127.3	.234	.954	153.6
.024	.477	128.1	.254	.982	155.2
.029	.486	128.6	.274	.996	156.0
.034	.494	128.7	.294	1.000	156.9
.039	.502	129.3	.314	.996	155.5
.044	.509	129.7	.334	.987	154.1
.049	.519	130.2	.354	.971	150.4
.054	.526	130.9	.374	.950	147.6
.064	.543	131.9	.414	.868	139.0
.074	.562	133.2	.454	.761	130.6
.084	.581	134.5	.494	.633	122.3
.094	.606	135.5	.534	.502	114.9
.104	.629	136.5	.574	.394	108.0
.114	.657	137.8	.614	.296	100.8
.124	.681	139.2	.654	.213	95.0
.134	.709	140.8	.694	.130	89.4
.154	.764	143.1	.734	.063	85.4

Velocity Profile

$u_j/u_{e_o} = \infty$

z = 0 Inches

Re_d = 106,800 x/d = 8.69

Y, in.	u/u_1	T, °F	Y, in.	u/u_1	T, °F
.004	.486	124.5	.254	.999	138.9
.009	.550	126.7	.274	1.000	137.6
.014	.604	127.4	.294	.997	137.2
.019	.628	127.9	.314	.981	135.3
.024	.642	128.2	.334	.961	134.3
.029	.654	128.8	.354	.932	132.0
.034	.666	129.0	.374	.897	130.5
.039	.672	129.5	.394	.862	127.7
.044	.683	129.8	.414	.817	125.5
.049	.693	130.0	.434	.777	123.0
.054	.700	130.5	.454	.734	121.2
.064	.715	131.3	.474	.683	119.1
.074	.731	131.7	.514	.599	113.6
.084	.750	132.3	.554	.514	109.4
.094	.765	133.0	.594	.436	105.1
.104	.782	133.7	.634	.362	101.0
.114	.801	134.1	.674	.295	97.5
.124	.820	134.7	.714	.233	93.7
.134	.835	135.3	.754	.174	90.8
.154	.871	136.4	.794	.121	88.5
.174	.909	137.7	.834	.075	85.9
.194	.940	138.2			
.214	.967	138.7			
.234	.987	138.8			

Velocity Profile

$u_j/u_{e_o} = \infty$

z = 0 Inches

Re_d = 106,800 x/d = 15.27

Y, in.	u/u_1	T, °F	Y, in.	u/u_1	T, °F
.004	.617	114.0	.274	.970	114.2
.009	.741	115.1	.294	.956	113.7
.014	.782	115.7	.314	.937	112.5
.019	.809	115.9	.334	.923	112.0
.024	.828	116.0	.354	.902	111.2
.029	.843	116.2	.374	.879	110.4
.039	.870	116.6	.394	.852	109.7
.044	.880	116.7	.414	.829	108.5
.049	.890	116.8	.434	.805	107.7
.054	.900	117.0	.454	.782	106.9
.064	.918	117.2	.474	.752	106.1
.074	.931	117.3	.514	.701	104.5
.084	.942	117.4	.554	.645	102.0
.094	.953	117.5	.594	.596	100.2
.104	.962	117.4	.634	.538	98.5
.114	.971	117.7	.674	.481	97.3
.124	.976	117.3	.714	.438	95.3
.134	.982	117.5	.754	.381	93.1
.144	.987	117.4	.794	.337	92.2
.154	.991	117.2	.834	.294	90.3
.174	.998	116.6	.874	.251	89.3
.194	1.000	116.3	.914	.209	87.3
.214	.995	115.9	.954	.168	86.0
.234	.992	115.2	.994	.127	85.1
.254	.983	114.7			

Velocity Profile

$u_j/u_{e_o} = \infty$

z = 0 Inches

Re_d = 106,800 x/d = 24.98

Y, in.	u/u_1	T, °F	Y, in.	u/u_1	T, °F
.004	.615	101.7	.274	.955	100.5
.009	.779	101.7	.294	.944	99.8
.014	.827	102.0	.314	.934	99.5
.019	.857	102.0	.334	.918	99.9
.024	.876	101.7	.354	.899	99.1
.029	.897	102.0	.394	.871	98.3
.034	.909	101.8	.434	.836	97.5
.039	.920	101.8	.474	.804	96.9
.044	.931	102.0	.514	.761	96.3
.049	.936	101.7	.554	.724	95.6
.054	.949	102.1	.594	.689	95.1
.064	.961	102.0	.634	.651	94.2
.074	.971	102.1	.674	.611	93.2
.084	.981	102.0	.714	.577	92.7
.104	.988	101.9	.754	.545	92.2
.154	1.000	101.6	.794	.514	91.6
.174	.996	101.4	.834	.476	90.9
.194	.993	101.3	.874	.445	90.3
.214	.984	101.0	.914	.417	89.0
.234	.982	100.5	.954	.385	88.3
.254	.967	100.7	.994	.350	87.4
			1.034	.319	87.7
			1.074	.297	86.6
			1.114	.264	85.4
			1.154	.243	84.8
			1.194	.214	85.0
			1.234	.183	85.1

Velocity Profile

$u_j/u_{e_o} = \infty$

z = 0 Inches

Re_d = 106,800 x/d = 35.68

Y, in.	u/u_1	T, °F	Y, in.	u/u_1	T, °F
.004	.568	91.6	.394	.921	90.1
.009	.763	91.6	.434	.898	89.7
.014	.816	91.5	.474	.875	89.2
.019	.844	91.3	.514	.856	89.6
.024	.860	91.6	.554	.835	89.1
.029	.881	91.8	.594	.811	88.4
.034	.893	91.6	.634	.789	88.2
.039	.919	91.7	.674	.767	88.0
.044	.923	91.8	.714	.744	87.5
.049	.931	91.7	.754	.718	87.0
.054	.941	91.9	.794	.689	86.8
.064	.949	91.8	.834	.672	86.6
.074	.969	91.7	.874	.653	86.5
.084	.969	91.9	.914	.624	85.8
.094	.972	91.6	.954	.598	85.3
.104	.985	91.7	.994	.580	85.1
.114	.981	91.5	1.034	.559	84.7
.124	.996	91.5	1.074	.535	84.7
.134	.987	91.6	1.114	.505	84.1
.144	1.000	91.5	1.154	.487	83.7
.154	.990	91.8	1.194	.470	84.1
.174	.997	91.3	1.234	.453	83.5
.194	.991	91.2	1.274	.430	82.9
.214	.994	91.3	1.314	.401	82.7
.234	.984	91.1	1.354	.384	82.5
.254	.975	91.4	1.394	.361	81.7
.274	.975	90.7	1.434	.336	81.7
.294	.962	90.9	1.474	.320	81.5
.314	.955	90.8	1.514	.301	80.9
.334	.951	90.4	1.554	.285	80.7
.354	.934	89.9			

APPENDIX B

PHASE 2 EXPERIMENTAL DATA

Phase 2 Data Summary

Initial Velocity Ratio = ∞

d = 0.444 Inch

h_{eq} = 0.056 Inch

x/d	x/h_{eq}	z in.	Re_d	u_j ft/sec	T_j °F	u_l ft/sec	τ_w lb/ft^2	$C_f^* \times 10^3$	Velocity Profile Index
5.42	42.96	0	53,400	300.5	146.9	253.0	0.1219	1.862	210
15.27	121.09	0	53,400	300.5	146.9	125.5	0.0949	5.586	211
15.27	121.09	2.727	53,400	300.5	146.9	127.1	---	---	212
15.27	121.09	- 2.727	53,400	300.5	146.9	125.7	---	---	213
20.94	166.0	0	53,400	300.5	146.9	94.1	0.0621	6.489	214
20.94	166.0	- 0.062	53,400	300.5	146.9	94.5	---	---	215
20.94	166.0	0.125	53,400	300.5	146.9	91.0	---	---	216
20.94	166.0	- 0.125	53,400	300.5	146.9	94.6	---	---	217
20.94	166.0	0.250	53,400	300.5	146.9	87.5	---	---	218
20.94	166.0	- 0.250	53,400	300.5	146.9	93.2	---	---	219

*Based on fluid properties at δ_1.

Phase 2 Data Summary

Initial Velocity Ratio = ∞

d = 0.444 Inch

h_{eq} = 0.056 Inch

x/d	x/h_{eq}	z in.	Re_d	u_j ft/sec	T_j °F	u_1 ft/sec	τ_w lb/ft^2	C_f^* x 10^3	Velocity Profile Index
20.94	166.0	0.500	53,400	300.5	146.9	76.0	---	---	220
20.94	166.0	- 0.500	53,400	300.5	146.9	85.2	---	---	221
20.94	166.0	0.750	53,400	300.5	146.9	64.7	---	---	222
20.94	166.0	- 0.750	53,400	300.5	146.9	73.0	---	---	223
20.94	166.0	1.000	53,400	300.5	146.9	56.0	---	---	224
20.94	166.0	- 1.000	53,400	300.5	146.9	62.6	---	---	225
20.94	166.0	1.363	53,400	300.5	146.9	51.2	0.0210	7.919	226
20.94	166.0	- 1.363	53,400	300.5	146.9	50.6	---	---	227
29.98	237.7	0	53,400	300.5	146.9	65.7	---	---	228

*Based on fluid properties at δ_1.

Phase 2 Data Summary

Initial Velocity Ratio = ∞

d = 0.444 Inch

h_{eq} = 0.056 Inch

x/d	x/h_{eq}	z in.	Re_d	u_j ft/sec	T_j °F	u_1 ft/sec	τ_w lb/ft^2	$C_f^* \times 10^3$	Velocity Profile Index
35.68	282.9	0	53,400	300.5	146.9	57.5	0.0244	6.732	229
35.68	282.9	1.363	53,400	300.5	146.9	53.4	0.0205	6.607	230
35.68	282.9	- 1.363	53,400	300.5	146.9	53.5	---	---	231
40.01	317.2	0	53,400	300.5	146.9	52.8	---	---	232
50.01	396.5	0	53,400	300.5	146.9	46.6	0.0147	6.205	233
50.01	396.5	- 0.062	53,400	300.5	146.9	45.8	---	---	234
50.01	396.5	0.125	53,400	300.5	146.9	45.9	---	---	235
50.01	396.5	- 0.125	53,400	300.5	146.9	46.1	---	---	236
50.01	396.5	0.500	53,400	300.5	146.9	46.0	---	---	237
50.01	396.5	- 0.500	53,400	300.5	146.9	45.9	---	---	238

*Based on fluid properties at δ_1.

Phase 2 Data Summary

Initial Velocity Ratio = ∞

d = 0.444 Inch

h_{eq} = 0.056 Inch

x/d	x/h_{eq}	z in.	Re_d	u_j ft/sec	T_j °F	u_1 ft/sec	τ_w lb/ft^2	$C_f^* \times 10^3$	Velocity Profile Index
50.01	396.5	1.363	53,400	300.5	146.9	45.7	0.0147	6.561	239
50.01	396.5	- 1.363	53,400	300.5	146.9	46.3	---	---	240
50.01	396.5	2.727	53,400	300.5	146.9	46.0	---	---	241
50.01	396.5	- 2.727	53,400	300.5	146.9	46.5	---	---	242
60.0	475.7	0	53,400	300.5	146.9	42.8	0.0118	5.876	243
60.0	475.7	1.363	53,400	300.5	146.9	42.3	0.0119	6.092	244
60.0	475.7	- 1.363	53,400	300.5	146.9	42.3	---	---	245
70.0	555	0	53,400	300.5	146.9	39.5	0.0104	6.171	246
70.0	555	1.363	53,400	300.5	146.9	38.6	0.0101	6.031	247
70.0	555	- 1.363	53,400	300.5	146.9	39.0	---	---	248

* Based on fluid properties at δ_1.

Velocity Profile

$u_j/u_{e_o} = \infty$

z = 0 Inches

Re_d = 53,400 x/d = 5.42

Y, in.	u/u_1	T, °F	Y, in.	u/u_1	T, °F
.015	.444	109.	.175	.673	119.7
.020	.471	110.9	.195	.725	121.1
.025	.489	111.0	.215	.785	122.5
.030	.498	111.6	.235	.843	123.9
.035	.508	111.7	.255	.899	125.2
.040	.510	112.3	.275	.943	126.1
.045	.512	112.5	.295	.975	126.3
.050	.516	113.0	.315	.994	125.9
.055	.521	113.7	.335	1.000	125.2
.065	.523	114.3	.355	.987	123.2
.075	.531	114.8	.375	.963	120.9
.085	.535	115.2	.415	.881	115.0
.095	.541	115.8	.455	.773	110.0
.105	.549	116.1	.495	.654	105.8
.115	.562	116.9	.535	.534	100.5
.125	.573	117.0	.575	.426	96.1
.135	.590	117.5	.615	.323	91.5
.145	.606	118.2	.655	.235	86.3
.155	.626	118.6	.695	.157	82.6

Velocity Profile

$u_j/u_{e_o} = \infty$

z = 0 Inches

Re_d = 53,400 x/d = 15.27

Y, in.	u/u_1	T, °F	Y, in.	u/u_1	T, °F
.015	.730	96.3	.275	.960	96.9
.020	.782	97.4	.295	.953	96.6
.025	.812	97.2	.315	.935	95.9
.030	.836	97.3	.335	.907	95.3
.035	.858	97.4	.355	.888	94.6
.040	.873	97.3	.375	.869	94.1
.045	.886	97.2	.395	.849	93.3
.050	.897	97.1	.415	.830	92.6
.055	.904	96.9	.435	.807	91.7
.065	.923	97.1	.455	.773	91.
.075	.936	97.1	.475	.754	90.3
.085	.949	97.1	.515	.715	89.3
.095	.959	97.	.555	.664	88.0
.105	.967	97.	.595	.617	86.7
.115	.973	97.1	.635	.565	85.8
.125	.979	97.3	.675	.521	84.6
.135	.987	97.4	.715	.468	83.6
.145	.993	97.4	.755	.421	82.7
.155	.993	97.7	.795	.384	81.8
.175	1.000	97.5	.835	.336	81.2
.195	.997	97.5	.875	.284	80.2
.215	.989	97.7	.915	.250	79.8
.235	.990	97.3	.955	.200	79.0
.255	.979	97.1	.995	.160	78.2

Velocity Profile

$u_j/u_{e_o} = \infty$

z = 2.727 Inches

Re_d = 53,400 x/d = 15.27

Y, in.	u/u_1	T, °F	Y, in.	u/u_1	T, °F
.015	.750	97.4	.255	.975	99.0
.020	.781	99.7	.275	.959	98.6
.025	.814	100.1	.295	.945	98.1
.030	.835	100.3	.315	.930	98.0
.035	.856	100.3	.335	.911	97.4
.040	.878	100.6	.355	.896	97.0
.045	.886	100.5	.375	.867	96.6
.050	.895	100.7	.395	.850	95.9
.055	.912	100.6	.415	.831	95.4
.065	.926	100.6	.435	.803	95.0
.075	.941	100.8	.455	.785	94.7
.085	.953	100.9	.475	.756	94.1
.095	.963	100.9	.515	.705	93.3
.105	.970	100.7	.555	.666	91.9
.115	.978	100.7	.595	.607	91.0
.125	.985	100.7	.635	.561	89.6
.135	.989	100.6	.675	.503	88.8
.145	.991	100.6	.715	.464	87.6
.155	.994	100.5	.755	.410	86.6
.175	1.000	100.2	.795	.362	85.7
.195	.997	99.9	.835	.316	84.5
.215	.991	99.7	.875	.269	83.5
.235	.986	99.4			

Velocity Profile

$u_j/u_{e_o} = \infty$

z =-2.727 Inches

Re_d = 53,400 x/d = 15.27

Y, in.	u/u_1	T, °F	Y, in.	u/u_1	T, °F
.015	.740	100.3	.255	.979	103.3
.020	.778	101.1	.275	.962	102.4
.025	.808	101.4	.295	.944	101.8
.030	.833	101.4	.315	.932	101.1
.035	.850	101.7	.335	.912	100.3
.040	.873	101.8	.355	.896	100.0
.045	.882	101.6	.375	.875	98.9
.050	.893	101.7	.395	.856	98.6
.055	.903	102.3	.415	.832	97.7
.065	.921	101.9	.435	.814	97.1
.075	.934	102.0	.455	.789	96.7
.085	.946	102.2	.475	.765	95.9
.095	.956	102.1	.515	.717	94.9
.105	.966	102.2	.555	.669	93.9
.115	.974	102.2	.595	.615	92.6
.125	.977	101.8	.635	.567	91.4
.135	.981	101.9	.675	.516	90.2
.145	.994	102.2	.715	.461	89.0
.155	.995	102.4	.755	.419	87.9
.175	.997	103.1	.795	.371	87.1
.195	1.000	103.4	.835	.326	85.9
.215	.996	103.0	.875	.284	84.7
.235	.991	103.5			

Velocity Profile

$u_j/u_{e_o} = \infty$

z = 0 Inches

Re_d = 53,400 x/d = 20.94

Y, in.	u/u_1	T, °F	Y, in.	u/u_1	T, °F
.015	.755	90.3	.230	.986	89.6
.020	.809	90.6	.240	.975	89.7
.025	.844	90.8	.260	.965	89.2
.030	.875	90.8	.280	.954	89.1
.035	.887	90.9	.300	.938	88.8
.040	.905	90.8	.320	.915	88.6
.050	.926	90.7	.340	.898	88.3
.060	.947	91.0	.360	.888	88.1
.070	.958	90.7	.400	.852	87.8
.080	.972	90.6	.440	.816	87.0
.090	.983	90.6	.480	.772	86.1
.100	.985	90.5	.520	.719	85.5
.110	.993	90.7	.560	.689	85.2
.120	.994	90.5	.600	.653	84.5
.130	.999	90.5	.640	.613	84.0
.140	.999	90.5	.680	.584	83.2
.150	.999	90.4	.720	.533	82.7
.160	1.000	90.3	.760	.490	81.9
.170	.999	90.2	.800	.464	81.3
.180	.998	90.1	.840	.424	80.9
.190	.994	89.9	.880	.389	80.3
.200	.991	90.0	.920	.355	79.6
.210	.987	89.9	.960	.317	78.8
.220	.989	89.8	1.000	.284	78.4

Velocity Profile

$u_j/u_{e_o} = \infty$

$z = -0.062$ Inch

$Re_d = 53,400$ $x/d = 20.94$

Y, in.	u/u_1	T, °F	Y, in.	u/u_1	T, °F
.015	.759	93.0	.230	.983	92.1
.020	.803	93.2	.240	.973	92.1
.025	.841	93.3	.260	.965	91.5
.030	.865	93.4	.280	.948	91.4
.035	.878	93.3	.300	.941	91.1
.040	.899	93.3	.320	.916	90.9
.050	.924	93.5	.340	.907	90.7
.060	.940	93.4	.360	.888	90.5
.070	.954	93.2	.400	.857	90.1
.080	.969	93.4	.440	.815	89.1
.090	.979	93.4	.480	.772	88.7
.100	.982	93.2	.520	.735	87.7
.110	.989	93.3	.560	.693	87.2
.120	.993	93.3	.600	.660	86.9
.130	.990	93.1	.640	.616	86.2
.140	.991	93.0	.680	.576	85.7
.150	.997	93.0	.720	.535	84.9
.160	.998	93.1	.760	.497	84.2
.170	.994	92.9	.800	.469	83.7
.180	.998	92.7	.840	.422	82.8
.190	.995	92.6	.880	.395	82.4
.200	1.000	92.4	.920	.367	81.7
.210	.992	92.3	.960	.322	81.1
.220	.986	92.1	1.000	.285	80.5

Velocity Profile

$u_j/u_{e_o} = \infty$

z = 0.125 Inch

Re_d = 53,400 x/d = 20.94

Y, in.	u/u_1	T, °F	Y, in.	u/u_1	T, °F
.015	.754	91.3	.230	.967	90.6
.020	.810	91.7	.240	.958	90.5
.025	.842	91.5	.260	.945	90.2
.030	.870	91.8	.280	.934	90.0
.035	.891	91.6	.300	.920	89.7
.040	.900	91.5	.320	.898	89.5
.050	.923	91.6	.340	.886	89.2
.060	.940	91.6	.360	.873	88.7
.070	.961	91.9	.400	.833	88.3
.080	.957	91.5	.440	.783	87.8
.090	.975	91.5	.480	.752	86.9
.100	.980	91.6	.520	.702	86.3
.110	.984	91.5	.560	.669	85.7
.120	.986	91.6	.600	.629	85.1
.130	.982	91.2	.640	.600	84.4
.140	.988	91.4	.680	.553	83.9
.150	.986	91.3	.720	.520	83.2
.160	1.000	91.2	.760	.491	82.9
.170	.988	91.4	.800	.436	82.0
.180	.983	91.0	.840	.403	81.4
.190	.982	91.0	.880	.367	80.8
.200	.985	90.6	.920	.331	80.2
.210	.978	90.6	.960	.315	79.6
.220	.981	90.6	1.000	.267	79.1

Velocity Profile

$u_j/u_{e_o} = \infty$

z = - 0.125 Inch

Re_d = 53,400 x/d = 20.94

Y, in.	u/u_1	T, °F	Y, in.	u/u_1	T, °F
.015	.755	92.5	.230	.982	91.5
.020	.807	92.7	.240	.977	91.4
.025	.840	92.7	.260	.967	91.1
.030	.868	92.7	.280	.950	90.7
.035	.890	92.7	.300	.936	90.5
.040	.901	92.6	.320	.920	90.4
.050	.928	92.7	.340	.906	90.1
.060	.943	92.8	.360	.888	89.8
.070	.958	92.7	.400	.855	89.1
.080	.966	92.8	.440	.816	88.5
.090	.983	92.7	.480	.778	88.1
.100	.982	92.7	.520	.739	87.4
.110	.990	92.4	.560	.696	86.9
.120	.988	92.6	.600	.649	86.1
.130	.996	92.3	.640	.614	85.7
.140	1.000	92.2	.680	.577	84.9
.150	.997	92.3	.720	.535	84.3
.160	.999	92.2	.760	.499	83.4
.170	.994	92.3	.800	.463	82.8
.180	.999	92.0	.840	.432	82.3
.190	.995	92.0	.880	.401	81.8
.200	.990	91.9	.920	.351	81.3
.210	.992	91.5	.960	.317	80.6
.220	.987	91.6	1.000	.278	80.0

Velocity Profile

$u_j/u_{e_o} = \infty$

z = 0.250 Inch

Re_d = 53,400 x/d = 20.94

Y, in.	u/u_1	T, °F	Y, in.	u/u_1	T, °F
.015	.747	92.7	.220	.956	91.9
.020	.815	92.8	.230	.951	91.7
.025	.845	92.9	.240	.957	91.5
.030	.874	93.2	.260	.933	91.0
.035	.895	92.9	.280	.928	91.3
.040	.915	93.0	.300	.916	91.0
.050	.933	93.1	.320	.889	90.8
.060	.946	93.1	.360	.851	90.4
.070	.957	92.9	.400	.811	89.5
.080	.969	92.7	.440	.779	89.2
.090	.970	92.7	.480	.752	88.4
.100	.969	92.8	.520	.700	87.8
.110	.985	92.6	.560	.658	87.0
.120	.987	92.7	.600	.613	86.6
.130	.988	92.6	.640	.569	85.9
.140	.993	92.6	.680	.549	85.5
.150	1.000	92.8	.720	.493	84.7
.160	.993	92.4	.760	.462	84.1
.170	.984	92.4	.800	.419	83.6
.180	.976	92.0	.840	.392	82.9
.190	.971	91.9	.880	.362	82.4
.200	.961	92.3	.920	.330	81.7
.210	.963	92.2	.960	.290	81.3

Velocity Profile

$u_j/u_{e_o} = \infty$

z = - 0.250 Inch

Re_d = 53,400 x/d = 20.94

Y, in.	u/u_1	T, °F	Y, in.	u/u_1	T, °F
.015	.751	94.6	.210	.988	93.8
.020	.798	94.8	.220	.982	93.6
.025	.834	94.7	.230	.981	93.6
.030	.861	94.7	.240	.975	93.4
.035	.885	94.9	.260	.966	93.1
.040	.898	94.5	.280	.954	93.0
.050	.921	94.7	.300	.939	92.9
.060	.942	94.9	.320	.919	92.1
.070	.951	95.0	.360	.889	91.7
.080	.958	95.0	.400	.851	91.1
.090	.974	94.8	.440	.811	90.5
.100	.973	94.7	.480	.775	89.8
.110	.988	94.5	.520	.737	89.4
.120	.991	94.5	.560	.697	88.8
.130	.991	94.5	.600	.658	88.1
.140	.993	94.5	.640	.613	87.2
.150	.998	94.5	.680	.577	86.4
.160	.998	94.3	.720	.535	86.0
.170	.996	94.1	.760	.501	85.7
.180	.995	94.1	.800	.451	84.8
.190	1.000	94.1	.840	.427	84.0
.200	.982	93.8	.880	.394	83.5

Velocity Profile

$u_j/u_{e_o} = \infty$

z = 0.500 Inch

Re_d = 53,400 x/d = 20.94

Y, in.	u/u_1	T, °F	Y, in.	u/u_1	T, °F
.015	.772	92.9	.210	.960	91.9
.020	.820	93.0	.220	.952	91.5
.025	.865	92.8	.230	.948	91.4
.030	.896	92.9	.240	.923	91.7
.035	.907	93.4	.260	.912	91.4
.040	.923	93.1	.280	.892	90.6
.050	.945	92.9	.320	.861	90.5
.060	.955	92.8	.360	.854	90.4
.070	.969	92.5	.400	.778	89.7
.080	.972	92.7	.440	.748	89.0
.090	.984	92.5	.480	.695	88.5
.100	.999	92.6	.520	.666	87.8
.110	.986	92.8	.560	.616	87.2
.120	.981	92.6	.600	.598	87.0
.130	.983	92.7	.640	.543	86.3
.140	.983	92.0	.680	.483	85.5
.150	1.000	92.3	.720	.471	85.2
.160	.990	92.1	.760	.435	84.3
.170	.992	92.3	.800	.392	84.1
.180	.981	92.4	.840	.378	83.3
.190	.977	92.1	.880	.311	83.2
.200	.980	92.0			

Velocity Profile

$u_j/u_{e_o} = \infty$

z = - 0.500 Inch

Re_d = 53,400 x/d = 20.94

Y, in.	u/u_1	T, °F	Y, in.	u/u_1	T, °F
.015	.752	95.1	.210	.985	94.1
.020	.803	95.0	.220	.989	94.1
.025	.838	95.2	.230	.979	94.1
.030	.877	95.1	.240	.962	93.6
.035	.887	95.3	.260	.940	93.6
.040	.907	95.0	.280	.943	93.0
.050	.931	95.1	.320	.906	92.6
.060	.945	95.1	.360	.879	92.3
.070	.960	95.3	.400	.823	91.4
.080	.962	94.9	.440	.801	90.7
.090	.968	95.0	.480	.745	89.8
.100	.987	95.1	.520	.702	89.5
.110	.992	94.9	.560	.673	88.9
.120	.983	95.0	.600	.642	88.5
.130	.982	94.8	.640	.585	87.7
.140	.977	94.6	.680	.553	87.0
.150	1.000	94.7	.720	.517	86.6
.160	.999	94.6	.760	.490	85.9
.170	.983	94.1	.800	.451	85.3
.180	.981	94.2	.840	.408	84.5
.190	.983	94.2	.880	.372	84.1
.200	.971	94.0			

Velocity Profile

$u_j/u_{e_o} = \infty$

$z = 0.750$ Inch

$Re_d = 53{,}400$ $x/d = 20.94$

Y, in.	u/u_1	T, °F	Y, in.	u/u_1	T, °F
.015	.773	92.2	.210	.967	91.1
.020	.837	92.0	.220	.947	90.8
.025	.857	92.2	.230	.940	90.8
.030	.892	92.2	.240	.933	90.8
.035	.912	92.3	.260	.910	90.6
.040	.941	92.2	.280	.907	90.5
.050	.946	92.1	.320	.873	90.1
.060	.971	92.2	.360	.819	89.7
.070	.965	92.0	.400	.805	89.6
.080	.988	91.8	.440	.740	88.9
.090	.985	91.9	.480	.709	88.4
.100	.982	92.0	.520	.667	87.9
.110	.992	91.8	.560	.623	87.4
.120	.986	91.5	.600	.600	86.9
.130	1.000	91.9	.640	.549	86.1
.140	.985	91.8	.680	.521	85.9
.150	.985	91.8	.720	.465	85.3
.160	.974	91.5	.760	.443	84.8
.170	.985	91.4	.800	.409	84.5
.180	.972	91.5	.840	.377	83.9
.190	.967	91.3	.880	.344	83.4
.200	.976	91.2			

Velocity Profile

$u_j/u_{e_o} = \infty$

z = - 0.750 Inch

Re_d = 53,400 x/d = 20.94

Y, in.	u/u_1	T, °F	Y, in.	u/u_1	T, °F
.015	.763	93.3	.210	.971	92.0
.020	.814	93.1	.220	.954	91.9
.025	.858	93.1	.230	.953	91.8
.030	.882	93.1	.240	.951	91.6
.035	.890	93.2	.260	.929	91.3
.040	.926	93.1	.280	.923	91.4
.050	.930	92.9	.320	.882	90.8
.060	.948	92.9	.360	.839	90.3
.070	.966	92.9	.400	.828	89.8
.080	.971	92.8	.440	.768	89.3
.090	.976	93.2	.480	.734	88.5
.100	.985	93.1	.520	.682	88.1
.110	.990	92.7	.560	.653	87.3
.120	.987	92.8	.600	.603	87.2
.130	.991	92.8	.640	.549	86.3
.140	.990	92.8	.680	.525	85.9
.150	.992	92.7	.720	.479	85.4
.160	.987	92.5	.760	.452	84.8
.170	1.000	92.3	.800	.412	84.2
.180	.960	92.4	.840	.378	83.8
.190	.993	92.4	.880	.344	83.2
.200	.950	92.1			

Velocity Profile

$u_j/u_{e_o} = \infty$

z = 1.000 Inch

Re_d = 53,400 x/d = 20.94

Y, in.	u/u_1	T, °F	Y, in.	u/u_1	T, °F
.015	.734	92.0	.210	.970	90.5
.020	.813	91.7	.220	.967	90.4
.025	.854	91.7	.230	.966	90.5
.030	.880	91.6	.240	.961	90.5
.035	.894	91.7	.260	.948	90.5
.040	.922	91.8	.280	.931	90.1
.050	.932	91.5	.320	.913	89.8
.060	.954	91.3	.360	.880	89.5
.070	.977	91.8	.400	.851	89.2
.080	.977	91.3	.440	.826	89.0
.090	.982	91.3	.480	.782	88.4
.100	.973	91.3	.520	.763	88.3
.110	.982	91.5	.560	.717	87.7
.120	.982	91.1	.600	.692	87.3
.130	.993	91.1	.640	.664	87.1
.140	.995	91.1	.680	.615	86.4
.150	.991	91.0	.720	.589	85.8
.160	1.000	91.4	.760	.539	85.4
.170	.979	90.7	.800	.525	85.1
.180	.986	90.6	.840	.469	84.3
.190	.984	90.8	.880	.447	83.9
.200	.975	90.6			

Velocity Profile

$u_j/u_{e_o} = \infty$

z = - 1.000 Inch

Re_d = 53,400 x/d = 20.94

Y, in.	u/u_1	T, °F	Y, in.	u/u_1	T, °F
.015	.763	97.9	.210	.972	96.6
.020	.830	97.7	.220	.949	96.7
.025	.863	97.9	.230	.963	96.7
.030	.878	97.8	.240	.950	96.7
.035	.916	97.7	.260	.937	96.3
.040	.923	97.8	.280	.913	96.1
.050	.940	97.8	.320	.883	95.7
.060	.976	97.9	.360	.845	95.5
.070	.976	98.1	.400	.813	95.1
.080	.967	97.9	.440	.775	94.5
.090	.969	97.5	.480	.723	94.2
.100	.985	97.7	.520	.698	93.9
.110	.985	97.7	.560	.667	93.4
.120	.994	97.5	.600	.635	92.7
.130	.999	97.3	.640	.586	92.2
.140	1.000	97.4	.680	.548	91.8
.150	.995	97.0	.720	.500	91.1
.160	.979	97.0	.760	.467	91.7
.170	.976	97.1	.800	.435	91.4
.180	.981	97.0	.840	.374	90.8
.190	.970	97.1	.880	.343	90.7
.200	.964	97.0			

Velocity Profile

$u_j/u_{e_o} = \infty$

z = 1.363 Inches

Re_d = 53,400 x/d = 20.94

Y, in.	u/u_1	T, °F	Y, in.	u/u_1	T, °F
.015	.730	91.4	.210	.990	90.3
.020	.784	91.3	.220	.983	90.2
.025	.846	91.2	.230	.983	90.5
.030	.858	91.0	.240	.979	90.2
.035	.886	91.1	.260	.975	90.2
.040	.909	90.9	.280	.961	89.8
.050	.933	90.7	.320	.941	89.9
.060	.938	90.9	.360	.917	89.4
.070	.951	90.6	.400	.893	89.3
.080	.959	90.7	.440	.871	89.2
.090	.974	90.7	.480	.834	88.8
.100	.980	90.4	.520	.804	88.1
.110	.987	90.7	.560	.783	87.7
.120	.979	90.7	.600	.759	87.3
.130	.988	90.5	.640	.716	86.9
.140	.997	90.6	.680	.681	86.5
.150	1.000	90.5	.720	.648	85.9
.160	.997	90.5	.760	.615	85.3
.170	.988	90.5	.800	.573	84.9
.180	.989	90.5	.840	.532	84.6
.190	.998	90.4	.880	.483	83.8
.200	.984	90.4			

Velocity Profile

$u_j/u_{e_o} = \infty$

z = - 1.363 Inches

Re_d = 53,400 x/d = 20.94

Y, in.	u/u_1	T, °F	Y, in.	u/u_1	T, °F
.015	.725	97.1	.210	.989	94.4
.020	.788	95.8	.220	.990	94.4
.025	.838	95.4	.230	.976	94.5
.030	.861	95.5	.240	.973	94.3
.035	.881	95.3	.260	.967	94.3
.040	.902	95.1	.280	.956	94.1
.050	.934	95.2	.320	.954	93.8
.060	.937	95.3	.360	.923	93.6
.070	.955	94.9	.400	.907	93.3
.080	.965	94.9	.440	.879	93.2
.090	.968	94.8	.480	.853	92.7
.100	.982	94.9	.520	.812	92.5
.110	.993	94.8	.560	.791	92.3
.120	.997	94.6	.600	.756	91.6
.130	.989	94.8	.640	.718	91.1
.140	.995	94.7	.680	.682	90.8
.150	.996	94.6	.720	.653	90.2
.160	.993	94.6	.760	.622	89.8
.170	.995	94.4	.800	.592	89.4
.180	1.000	94.6	.840	.529	88.9
.190	.992	94.5	.880	.496	88.7
.200	.991	94.5			

Velocity Profile

$u_j/u_{e_o} = \infty$

z = 0 Inches

Re_d = 53,400 x/d = 29.98

Y, in.	u/u_1	T, °F	Y, in.	u/u_1	T, °F
.015	.758	90.2	.295	.941	88.3
.020	.769	90.1	.315	.947	88.3
.025	.829	89.9	.335	.927	88.1
.030	.864	90.0	.355	.923	88.1
.035	.883	89.8	.395	.893	87.6
.040	.902	89.8	.435	.877	87.6
.045	.914	89.8	.475	.847	87.3
.050	.926	89.7	.515	.805	87.0
.055	.932	89.6	.555	.787	86.8
.065	.943	89.6	.595	.757	86.4
.075	.961	89.4	.635	.739	86.0
.085	.973	89.3	.675	.705	85.9
.095	.979	89.6	.715	.676	85.4
.105	.989	89.5	.755	.651	85.1
.115	.988	89.5	.795	.618	84.8
.125	1.000	89.3	.835	.595	84.4
.135	.995	89.4	.875	.570	84.2
.145	.995	89.3	.915	.539	83.9
.155	.995	89.1	.955	.520	83.5
.175	.994	89.1	.995	.496	83.5
.195	.993	89.1	1.035	.468	83.0
.215	.99	89.1	1.075	.445	82.7
.235	.979	88.6	1.115	.399	82.5
.255	.975	88.6	1.155	.392	82.0
.275	.960	88.6	1.195	.355	81.8

Velocity Profile

$u_j/u_{e_o} = \infty$

z = 0 Inches

Re_d = 53,400 x/d = 35.68

Y, in.	u/u_1	T, °F	Y, in.	u/u_1	T, °F
.015	.681	83.8	.395	.945	82.0
.020	.763	83.5	.435	.922	81.8
.025	.812	83.5	.475	.901	81.6
.030	.844	83.6	.515	.884	81.5
.035	.869	83.3	.555	.869	81.1
.040	.883	83.5	.595	.846	80.9
.045	.902	83.4	.635	.826	80.7
.050	.912	83.1	.675	.805	80.4
.055	.923	83.4	.715	.782	80.2
.065	.936	83.3	.755	.758	79.8
.075	.951	83.3	.795	.739	79.8
.085	.970	83.3	.835	.721	79.7
.095	.966	83.0	.875	.697	79.3
.105	.979	83.1	.915	.678	79.0
.115	.980	83.1	.955	.651	78.6
.125	.986	83.1	.995	.631	78.5
.135	.992	83.0	1.035	.610	78.2
.145	.999	83.2	1.075	.593	78.2
.155	.993	83.1	1.115	.566	77.8
.175	1.000	82.9	1.155	.546	77.5
.195	.997	82.7	1.195	.529	77.1
.215	.993	82.7	1.235	.512	77.1
.235	.991	82.6	1.275	.490	76.7
.255	.984	82.7	1.315	.469	76.6
.275	.988	82.5	1.355	.451	76.5
.295	.978	82.3	1.395	.427	75.9
.315	.973	82.5	1.435	.402	75.8
.335	.975	82.5	1.475	.399	75.7
.355	.961	82.3	1.515	.370	75.3

Velocity Profile

$u_j/u_{e_o} = \infty$

z = 1.363 Inches

Re_d = 53,400 x/d = 35.68

Y, in.	u/u_1	T, °F	Y, in.	u/u_1	T, °F
.015	.661	84.3	.395	.982	83.6
.020	.742	84.2	.435	.963	83.6
.025	.790	84.4	.475	.946	83.5
.030	.818	84.2	.515	.941	83.3
.035	.838	84.2	.555	.925	83.4
.040	.868	84.1	.595	.916	83.2
.045	.881	84.3	.635	.895	83.0
.050	.891	84.2	.675	.867	82.7
.055	.893	84.2	.715	.862	82.6
.065	.909	84.1	.755	.837	82.3
.075	.924	84.1	.795	.820	82.1
.085	.940	84.3	.835	.801	81.9
.095	.953	84.1	.875	.782	81.7
.105	.961	84.2	.915	.752	81.5
.115	.965	84.2	.955	.742	81.5
.125	.969	84.1	1.035	.683	80.8
.135	.974	84.3	1.075	.670	80.8
.145	.979	84.2	1.115	.647	80.5
.155	.981	84.3	1.155	.614	80.3
.175	.979	84.2	1.195	.600	80.0
.195	.994	84.2	1.235	.572	79.9
.215	.993	84.1	1.275	.540	79.5
.235	1.000	84.2	1.315	.533	79.4
.255	.997	84.1	1.355	.510	79.3
.275	.992	84.0	1.395	.490	79.3
.295	.987	84.1	1.435	.455	78.7
.315	.988	84.0	1.475	.411	78.5
.335	.980	84.2	1.515	.405	78.3
.355	.978	84.1			

Velocity Profile

$u_j/u_{e_o} = \infty$

z = - 1.363 Inches

Re_d = 53,400 x/d = 35.68

Y, in.	u/u_1	T, °F	Y, in.	u/u_1	T, °F
.015	.658	85.2	.395	.978	84.1
.020	.742	85.1	.435	.965	84.1
.025	.785	85.2	.475	.959	83.9
.030	.815	85.0	.515	.937	83.8
.035	.841	85.0	.555	.924	83.5
.040	.862	85.0	.595	.917	83.4
.045	.882	85.0	.635	.894	83.4
.050	.889	85.1	.675	.880	83.2
.055	.886	84.9	.715	.863	82.9
.065	.913	84.9	.755	.841	82.8
.075	.932	85.1	.795	.825	82.5
.085	.941	85.1	.835	.809	82.1
.095	.951	85.0	.875	.781	82.0
.105	.957	85.0	.915	.754	82.0
.115	.967	84.9	.955	.744	81.7
.125	.972	84.9	.995	.725	81.4
.135	.976	84.9	1.035	.690	81.3
.145	.980	84.9	1.075	.669	81.0
.155	.985	84.9	1.115	.664	80.7
.175	.987	84.8	1.155	.630	80.6
.195	.983	84.7	1.195	.600	80.3
.215	1.000	84.7	1.235	.574	80.0
.235	.988	84.6	1.275	.565	80.0
.255	.999	84.6	1.315	.542	79.5
.275	.991	84.6	1.355	.517	79.5
.295	.994	84.5	1.395	.483	79.2
.315	.983	84.7	1.435	.457	78.8
.335	.980	84.3	1.475	.445	78.8
.355	.974	84.4	1.515	.409	78.5

Velocity Profile

$u_j/u_{e_o} = \infty$

z = 0 Inches

Re_d = 53,400 x/d = 40.01

Y, in.	u/u_1	T, °F	Y, in.	u/u_1	T, °F
.015	.652	85.6	.295	.980	85.4
.020	.744	85.5	.315	.978	85.2
.025	.797	85.6	.335	.966	85.2
.030	.830	85.5	.355	.971	85.0
.035	.853	85.4	.405	.948	85.1
.040	.868	85.5	.455	.938	85.0
.045	.888	85.5	.505	.917	84.8
.050	.901	85.6	.555	.890	84.6
.055	.910	85.6	.605	.864	84.4
.065	.927	85.6	.655	.849	84.1
.075	.945	85.4	.705	.838	83.9
.085	.957	85.4	.755	.795	83.7
.095	.962	85.5	.805	.797	83.4
.105	.973	85.4	.855	.756	83.3
.115	.964	85.4	.905	.737	83.0
.125	.980	85.3	.955	.713	82.7
.135	.984	85.5	1.005	.691	82.4
.145	.980	85.5	1.055	.662	82.1
.155	.984	85.4	1.105	.642	81.8
.165	.981	85.3	1.155	.613	81.6
.175	.991	85.4	1.205	.595	81.3
.185	.999	85.2	1.255	.569	81.1
.195	.997	85.2	1.305	.543	80.9
.205	1.000	85.1	1.355	.528	80.6
.215	.992	85.1	1.405	.487	80.5
.225	.984	85.0	1.455	.464	80.3
.235	.991	85.4	1.505	.429	80.0
.245	.986	85.1	1.555	.424	79.7
.255	.985	85.4	1.605	.415	79.5
.275	.991	85.2	1.655	.367	79.2

Velocity Profile

$u_j/u_{e_o} = \infty$

z = 0 Inches

Re_d = 53,400 x/d = 50.01

Y, in.	u/u_1	T, °F	Y, in.	u/u_1	T, °F
.015	.607	84.2	.395	.985	83.7
.020	.704	84.2	.435	.975	83.5
.025	.751	84.1	.475	.966	83.4
.030	.794	84.0	.515	.945	83.3
.035	.829	84.2	.555	.956	83.5
.040	.828	83.9	.595	.941	83.2
.045	.858	84.2	.635	.919	83.0
.050	.876	84.0	.675	.927	83.1
.055	.882	83.9	.715	.890	82.9
.065	.895	83.9	.755	.875	82.7
.075	.921	84.1	.795	.853	82.8
.085	.925	84.0	.835	.847	82.5
.095	.933	83.8	.875	.839	82.5
.105	.953	83.8	.915	.834	82.4
.115	.960	84.0	.955	.806	82.3
.125	.964	83.9	.995	.783	82.0
.135	.964	84.0	1.035	.796	82.1
.145	.968	83.8	1.075	.752	81.8
.155	.980	83.8	1.115	.763	81.7
.165	.977	83.8	1.155	.733	81.6
.175	.980	83.9	1.195	.712	81.4
.185	.995	84.1	1.235	.720	81.4
.195	.981	83.9	1.275	.695	81.3
.205	.984	84.0	1.315	.665	81.0
.215	.995	84.2	1.355	.641	80.7
.225	.991	84.0	1.395	.647	80.7
.235	.994	83.7	1.435	.644	80.7
.245	.998	84.0	1.475	.601	80.4
.255	1.000	83.9	1.515	.596	80.2
.275	.980	83.9	1.555	.573	80.1
.295	.986	83.7	1.595	.552	80.0
.315	.992	84.0	1.635	.529	79.7
.335	.986	83.7	1.675	.525	79.7
.355	.975	83.8	1.715	.517	79.6

Velocity Profile

$u_j/u_{e_o} = \infty$

z = - 0.062 Inch

Re_d = 53,400 x/d = 50.01

Y, in.	u/u_1	T, °F	Y, in.	u/u_1	T, °F
.015	.609	85.5	.395	.998	84.7
.025	.762	85.4	.435	.979	84.5
.035	.808	85.4	.475	.969	84.5
.045	.861	85.4	.515	.970	84.4
.055	.886	85.3	.555	.954	84.4
.065	.910	85.6	.635	.915	84.1
.075	.926	85.5	.715	.902	83.6
.095	.937	85.3	.795	.874	83.3
.115	.960	85.3	.875	.852	83.3
.135	.971	85.2	.955	.815	83.1
.155	.983	85.1	1.035	.790	82.9
.175	.988	85.2	1.115	.763	82.4
.195	.992	85.2	1.195	.725	82.1
.215	1.000	85.1	1.275	.685	81.8
.235	.998	84.9	1.355	.665	81.6
.255	1.000	85.0	1.435	.639	81.3
.275	.994	85.0	1.515	.592	81.1
.295	.997	84.9	1.595	.579	80.6
.315	.994	84.8	1.675	.539	80.5
.335	.999	84.8	1.755	.511	80.2
.355	1.000	84.7	1.835	.466	79.8

Velocity Profile

$u_j/u_{e_o} = \infty$

z = 0.125 Inch

Re_d = 53,400 x/d = 50.01

Y, in.	u/u_1	T, °F	Y, in.	u/u_1	T, °F
.015	.613	92.5	.395	.985	91.6
.025	.743	92.5	.435	.964	91.5
.035	.810	92.4	.475	.969	91.5
.045	.852	92.4	.515	.966	91.3
.055	.876	92.5	.555	.954	91.1
.065	.893	92.3	.635	.924	91.1
.075	.914	92.2	.715	.915	90.8
.095	.939	92.3	.795	.870	90.6
.115	.954	92.3	.875	.853	90.1
.135	.962	92.1	.955	.803	90.0
.155	.973	92.0	1.035	.808	89.7
.175	.991	92.2	1.115	.760	89.5
.195	.987	92.0	1.195	.730	89.1
.215	1.000	92.0	1.275	.703	88.8
.235	.991	91.9	1.355	.674	88.4
.255	.998	92.1	1.435	.647	88.2
.275	1.000	92.0	1.515	.608	88.0
.295	.998	91.7	1.595	.569	87.6
.315	1.000	91.7	1.675	.558	87.4
.335	.995	91.6	1.755	.507	87.1
.355	.996	92.0			

Velocity Profile

$u_j/u_{e_o} = \infty$

z = - 0.125 Inch

Re_d = 53,400 x/d = 50.01

Y, in.	u/u_1	T, °F	Y, in.	u/u_1	T, °F
.015	.603	93.1	.395	.988	92.2
.025	.755	93.1	.435	.986	92.0
.035	.825	93.1	.475	.966	91.8
.045	.856	92.9	.515	.975	91.9
.055	.884	93.0	.555	.960	91.7
.065	.902	93.0	.635	.919	91.6
.075	.918	92.9	.715	.904	91.2
.095	.946	93.0	.795	.884	91.1
.115	.958	92.9	.875	.841	90.6
.135	.967	92.9	.955	.833	90.3
.155	.983	92.9	1.035	.788	90.2
.175	.987	92.9	1.115	.760	89.9
.195	.983	92.8	1.195	.719	89.6
.215	.993	92.7	1.275	.696	89.1
.235	.999	92.7	1.355	.671	88.9
.255	.998	92.7	1.435	.640	88.7
.275	.993	92.4	1.515	.610	88.3
.295	1.000	92.4	1.595	.568	88.2
.315	.990	92.4	1.675	.531	87.8
.335	1.000	92.4	1.755	.514	87.5
.355	.999	92.3	1.835	.479	87.1

Velocity Profile

$u_j/u_{e_o} = \infty$

z = 0.500 Inch

Re_d = 53,400 x/d = 50.01

Y, in.	u/u_1	T, °F	Y, in.	u/u_1	T, °F
.015	.609	81.9	.395	.979	81.7
.025	.753	81.8	.435	.966	81.4
.035	.820	82.1	.475	.977	81.5
.045	.859	82.0	.515	.959	81.3
.055	.875	82.1	.555	.949	81.0
.065	.894	82.2	.635	.927	81.0
.075	.911	82.0	.715	.914	81.0
.095	.941	82.0	.795	.878	80.5
.115	.949	82.1	.875	.862	80.4
.135	.963	82.1	.955	.828	80.1
.155	.969	81.9	1.035	.794	79.9
.175	.995	81.6	1.115	.757	79.6
.195	.995	81.9	1.195	.746	79.3
.215	.993	81.9	1.275	.710	78.8
.235	.990	81.9	1.355	.675	78.9
.255	.998	81.8	1.435	.642	78.7
.275	.985	81.7	1.515	.618	78.4
.295	1.000	81.8	1.595	.582	78.1
.315	.989	81.7	1.675	.551	77.7
.335	.986	81.7	1.755	.487	77.5
.355	.999	81.7	1.835	.465	77.3

Velocity Profile

$u_j/u_{e_o} = \infty$

$z = -0.500$ Inch

$Re_d = 53{,}400$ $x/d = 50.01$

Y, in.	u/u_1	T, °F	Y, in.	u/u_1	T, °F
.015	.598	83.6	.395	.991	82.9
.025	.769	83.5	.435	.976	82.8
.035	.825	83.5	.475	.980	83.0
.045	.861	83.4	.515	.959	82.5
.055	.880	83.5	.555	.948	82.3
.065	.906	83.5	.635	.927	81.9
.075	.928	83.7	.715	.901	82.0
.095	.937	83.4	.795	.867	81.7
.115	.966	83.5	.875	.836	81.3
.135	.977	83.6	.955	.823	81.1
.155	.969	83.2	1.035	.793	80.9
.175	.977	83.3	1.115	.749	80.5
.195	.993	83.3	1.195	.723	80.2
.215	.992	83.2	1.275	.693	79.9
.235	.995	83.2	1.355	.657	79.8
.255	.991	83.0	1.435	.630	79.4
.275	.997	82.9	1.515	.591	79.1
.295	1.000	82.8	1.595	.559	79.1
.315	.993	82.9	1.675	.515	78.6
.335	.997	82.9	1.755	.499	78.4
.355	.991	82.9	1.835	.467	78.1

Velocity Profile

$u_j/u_{e_o} = \infty$

z = 1.363 Inches

Re_d = 53,400 x/d = 50.01

Y, in.	u/u_1	T, °F	Y, in.	u/u_1	T, °F
.015	.600	93.3	.395	.987	92.5
.025	.744	93.1	.435	.985	92.3
.035	.824	93.2	.475	.981	92.3
.045	.857	93.2	.515	.971	92.3
.055	.875	93.2	.555	.952	92.1
.065	.894	93.4	.635	.934	91.8
.075	.909	93.3	.715	.912	91.5
.095	.935	93.2	.795	.882	91.2
.115	.949	93.0	.875	.867	91.0
.135	.968	93.0	.955	.831	90.7
.155	.977	93.1	1.035	.809	90.5
.175	.913	93.1	1.115	.776	90.2
.195	.994	92.8	1.195	.751	89.9
.215	.993	92.8	1.275	.727	89.4
.235	.989	92.7	1.355	.681	89.1
.255	1.000	92.7	1.435	.663	88.9
.275	.998	92.6	1.515	.619	88.7
.295	1.000	92.8	1.595	.588	88.4
.315	.996	92.6	1.675	.555	88.2
.335	.987	92.6	1.755	.491	87.8
.355	.996	92.7	1.835	.494	87.5

Velocity Profile

$u_j/u_{e_o} = \infty$

z = - 1.363 Inches

Re_d = 53,400 x/d = 50.01

Y, in.	u/u_1	T, °F	Y, in.	u/u_1	T, °F
.015	.598	93.4	.395	.969	92.3
.025	.735	93.3	.435	.976	91.9
.035	.797	93.2	.475	.969	91.8
.045	.851	93.1	.515	.957	91.6
.055	.872	93.3	.555	.935	91.4
.065	.873	93.2	.635	.920	91.5
.075	.903	93.0	.715	.911	91.1
.095	.918	93.0	.795	.889	90.9
.115	.934	92.9	.875	.848	90.5
.135	.942	93.0	.955	.825	90.2
.155	.965	92.8	1.035	.797	89.9
.175	.968	92.9	1.115	.757	89.7
.195	.977	92.7	1.195	.737	89.5
.215	.987	92.7	1.275	.708	89.1
.235	.980	92.7	1.355	.678	88.6
.255	1.000	92.3	1.435	.650	88.4
.275	.976	92.4	1.515	.623	88.0
.295	.991	92.3	1.595	.587	87.6
.315	.990	92.5	1.675	.557	87.5
.335	.989	92.4	1.755	.531	87.0
.355	.984	92.3	1.835	.489	86.6

Velocity Profile

$u_j/u_{e_o} = \infty$

z = 2.727 Inches

Re_d = 53,400 x/d = 50.01

Y, in.	u/u_1	T, °F	Y, in.	u/u_1	T, °F
.015	.590	84.1	.395	.975	83.2
.025	.755	84.0	.435	.965	83.3
.035	.824	84.1	.475	.952	83.3
.045	.862	84.0	.515	.939	83.0
.055	.891	84.0	.555	.935	82.8
.065	.899	84.0	.635	.926	82.7
.075	.916	84.0	.715	.894	82.3
.095	.939	83.8	.795	.844	82.3
.115	.954	83.8	.875	.825	82.0
.135	.966	83.8	.955	.807	81.7
.155	.979	83.7	1.035	.781	81.4
.175	.982	83.8	1.115	.738	81.4
.195	.985	83.7	1.195	.689	81.0
.215	.988	84.0	1.275	.663	80.7
.235	.992	83.9	1.355	.631	80.3
.255	.985	83.7	1.435	.624	80.2
.275	1.000	83.7	1.515	.573	79.7
.295	.996	83.7	1.595	.554	79.6
.315	.994	83.6	1.675	.492	79.2
.335	.986	83.7	1.755	.484	78.9
.355	.985	83.3	1.835	.468	78.6

Velocity Profile

$u_j/u_{e_o} = \infty$

z = - 2.727 Inches

Re_d = 53,400 x/d = 50.01

Y, in.	u/u_1	T, °F	Y, in.	u/u_1	T, °F
.015	.623	85.3	.395	.987	84.4
.025	.745	85.3	.435	.979	84.3
.035	.816	85.2	.475	.968	84.4
.045	.862	85.4	.515	.961	84.3
.055	.874	85.3	.555	.943	84.1
.065	.887	85.3	.635	.936	84.0
.075	.925	85.1	.715	.896	83.6
.095	.933	85.1	.795	.867	83.4
.115	.950	85.0	.875	.843	83.0
.135	.971	85.0	.955	.812	82.7
.155	.977	85.0	1.035	.794	82.5
.175	.985	85.0	1.115	.768	82.2
.195	.985	84.9	1.195	.727	81.9
.215	.994	84.9	1.275	.698	81.4
.235	.994	84.7	1.355	.673	81.2
.255	1.000	84.7	1.435	.645	81.1
.275	.987	84.8	1.515	.603	80.9
.295	.998	84.9	1.595	.562	80.5
.315	.995	84.7	1.675	.541	80.2
.335	.992	84.6	1.755	.513	79.8
.355	.993	84.5	1.835	.478	79.6

Velocity Profile

$u_j/u_{e_o} = \infty$

z = 0 Inches

Re_d = 53,400 x/d = 60.0

Y, in.	u/u_1	T, °F	Y, in.	u/u_1	T, °F
.015	.519	84.4	.365	.976	83.7
.025	.692	84.5	.385	.990	83.8
.035	.782	84.5	.405	.993	84.0
.045	.809	84.5	.425	.983	83.9
.055	.849	84.4	.445	.986	83.7
.065	.861	84.5	.465	.973	83.7
.075	.879	84.4	.505	.975	83.6
.085	.893	84.3	.545	.955	83.7
.095	.916	84.4	.625	.942	83.4
.105	.905	84.3	.705	.927	83.3
.115	.910	84.3	.785	.907	83.0
.125	.931	84.1	.865	.880	82.8
.135	.946	84.2	.945	.883	82.7
.145	.954	84.1	1.025	.841	82.4
.155	.938	84.0	1.105	.811	82.3
.165	.959	84.1	1.185	.805	82.0
.175	.958	84.0	1.265	.772	81.8
.185	.975	84.1	1.345	.771	81.9
.195	.964	84.1	1.425	.714	81.5
.205	.968	84.1	1.505	.720	81.5
.215	.956	84.1	1.585	.680	80.9
.225	.966	84.1	1.665	.634	81.0
.235	.992	84.1	1.745	.623	80.6
.245	.983	84.1	1.825	.588	80.4
.255	.983	84.0	1.905	.579	80.2
.265	.985	84.0	1.985	.551	80.1
.285	.993	84.0	2.065	.520	79.9
.305	1.000	84.1	2.145	.492	79.5
.325	.990	83.9	2.225	.458	79.5
.345	.985	83.9	2.305	.411	79.3

Velocity Profile

$u_j/u_{e_o} = \infty$

z = 1.363 Inches

Re_d = 53,400 x/d = 60.0

Y, in.	u/u_1	T, °F	Y, in.	u/u_1	T, °F
.015	.475	84.9	.365	1.000	84.3
.025	.693	84.7	.385	.990	84.3
.035	.781	84.8	.405	.998	84.6
.045	.832	84.9	.425	.998	84.5
.055	.849	84.8	.445	.995	84.1
.065	.870	84.7	.465	.988	84.2
.075	.891	84.8	.505	.977	84.3
.085	.892	84.7	.545	.963	83.9
.095	.915	84.6	.625	.955	83.9
.105	.930	84.7	.705	.938	83.6
.115	.925	84.6	.785	.925	83.4
.125	.941	84.7	.865	.896	83.3
.135	.938	84.5	.945	.865	83.2
.145	.960	84.5	1.025	.845	82.9
.155	.937	84.9	1.105	.828	82.7
.165	.951	84.7	1.185	.815	82.6
.175	.963	84.5	1.265	.789	82.5
.185	.974	84.8	1.345	.767	82.4
.195	.969	84.5	1.425	.720	82.3
.205	.971	84.4	1.505	.716	82.1
.215	.967	84.6	1.585	.677	81.7
.225	.986	84.5	1.665	.680	81.7
.235	.991	84.5	1.745	.623	81.3
.245	.981	84.6	1.825	.599	81.2
.255	.979	84.4	1.905	.563	80.7
.265	.990	84.5	1.985	.553	80.5
.285	.988	84.4	2.065	.484	80.3
.305	.988	84.3	2.145	.485	80.1
.325	.987	84.4	2.225	.460	79.9
.345	.988	84.3	2.305	.443	79.8

Velocity Profile

$u_j/u_{e_o} = \infty$

$z = -1.363$ Inches

$Re_d = 53{,}400$ $\quad x/d = 60.0$

Y, in.	u/u_1	T, °F	Y, in.	u/u_1	T, °F
.015	.527	86.2	.365	1.000	85.1
.025	.712	86.2	.385	.998	85.1
.035	.789	86.2	.405	.984	85.1
.045	.814	86.0	.425	.977	84.8
.055	.834	85.9	.445	.988	84.7
.065	.884	85.9	.465	.991	84.8
.075	.890	85.9	.505	.977	84.8
.085	.894	85.9	.545	.973	84.5
.095	.914	85.7	.625	.945	84.4
.105	.927	85.6	.705	.949	84.3
.115	.935	85.7	.785	.917	84.1
.125	.931	85.5	.865	.877	83.8
.135	.949	85.4	.945	.884	83.5
.145	.963	85.6	1.025	.853	83.5
.155	.968	85.5	1.105	.838	83.3
.165	.966	85.4	1.185	.820	83.3
.175	.980	85.5	1.265	.777	82.8
.185	.965	85.5	1.345	.742	82.6
.195	.959	85.3	1.425	.749	82.5
.205	.987	85.3	1.505	.721	82.2
.215	.985	85.3	1.585	.689	82.0
.225	.989	85.3	1.665	.656	81.9
.235	.987	85.4	1.745	.630	81.5
.245	.983	85.2	1.825	.630	81.3
.255	.996	85.0	1.905	.588	81.3
.265	.983	85.3	1.985	.547	80.8
.285	.983	85.2	2.065	.534	80.9
.305	.983	85.3	2.145	.505	80.6
.325	.987	85.0	2.225	.472	80.3
.345	.999	84.9	2.305	.458	80.1

Velocity Profile

$u_j/u_{e_o} = \infty$

z = 0 Inches

Re_d = 53,400 x/d = 70.0

Y, in.	u/u_1	T, °F	Y, in.	u/u_1	T, °F
.015	.464	84.8	.425	.979	83.8
.025	.655	84.6	.445	.971	83.7
.035	.731	84.6	.465	.972	83.9
.045	.791	84.6	.505	.959	83.8
.055	.823	84.5	.545	.965	83.6
.065	.844	84.6	.585	.968	83.8
.075	.869	84.6	.625	.948	83.5
.085	.872	84.4	.665	.927	83.3
.095	.892	84.3	.705	.941	83.3
.105	.888	84.5	.745	.924	83.3
.115	.913	84.6	.785	.923	83.3
.125	.915	84.4	.825	.921	83.0
.135	.894	84.4	.865	.921	83.2
.145	.913	84.3	.945	.873	83.1
.155	.930	84.3	1.025	.864	82.9
.165	.936	84.2	1.105	.847	82.6
.175	.947	84.3	1.185	.840	82.4
.185	.957	84.2	1.265	.822	82.3
.195	.940	84.2	1.345	.784	82.2
.205	.960	84.2	1.425	.781	81.9
.215	.962	84.2	1.505	.762	81.8
.225	.966	84.4	1.585	.718	81.6
.235	.957	84.3	1.665	.700	81.4
.245	.956	84.1	1.745	.690	81.2
.255	.955	84.0	1.825	.680	81.1
.265	.954	84.0	1.905	.632	81.1
.275	.966	84.0	1.985	.595	80.8
.285	.966	84.0	2.065	.604	80.6
.295	.975	84.0	2.145	.588	80.3
.305	.975	84.2	2.225	.562	80.1
.315	.975	84.2	2.305	.527	80.1
.325	.985	84.1	2.385	.506	80.1
.335	.959	84.0	2.465	.468	79.7
.345	.974	84.1	2.545	.438	79.4
.355	.979	83.9	2.625	.454	79.0
.365	.975	84.0	2.705	.422	79.1
.385	1.000	84.2	2.785	.398	78.9
.405	.963	84.0			

Velocity Profile

$u_j/u_{e_o} = \infty$

z = 1.363 Inches

Re_d = 53,400 x/d = 70.0

Y, in.	u/u_1	T, °F	Y, in.	u/u_1	T, °F
.015	.474	84.7	.425	.989	83.8
.025	.685	84.7	.445	.989	83.8
.035	.776	84.6	.465	.984	83.8
.045	.817	84.6	.505	.978	83.6
.055	.831	84.6	.545	.969	83.6
.065	.865	84.6	.625	.957	83.4
.075	.863	84.6	.705	.949	83.4
.085	.893	84.5	.785	.939	83.2
.095	.909	84.7	.865	.907	83.0
.105	.912	84.5	.945	.896	83.0
.115	.931	84.5	1.025	.861	82.7
.125	.931	84.6	1.105	.854	82.5
.135	.939	84.3	1.185	.838	82.4
.145	.949	84.5	1.265	.823	82.2
.155	.943	84.2	1.345	.797	81.9
.165	.952	84.4	1.425	.782	81.9
.175	.963	84.2	1.505	.775	81.8
.185	.967	84.3	1.585	.756	81.5
.195	.957	84.2	1.665	.707	81.5
.205	.967	84.5	1.745	.692	81.1
.215	.973	84.3	1.825	.688	80.9
.225	.976	84.2	1.905	.641	80.8
.235	.982	84.3	1.985	.598	80.7
.245	.976	84.3	2.065	.594	80.5
.255	.976	84.2	2.145	.581	80.4
.265	.985	84.3	2.225	.573	80.0
.285	.976	84.1	2.305	.547	79.8
.305	.988	84.1	2.385	.501	79.7
.325	.982	84.0	2.465	.495	79.5
.345	1.000	84.1	2.545	.474	79.4
.365	.990	84.1	2.625	.432	79.1
.385	.985	83.9	2.705	.400	78.8
.405	.982	83.8	2.785	.425	78.6

Velocity Profile

$u_j/u_{e_o} = \infty$

z = - 1.363 Inches

Re_d = 53,400 x/d = 70.0

Y, in.	u/u_1	T, °F	Y, in.	u/u_1	T, °F
.015	.477	84.6	.425	.988	83.5
.025	.684	84.5	.445	.983	83.5
.035	.761	84.6	.465	.989	83.4
.045	.816	84.5	.505	.985	83.5
.055	.830	84.4	.545	.985	83.5
.065	.854	84.3	.625	.980	83.2
.075	.870	84.4	.705	.952	83.1
.085	.899	84.3	.785	.955	82.9
.095	.895	84.3	.865	.928	82.9
.105	.917	84.5	.945	.915	82.6
.115	.921	84.4	1.025	.887	82.5
.125	.933	84.3	1.105	.879	82.3
.135	.921	84.3	1.185	.845	82.2
.145	.950	84.2	1.265	.838	82.0
.155	.956	84.2	1.345	.825	81.9
.165	.952	84.2	1.425	.796	81.5
.175	.957	84.2	1.505	.759	81.5
.185	.962	84.3	1.585	.763	81.5
.195	.959	84.2	1.665	.716	81.3
.205	.956	83.9	1.745	.715	80.9
.215	.974	83.8	1.825	.671	80.7
.225	.983	83.9	1.905	.651	80.5
.235	.979	84.0	1.985	.649	80.5
.245	.985	84.0	2.065	.609	80.2
.255	.993	84.0	2.145	.599	79.9
.265	.999	83.8	2.225	.566	79.8
.285	.979	83.9	2.305	.523	79.5
.305	.991	83.9	2.385	.520	79.3
.325	1.000	83.9	2.465	.526	79.1
.345	.988	83.8	2.545	.487	79.1
.365	.991	83.7	2.625	.451	78.6
.385	.989	83.7	2.705	.461	78.6
.405	.986	83.7			

APPENDIX C

PHASE 3 EXPERIMENTAL DATA

Phase 3 Data Summary

Initial Velocity Ratio = 2.0

d = 0.444 Inch

$\theta_{I.M._o}$ = 0.0458 Inch

x/d	x/h_{eq}	Z, in.	Re_d	u_j ft/sec	T_j °F	u_1 ft/sec	τ_w lb/ft^2	$C_f^* \times 10^3$	Velocity Profile Index
8.20	65.01	0	43,600	242.31	135.8	185.59	.1060	2.929	254
8.20	65.01	1.363	43,600	242.31	135.8	---	---	---	255
8.20	65.01	- 1.363	43,600	242.31	135.8	---	.0324	2.469	256
12.25	97.09	0	43,600	242.31	135.8	160.60	.1108	4.152	257
12.25	97.09	0.125	43,600	242.31	135.8	155.54	---	---	258
12.25	97.09	- 0.125	43,600	242.31	135.8	161.89	---	---	259
12.25	97.09	0.250	43,600	242.31	135.8	141.58	---	---	260
12.25	97.09	- 0.250	43,600	242.31	135.8	150.73	---	---	261
12.25	97.09	0.312	43,600	242.31	135.8	127.27	---	---	262
12.25	97.09	- 0.312	43,600	242.31	135.8	141.57	---	---	263

*Bases on fluid properties at δ_1.

Phase 3 Data Summary

Initial Velocity Ratio = 2.0

d = 0.444 Inch

$\theta_{I.M._o}$ = 0.0458 Inch

x/d	x/h_{eq}	Z, in.	Re_d	u_j ft/sec	T_j °F	u_1 ft/sec	τ_w lb/ft^2	$C_f^* \times 10^3$	Velocity Profile Index
12.25	97.09	0.437	43,600	242.31	135.8	---	---	---	264
12.25	97.09	- 0.437	43,600	242.31	135.8	118.14	---	---	265
12.25	97.09	0.500	43,600	242.31	135.8	---	---	---	266
12.25	97.09	- 0.500	43,600	242.31	135.8	---	---	---	267
12.25	97.09	0.937	43,600	242.31	135.8	---	---	---	268
12.25	97.09	- 0.937	43,600	242.31	135.8	---	---	---	269
12.25	97.09	1.363	43,600	242.31	135.8	---	---	---	270
12.25	97.09	- 1.363	43,600	242.31	135.8	---	0.0387	2.885	271
16.26	128.89	0	43,600	242.31	135.8	150.95	0.1090	4.529	272
16.26	128.89	1.363	43,600	242.31	135.8	---	---	---	273
16.26	128.89	- 1.363	43,600	242.31	135.8	---	0.0412	3.005	274

*Based on fluid properties at δ_1.

Phase 3 Data Summary

Initial Velocity Ratio = 2.0

d = 0.444 Inch

$\theta_{I.M._o}$ = 0.0458 Inch

x/d	x/h_{eq}	Z, in.	Re_d	u_j ft/sec	T_j °F	u_1 ft/sec	τ_w lb/ft^2	$C_f^* \times 10^3$	Velocity Profile Index
24.46	193.91	0	43,600	242.31	135.8	141.00	0.0983	4.585	275
24.46	193.91	0.125	43,600	242.31	135.8	136.69	---	---	276
24.46	193.91	- 0.125	43,600	242.31	135.8	140.73	---	---	277
24.46	193.91	0.250	43,600	242.31	135.8	128.91	---	---	278
24.46	193.91	- 0.250	43,600	242.31	135.8	135.18	---	---	279
24.46	193.91	0.312	43,600	242.31	135.8	123.18	---	---	280
24.46	193.91	- 0.312	43,600	242.31	135.8	131.37	---	---	281
24.46	193.91	0.437	43,600	242.31	135.8	---	---	---	282
24.46	193.91	- 0.437	43,600	242.31	135.8	123.30	---	---	283
24.46	193.91	0.500	43,600	242.31	135.8	---	---	---	284
24.46	193.91	- 0.500	43,600	242.31	135.8	119.91	---	---	285

*Based on fluid properties at δ_1.

Phase 3 Data Summary

Initial Velocity Ratio = 2.0

d = 0.444 Inch

$\theta_{I.M._o}$ = 0.0458 Inch

x/d	x/h_{eq}	Z, in.	Re_d	u_j ft/sec	T_j °F	u_1 ft/sec	τ_w lb/ft^2	$C_f^* \times 10^3$	Velocity Profile Index
24.46	193.91	0.937	43,600	242.31	135.8	---	---	---	286
24.46	193.91	- 0.937	43,600	242.31	135.8	---	---	---	287
24.46	193.91	1.363	43,600	242.31	135.8	---	---	---	288
24.46	193.91	- 1.363	43,600	242.31	135.8	---	0.0431	3,020	289
35.68	282.91	0	43,600	242.31	135.8	132.35	0.0827	4.399	290
35.68	282.91	1.363	43,600	242.31	135.8	---	---	---	291
35.68	282.91	- 1.363	43,600	242.31	135.8	---	0.0469	3.317	292

*Based on fluid properties at δ_1.

Velocity Profile

$u_j/u_{e_o} = 2.0$

Z = 0 Inches $p_a = 29.1$ Inches Hg

$Re_d = 43{,}600$ $x/d = 5.42$

Y, in.	u ft/sec	p mm Hg	T °F	Y, in.	u ft/sec	p mm Hg	T °F
.015	102.63	.701	107.7	.375	185.59	.256	113.5
.035	121.49	.550	110.4	.425	179.62	.235	109.4
.055	126.67	.513	111.1	.475	163.41	.264	105.3
.075	129.17	.475	111.5	.525	145.44	.307	100.9
.095	129.87	.457	111.9	.575	127.59	.367	96.6
.115	131.75	.433	112.6	.625	115.20	.428	91.9
.135	133.64	.423	112.8	.675	110.88	.480	89.2
.155	136.69	.413	113.4	.775	110.01	.526	88.1
.175	140.41	.390	114.3	.875	109.56	.505	88.1
.195	144.67	.379	114.7	.975	109.47	.506	88.0
.215	149.93	.365	115.3	1.075	110.12	.482	87.8
.235	155.80	.363	116.1	1.175	110.01	.471	88.1
.255	161.43	.350	116.2	1.375	110.90	.432	88.2
.275	167.77	.338	116.3	1.575	110.43	.416	88.2
.295	172.99	.331	116.7	1.625	110.23	.405	88.2
.315	177.93	.300	116.3	1.675	110.97	.392	88.2
.335	182.16	.287	115.8	1.725	110.65	.389	88.4
.355	184.20	.267	114.8	1.825	110.5	.380	88.6

Velocity Profile

$u_j/u_{e_o} = 2.0$

Z = 1.363 Inches p_a = 29.105 Inches Hg

Re_d = 43,600 x/d = 5.42

Y, in.	u ft/sec	p mm Hg	T °F	Y, in.	u ft/sec	p mm Hg	T °F
.015	45.73	.590	91.7	.335	90.57	.551	89.2
.035	56.65	.566	90.2	.355	93.19	.550	89.2
.055	59.23	.563	90.1	.375	95.29	.550	89.0
.075	62.02	.555	89.8	.425	99.51	.552	89.0
.095	63.05	.545	89.6	.475	102.39	.549	89.3
.115	64.57	.545	89.8	.525	105.38	.554	89.3
.135	67.12	.530	89.6	.575	107.25	.555	89.1
.155	68.97	.539	89.3	.625	108.04	.547	89.3
.175	71.51	.532	89.4	.675	109.40	.537	89.3
.195	74.05	.536	89.3	.775	109.66	.520	89.5
.215	75.95	.534	89.2	.875	109.93	.515	89.4
.235	77.87	.541	89.1	.975	109.97	.503	89.3
.255	81.72	.539	89.3	1.075	109.64	.487	89.4
.275	83.02	.539	89.2	1.175	109.90	.464	89.6
.295	86.46	.537	89.0	1.375	109.80	.437	89.4
.315	88.97	.546	89.2	1.575	110.09	.408	89.4

Velocity Profile

$u_j/u_{e_o} = 2.0$

Z = - 1.363 Inches p_a = 29.1 Inches Hg

Re_d = 43,600 x/d = 5.42

Y, in.	u ft/sec	p mm Hg	T °F	Y, in.	u ft/sec	p mm Hg	T °F
.015	46.73	.581	93.2	.335	91.25	.541	90.2
.035	57.77	.577	91.2	.355	93.00	.548	90.2
.055	60.07	.563	91.0	.375	95.07	.549	90.1
.075	62.22	.546	91.0	.425	98.84	.554	90.1
.095	63.82	.551	90.9	.475	102.29	.556	90.0
.115	66.36	.542	90.5	.525	104.37	.555	90.1
.135	67.19	.534	90.6	.575	107.27	.543	90.2
.155	69.47	.536	90.6	.625	107.83	.543	90.1
.175	71.95	.538	90.4	.675	109.16	.546	90.1
.195	74.50	.536	90.2	.775	109.41	.520	90.2
.215	76.99	.542	90.4	.875	109.53	.510	90.0
.235	79.43	.529	90.3	.975	109.63	.499	90.1
.255	81.60	.531	90.2	1.075	109.95	.489	90.2
.275	84.69	.542	90.2	1.175	109.96	.470	90.2
.295	86.69	.538	90.2	1.375	109.41	.435	90.3
.315	89.84	.540	90.2	1.575	110.36	.411	90.2

Velocity Profile

$u_j/u_{e_o} = 2.0$

Z = 0 Inches $p_a = 28.91$ Inches Hg

$Re_d = 43,600$ $x/d = 12.25$

Y, in.	u ft/sec	p mm Hg	T °F	Y, in.	u ft/sec	p mm Hg	T °F
.015	102.27	.422	108.5	.465	152.93	.174	105.3
.035	118.92	.379	110.0	.515	146.44	.185	103.2
.055	125.17	.354	110.1	.565	138.62	.205	100.5
.075	129.69	.327	110.7	.615	129.73	.226	98.2
.095	133.03	.306	111.0	.665	122.40	.253	95.3
.115	135.87	.293	111.2	.715	117.05	.283	93.0
.135	138.35	.279	111.3	.815	112.69	.324	90.1
.155	141.10	.265	111.7	.915	111.81	.345	89.0
.175	143.91	.257	111.6	1.015	112.00	.340	89.4
.195	146.60	.238	111.8	1.115	111.71	.339	88.9
.215	149.81	.230	112.0	1.215	112.14	.337	89.0
.265	155.63	.208	111.4	1.415	112.04	.324	88.6
.315	159.25	.187	110.2	1.615	111.84	.313	89.0
.365	160.60	.171	108.9	1.815	112.17	.300	89.1
.415	158.65	.165	106.9	2.015	112.27	.285	89.4

Velocity Profile

$u_j/u_{e_o} = 2.0$

Z = 0.125 Inch p_a = 29.25 Inches Hg

Re_d = 43,600 x/d = 12.25

Y, in.	u ft/sec	p mm Hg	T °F	Y, in.	u ft/sec	p mm Hg	T °F
.015	99.57	.434	101.4	.335	155.21	.167	103.4
.035	115.60	.389	103.0	.355	155.54	.156	102.9
.055	121.83	.354	103.6	.375	155.50	.161	102.6
.075	125.92	.319	103.8	.425	152.43	.165	100.8
.095	129.88	.293	103.6	.475	146.51	.177	98.7
.115	132.96	.273	104.3	.525	140.01	.200	96.7
.135	135.70	.248	104.3	.575	132.36	.226	94.6
.155	138.26	.239	104.9	.625	125.29	.255	92.2
.175	140.82	.230	104.7	.675	118.96	.284	89.7
.195	143.84	.210	104.7	.775	113.48	.326	86.0
.215	145.86	.203	104.8	.875	112.33	.345	85.0
.235	148.68	.192	104.6	.975	112.16	.351	84.6
.255	150.36	.182	104.6	1.075	112.03	.345	84.5
.275	152.16	.182	104.6	1.175	112.34	.338	84.6
.295	153.53	.175	104.0	1.375	112.36	.333	84.6
.315	154.18	.175	103.7				

Velocity Profile

$u_j/u_{e_o} = 2.0$

$Z = -0.125$ Inch $\quad p_a = 29.25$ Inches Hg

$Re_d = 43{,}600 \quad x/d = 12.25$

Y, in.	u ft/sec	p mm Hg	T °F	Y, in.	u ft/sec	p mm Hg	T °F
.015	109.32	.430	105.4	.335	161.89	.195	105.3
.035	126.51	.376	107.3	.355	161.47	.183	105.1
.055	132.47	.360	107.6	.375	160.97	.181	104.5
.075	136.69	.329	107.9	.425	157.41	.170	102.8
.095	139.35	.312	108.1	.475	150.91	.188	100.6
.115	142.59	.302	108.3	.525	143.45	.197	98.6
.135	144.98	.281	108.3	.575	134.88	.211	96.3
.155	147.19	.278	107.9	.625	127.07	.238	93.7
.175	149.64	.266	108.0	.675	120.49	.260	91.3
.195	151.91	.255	108.0	.775	113.52	.323	87.7
.215	154.70	.247	107.9	.875	112.30	.347	86.2
.235	156.52	.233	107.3	.975	112.22	.346	85.8
.255	158.40	.223	107.5	1.075	112.09	.347	85.5
.275	160.06	.220	107.3	1.175	111.63	.342	85.8
.295	161.37	.210	106.6	1.375	111.95	.336	85.9
.315	161.78	.196	106.1				

Velocity Profile

$u_j/u_{e_o} = 2.0$

$Z = 0.250$ Inch $\quad p_a = 28.89$ Inches Hg

$Re_d = 43{,}600 \quad x/d = 12.25$

Y, in.	u ft/sec	p mm Hg	T °F	Y, in.	u ft/sec	p mm Hg	T °F
.015	96.52	.406	105.5	.335	140.90	.173	105.4
.035	112.03	.356	106.2	.355	141.58	.172	105.1
.055	118.23	.322	106.3	.375	140.87	.176	104.6
.075	121.06	.291	106.2	.425	138.27	.190	103.2
.095	123.52	.266	106.5	.475	132.87	.224	101.8
.115	125.94	.243	106.3	.525	127.43	.238	100.0
.135	127.86	.226	106.1	.575	123.05	.270	97.9
.155	130.14	.209	106.3	.625	118.15	.293	95.8
.175	132.70	.200	106.8	.675	114.83	.311	94.0
.195	134.53	.189	106.7	.775	112.47	.341	92.1
.215	136.13	.184	106.8	.875	112.33	.346	91.4
.235	137.63	.175	106.6	.975	112.23	.346	91.4
.255	139.46	.171	106.3	1.075	111.55	.342	91.2
.275	140.40	.171	106.3	1.175	111.78	.334	91.3
.295	140.81	.171	105.6	1.375	111.64	.326	91.3
.315	140.52	.173	105.4				

Velocity Profile

$u_j/u_{e_o} = 2.0$

Z = - 0.250 Inch p_a = 28.91 Inches Hg

Re_d = 43,600 x/d = 12.25

Y, in.	u ft/sec	p mm Hg	T °F	Y, in.	u ft/sec	p mm Hg	T °F
.015	104.84	.400	110.6	.335	150.73	.172	109.2
.035	120.59	.367	111.2	.355	150.08	.168	108.9
.055	126.81	.335	111.5	.375	148.93	.169	108.6
.075	129.90	.312	111.5	.425	145.23	.172	107.1
.095	132.76	.293	112.0	.475	139.15	.187	105.1
.115	134.68	.276	111.7	.575	126.13	.229	101.0
.135	136.51	.261	111.5	.625	119.92	.252	98.9
.155	138.04	.252	111.5	.675	116.21	.281	97.1
.175	139.94	.240	111.0	.775	112.87	.322	94.5
.195	141.62	.224	111.4	.875	111.81	.345	93.2
.215	143.73	.218	110.9	.975	111.63	.342	93.2
.235	145.73	.207	111.1	1.075	112.05	.336	93.3
.255	147.57	.197	111.0	1.175	111.98	.333	93.4
.275	148.69	.194	110.5	1.375	111.50	.324	93.0
.295	149.68	.186	110.4				
.315	150.54	.179	109.8				

Velocity Profile

$u_j/u_{e_o} = 2.0$

Z = 0.312 Inch p_a = 29.05 Inches Hg

Re_d = 43,600 x/d = 12.25

Y, in.	u ft/sec	p mm Hg	T °F	Y, in.	u ft/sec	p mm Hg	T °F
.015	87.69	.394	105.6	.335	126.74	.219	104.5
.035	102.01	.350	106.2	.355	127.27	.216	104.2
.055	106.60	.318	105.9	.375	126.80	.219	103.7
.075	110.36	.291	106.0	.425	125.33	.240	102.7
.095	112.24	.281	106.0	.475	122.33	.270	101.1
.115	114.85	.259	106.0	.525	118.93	.287	99.3
.135	115.53	.249	105.9	.575	116.40	.305	97.6
.155	117.26	.239	105.9	.625	114.13	.320	95.9
.175	119.20	.220	105.7	.675	112.93	.324	94.6
.195	120.92	.209	105.8	.775	111.58	.353	93.4
.215	122.93	.203	105.8	.875	111.31	.349	93.0
.235	123.49	.215	105.5	.975	111.53	.342	92.9
.255	124.95	.210	105.4	1.075	111.36	.339	93.0
.275	125.84	.207	105.0	1.175	111.31	.343	93.0
.295	125.87	.214	104.7	1.375	111.58	.338	93.4
.315	126.67	.218	104.6				

Velocity Profile

$u_j/u_{e_o} = 2.0$

Z = - 0.312 Inch p_a = 29.05 Inches Hg

Re_d = 43,600 x/d = 12.25

Y, in.	u ft/sec	p mm Hg	T °F	Y, in.	u ft/sec	p mm Hg	T °F
.015	98.34	.431	111.6	.335	141.57	.169	110.4
.035	114.66	.362	113.0	.355	140.89	.182	110.0
.055	120.15	.336	113.3	.375	139.98	.185	109.4
.075	121.89	.318	113.2	.425	137.06	.191	107.8
.095	124.63	.295	113.1	.475	132.15	.210	105.9
.115	126.38	.270	113.1	.525	126.87	.221	103.8
.135	128.59	.261	112.9	.575	121.33	.251	101.4
.155	129.34	.249	112.6	.625	116.97	.269	98.7
.175	131.18	.244	112.6	.675	114.05	.292	96.6
.195	132.51	.231	112.2	.775	111.88	.329	94.1
.215	134.63	.223	112.1	.875	111.49	.349	93.2
.235	136.05	.205	112.2	.975	111.12	.355	93.1
.255	137.98	.207	111.7	1.075	111.45	.342	93.0
.275	139.75	.201	111.5	1.175	111.57	.331	93.1
.295	140.91	.192	111.2	1.375	111.07	.331	93.0
.315	141.23	.191	110.7				

Velocity Profile

$u_j/u_{e_o} = 2.0$

Z = 0.437 Inch p_a = 29.05 Inches Hg

Re_d = 43,600 x/d = 12.25

Y, in.	u ft/sec	p mm Hg	T °F	Y, in.	u ft/sec	p mm Hg	T °F
.015	72.59	.364	101.4	.335	106.75	.285	98.0
.035	87.45	.317	100.8	.355	107.31	.290	97.6
.055	91.06	.321	100.9	.375	107.01	.300	97.5
.075	92.55	.300	100.7	.425	108.72	.304	96.7
.095	93.69	.291	100.3	.475	109.99	.317	95.9
.115	95.33	.284	100.0	.525	110.35	.334	94.8
.135	96.27	.291	99.9	.575	110.54	.326	94.5
.155	97.11	.279	99.8	.625	110.96	.341	93.8
.175	98.48	.261	99.6	.675	111.67	.356	93.4
.195	99.51	.267	99.5	.775	111.15	.360	93.0
.215	100.47	.256	99.1	.875	111.21	.353	93.1
.235	101.65	.264	99.1	.975	111.37	.345	93.1
.255	102.74	.279	98.8	1.075	111.08	.348	93.1
.275	103.42	.284	98.4	1.175	111.15	.342	93.0
.295	104.10	.282	98.3	1.375	111.38	.334	93.2
.315	105.76	.275	98.1				

Velocity Profile

$u_j/u_{e_o} = 2.0$

Z = - 0.437 Inch p_a = 29.06 Inches Hg

Re_d = 43,600 x/d = 12.25

Y, in.	u ft/sec	p mm Hg	T °F	Y, in.	u ft/sec	p mm Hg	T °F
.015	81.06	.389	107.3	.335	117.68	.223	104.0
.035	94.00	.345	107.5	.355	117.95	.227	103.3
.055	98.71	.314	107.8	.375	118.14	.233	103.1
.075	100.72	.294	107.3	.425	117.70	.236	101.9
.095	102.67	.289	106.7	.475	116.04	.261	100.4
.115	103.86	.274	106.4	.525	113.88	.279	98.7
.135	104.99	.261	106.4	.575	112.97	.293	97.2
.155	105.73	.258	105.9	.625	112.63	.317	95.5
.175	107.02	.250	105.5	.675	112.14	.328	94.6
.195	107.96	.231	105.4	.775	111.96	.341	93.3
.215	110.00	.244	105.4	.875	111.36	.356	93.1
.235	111.82	.233	104.9	.975	111.16	.343	93.0
.255	113.02	.234	104.7	1.075	111.51	.352	93.2
.275	115.15	.230	104.6	1.175	111.61	.335	93.0
.295	116.33	.232	104.3	1.375	111.19	.339	93.0
.315	117.33	.215	104.2				

Velocity Profile

$u_j/u_{e_o} = 2.0$

Z = 0.500 Inch p_a = 28.92 Inches Hg

Re_d = 43,600 x/d = 12.25

Y, in.	u ft/sec	p mm Hg	T °F	Y, in.	u ft/sec	p mm Hg	T °F
.015	69.69	.347	96.7	.335	101.69	.298	93.5
.035	82.12	.325	96.2	.355	102.68	.305	93.7
.055	85.74	.316	96.3	.375	104.20	.303	93.4
.075	87.55	.310	96.0	.425	106.15	.316	93.0
.095	89.10	.297	95.7	.475	108.15	.330	92.2
.115	89.56	.293	95.5	.525	109.34	.338	91.6
.135	90.16	.291	95.2	.575	110.66	.343	91.3
.155	90.95	.289	95.0	.625	110.96	.344	91.1
.175	92.53	.284	94.9	.675	112.03	.349	91.0
.195	93.33	.284	94.7	.775	111.77	.354	90.6
.215	94.35	.278	94.7	.875	111.99	.346	90.7
.235	96.64	.278	94.6	.975	112.10	.342	90.7
.255	96.71	.288	94.4	1.075	111.72	.340	90.9
.275	98.36	.287	94.3	1.175	111.76	.332	91.0
.295	99.16	.289	93.8	1.375	111.64	.327	90.4
.315	100.59	.290	93.8				

Velocity Profile

$u_j/u_{e_o} = 2.0$

Z = - 0.500 Inch $p_a = 28.93$ Inches Hg

$Re_d = 43{,}600$ $x/d = 12.25$

Y, in.	u ft/sec	p mm Hg	T °F	Y, in.	u ft/sec	p mm Hg	T °F
.015	67.96	.360	101.3	.335	107.38	.261	97.1
.035	83.45	.328	101.0	.355	108.49	.263	97.4
.055	88.08	.310	100.9	.375	109.88	.265	97.0
.075	90.10	.300	100.5	.425	110.78	.281	95.8
.095	91.94	.289	100.4	.475	111.33	.295	94.7
.115	92.99	.277	99.8	.525	111.58	.307	94.2
.135	94.19	.271	99.5	.575	111.45	.323	93.0
.155	95.41	.264	99.4	.625	111.87	.333	92.2
.175	96.21	.264	98.7	.675	111.97	.339	92.2
.195	97.55	.259	98.6	.775	111.68	.348	91.6
.215	99.42	.255	98.4	.875	111.78	.346	91.8
.235	100.81	.252	98.1	.975	111.36	.342	91.6
.255	102.62	.252	97.7	1.075	111.95	.340	91.5
.275	103.87	.258	97.7	1.175	111.97	.331	91.8
.295	105.68	.253	97.7	1.375	112.04	.323	91.6
.315	107.08	.264	97.4				

Velocity Profile

$u_j/u_{e_o} = 2.0$

Z = 0.937 Inch p_a = 28.91 Inches Hg

Re_d = 43,600 x/d = 12.25

Y, in.	u ft/sec	p mm Hg	T °F	Y, in.	u ft/sec	p mm Hg	T °F
.015	52.56	.341	93.2	.335	89.01	.325	89.9
.035	62.90	.333	92.7	.355	91.95	.315	90.1
.055	65.71	.325	92.2	.375	92.72	.333	89.9
.075	68.70	.321	91.9	.425	97.89	.332	89.8
.095	69.84	.311	91.8	.475	101.57	.337	89.8
.115	71.85	.312	91.7	.525	104.73	.344	90.1
.135	72.95	.311	91.7	.575	107.41	.347	90.0
.155	74.35	.309	91.3	.625	109.39	.348	90.2
.175	76.32	.302	91.0	.675	110.80	.355	89.9
.195	76.94	.307	91.3	.775	111.98	.348	89.9
.215	79.72	.305	91.1	.875	111.94	.351	89.8
.235	80.00	.311	91.4	.975	111.92	.342	89.8
.255	82.45	.305	91.0	1.075	112.07	.334	90.0
.275	83.76	.315	90.3	1.175	111.97	.329	90.2
.295	85.80	.313	90.2	1.375	112.32	.314	89.9
.315	87.43	.310	90.2				

Velocity Profile

$u_j/u_{e_o} = 2.0$

Z = - 0.937 Inch p_a = 28.92 Inches Hg

Re_d = 43,600 x/d = 12.25

Y, in.	u ft/sec	p mm Hg	T °F	Y, in.	u ft/sec	p mm Hg	T °F
.015	53.64	.353	92.2	.335	96.32	.326	90.2
.035	66.87	.336	91.6	.355	98.47	.321	90.4
.055	69.73	.336	91.0	.375	99.61	.329	90.2
.075	72.94	.325	91.0	.425	103.44	.334	90.4
.095	74.94	.318	90.9	.475	106.93	.341	90.4
.115	76.12	.314	91.0	.525	108.80	.350	90.4
.135	78.11	.313	90.6	.575	110.47	.351	90.1
.155	79.42	.315	91.0	.625	111.14	.353	90.6
.175	81.42	.309	90.6	.675	111.47	.354	90.3
.195	83.58	.312	90.4	.775	111.89	.349	90.2
.215	85.54	.311	90.6	.875	111.75	.349	90.4
.235	86.78	.313	90.6	.975	112.03	.342	90.6
.255	88.43	.314	90.3	1.075	111.97	.334	90.2
.275	90.67	.316	90.3	1.175	111.81	.335	90.2
.295	92.60	.317	90.1	1.375	111.95	.324	90.5
.315	94.22	.318	90.4				

Velocity Profile

$u_j/u_{e_o} = 2.0$

Z = 1.363 Inches p_a = 28.92 Inches Hg

Re_d = 43,600 x/d = 12.25

Y, in.	u ft/sec	p mm Hg	T °F	Y, in.	u ft/sec	p mm Hg	T °F
.015	51.13	.347	92.8	.335	92.26	.318	91.5
.035	64.52	.333	92.4	.355	94.65	.324	91.5
.055	68.33	.325	92.0	.375	96.52	.323	91.4
.075	70.84	.320	92.1	.425	100.73	.330	91.2
.095	72.05	.314	91.9	.475	104.34	.343	91.1
.115	73.74	.316	91.8	.525	107.50	.347	91.2
.135	74.57	.314	91.4	.575	109.50	.345	91.4
.155	76.73	.306	91.8	.625	110.68	.353	91.2
.175	77.82	.309	91.7	.675	111.20	.350	91.2
.195	79.32	.309	91.7	.775	111.77	.348	91.1
.215	81.34	.308	91.4	.875	111.47	.344	91.1
.235	83.74	.310	91.3	.975	111.76	.341	91.1
.255	85.23	.308	91.8	1.075	112.35	.336	90.9
.275	87.73	.311	91.4	1.175	112.25	.331	91.1
.295	88.93	.314	91.7	1.375	111.97	.323	91.0
.315	91.58	.313	91.5				

Velocity Profile

$u_j/u_{e_o} = 2.0$

Z = - 1.363 Inches $\quad p_a = 28.57$ Inches Hg

$Re_d = 43{,}600 \quad x/d = 12.25$

Y, in.	u ft/sec	p mm Hg	T °F	Y, in.	u ft/sec	p mm Hg	T °F
.015	53.20	.342	92.5	.335	94.81	.311	90.2
.035	64.97	.336	91.2	.355	96.33	.317	89.9
.055	69.33	.326	91.4	.375	98.45	.316	90.2
.075	70.98	.317	90.7	.425	102.18	.321	90.1
.095	72.68	.313	90.9	.475	105.32	.334	90.1
.115	74.57	.313	90.6	.525	107.66	.339	90.1
.135	76.19	.309	90.4	.575	109.65	.342	90.3
.155	78.01	.305	90.6	.625	110.98	.343	90.5
.175	79.73	.308	90.5	.675	111.67	.351	90.2
.195	81.76	.304	90.2	.775	111.88	.347	90.2
.215	83.71	.311	90.6	.875	112.02	.344	90.3
.235	84.75	.303	89.9	.975	111.72	.342	90.2
.255	87.01	.311	90.2	1.075	111.62	.334	90.2
.275	88.84	.313	90.2	1.175	111.82	.331	90.5
.295	90.42	.312	90.2	1.375	111.82	.320	90.3
.315	93.08	.310	90.2				

Velocity Profile

$u_j/u_{e_o} = 2.0$

Z = 0 Inches p_a = 29.09 Inches Hg

Re_d = 43,600 x/d = 16.26

Y, in.	u ft/sec	p mm Hg	T °F	Y, in.	u ft/sec	p mm Hg	T °F
.015	99.50	.347	109.6	.355	150.81	.139	108.9
.035	117.64	.278	111.2	.375	151.00	.146	108.3
.055	125.28	.243	111.9	.425	149.04	.136	106.9
.075	129.78	.240	112.1	.475	145.43	.135	105.5
.095	132.67	.214	112.3	.525	140.82	.140	103.9
.115	134.91	.211	112.2	.575	136.38	.151	102.3
.135	137.72	.196	112.1	.625	130.71	.175	100.5
.155	139.75	.194	112.1	.675	125.75	.191	98.7
.175	141.53	.176	111.7	.775	117.59	.217	95.1
.195	114.12	.168	111.9	.875	113.22	.229	92.6
.215	145.83	.163	111.4	.975	112.50	.250	91.3
.235	147.24	.162	111.3	1.075	112.17	.259	91.0
.255	148.69	.156	111.0	1.175	112.61	.253	90.9
.275	149.97	.160	110.6	1.375	112.25	.248	91.0
.295	150.47	.144	110.5	1.575	112.13	.247	91.0
.315	150.96	.144	109.8	1.775	112.57	.234	90.9
.335	150.95	.147	109.5	1.975	111.78	.237	90.8

Velocity Profile

$u_j/u_{e_o} = 2.0$

Z = 1.363 Inches p_a = 29.07 Inches Hg

Re_d = 43,600 x/d = 16.26

Y, in.	u ft/sec	p mm Hg	T °F	Y, in.	u ft/sec	p mm Hg	T °F
.015	55.78	.244	93.9	.335	95.79	.210	91.4
.035	68.10	.229	92.8	.355	97.13	.220	91.4
.055	73.22	.215	92.6	.375	99.20	.211	91.4
.075	75.04	.213	92.2	.425	102.80	.227	91.3
.095	77.91	.198	92.1	.475	104.86	.231	91.2
.115	78.91	.212	92.2	.525	108.91	.245	91.2
.135	80.36	.203	91.9	.575	110.44	.243	91.4
.155	81.99	.207	91.8	.625	111.35	.250	91.4
.175	84.29	.198	91.8	.675	112.31	.247	91.4
.195	85.18	.203	91.8	.775	112.71	.247	91.4
.215	86.39	.207	91.7	.875	112.32	.255	91.4
.235	87.77	.211	91.7	.975	113.04	.251	91.4
.255	89.59	.205	91.4	1.075	112.65	.253	91.4
.275	91.26	.212	91.5	1.175	112.22	.244	91.4
.295	92.67	.205	91.4	1.375	112.15	.250	91.6
.315	94.31	.208	91.4	1.575	112.05	.233	91.4

Velocity Profile

$u_j/u_{e_o} = 2.0$

Z = - 1.363 Inches $p_a = 29.06$ Inches Hg

$Re_d = 43,600$ $x/d = 16.26$

Y, in.	u ft/sec	p mm Hg	T °F	Y, in.	u ft/sec	p mm Hg	T °F
.015	53.91	.236	95.0	.335	95.31	.209	92.2
.035	67.89	.218	93.7	.355	96.39	.212	92.2
.055	72.75	.210	93.4	.375	98.17	.215	92.0
.075	74.86	.217	93.0	.425	101.97	.219	91.8
.095	76.75	.200	92.9	.475	105.47	.215	92.0
.115	78.64	.209	92.6	.525	108.16	.233	92.2
.135	80.03	.196	92.6	.575	109.72	.240	92.1
.155	81.66	.202	92.5	.625	111.08	.253	91.9
.175	81.98	.200	92.6	.675	112.24	.257	91.8
.195	84.88	.205	92.6	.775	112.19	.262	92.1
.215	85.52	.201	92.3	.875	112.14	.264	92.0
.235	87.08	.204	92.3	.975	112.36	.247	92.2
.255	88.63	.208	92.2	1.075	112.59	.254	92.1
.275	90.64	.208	92.2	1.175	112.35	.252	91.9
.295	91.83	.202	92.1	1.375	112.24	.245	92.2
.315	93.57	.207	92.2	1.575	112.59	.242	92.2

Velocity Profile

$u_j/u_{e_o} = 2.0$

Z = 0 Inches $p_a = 29.25$ Inches Hg

$Re_d = 43{,}600$ $x/d = 24.46$

Y, in.	u ft/sec	p mm Hg	T °F	Y, in.	u ft/sec	p mm Hg	T °F
.015	94.77	.153	100.6	.515	135.93	.078	97.3
.035	111.11	.145	101.8	.535	135.17	.083	96.7
.055	119.01	.124	101.9	.555	134.32	.081	96.7
.075	123.44	.111	102.2	.575	133.32	.085	96.3
.095	127.46	.105	102.2	.625	130.59	.085	95.4
.115	129.85	.107	101.9	.675	128.06	.095	94.2
.135	131.62	.102	102.0	.725	125.72	.094	93.0
.155	133.93	.094	101.9	.775	122.86	.099	92.3
.175	135.23	.092	101.8	.825	120.62	.112	91.4
.195	136.80	.085	101.7	.975	115.71	.125	88.7
.215	137.93	.089	101.8	1.075	114.26	.137	87.7
.235	139.15	.081	101.1	1.175	114.12	.140	87.2
.255	139.46	.085	100.9	1.275	114.07	.136	86.9
.275	140.00	.085	100.9	1.475	113.64	.145	86.8
.295	140.57	.086	100.3	1.675	114.15	.138	87.0
.315	141.00	.069	100.5	1.875	113.98	.133	87.0
.335	140.95	.072	100.3	2.075	113.48	.136	87.0
.355	140.82	.081	99.6	2.275	113.55	.131	87.1
.375	140.60	.075	99.4	2.475	113.44	.131	86.9
.395	140.09	.076	99.1	2.675	113.63	.125	87.3
.415	139.63	.084	98.7	2.875	113.51	.128	87.2
.435	139.26	.073	98.6	3.075	113.23	.127	87.3
.455	138.40	.078	98.5	3.275	113.22	.121	87.4
.475	137.82	.077	98.1	3.475	113.24	.118	87.4
.495	136.87	.086	97.5				

Velocity Profile

$u_j/u_{e_o} = 2.0$

Z = 0.125 Inch p_a = 29.28 Inches Hg

Re_d = 43,600 x/d = 24.46

Y, in.	u ft/sec	p mm Hg	T °F	Y, in.	u ft/sec	p mm Hg	T °F
.015	93.45	.147	98.6	.435	135.61	.073	96.2
.035	109.31	.140	99.5	.455	134.61	.075	96.1
.055	116.76	.124	99.8	.475	134.01	.071	95.9
.075	121.50	.114	99.9	.495	133.92	.066	95.5
.095	125.00	.103	99.7	.515	133.01	.079	95.1
.115	126.91	.103	99.4	.535	132.04	.079	95.3
.135	129.21	.088	99.9	.555	131.43	.078	94.7
.155	130.65	.089	99.8	.575	130.99	.082	94.3
.175	132.07	.083	99.5	.625	128.62	.084	93.4
.195	133.16	.085	99.2	.675	126.06	.088	92.2
.215	134.20	.077	99.2	.725	123.70	.097	91.6
.235	135.03	.078	98.7	.775	121.85	.104	90.6
.255	135.87	.071	98.6	.825	119.49	.116	89.4
.275	136.35	.067	98.4	.875	117.67	.122	88.3
.295	136.57	.075	98.3	.975	115.64	.137	87.4
.315	136.48	.079	97.9	1.075	114.70	.139	86.2
.335	136.43	.063	97.5	1.175	114.58	.141	86.1
.355	136.69	.065	97.6	1.275	114.15	.140	85.8
.375	136.62	.071	97.4	1.475	114.03	.140	85.3
.395	136.05	.070	97.2	1.675	114.15	.135	85.4
.415	135.62	.073	96.9	1.875	113.92	.137	85.6

Velocity Profile

$u_j/u_{e_o} = 2.0$

$Z = -0.125$ $\quad p_a = 29.29$ Inches Hg

$Re_d = 43{,}600$ $\quad x/d = 24.46$

Y, in.	u ft/sec	p mm Hg	T °F	Y, in.	u ft/sec	p mm Hg	T °F
.015	95.57	.159	100.2	.435	138.61	.084	98.3
.035	111.70	.140	101.8	.455	137.93	.085	98.0
.055	119.43	.123	101.9	.475	137.25	.086	97.5
.075	123.99	.111	102.3	.495	136.69	.085	97.6
.095	127.73	.110	102.3	.515	136.11	.081	97.1
.115	130.21	.105	101.9	.535	135.04	.081	96.8
.135	132.49	.093	102.3	.555	134.09	.083	96.7
.155	133.96	.095	101.9	.575	133.29	.084	96.4
.175	135.67	.091	101.6	.625	130.61	.083	95.5
.195	136.66	.091	101.7	.675	127.47	.092	94.4
.215	137.69	.087	101.5	.725	125.68	.100	93.6
.235	138.67	.086	101.2	.775	122.93	.100	92.1
.255	139.33	.085	101.1	.825	120.67	.109	91.4
.275	139.77	.083	100.7	.875	118.45	.113	90.0
.295	140.04	.084	100.3	.975	115.90	.122	88.5
.315	140.51	.080	100.3	1.075	114.28	.141	87.4
.335	140.73	.080	100.2	1.175	114.44	.140	86.9
.355	140.59	.081	99.6	1.275	113.91	.143	86.7
.375	140.10	.083	99.0	1.475	114.09	.147	86.6
.395	139.95	.077	99.1	1.675	113.99	.144	86.7
.415	139.44	.080	98.7	1.875	113.97	.134	86.8

Velocity Profile

$u_j/u_{e_o} = 2.0$

Z = 0.250 Inch p_a = 29.23 Inches Hg

Re_d = 43,600 x/d = 24.46

Y, in.	u ft/sec	p mm Hg	T °F	Y, in.	u ft/sec	p mm Hg	T °F
.015	91.19	.149	99.6	.435	128.23	.060	97.3
.035	106.58	.132	100.5	.455	127.39	.066	97.3
.055	113.39	.113	100.3	.475	127.62	.065	96.7
.075	117.35	.102	100.4	.495	127.70	.066	96.7
.095	120.21	.096	100.4	.515	126.59	.068	96.6
.115	122.09	.084	100.3	.535	126.39	.075	96.1
.135	123.98	.082	100.4	.555	126.05	.074	96.2
.155	125.01	.073	99.9	.575	125.16	.080	95.6
.175	126.20	.076	100.1	.625	124.04	.087	95.1
.195	127.53	.062	99.9	.675	122.17	.099	93.8
.215	127.52	.069	99.5	.725	120.31	.103	93.0
.235	127.67	.065	99.4	.775	118.96	.107	92.3
.255	128.26	.067	99.1	.825	117.57	.121	91.4
.275	128.91	.053	99.1	.875	116.61	.124	90.4
.295	128.28	.058	98.7	.975	115.23	.123	89.5
.315	128.45	.058	98.5	1.075	114.43	.140	88.8
.335	128.29	.066	98.4	1.175	114.31	.131	88.5
.355	128.31	.057	98.3	1.275	114.04	.143	88.3
.375	128.73	.062	97.8	1.475	114.01	.140	88.7
.395	128.55	.065	97.8	1.675	113.78	.142	88.5
.415	128.27	.057	97.7	1.875	113.94	.133	88.4

Velocity Profile

$u_j/u_{e_o} = 2.0$

Z = - 0.250 Inch $p_a = 29.21$ Inches Hg

$Re_d = 43{,}600$ $x/d = 24.46$

Y, in.	u ft/sec	p mm Hg	T °F	Y, in.	u ft/sec	p mm Hg	T °F
.015	94.33	.152	102.0	.435	134.32	.073	100.6
.035	110.84	.133	103.4	.455	133.70	.080	100.2
.055	117.51	.119	103.5	.475	133.12	.079	99.9
.075	122.51	.103	103.9	.495	132.69	.077	99.5
.095	125.03	.104	103.9	.515	132.08	.075	99.4
.115	127.32	.095	103.5	.535	131.64	.078	99.0
.135	128.78	.097	103.5	.555	130.73	.085	99.0
.155	130.12	.088	103.5	.575	129.44	.089	98.3
.175	131.25	.087	102.9	.625	127.48	.091	97.5
.195	132.21	.084	103.0	.675	125.58	.096	96.4
.215	132.45	.080	102.7	.725	123.22	.093	95.8
.235	133.43	.080	102.7	.775	120.83	.104	94.7
.255	134.04	.079	102.3	.825	119.05	.117	93.6
.275	134.38	.078	102.2	.875	117.45	.120	92.5
.295	134.32	.078	102.2	.975	115.23	.126	91.0
.315	135.18	.073	101.7	1.075	113.79	.135	90.0
.335	134.79	.077	101.7	1.175	113.99	.141	89.7
.355	134.83	.077	101.4	1.275	114.04	.145	89.4
.375	134.55	.074	101.0	1.475	114.01	.141	89.4
.395	134.57	.078	100.8	1.675	113.85	.141	89.6
.415	134.21	.078	100.7	1.875	113.79	.136	89.5

Velocity Profile

$u_j/u_{e_o} = 2.0$

Z = 0.312 Inch p_a = 29.10 Inches Hg

Re_d = 43,600 x/d = 24.46

Y, in.	u ft/sec	p mm Hg	T °F	Y, in.	u ft/sec	p mm Hg	T °F
.015	86.04	.175	103.7	.415	122.63	.059	100.7
.035	102.71	.127	103.9	.435	123.18	.064	100.7
.055	108.77	.112	104.3	.455	121.88	.082	100.3
.075	112.51	.102	104.2	.475	121.88	.066	100.1
.095	114.73	.088	104.7	.495	123.13	.066	99.9
.115	116.36	.089	103.9	.515	121.94	.072	99.6
.135	117.53	.085	103.7	.535	121.41	.092	99.5
.155	119.21	.083	103.5	.555	121.64	.091	99.1
.175	119.98	.075	103.3	.575	120.98	.089	99.0
.195	120.23	.072	103.1	.625	120.21	.104	98.3
.215	120.47	.076	102.9	.675	118.88	.115	97.4
.235	121.34	.066	102.6	.725	117.64	.113	96.7
.255	121.29	.065	102.8	.775	116.75	.135	95.7
.275	120.90	.060	102.3	.825	116.04	.131	94.9
.295	122.17	.062	101.9	.875	115.04	.138	94.4
.315	121.41	.056	101.5	.975	114.25	.151	93.5
.335	122.55	.074	101.5	1.075	113.58	.146	93.0
.355	121.63	.056	101.3	1.175	113.41	.145	92.6
.375	122.42	.072	101.2	1.275	113.46	.156	92.7
.395	122.49	.069	101.3	1.475	113.65	.146	92.7

Velocity Profile

$u_j/u_{e_o} = 2.0$

Z = - 0.312 Inch p_a = 29.09 Inches Hg

Re_d = 43,600 x/d = 24.46

Y, in.	u ft/sec	p mm Hg	T °F	Y, in.	u ft/sec	p mm Hg	T °F
.015	93.19	.178	106.7	.415	130.74	.088	104.3
.035	109.26	.140	107.3	.435	130.79	.082	103.8
.055	115.36	.116	107.6	.455	130.42	.086	103.8
.075	120.82	.117	107.6	.475	129.95	.095	103.4
.095	123.24	.103	107.5	.495	129.41	.091	103.0
.115	125.28	.093	107.7	.515	129.63	.086	102.7
.135	127.10	.080	107.5	.535	128.52	.096	102.7
.155	127.22	.089	107.3	.555	128.26	.077	102.2
.175	128.15	.098	106.8	.575	127.74	.088	101.9
.195	128.70	.084	106.8	.625	125.30	.093	101.1
.215	129.26	.088	106.4	.675	123.46	.109	100.0
.235	129.76	.084	106.2	.725	121.49	.108	99.0
.255	130.08	.078	106.2	.775	119.33	.112	97.9
.275	130.48	.081	105.9	.825	117.86	.126	96.9
.295	130.46	.091	105.4	.875	116.40	.126	95.9
.315	131.30	.078	105.7	.975	114.31	.142	94.3
.335	131.37	.076	105.3	1.075	113.66	.135	93.4
.355	130.88	.082	105.0	1.175	113.63	.145	93.0
.375	131.27	.080	104.8	1.275	113.80	.148	93.0
.395	131.37	.079	104.5	1.475	113.51	.137	92.9

Velocity Profile

$u_j/u_{e_o} = 2.0$

Z = 0.437 Inch p_a = 29.09 Inches Hg

Re_d = 43,600 x/d = 24.46

Y, in.	u ft/sec	p mm Hg	T °F	Y, in.	u ft/sec	p mm Hg	T °F
.015	81.19	.149	94.3	.415	113.25	.079	92.6
.035	96.24	.126	94.6	.435	113.99	.085	92.2
.055	101.59	.108	95.0	.455	113.70	.080	92.2
.075	104.92	.095	95.0	.475	114.49	.078	92.2
.095	107.11	.093	94.7	.495	114.01	.088	91.9
.115	107.41	.085	94.4	.515	114.44	.089	91.8
.135	108.45	.087	94.3	.535	114.64	.102	91.6
.155	110.17	.075	94.0	.555	114.62	.102	91.4
.175	110.05	.073	94.0	.575	114.99	.101	91.4
.195	110.66	.074	93.8	.625	115.48	.117	90.7
.215	111.33	.066	93.6	.675	115.29	.119	90.4
.235	111.33	.063	93.5	.725	115.41	.124	89.8
.255	110.99	.067	93.4	.775	114.52	.140	89.4
.275	110.51	.064	93.4	.825	114.66	.134	89.1
.295	111.27	.071	93.0	.875	114.15	.141	88.6
.315	111.75	.070	93.0	.975	114.51	.140	88.2
.335	111.44	.067	92.9	1.075	114.07	.147	87.8
.355	111.97	.071	92.6	1.175	113.55	.151	87.8
.375	112.35	.075	92.5	1.275	113.47	.157	87.8
.395	113.05	.071	92.5	1.474	113.54	.146	87.8

Velocity Profile

$u_j/u_{e_o} = 2.0$

Z = - 0.437 Inch p_a = 29.07 Inches Hg

Re_d = 43,600 x/d = 24.46

Y, in.	u ft/sec	p mm Hg	T °F	Y, in.	u ft/sec	p mm Hg	T °F
.015	87.01	.163	104.6	.435	123.25	.079	102.0
.035	102.33	.129	105.7	.455	123.17	.095	101.8
.055	108.71	.118	105.9	.475	123.13	.093	101.5
.075	112.38	.093	105.7	.495	122.58	.078	101.2
.095	114.34	.096	105.8	.515	123.30	.085	101.2
.115	115.83	.097	105.4	.535	122.71	.088	101.1
.135	116.88	.097	105.3	.555	122.55	.093	100.6
.155	117.32	.075	105.1	.575	122.26	.097	100.3
.175	118.39	.077	104.8	.625	121.13	.099	99.7
.195	118.50	.083	104.5	.675	119.68	.106	98.7
.215	118.96	.077	104.1	.725	118.27	.118	97.9
.235	120.09	.072	103.9	.775	116.83	.117	96.8
.255	119.77	.081	103.9	.825	116.07	.136	95.9
.275	120.73	.071	103.5	.875	114.90	.128	95.1
.295	121.03	.075	103.5	.975	114.41	.130	94.2
.315	121.22	.087	103.4	1.075	113.45	.152	93.3
.335	121.32	.076	103.0	1.175	113.28	.153	93.0
.355	121.83	.076	103.0	1.275	113.31	.133	93.0
.375	121.78	.080	102.6	1.475	113.89	.142	93.0
.395	122.42	.078	102.7	1.675	113.13	.150	93.2
.415	123.10	.069	102.6	1.875	112.95	.149	92.9

Velocity Profile

$u_j/u_{e_o} = 2.0$

Z = 0.500 Inch p_a = 29.19 Inches Hg

Re_d = 43,600 x/d = 24.46

Y, in.	u ft/sec	p mm Hg	T °F	Y, in.	u ft/sec	p mm Hg	T °F
.015	78.63	.120	97.9	.435	110.06	.075	94.3
.035	92.36	.111	97.8	.455	110.09	.079	94.3
.055	98.04	.099	98.2	.475	111.23	.079	94.3
.075	100.72	.089	98.1	.495	111.21	.085	94.3
.095	102.63	.083	97.7	.515	111.66	.090	94.2
.115	103.99	.073	97.5	.535	111.73	.104	93.5
.135	104.51	.074	97.2	.555	112.44	.096	93.7
.155	104.99	.067	96.6	.575	112.71	.101	93.6
.175	105.52	.071	96.6	.625	114.06	.108	92.8
.195	105.99	.068	96.7	.675	114.20	.114	92.5
.215	105.97	.062	96.4	.725	114.60	.124	91.8
.235	106.54	.062	96.2	.775	114.48	.133	91.5
.255	106.33	.061	96.0	.825	114.58	.126	91.3
.275	106.72	.064	95.9	.875	114.56	.131	90.7
.295	106.51	.061	95.7	.975	114.22	.141	90.3
.315	107.14	.062	95.3	1.075	113.95	.143	90.2
.335	106.88	.069	95.5	1.175	113.92	.146	90.2
.355	107.80	.073	95.1	1.275	113.76	.142	90.4
.375	107.72	.070	95.2	1.474	113.97	.137	90.3
.395	108.45	.071	94.7	1.675	113.65	.137	90.1
.415	109.33	.076	94.6	1.875	113.63	.138	90.2

Velocity Profile

$u_j/u_{e_o} = 2.0$

Z = - 0.500 Inch $p_a = 29.27$ Inches Hg

$Re_d = 43,600$ $x/d = 24.46$

Y, in.	u ft/sec	p mm Hg	T °F	Y, in.	u ft/sec	p mm Hg	T °F
.015	82.54	.140	93.4	.435	118.47	.079	91.0
.035	97.16	.115	94.2	.455	119.02	.082	91.3
.055	102.27	.109	94.2	.475	119.63	.081	91.3
.075	106.33	.096	93.9	.495	119.61	.085	91.0
.095	108.09	.082	94.0	.515	119.91	.083	90.6
.115	109.78	.080	93.7	.535	119.57	.086	90.7
.135	110.69	.082	93.4	.555	119.52	.097	90.5
.155	111.90	.076	93.3	.575	119.49	.094	90.0
.175	111.73	.082	92.9	.625	118.87	.102	89.6
.195	112.32	.073	93.3	.675	118.14	.111	88.8
.215	113.07	.077	92.6	.725	117.94	.121	88.1
.235	113.79	.075	92.6	.775	116.65	.121	87.3
.255	114.29	.069	92.6	.825	115.66	.128	86.5
.275	114.46	.070	92.3	.875	115.56	.127	85.9
.295	115.15	.077	92.0	.975	114.45	.137	85.3
.315	116.05	.067	92.2	1.075	114.49	.141	84.6
.335	116.26	.077	91.8	1.175	114.00	.139	84.6
.355	116.50	.072	91.9	1.275	114.03	.148	84.6
.375	117.52	.072	91.4	1.475	114.31	.141	84.3
.395	118.42	.077	91.8	1.675	113.87	.140	84.6
.415	118.40	.075	91.2	1.875	113.74	.143	84.6

Velocity Profile

$u_j/u_{e_o} = 2.0$

Z = 0.937 Inch p_a = 29.27 Inches Hg

Re_d = 43,600 x/d = 24.46

Y, in.	u ft/sec	p mm Hg	T °F	Y, in.	u ft/sec	p mm Hg	T °F
.015	56.58	.111	89.9	.435	99.95	.105	87.7
.035	68.39	.104	89.2	.455	100.91	.104	87.6
.055	72.92	.097	88.8	.475	102.05	.110	87.4
.075	75.57	.093	88.6	.495	103.19	.110	87.4
.095	78.57	.089	88.2	.515	103.97	.117	87.6
.115	79.97	.091	88.6	.535	105.07	.123	87.7
.135	81.38	.083	88.5	.555	106.16	.120	87.4
.155	83.12	.084	88.1	.575	107.38	.121	87.5
.175	84.40	.082	88.4	.625	109.31	.128	87.4
.195	85.76	.082	88.1	.675	111.21	.132	87.8
.215	86.77	.087	87.8	.725	112.72	.138	87.4
.235	88.07	.083	88.0	.775	113.31	.139	87.5
.255	88.95	.090	87.8	.825	113.98	.137	87.6
.275	90.82	.085	87.9	.875	114.28	.138	87.5
.295	91.77	.081	87.9	.975	114.27	.141	87.6
.315	92.93	.096	87.5	1.075	114.22	.142	87.4
.335	93.95	.093	87.8	1.175	114.19	.136	87.9
.355	94.62	.100	87.5	1.275	114.07	.141	87.8
.375	95.83	.094	88.0	1.475	114.28	.133	87.8
.395	97.41	.099	87.8	1.675	114.17	.133	87.4
.415	98.07	.107	87.8	1.875	113.64	.133	87.5

Velocity Profile

$u_j/u_{e_o} = 2.0$

Z = - 0.937 Inch p_a = 29.25 Inches Hg

Re_d = 43,600 x/d = 24.46

Y, in.	u ft/sec	p mm Hg	T °F	Y, in.	u ft/sec	p mm Hg	T °F
.015	59.30	.115	91.4	.435	106.03	.111	88.9
.035	72.91	.104	90.7	.455	106.97	.106	88.9
.055	77.69	.100	90.6	.475	108.09	.110	89.1
.075	81.18	.090	90.4	.495	109.21	.116	88.9
.095	84.02	.093	90.4	.515	109.75	.115	88.9
.115	85.13	.093	89.9	.535	110.23	.119	88.9
.135	87.16	.092	89.8	.555	111.16	.122	88.8
.155	88.08	.089	89.9	.575	111.93	.120	88.7
.175	90.10	.088	89.8	.625	113.05	.121	89.0
.195	91.44	.084	89.9	.675	113.79	.129	88.9
.215	92.56	.088	89.8	.725	113.39	.141	88.2
.235	93.68	.091	89.6	.775	113.89	.136	88.6
.255	95.32	.089	89.7	.825	114.15	.136	88.6
.275	96.73	.089	89.4	.875	114.07	.136	88.5
.295	98.55	.089	89.4	.975	114.19	.138	88.5
.315	99.02	.094	89.4	1.075	113.96	.139	88.6
.335	100.75	.095	89.5	1.175	113.91	.140	88.6
.355	101.72	.099	89.4	1.275	113.76	.142	88.6
.375	102.72	.100	89.0	1.475	113.81	.139	88.4
.395	103.82	.101	89.1	1.675	113.88	.136	88.6
.415	105.18	.109	89.0	1.875	113.59	.137	88.6

Velocity Profile

$u_j/u_{e_o} = 2.0$

Z = 1.363 Inches $p_a = 29.23$ Inches Hg

$Re_d = 43,600$ $x/d = 24.46$

Y, in.	u ft/sec	p mm Hg	T °F	Y, in.	u ft/sec	p mm Hg	T °F
.015	59.46	.111	91.6	.435	102.67	.109	89.3
.035	71.96	.100	90.6	.455	104.07	.105	89.2
.055	76.51	.094	90.6	.475	105.37	.112	89.1
.075	79.60	.090	90.3	.495	106.61	.106	89.4
.095	81.99	.088	90.0	.515	107.71	.117	89.3
.115	84.09	.089	89.8	.535	108.59	.111	89.0
.135	84.96	.087	90.2	.555	109.06	.121	89.0
.155	86.75	.087	89.9	.575	109.97	.118	89.5
.175	88.20	.090	89.8	.625	111.20	.126	89.5
.195	89.28	.091	89.8	.675	113.11	.132	89.6
.215	90.59	.089	89.4	.725	113.63	.132	89.4
.235	91.80	.087	89.6	.775	113.75	.135	89.5
.255	93.07	.088	89.4	.825	114.07	.135	89.4
.275	94.46	.091	89.4	.875	114.16	.137	89.5
.295	95.80	.085	89.5	.975	114.25	.135	89.5
.315	96.82	.095	89.8	1.075	114.03	.142	89.2
.335	97.80	.094	89.5	1.175	113.61	.138	89.4
.355	98.59	.096	89.4	1.275	113.83	.138	89.3
.375	100.28	.101	89.6	1.475	113.89	.136	89.4
.395	101.23	.099	89.5	1.675	113.91	.134	89.6
.415	102.34	.101	89.4	1.875	113.55	.140	89.4

Velocity Profile

$u_j/u_{e_o} = 2.0$

Z = - 1.363 Inches p_a = 29.20 Inches Hg

Re_d = 43,600 x/d = 24.46

Y, in.	u ft/sec	p mm Hg	T °F	Y, in.	u ft/sec	p mm Hg	T °F
.015	58.04	.108	92.7	.435	103.24	.099	90.4
.035	70.62	.097	91.7	.455	104.54	.098	90.5
.055	75.23	.096	91.4	.475	105.86	.099	90.5
.075	78.48	.094	91.0	.495	106.75	.101	90.4
.095	81.15	.086	91.3	.515	107.67	.105	90.6
.115	82.29	.093	91.0	.535	108.80	.106	90.5
.135	84.24	.085	91.0	.535	109.31	.116	90.6
.155	85.82	.085	91.0	.555	109.31	.116	90.6
.175	86.86	.080	91.1	.575	110.31	.116	90.2
.195	88.65	.085	90.7	.625	112.11	.121	90.5
.215	90.03	.084	90.9	.675	113.45	.127	90.1
.235	90.89	.088	90.8	.725	114.20	.131	90.5
.255	92.63	.088	90.5	.775	114.10	.129	90.4
.275	93.73	.086	90.6	.825	114.02	.135	90.4
.295	94.71	.092	90.2	.975	113.70	.142	90.6
.315	95.98	.092	90.8	1.075	114.14	.142	90.5
.335	97.15	.092	90.5	1.175	113.89	.141	90.5
.355	98.78	.090	90.5	1.275	114.02	.135	90.6
.375	100.08	.094	90.2	1.475	114.04	.136	90.6
.395	101.26	.093	90.3	1.675	113.63	.142	90.5
.415	101.98	.100	90.5	1.875	113.58	.137	90.6

Velocity Profile

$u_j/u_{e_o} = 2.0$

Z = 0 Inches $p_a = 29.19$ Inches Hg

$Re_d = 43,600$ $x/d = 35.68$

Y, in.	u ft/sec	p mm Hg	T °F	Y, in.	u ft/sec	p mm Hg	T °F
.015	85.27	.079	102.3	.435	131.81	.044	101.3
.035	100.93	.066	103.5	.455	131.52	.038	101.1
.055	108.50	.053	103.9	.475	131.10	.044	101.1
.075	113.51	.052	103.5	.495	130.68	.041	100.7
.095	117.38	.043	103.9	.515	130.65	.037	100.6
.115	119.77	.048	103.9	.535	129.93	.039	100.2
.135	122.43	.044	103.5	.555	129.61	.039	99.9
.155	124.41	.041	103.7	.575	128.93	.040	99.9
.175	126.09	.038	103.8	.625	127.76	.042	99.0
.195	127.61	.047	102.9	.675	126.37	.046	98.4
.215	128.87	.044	103.1	.725	124.74	.048	97.6
.235	129.55	.037	103.1	.775	123.49	.051	97.4
.255	130.65	.042	103.0	.825	121.89	.052	96.4
.275	130.86	.041	103.0	.875	120.20	.063	95.5
.295	131.71	.043	102.7	.975	117.83	.064	94.2
.315	131.68	.040	102.5	1.075	116.28	.071	92.9
.335	131.84	.041	102.3	1.175	115.29	.068	92.1
.355	131.96	.040	102.1	1.275	115.02	.074	91.8
.375	132.18	.040	101.9	1.475	113.93	.081	91.4
.395	132.35	.042	101.5	1.675	114.52	.077	91.4
.415	132.11	.039	101.5	1.875	114.50	.082	91.2

Velocity Profile

$u_j/u_{e_o} = 2.0$

Z = 1.363 Inches p_a = 29.05 Inches Hg

Re_d = 43,600 x/d = 35.68

Y, in.	u ft/sec	p mm Hg	T °F	Y, in.	u ft/sec	p mm Hg	T °F
.015	60.05	.059	95.4	.435	104.66	.044	93.1
.035	73.27	.041	94.7	.455	105.31	.050	93.0
.055	78.01	.040	94.4	.475	106.45	.049	92.9
.075	82.34	.025	94.0	.495	106.75	.044	93.0
.095	84.36	.035	94.0	.515	107.23	.059	93.0
.115	86.84	.028	94.0	.535	108.39	.053	93.0
.135	88.15	.032	93.8	.555	108.94	.054	93.0
.155	89.50	.031	93.8	.575	109.16	.063	93.0
.175	91.22	.025	93.5	.625	111.31	.056	93.0
.195	92.65	.029	93.4	.675	112.15	.066	92.9
.215	94.01	.021	93.5	.725	113.07	.074	93.0
.235	94.89	.034	93.4	.775	113.32	.084	93.0
.255	96.17	.032	93.4	.825	114.13	.079	93.0
.275	96.76	.021	93.4	.875	113.89	.087	92.8
.295	97.53	.033	93.3	.975	114.21	.075	93.0
.315	99.12	.035	93.4	1.075	114.36	.085	92.8
.335	99.89	.024	93.4	1.175	114.18	.083	92.6
.355	101.23	.033	93.2	1.275	114.49	.082	93.0
.375	101.88	.041	93.1	1.475	114.11	.082	93.1
.395	102.67	.036	93.0	1.675	114.06	.089	92.9
.415	103.19	.045	93.1	1.875	114.04	.079	93.0

Velocity Profile

$u_j/u_{e_o} = 2.0$

Z = - 1.363 Inches p_a = 29.05 Inches Hg

Re_d = 43,600 x/d = 35.68

Y, in.	u ft/sec	p mm Hg	T °F	Y, in.	u ft/sec	p mm Hg	T °F
.015	58.53	.056	96.0	.435	103.85	.047	92.6
.035	71.78	.038	94.1	.455	104.45	.041	92.7
.055	76.51	.030	93.9	.475	105.13	.045	92.8
.075	79.43	.026	93.8	.495	106.73	.049	92.6
.095	82.23	.022	93.7	.515	106.83	.054	92.9
.115	84.35	.034	93.4	.535	107.55	.046	92.6
.135	85.81	.023	93.5	.555	108.64	.056	92.6
.155	87.88	.026	93.4	.575	109.37	.054	92.7
.175	89.59	.027	93.1	.625	110.82	.066	92.6
.195	90.73	.028	93.2	.675	112.13	.068	92.5
.215	92.45	.027	93.2	.725	113.60	.056	92.6
.235	93.14	.028	93.0	.775	113.76	.069	92.6
.255	94.39	.028	93.0	.825	113.75	.080	92.6
.275	95.82	.030	92.9	.875	114.36	.085	92.6
.295	96.69	.032	93.0	.975	114.09	.081	92.5
.315	97.96	.032	93.0	1.075	114.25	.080	92.6
.335	98.07	.041	92.9	1.175	114.13	.086	92.4
.355	99.79	.035	92.7	1.275	114.14	.077	92.6
.375	100.51	.032	92.9	1.475	113.83	.088	92.6
.395	101.88	.036	93.0	1.675	114.03	.081	92.6
.415	102.53	.042	93.0	1.875	113.48	.088	92.6

APPENDIX D

DERIVATION OF INTEGRATED MEAN THICKNESSES

Displacement Thickness

For a three-dimensional, compressible boundary layer flow, where $u_e \neq u_e(z)$, $\delta \neq \delta(z)$, $\rho_e \neq \rho_e(z)$,

$$\begin{matrix}\text{Mass flow rate} \\ \text{in the boundary layer}\end{matrix} = \dot{m}_{B.L.} = \int_{z_1}^{z_n} \int_{o}^{\delta} \rho u \, dy \, dz$$

and

$$\begin{bmatrix}\text{The reduction in mass} \\ \text{flow rate in the boundary} \\ \text{layer caused by viscosity}\end{bmatrix} = \dot{m}_{IDEAL} - \dot{m}_{B.L.}$$

$$= \int_{z_1}^{z_n} \int_{o}^{\delta} (\rho_e u_e - \rho u) \, dy \, dz$$

Now let this reduction be represented by a height, $\delta^*_{I.M.}$, of freestream flow:

$$\rho_e u_e \, \delta^*_{I.M.} \, \Delta z = \int_{z_1}^{z_n} \int_{o}^{\delta} (\rho_e u_e - \rho u) \, dy \, dz$$

where $\Delta z = z_n - z_1$

Thus,

$$\delta^*_{I.M.} = \frac{1}{\Delta z} \int_{z_1}^{z_n} \int_{o}^{\delta} \left(1 - \frac{\rho u}{\rho_e u_e}\right) dy \, dz \, .$$

Momentum Thickness

For the same flow assumptions,

$$\text{Momentum flux through the boundary layer} = \int_o^{\delta} u \, d\dot{m}$$

$$= \int_{z_1}^{z_n} \int_o^{\delta} \rho u^2 \, dy \, dz$$

$$\text{Momentum flux without viscosity} = \int_o^{\delta} u_e \, d\dot{m}$$

$$= \int_{z_1}^{z_n} \int_o^{\delta} \rho u_e u \, dy \, dz$$

and,

$$\left[\begin{array}{l}\text{The reduction in momentum} \\ \text{flux in the B.L. due to} \\ \text{viscosity}\end{array}\right] = \int_{z_1}^{z_n} \int_o^{\delta} \rho u(u_e - u) \, dy \, dz$$

Now let this reduction in momentum flux be represented by a height, $\theta_{I.M.}$, of freestream flow:

$$\rho_e u_e^2 \, \theta_{I.M.} \, \Delta z = \int_{z_1}^{z_n} \int_o^{\delta} \rho u(u_e - u) \, dy \, dz$$

Thus,

$$\theta_{I.M.} = \frac{1}{\Delta z} \int_{z_1}^{z_n} \int_o^{\delta} \frac{\rho u}{\rho_e u_e} \left(1 - \frac{u}{u_e}\right) dy \, dz$$

Dissipation-Energy Thickness

For the same flow assumptions,

$$\text{Mechanical energy flux through the boundary layer} = \int_o^{\delta} \frac{u^2}{2}\, \dot{dm}$$

$$= \int_{z_1}^{z_n} \int_o^{\delta} \frac{\rho u^3}{2}\, dy\, dz$$

$$\text{Mechanical energy flux without viscosity} = \int_o^{\delta} \frac{u_e^2}{2}\, \dot{dm}$$

$$= \int_{z_1}^{z_n} \int_o^{\delta} \rho \frac{u_e^2}{2}\, u\, dy\, dz$$

and

$$\left[\begin{array}{l}\text{The reduction in mechanical} \\ \text{energy flux in the boundary} \\ \text{layer due to viscosity}\end{array}\right] = \int_{z_1}^{z_n} \int_o^{\delta} \frac{\rho u}{2} (u_e^2 - u^2)\, dy\, dz$$

Now let this reduction in mechanical energy flux be represented by a height, $\delta^{**}_{I.M.}$, of freestream flow:

$$\frac{\rho_e u_e^3}{2} \delta^{**}_{I.M.} \Delta z = \int_{z_1}^{z_n} \int_o^{\delta} \frac{\rho u}{2} (u_e^2 - u^2)\, dy\, dz$$

Thus,

$$\delta^{**}_{I.M.} = \frac{1}{\Delta z} \int_{z_1}^{z_n} \int_o^{\delta} \frac{\rho u}{\rho_e u_e} \left(1 - \frac{u^2}{u_e^2}\right) dy\, dz\ .$$

BIBLIOGRAPHY

1. Covault, C., "Upper-surface-blowing Cost Gains Cited," Aviation Week and Space Technology, Vol. 100, May 13, 1974.

2. Wolf, R. A., Editor, "The Status of V/STOL Aircraft Technology," School of Aerospace Engineering, Georgia Institute of Technology, September 1971.

3. Robinson, C. A., "XFV-12 May Spur Navy VTOL Family," Aviation Week and Space Technology, Vol. 98, April 16, 1973.

4. Whittley, D. C., "The Augmentor Wing: A New Means of Engine-Airframe Integration for STOL Aircraft," Proc. of the 4th Congress of the International Council of the Aeronautical Sciences, Paris, France, August 24-28, 1964.

5. Quinn, B. P., "Wind Tunnel Investigation of the Forces Acting on an Ejector in Flight," Aerospace Research Laboratory Report 70-0141, July 1970.

6. Quinn, B. P., "Experiments with Hypermixing Nozzles in an Area Ratio 23 Ejector," Aerospace Research Laboratory Report 72-0084, February 1972.

7. Quinn, B. P., "Recent Developments in Large Area Ratio Thrust Augmentors," AIAA Paper 72-1174, 1972.

8. Fiedler, R. A., and Gessner, F. B., "Influence of Tangential Fluid Injection on the Performance of Two-Dimensional Diffusers," Trans. of ASME, J. of Basic Engineering, September 1972.

9. McGregor, I., "Some Applications of BLC by Blowing to Air Inlets for V/STOL Aircraft," AGARD-CP-91-71, December 1971.

10. Harley, K. G., and Burdsall, E. A., "High-loading Low-speed Fan Study, Part II--Data and Performance, Unslotted Blades and Vanes," NASA CR-72667, 1969.

11. Mertaugh, L. J., and Roberts, S. C., "XV-11A Flight Test Programs," U.S. Army AVLABS-TR-70-37, November 1970.

12. Moon, I. M., "Distributed Suction Boundary Layer Control on Conical Diffusers," Mississippi State University, Aerophysics Dept. Res. Rpt. No. 17, August 1958.

BIBLIOGRAPHY (Continued)

13. Neale, D. H., "Experimental Study of Two-Dimensional Turbulent Wall Jet Development with and without Longitudinal Free Stream Pressure Gradients," Ph.D. Thesis, Georgia Institute of Technology, June 1971.

14. Gartshore, I. S., and Newman, B. G., "The Turbulent Wall Jet in an Arbitrary Pressure Gradient," The Aeronautical Quarterly, February 1969.

15. Harris, G. L., "The Turbulent Wall Jet on Plane and Curved Surfaces Beneath an External Stream," von Karman Institute for Fluid Dynamics, Technical Note 27, 1965.

16. Erin, F., and Eskinazi, S., "The Wall Jet in a Longitudinal Pressure Gradient," Syracuse University, Mechanical Engineering Department, Report ME-937-6410F, October 1964.

17. Nicoll, W. B., and Ramaprian, B. R., "Performance of Conical Diffusers with Annular Injection at Inlet," Trans. of ASME, J. of Basic Engineering, Vol. 92, No. 4, December 1970.

18. Knystautas, R., "A Turbulent Jet from a Series of Holes in Line," The Aeronautical Quarterly, Vol. 15, February 1964.

19. Naib, S. K. A., "Spreading and Development of the Parallel Wall Jet," Aircraft Engineering, Vol. 40, December 1968.

20. Foss, J. F., and Kleis, S. J., "A Study of the Round-Jet/Plane Wall Flow Field," Michigan State University, Div. of Engineering Research, First Annual Report, Grant NGR-23-004-068, October 1971.

21. Newman, B. G., Patel, R. P., Savage, S. B., and Tjio, H. K., "Three-Dimensional Wall Jet Originating from a Circular Orifice," The Aeronautical Quarterly, August 1972.

22. Chesters, J. H., Holden, C., and Robertson, A. D., "Protection of Refractories by Moving Air Curtains," J. of the Iron and Steel Institute, February 1957.

23. Smith, V. K., "Investigation of a Turbulent Wall Jet," Master's Degree Special Project Report, Georgia Institute of Technology, December 1970.

24. Utterback, N. G., and Griffith, T., "Reliable Submicron Pressure Readings with a Capacitance Manometer," Rev. of Scientific Instruments, Vol. 37, July 1966.

BIBLIOGRAPHY (Continued)

25. Patel, V. C., "Calibration of the Preston Tube and Limitations on Its Use in Pressure Gradients," J. of Fluid Mechanics, Vol. 23, September 1965.

26. Rayle, R. E., "An Investigation of the Influence of Orifice Geometry on Static Pressure Measurements," Master's Thesis, Mechanical Engineering Dept., Massachusetts Institute of Technology, 1949.

27. Ames Research Staff, "Equations, Tables and Charts for Compressible Flow," NACA Report 1135, 1953.

28. Scarborough, J. B., Numerical Mathematical Analysis, Fifth Edition, The Johns Hopkins Press, Baltimore, 1962.

29. Abramovich, G. N., The Theory of Turbulent Jets, MIT Press, Cambridge, Massachusetts, 1963.

30. Verhoff, A., "The Two-Dimensional, Turbulent Wall Jet with and without an External Free Stream," Princeton University Report No. 626, May 1963.

31. Gartshore, I. S., "Jets and Wall Jets in Uniform Streaming Flow," Mechanical Engineering Research Laboratories, McGill University, Report 64-4, May 1964.

32. Weinstein, A. S., Osterle, J. F., and Forstall, W., "Momentum Diffusion from a Slot Jet into a Moving Secondary," J. of Applied Mechanics, Vol. 23, No. 9, 1956.

33. Liaw, J., "Analysis of Two-dimensional Turbulent Wall Jets," Ph.D. Thesis, Georgia Institute of Technology, June 1975.

34. Schlichting, H., Boundary Layer Theory, Sixth Edition, McGraw-Hill Book Company, Inc., New York, 1968.

35. Bradshaw, P., and Gee, M. T., "Turbulent Wall Jets with and without an External Stream," Aeronautical Research Council R&M No. 3252, June 1960.

36. Coles, D. E., and Hirst, E. A., "Computation of Turbulent Boundary Layers," AFOSR-IFP-Stanford Conference, Vol. 2, 1968.

VITA

Virgil K. Smith, III, the elder son of Mr. and Mrs. Virgil K. Smith, Jr., was born in Hattiesburg, Mississippi on September 24, 1942. He attended elementary and secondary schools in Ackerman and Gulfport, Mississippi and graduated from Gulfport High School in June, 1960. Mr. Smith entered Mississippi State University in June, 1960 and transferred to Purdue University in June, 1961. He received his Bachelor of Science in Aerospace Engineering in June, 1965. At that time, he was also awarded a Commission in the U. S. Air Force and cited as a Distinguished Military Graduate. As an undergraduate, he was a member of the Arnold Air Society, the Air Force ROTC honorary society.

Mr. Smith was assigned as an aeronautical engineer in the Air Force Aero Propulsion Laboratory at Wright-Patterson AFB, Ohio from August, 1965 through July, 1969. His prime work area was in turbine engine research and development, serving as the U. S. Project Engineer for the U.S./U.K. Direct Lift Engine Project. He was awarded the USAF Commendation Medal for his contributions to the Laboratory's mission.

In September, 1969, Mr. Smith entered the Georgia Institute of Technology and began a graduate program in Aerospace Engineering. He also served as a graduate research assistant. Mr. Smith received his Master of Science in Aerospace Engineering in December, 1970.

In January, 1971, Mr. Smith entered the doctoral program in Aerospace Engineering. He was awarded a National Science Foundation Graduate

Traineeship and also served as a graduate research assistant. He was a student member of the American Institute of Aeronautics and Astronautics (AIAA).

In September, 1974, Mr. Smith accepted an appointment as an Assistant Professor of Aerospace and Mechanical Engineering at the University of Tennessee Space Institute. He currently teaches courses in airbreathing jet propulsion, aircraft performance and fluid mechanics. He organizes and conducts short courses in aeropropulsion and aeronautical ground testing, and conducts research in fluid mechanics. He is Educational Chairman of the Tennessee Section of AIAA and a member of the Society of the Sigma Xi.

On August 21, 1965, Mr. Smith married the former Patricia Ann Slade of Gulfport, Mississippi. They have a son, Kirk, and a daughter, Alexis Ann.